Aalborg Universitet

AALBORG UNIVERSITY
DENMARK

Chiroptical Metamaterials and Their Use in Bio-Sensing

Slyngborg, Morten

DOI (link to publication from Publisher):
10.5278/VBN.PHD.ENGSCI.00121

Publication date:
2016

Document Version
Publisher's PDF, also known as Version of record

Link to publication from Aalborg University

Citation for published version (APA):
Slyngborg, M. (2016). *Chiroptical Metamaterials and Their Use in Bio-Sensing*. Aalborg Universitetsforlag. Ph.d.-serien for Det Teknisk-Naturvidenskabelige Fakultet, Aalborg Universitet
https://doi.org/10.5278/VBN.PHD.ENGSCI.00121

General rights
Copyright and moral rights for the publications made accessible in the public portal are retained by the authors and/or other copyright owners and it is a condition of accessing publications that users recognise and abide by the legal requirements associated with these rights.

? Users may download and print one copy of any publication from the public portal for the purpose of private study or research.
? You may not further distribute the material or use it for any profit-making activity or commercial gain
? You may freely distribute the URL identifying the publication in the public portal ?

Take down policy
If you believe that this document breaches copyright please contact us at vbn@aub.aau.dk providing details, and we will remove access to the work immediately and investigate your claim.

Downloaded from vbn.aau.dk on: November 29, 2020

CHIROPTICAL METAMATERIALS AND THEIR USE IN BIO-SENSING

BY
MORTEN SLYNGBORG

DISSERTATION SUBMITTED 2016

AALBORG UNIVERSITY
DENMARK

Chiroptical Metamaterials and Their Use in Bio-Sensing

Ph.D. Dissertation

Morten Slyngborg

Dissertation submitted June, 2016

Thesis submitted: July 30, 2016

PhD Supervisors: Assoc. Prof. Peter Fojan, Aalborg University Prof. Thomas Garm Pedersen, Aalborg University

PhD Committee: Associate Professor Lars Diekhöner (chairman)
Department of Physics and Nanotechnology
Aalborg University, Denmark

Senior Researcher Morten Foss Interdisciplinary
Nanoscience Center
Aarhus University, Denmark

T.D. Researcher Giorgia Brancolini
Institute Nanoscience
CNR NANO, Modena, Italy

PhD Series: Faculty of Engineering and Science, Aalborg University

ISSN (online): 2246-1248
ISBN (online): 978-87-7112-736-2

Published by:
Aalborg University Press
Skjernvej 4A, 2nd floor
DK – 9220 Aalborg Ø
Phone: +45 99407140
aauf@forlag.aau.dk
forlag.aau.dk

© Copyright by author

Printed in Denmark by Rosendahls, 2016

Curriculum Vitae

Morten Slyngborg

Morten received his Master degree in Nanobiotechnology from the Department of Physics and Nanotechnology at Aalborg University, Denmark in 2011. Afterwards, Morten worked as a Ph.D. student at the Department of Physics and Nanotechnology at Aalborg University. His research is focused on sensors based on chiral plasmonic nanostructures for detection of biomolecules. Furthermore, his research interests are centered on biological and small molecules and their interactions with cells, proteins and surfaces in general, for medical and sensory applications and as antibacterial agents.

Abstract

The general purpose of this Ph.D. study was to develop plasmonic chiral metamaterials for biomolecule sensing based on circular dichroism spectroscopy.

Planar chiral metamaterials were fabricated to reproduce and improve upon previously reported sensing results [1]. Large-scale fabrication has been shown to produce heterogeneous samples due to drifting stigma in the e-beam lithography system. However, the many substructures resulted in many plasmonic resonance wavelengths, which were observed to yield a much more detailed protein fingerprint.

As e-beam lithography is inherently expensive, time-consuming and difficult, different approaches to develop other metamaterial fabrication methods were investigated. One such approach used polystyrene nanospheres arranged in self-assembled closely packed monolayers as nanolenses for UV lithography, glancing angle deposition and masks for selective etching in films or selective nanoparticle deposition. However, the formation of perfect closely packed monolayers proved difficult and the subsequent metamaterials hence contained many defects.

Instead, another high-throughput fabrication route was developed that produced extrinsic chiral metamaterials by a combination of anodic oxidation of aluminium, thermal nanoimprint and glancing angle deposition. These structures showed significant improvements compared to intrinsic chiral metamaterials, regarding chiroptical intensity, sensing reliability, ease of acquiring a protein fingerprint, fabrication through-put and production cost.

To verify a previous hypothesis that chiral metamaterials yield a distinct fingerprint for proteins that forms amyloid fibers [1], a peptide was designed and investigated by computational means. This peptide was used to probe the sensing abilities of the fabricated metamaterials towards amyloid fibers as proof of concept. The peptide was also experimentally studied and observed to form fibers that entangle into solid spheres. However, the fibers entanglement counteracted the uniqueness of amyloids in this regard. In addition, the peptide concentration, at which free fibers were formed, was too diluted to be measurable.

Resumé

Det overordnede formål med dette Ph.D. studie var at udvikle plasmoniske kirale metamaterialer til biomolekyle detektion baseret på cirkulær dikroisme spektroskopi.

Plane kirale metamaterialer blev fremstillet for at replikere og forbedre tidligere reporterede detektionsresultater [1]. Fabrikation på en stor størrelse har vist sig at producere heterogene prøver på grund af drivende stigma i e-stråle litografi systemet. Imidlertid resulterede de mange substrukturer i mange plasmoniske resonans bølgelængder, som førte til et mere detaljeret protein fingeraftryk.

Eftersom e-stråle litografi i sin natur er dyrt, tidskrævende og besværligt, blev forskellige tilgange til at udvikle andre metamateriale fabrikationsmetoder undersøgt. Sådan en tilgang anvendte polystyrene nanokugler, der var arrangeret i selv-samlende tætpakkede monolag som nanolinser til UV litografi, strejfende vinkel deponering og masker til selektivt ætsning i film eller selektivt nanopartikel deponering. Dog viste det sig at være svært at danne perfekte tætpakkede monolag og de resulterende metamaterialer indeholder derfor mange fejl.

I stedet for blev en anden hurtig-produktions rute udviklet, der producerede udefra virkende kirale metamaterialer ved en kombination af anodisk oxidering af aluminium, termisk nanoaftrykning og strejfende vinkel deponering. Disse strukturer udviste signifikante forbedringer i forhold til indefra virkende kirale metamaterialer med hensyn til kiroptisk intensitet, detektions pålidelighed, lethed af at opnå protein fingeraftrykket, fabrikationshastigheden og fabrikationsprisen.

For at verificere en tidligere hypotese om at kirale metamaterialer giver et tydeligt fingeraftryk for proteiner, der danner amyloid fibre [1], blev et peptide designet og undersøgt via computermidler. Dette peptide blev brugt til at undersøge detektions sensitiviteten af de fremstillede metamaterialer overfor amyloid fibre som et bevis for konceptet. Endvidere blev peptidet også eksperimentelt studeret og det blev observeret, at det danner fibre, der krøller sig sammen til solide kugler. Dog modvirker denne fibersammenkrølning det unikke ved amyloids i denne sammenhæng. Desuden var den peptide koncentration, hvor frie fibre blev dannet, for fortyndet til at kunne blive målt.

Contents

Thesis Details

Thesis Title:	Chiroptical Metamaterials and Their Use in Bio-Sensing
Ph.D. Student:	Morten Slyngborg
Supervisors:	Assoc. Prof. Peter Fojan, Aalborg University
	Prof. Thomas Garm Pedersen, Aalborg University

The main body of this thesis consist of the following papers.

[A] **Morten Slyngborg** and Peter Fojan, "A computational study of the self-assembly of the RFFFR peptide," *Phys. Chem. Chem. Phys.*, vol. 17, no. 44, pp. 30023-30036, 2015.

[B] **Morten Slyngborg**, Yao-Chung Tsao and Peter Fojan, "Large-scale fabrication of achiral plasmonic metamaterials with giant chiroptical response," *Beilstein Journal of Nanotechnology*, vol. 7, issn. 2190-4286, pp. 914-925, 2016.

[C] **Morten Slyngborg**, Dennis Achton Nielsen and Peter Fojan, "The Physical Properties and Self-Assembly Potential of the RFFFR Peptide," submitted to Langmuir, 7th May 2016.

In addition to the main papers, the following publications have also been made.

[2] **Morten Slyngborg**, Esben Skovsen and Peter Fojan, "An Investigation of the Interaction between Melittin and a Model Lipid Bilayer," *Journal of Self-Assembly and Molecular Electronics*, vol. 2, no. 1, pp. 53-76, 2014.

This thesis has been submitted for assessment in partial fulfilment of the Ph.D. degree. The thesis is based on the submitted or published scientific papers which are listed above. Parts of the papers are used directly or indirectly in the extended summary of the thesis. As part of the assessment, co-author statements have been made available to the assessment committee and are also available at the Faculty. The thesis is not in its present form acceptable for open publication but only in limited and closed circulation as copyright may not be ensured.

Preface

This thesis summarizes the main results achieved during my time as a Ph.D. student at the Department of Physics and Nanotechnology, Aalborg University, from December 2011 to June 2016 under the supervision of Associate Professor Peter Fojan. My main work during the Ph.D. study has been focused on plasmonic metamaterial fabrication for biomolecule sensing based on circular dichroism spectroscopy. As a model system for detection analyte, a peptide that self-assembles into amyloid fibers was developed and investigated experimentally and by computational means.

Acknowledgements

First, I would like to address a special thanks to my supervisor **Peter Fojan** for his guidance and very useful help even at busy times. I would also like to thank **Peter K. Kristensen** for his assistance in the cleanroom and for training me in the operation of the EBL system. **Leonid Gurevich** also deserves thanks for participating in academic discussions on my research and manuscripts and for sharing his experimental experiences. Additionally, **Hans Nilsson** and **Karina B. Jensen** also deserve thanks for creating sample holders and their assistance with ordering chemicals. I would also like to thank **Paw Simesen** and **Yao-Chung Tsao** for the good times we shared in the office and all my colleagues at the department in general for all the informal discussions.

Finally, a special thanks goes to my friends, family and girlfriend **Nadja** for understanding that science sometimes took precedence over my social life, their support and continued encouragement.

Morten Slyngborg
Aalborg University, June 28, 2016

Part I

Introduction

Chapter 1

Introduction

The development of modern technology is often inspired by phenomena occurring in nature that are governed by classical physics. Examples include the invention of self-cleaning surfaces by using the lotus effect inspired by the lotus plant leaf [3] or the water distilling membranes utilizing the protein, aquaporin [4], which allows water to pass through otherwise impenetrable cell walls in nature.

However, some materials are developed with properties that do not exist in nature. These materials are known as metamaterials and at times display characteristics that may seem supernatural as they contravene intuitive physical laws. Their applications are numerous and are relevant to many disciplines. For instance in the field of optics, metamaterials enable the fabrication of superlenses [5–7], invisibility cloaking devices [8] and lossless waveguide benders [9]. Other applications include the creation of artificial magnetism [10], more efficient solar cells [11], THz generation and THz optical components [12], beam broadband to create internet everywhere [13] and more advanced antennas such as wi-fi transmitters and receivers on a single chip at low cost that allows for integrating internet connection in more products [14]. In biotechnology, metamaterials show promise as enhancing contrast agents in photoacoustic tomography [15], spectroscopic labels or probes [16], sensors with unprecedented sensitivity [1] able to detect even single molecules [17], as well as surface enhancement of Raman spectroscopy [18], drug delivery vehicles [19] and photothermal therapy for cancer [20]. Many of these applications are only possible as a result of the unique properties of the metamaterials, others are significant improvements compared to alternative applications based on traditional materials. Consequently, the design of metamaterials and their properties have attracted an increased amount of interest [21].

The properties of metamaterials originate from the constituting substruc-

tures being smaller than the operating wavelength, shape, composition and arrangement [22]. The metamaterial substructures are often composed of noble metals with various structures arranged in periodically ordered arrays and long-range order is typically required. This yields a non-intuitive response from the interaction with electromagnetic waves having a comparable or smaller wavelength.

Standard fabrication techniques of metamaterials with substructures on the nanoscale are "top-down" approaches such as electron beam lithography (EBL) or focused ion beam (FIB) milling. These methods are inherently expensive and time-consuming, and hence concepts such as an invisibility cloak are often demonstrated with operating wavelengths in the microwave range [8]. However, the applications of metamaterials typically require operating wavelengths in the infrared (IR) or visible range. For this reason, metamaterials have so far been largely limited to academic research, rather than being integrated as an active part in consumer devices. To address this obstacle, new fabrication approaches utilizing "bottom-up" self-assembly have been attempted with different degrees of success [23–26].

This work is based on the previously demonstrated sensor applications of chiral metamaterials for use in circular dichroism (CD) spectroscopy [1]. CD spectroscopy is a powerful tool for the analysis of chiral molecules, which comprise most of the building-blocks in life such as proteins and DNA. It measures the small differences in the absorption of left- and right-circular polarized light to yield information about the structure of the analyte. However, the measurements require relatively high amounts of analyte in the microgram level, which is not sensible for sensor applications or medical applications [1, 27]. Compared to traditional CD spectroscopy of organic molecules, metamaterial based CD spectroscopy yields a very high response [1]. Typically, billions of molecules are needed to observe a CD response with traditional CD spectroscopy, but in this work 1.5 million PCM substructures were sufficient to acquire a measurable response. This large difference is related to the optical excitation of localized surface plasmons that greatly enhance the CD response at the localized surface plasmon resonance (LSPR) wavelengths. As the metamaterial geometry is chiral, the enhancement of the electric field is also chiral, which is termed superchiral fields [1]. Opposed to traditional CD spectroscopy where the measurements are directly related to the analyte, metamaterial based CD spectroscopy measures the small changes in the CD response from the metamaterials upon adsorption of an analyte of interest. These changes are induced because the LSPR wavelengths are sensitive to the dielectric environment of the near metamaterial surface, enabling the detection in the picogram range [1, 27]. When the analyte is adsorbed in an anisotropic way the coupling between the superchiral field and the adsorbed molecules is very large, resulting in a dissymetry factor. The dissymetry factor of many LSPR modes has been observed to be a fingerprint of the

adsorbed protein, enabling the identification of proteins based on their secondary structure [1].

This work has attempted both to replicate and improve upon the PCM subunit structure of the previously reported sensor system [1] in regard to an enhanced CD response, fabrication throughput and experimental reliability. Similar PCM subunit structures were fabricated with EBL and the sensing capabilities were tested with a variety of proteins.

In an attempt to fabricate PCMs in a high-throughput way, closely packed monolayers of polystyrene (PS) nanospheres (NS) were used as nanolenses in a UV-lithography process. These closely packed PS NS were also used as a mask for gold nanoparticle deposition in attempts to avoid expensive e-beam evaporation techniques. Furthermore, the hole arrays, fabricated in the PS NS UV lithography process, were used as a mask to etch subwavelength hole arrays in gold films. Such hole arrays have recently been demonstrated to function as extrinsic chiral metamaterials (ECMs) meaning that the subunits are not chiral, but exhibit a CD response when the sample is tilted relative to the normal angle of incidence [28]. Compared to PCMs, ECMs exhibit a huge CD response and are also less sensitive to structural defects [28].

Very few different ECMs have so far been reported and including theoretical suggestions only comprise hole arrays [28–30], U-shaped arrays [31, 32], split ring arrays [31], plasma sphere arrays [33], gold dot arrays [34], gold square arrays [35], metal disk arrays [36], two layer hole arrays [37], PS NS templates for gold deposition [38] and structures formed by carbon nanotubes [39]. Very few of these structures are produced by high-throughput techniques. However, based on three large-scale methods, anodic oxidation of aluminum, thermal nanoimprint and glancing angle deposition, a variety of new ECMs were fabricated in this work. The structures achieved through anodic oxidation of aluminium and thermal nanoimprint have previously been reported with respect to improving the efficiency of solar cells [40, 41]. Furthermore, nanoimprint has also previously been used for fabrication of larger U-shaped ECM substructures [32]. In general, nanoimprint is gaining interest due to the simplicity, low-cost, and high-throughput compared to other "top-down" nanofabrication approaches [42]. The lowest reported feature sizes are in the sub 50 nm range [43, 44], which does not quite compare to those obtained by EBL, FIB methods or extreme UV lithography. However, the aforementioned advantages render nanoimprint applicable for the commercial fabrication of many different devices. Hence nanoimprint is an ideal method for ECM fabrication.

One of the biological phenomena that ECM based CD spectroscopy is particularly suitable for is the study of self-assembled peptide structures. While CD spectroscopy is a powerful tool to study self-assembly, traditional CD spectroscopy requires a high peptide concentration [27], particularly when supramolecular structures are formed. Hence it is inherently difficult to

study peptide structures that exist at low concentration or when diluting below the critical self-assembly concentration. Such an example could be the detection of peptides or proteins related to amyloid diseases that typically exist at very low global concentrations and cannot be diagnosed by circumstantial evidence [45, 46]. Therefore it is difficult to treat many amyloid diseases, even though type-specific therapies are available, as the diagnosis requires direct study of the related protein which can be very difficult [45–47]. However, it has been postulated that the unique secondary and supramolecular structure of amyloids yields a specific protein fingerprint when probed by chiral metamaterial CD spectroscopy, enabling a very sensitive diagnosis method [1].

To probe this hypothesis, an amyloid model system was developed by virtually screening some short peptides for their propensity to self-assemble into amyloid fibers. One peptide, RFFFR, showed more potential than the others and was designed and inspired by the LVFFA motif from the β-amyloid peptide that plays a crucial role in Alzheimers disease [48]. Other peptides inspired by LVFFA include FF [49, 50] and FFF [51, 52] but these do not form amyloid like structures. However, the arginine residues in RFFFR restrict the interactions of peptides to one direction, enforcing a fiber formation with an amyloid structure. The self-assembly of the RFFFR peptide was investigated by computational means at different levels. Coarse-grained molecular dynamics simulations enabled very long timescales to monitor the self-assembly process. To achieve more detailed information, these coarse-grained simulations were then converted into full atomistic detail and used for atomistic molecular dynamics simulations. The results and the overall stability of the self-assembly were then verified by semi-empirical quantum mechanical calculations.

The self-assembly process was also investigated with different biophysical methods such as spectroscopy, atomic force microscopy and scanning electron microscopy. These measurements indicated a good agreement between the simulations and the empirically determined results. However, it was also observed that the peptides not only form 1-dimensional fibers as predicted by the simulations, but form more complex 3-dimensional fiber entangled structures in solution instead. RFFFR peptide structures were then used as a model amyloid system to probe the applicability of the fabricated ECM structures as a detection system of amyloid related diseases.

Chapter 2

Planar Chiral Metamaterials

Chirality was first observed by Louis Pasteur in 1848 [53] and later defined by Lord Kelvin [54]. Today, it is known that chirality is a major part of chemistry and biology. The spectroscopic tools available to study chiral structures primarily constitute CD spectroscopy variants such as standard UV/visible/IR CD [27], fluorescence detected CD [55] and vibrational CD [56] spectroscopy as well as optical rotatory dispersion [57]. These methods are important as two isomers have the same chemical structure but can exhibit significantly different biological properties regarding pharmacology, toxicology, pharmacokinetics and metabolism [58]. Furthermore, the measurements yield structural information such as the secondary or tertiary structure of proteins that are applicable in many different studies. However, the applications of CD spectroscopy are limited by a poor concentration sensitivity and the lowest amount of probable analyte is in the microgram range [1, 27].

Inorganic chiral materials, such as planar chiral metamaterials (PCMs), have demonstrated larger chiroptical responses compared to biomolecules [1]. PCMs consist of subwavelength metallic structures, arranged in a periodic order that cannot be brought into congruence with their mirror image (the enantiomer) unless lifted off the substrate. Thus these structures absorb right and left circular polarized light differently, which gives rise to a CD response. Though the generation of unusually large CD responses from PCMs has been known for a long time [59], the origin was first suggested later [60]. When probed, optical excitation of PCMs generates a collective oscillation of the conduction electrons in the metal surface. This oscillation of electrons at the surface is also known as localized surface plasmons. At certain wavelengths the coupling between photons and the conduction electrons at the interface is particularly strong (the LSPR wavelengths), yielding an enhanced CD response and electric field at these wavelengths. However, since PCM substructures are chiral, the enhancement of electric fields is also

chiral, a phenomena termed superchiral fields [1, 60]. Later the application of superchiral fields for biosensing was demonstrated to increase the sensitivity of CD spectroscopy to render detection of biomolecules in the picogram quantity possible [1].

When biomolecules are adsorbed on the surface of PCMs, it causes a shift in LSPR wavelength as it induces a change in the dielectric environment near the surface of the PCM structures. It has been observed that different proteins induce different shifts and the plasmonic resonance modes are not equally sensitive towards changes in the dielectric environment [1]. Furthermore, the enantiomeric structures result in the same LSPR wavelengths but the handedness governs whether right or left circular polarized light is absorbed more. Hence the CD response of enantiomeric PCMs will be mirror images. The mirror image modes located at the same LSPR wavelengths are not always similarly affected by a change in dielectric constant, resulting in different degrees of wavelength shifts. This difference is parameterized as the dissymmetry factor: $\triangle\triangle\lambda = \triangle\lambda_{righthanded} - \triangle\lambda_{lefthanded}$. The dissymmetry factor of more modes thus yields a protein fingerprint that is sensitive towards the protein secondary structure. Proteins having a $\triangle\triangle\lambda \neq 0$ are adsorbed as an anisotropic layer on the PCM surface and are mainly β-sheet rich proteins, while α-helix rich proteins adsorb as an isotropic layer and have a $\triangle\triangle\lambda = 0$ [1]. For this reason, PCM based CD spectroscopy only yields a fingerprint of β-sheet rich proteins.

Today, a large variety of PCMs have been reported [1, 59, 61–64]. Yet the number of papers to actually demonstrate sensing of any molecules using chiral metamaterials, and not just PCMs, is very small [1, 65] and most papers only suggest that their chiral metamaterials are applicable for sensing of biomolecules. While this is true for chiral metamaterials, sensing by metamaterials using plasmonic resonance shifts is generally well studied [17, 66–69]. The advantage of PCMs over traditional metamaterial sensing is that the protein fingerprint is obtained and that the sensing is by label free means. Hence a biomolecule can be recognized and studied in a more natural state after which the PCM sample can be reused many times. Traditional metamaterial sensing generally requires functionalization of the surface. Otherwise, it is impossible to differentiate adsorbed molecules based on similar plasmonic resonance shifts. For these reasons, efforts to replicate the reported PCM sensing results [1] were attempted in this work with the goal of optimizing the sensing capabilities.

In general, the fabrication of metamaterials with LSPR in the visible to near-IR wavelength area is inherently difficult and requires advanced techniques such as electron beam lithography (EBL) or focused ion beam (FIB) milling/deposition/lithography. The relation between the metamaterial structure and the resulting LSPR wavelengths is not intuitive as it depends on the size, shape, composition and local environment of the metamaterial sur-

face [22]. For biosensing applications, gold (Au) is the most common material even though silver and aluminium generally yield lower LSPR wavelengths [70, 71], but the Au surface does not oxidize and for this reason no dampening effect of the LSPR is observed over time [72]. The relation between the smallest structural feature and resulting LSPR wavelength has been studied for some structures [71, 73]. From these studies it is observed that structures having a 60 nm feature or smaller have major LSPR within the 350-900 nm wavelength range [71, 73], used for obtaining a protein fingerprint by CD spectroscopy [1]. However, gammadions that have a feature size as large as 80 nm have previously been reported to demonstrate a strong chiroptical response in the 350-900 nm wavelength range [1]. From the list of reported Au structures and their resulting CD response wavelength range in Table 2.1, it is estimated that the largest feature size that will result in an applicable CD response is approximately 100 nm.

Table 2.1: List of reported Au metamaterial structure and the resulting CD response range.

Metamaterial structure	Smallest feature	Unit cell	CD response range	Source
Arranged nanoparticles	20-80 nm	-	Visible	[74]
Gammadion	80 nm	400 nm	Visible-near IR	[1]
Sawtooth gratings	110 nm	450 nm	Visible-near IR	[75]
Trisceli structure	60 nm	400	near IR	[76]
3D spiral	300-500 nm	2000 nm	Mid IR	[77]

Such high resolution is slightly outside of the achievable resolution of direct-laser writing and requires EBL or FIB methods, which are routine top-down fabrication techniques for metamaterials. While EBL and FIB methods can produce isolation features and a half-pitch as low as 2 and 5 nm, respectively [78, 79]. Extreme UV lithography can produce a high resolution with a half-pitch of 18 nm [80], but is much more expensive and not sensible for prototype development of metamaterials. The major disadvantage of EBL and FIB methods is the low throughput due to the time required for resist exposure/milling/deposition, stage movement and beam settling. The typical reported area of metamaterials is in the mm^2 range (Table 2.2). However, these areas are still sufficient to produce a significant CD response [1] and hence this work has attempted to fabricate gammadions and other structures with features suitable for generation of LSPR in the visible wavelength range by EBL.

Table 2.2: List of reported metamaterials areas fabricated by EBL or FIB.

Metamaterial structure	Area	Technique	Source
Hole array	$5 \times 5\ mm^2$	EBL	[81]
Gammadion	$5 \times 5\ mm^2$	EBL	[1]
Gammadion	$400 \times 400\ \mu m^2$	EBL	[82]
Rectangles	$400 \times 400\ \mu m^2$	FIB	[35]
Hole array	$200 \times 200\ \mu m^2$	FIB	[30]
Hole array	$200 \times 200\ \mu m^2$	FIB	[28]
VU shape	$90 \times 90\ \mu m^2$	EBL	[83]
Groovy lines	$70 \times 70\ \mu m^2$	EBL	[83]

1 PCM Fabrication by E-beam Lithography

The gammadion is one of the simplest chiral patterns and was also used in the first paper to report of biosensing based on PCMs [1]. For these reasons, it was chosen as the first structure to be fabricated by EBL in this work. Initially, different sized structures were fabricated with success. Structures as small as 1000 nm were fabricated without any defects (Figure 2.1a). However, smaller structures were required to yield plasmonic resonance in the visible and near-UV wavelength range (Table 2.1). Structures with features similar to the reported gammadions [1] were fabricated with a size of 400 nm (Figure 2.2). At this size, the quality of the structures depends on all factors in the fabrication process but most heavily on exposure dose, stigmatism, focus, development method and calibration of the sample tilt. After much optimization of all steps, structures slightly better than those previously reported [1] were achieved (Figure 2.1b). Still, some proximity effect problems in corners and some stigma errors are observed. Furthermore, even small differences in equipment calibrations were sufficient to create very different results in structure quality, meaning that the structures could not be reliably reproduced from sample to sample. Hence a large amount of time was spent on preparing for the fabrication of very expensive samples with structures covering large areas, required when measuring a CD response.

The fabrication of samples with structures covering $1 \times 1 mm^2$, required 12 hours of writing in the EBL system. During this time, the stigma would drift significantly, resulting in initially good quality structures (Figure 2.3a) but deformed structures by the end of the writing process (Figure 2.3b). As this was a gradual drift, many structures in between these two extremes were observed on the same sample. To solve the problem, the division of the writing process into small sessions and performing calibrations in between each session was considered. However, this would require an extreme amount of continuous work, which was not feasible for one person. Furthermore, breaks

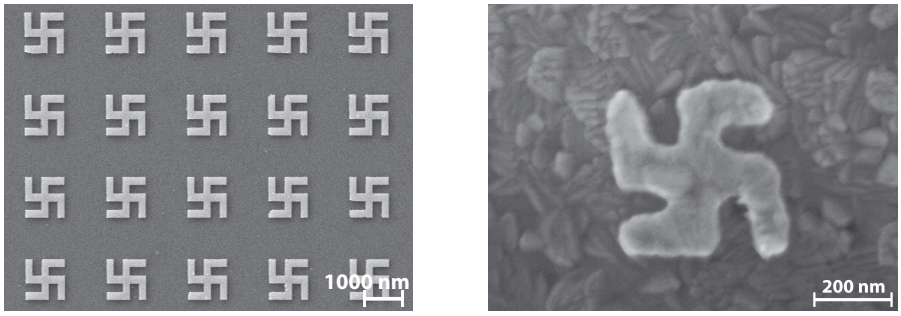

Figure 2.1: SEM pictures of gold PCM gammadions in different sizes, fabricated on indium tin oxide coated quartz by EBL. The contrast difference is caused by a differencet structure height. (a)1000 nm gammadions, showing no stigma problems. (b) 400 nm gammadions, showing some stigma problems and proximity effects.

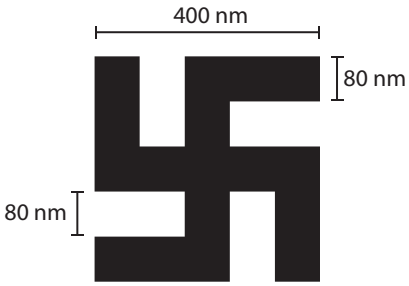

Figure 2.2: The model after which the gammadion in Figure 2.1b was exposed in the EBL process.

would require realignment, which was determined to be impossible. Another solution was attempted by using the proximity effect of underexposed lines that would only be sufficiently exposed when having two neighbour lines. Through careful optimization, very fine gammadions with features as small as 31 nm were fabricated (Figure 2.4a). Further optimization would be able to remove the defects observed in the corners by adding or removing lines in underexposed or overexposed areas, respectively. However, the time required for exposure also increased dramatically, rendering the fabrication of large areas infeasible.

Later, a script that performs an auto-stigma adjustment with different time intervals was tested. This script eliminated any problems with drifting stigma (Figure 2.4b), enabling very long writing periods. However, several large-scale fabrication techniques were being developed (to be described later in this work) before the auto-stigma adjustment script was tested. Hence it was decided not to attempt further fabrication of PCMs by EBL during this work.

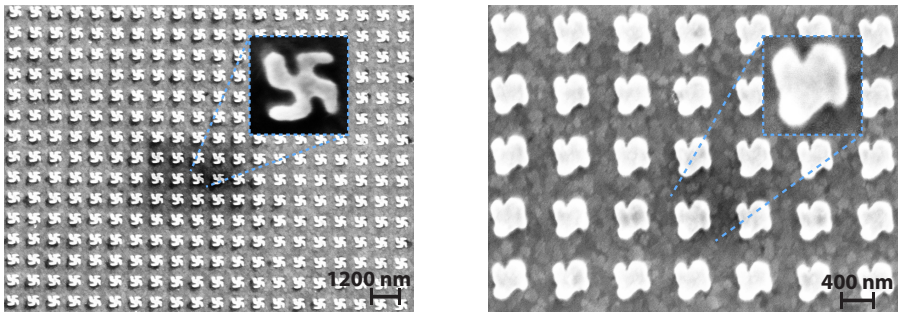

(a) (b)

Figure 2.3: SEM pictures of the sample with a large area of fabricated PCM gammadions on indium tin oxide coated quartz by EBL with a height of 50 nm. The EBL of large areas had trouble with drifting stigma. Hence the gammadions were gradually deformed. (a) The gammadions in the beginning of the EBL. (b) The most deformed gammadions, resulting in a N-shaped PCM structure. Different structures in between the two extremes were present on the sample sample.

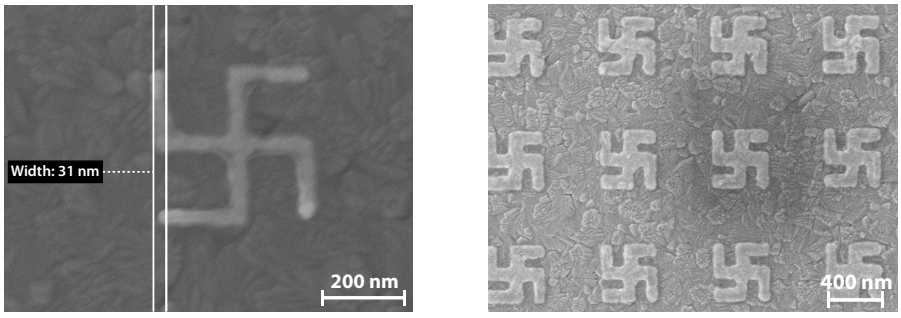

(a) (b)

Figure 2.4: SEM pictures of gold gammadions fabricated by EBL showing little to no stigma problems. (a) A gammadion structure that was fabricated by use of the proximity effect of neighbouring lines. The exposure dose was optimized so a single or double line would not be developed, but only lines with two neighbouring lines. Hence, very fine features could be created at the expense of writing time. (b) Gammadions that were created without manual stigma calibration, but with an automated calibration script, eliminate stigma drifting.

2 Chiral Molecule Sensing

The most successfully fabricated sample with a large area of structures, was the sample described above with many different substructures on the same sample and is depicted in Figure 2.3. This PCM sample exhibits a large amount of LSPRs when probed by CD spectroscopy (Figure 2.5a). Generally, when compared to other chiral metamaterials, and not just PCMs, the amount of resonance modes is very large (Table 2.3). This is likely explained

Table 2.3: Table of reported chiral metamaterials and the resulting amount of LSPR observed when probed by CD spectroscopy.

Metamaterial structure	# of modes	Source
This work	8	Figure 2.5a
Chiral shell like structures	7	[84]
Gammadion	4	[1]
Chiral hole array	3	[85]
Triangle oligomers in spiral-like shapes	3	[86]
Dual layered gammadion	2	[61]
DNA scaffold nanoparticle ornamentions	2	[74]
Nanorods with collective chiral geometry	1	[87]
3D spirals and rods	1	[88]

by the many different substructures on the same sample. In spite of this, the observed LSPRs are predominantly very narrow. Hence the current PCMs could yield an improved protein fingerprint, as more LSPRs yield more information to identify the protein on.

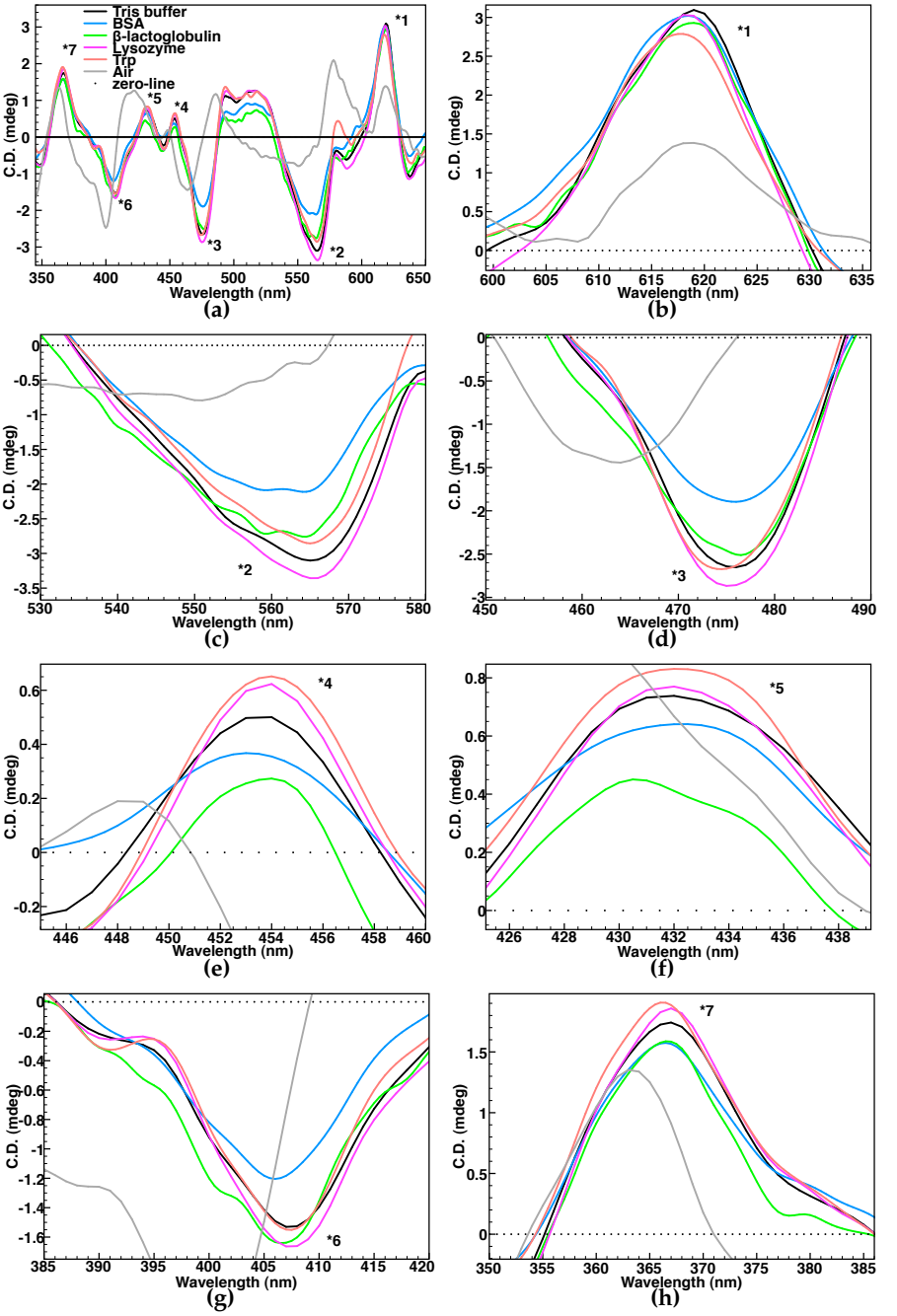

Figure 2.5: The resulting CD response from the fabricated large area PCM sample depicted in Figure 2.3, with different proteins, tryptophan, Tris buffer and air molecules adsorbed on the PCM surface. (a) The whole recorded CD wavelength spectrum. (b) Plasmonic resonance mode *1. (c) Plasmonic resonance mode *2. (d) Plasmonic resonance mode *3. (e) Plasmonic resonance mode *4. (f) Plasmonic resonance mode *5. (g) Plasmonic resonance mode *6. (h) Plasmonic resonance mode *7.

The intensity of the CD response is low compared to another report of the gammadion structure [1]. However, considering that the PCM area in this work is 25 times smaller than the one previously reported, the difference is not large. When scaling the observed modes (Figure 2.5a) by 25, several modes are comparable to the 120 mdeg response of the strongest mode from the previously reported gammadions [1]. Hence the intensity has not suffered significantly from the diverse substructure geometries on the same sample.

Measuring the dissymmetry factor ($\triangle\triangle\lambda = \triangle\lambda_{righthanded} - \triangle\lambda_{lefthanded}$) requires the measurement of both enantiomeric PCMs with a protein of interest adsorbed on the surface. Due to instabilities of the EBL system, it was impossible to produce a mirror image of the existing PCM sample. Hence the dissymmetry factor, used to determine if a protein adsorbs in an isotropic or anisotropic way on the PCM surface, was not directly measurable. However, as proof of concept and to probe the applicability of the fabricated PCM sample, different proteins and the amino acid tryptophan were individually adsorbed on the PCM surface, to measure the resulting LSPR shifts (Figure 2.5). The position of suitable CD modes and the shifts induced by the different biomolecules are listed in Table 2.4. Compared to the wavelength repeatability of the used CD spectroscope, $\pm$0.1 nm in the 250 to 500 nm wavelength interval and $\pm$0.2 nm in the 500 to 1100 nm wavelength interval, some of the induced shifts are very large compared to what has previously reported [1]. Hence the amount of different substructures on the same sample has not diminished the sensitivity of the fabricated PCM either.

The shifts induced by air are larger than those induced by the proteins by an order of magnitude. The degree of the shifts is governed by the change in dielectric constant of the near PCM surface environment, the coverage and thickness of the adsorbed molecules. The sensing distance perpendicular to the gold surface (decay length) is in the range of 10-50 nm in the measured wavelength range for localized surface plasmons [89–91], hence all molecules within this distance from the PCM surface contribute to the LSPR wavelength location. It is therefore not possible to achieve a protein adsorption thickness comparable to the decay length. For this reason the shifts of air represent the maximum achievable shift relative to the buffer and are a measure of the sensitivity of the PCM structure.

The relation between a mode shift and the characteristics of an adsorbed molecule seems rather complicated. However, some modes are distinctly sensitive to the secondary structure of the adsorbed protein. For instance, a positive mode shift is observed for all proteins that contain β-sheets in mode *4, while BSA consists almost purely of α-helix secondary structure and induces a negative shift. Furthermore, mode *5 displays the opposite tendency as all proteins induce a positive shift, except β-lactoglobulin that consists of a very high β-sheet content and induces a negative shift. Generally, it is expected that all proteins induce a shift in the same direction as air

(negative shift), as the adsorption of a protein represents a decrease in the net dielectric constant of the near PCM surface environment. Any modes that deviate from this have sensitivity towards the secondary structure of proteins. Hence mode *4 is actually sensitive to β-sheet structure, while mode *5 is sensitive to α-helix structure.

Table 2.4: Table listing the position of the plasmonic resonance modes from the CD spectroscopy measurements (Figure 2.5) of the large area PCM sample (Figure 2.3). Also listing the resulting shifts, observed in Figure 2.5, of the modes when different proteins, tryptophan and air is adsorbed on the PCM surface relative to the wavelength position when Tris buffer is used.

Mode position [nm]	*1	*2	*3	*4	*5	*6	*7
Tris buffer	619.0	565.1	475.9	453.8	432.0	407.3	367.0

Mode shift [nm]	*1	*2	*3	*4	*5	*6	*7
BSA	-0.6	-3.6	0.0	-0.8	0.5	-1.3	-0.5
β-lactoglobulin	0.0	-3.1	-0.4	0.1	-1.5	-0.8	-0.4
Lysozyme	-0.7	0.5	-0.7	0.2	0.0	0.1	0.0
tryptophan	-1.3	0.0	-1.6	0.1	0.2	0.1	-0.8
Air	-0.3	blank	-12.2	-5.2	-10.0	-7.3	-4.0

3 Conclusion

Gammadions with improved structural features compared to the previously reported gammadions [1] were fabricated by EBL in small areas. Features as low as 31 nm, which is far better than what is required for LSPR in the visible wavelength range, were fabricated using the proximity effect. However, these required a significantly higher exposure time and were hence not suitable for large area fabrication.

A sample with a large area of PCMs had many different substructures on the same sample. This yielded a large amount of CD modes with a high intensity compared to what is expected for many different structures and many modes. The many CD modes resulted in a far more complicated protein fingerprint, which could be used for identifying proteins much more precisely. Some of the CD modes were sensitive to β-sheet secondary structure, while other modes were sensitive to α-helix secondary structure. This possibly allows for secondary structure studies of proteins at very low concentrations.

However, because the reproducibility of the fabrication PCM sample was very poor, a sample with opposite handedness could not be fabricated. Even stable EBL systems produce imperfect mirror image structures that result in differences in the CD responses [1]. Furthermore, the protein fingerprint is acquired by two independent experiments and relies on very small differences.

Hence the imperfections of the mirror image sample and the uncertainty of the two experiments renders the protein fingerprint difficult to acquire from PCMs in general.

It has previously been observed that the intensity of the modes is greatly affected by the adsorption of proteins [1]. The same was observed during the sensing experiments in the present work. Generally, some proteins induce an increase in the intensity of all modes while other proteins induce a decrease in all modes. The effect of air is non-intuitive as it increases the intensity in some modes and decreases it in others. Furthermore, the increase and decrease of the proteins vary in magnitude for each mode. Hence the intensity of the modes is apparently sensitive to the secondary structure of proteins and could form the basis for another route towards sensing in the future.

4 Methods

PCM fabrication

The fabricated gammadions were designed with a line width of 80 nm and a periodicity of 800 nm. Approximately 1.5×10^6 PCM substructures were fabricated corresponding to a total area of $1 \times 1\ mm^2$, however, some may not have been chiral due to stigma drift that gradually deformed the structures over time. The samples were fabricated on indium tin oxide coated quartz to make it conductive. The size of the sample matched that of commercial grade dismantled cuvettes with a pathlength of 0.1 mm (Hellma, Müllheim, Germany) in order for it to replace the cover glass. The slides were cleaned for 10 min in ethanol, 10 min in acetone and 5 min in isopropanol all under ultrasonic agitation before being blown dry in a stream of nitrogen. A bi-layer of PMMA was spun to a thickness of 100 nm and baked at $180°C$ for 1 hour. The pattern was exposed in a Zeiss 1540XB SEM modified with a Raith ELPHY plus lithography tool at the exact position were the CD spectroscope would probe the sample. After exposing the sample, the pattern was developed with IPA:MIBK:MEK (3:1:1.5%) at 4 $°C$ for 1 min after which it was rinsed and soaked in IPA. 3 nm Cr, used as an adhesion layer, followed by 50 nm of Au was deposited by e-beam deposition in a Cryofox 600 explorer. The final patterns were achieved in a lift-off process by heating the sample to $180°C$ and submerging it into preheated acetone near the boiling point and leaving the samples in the acetone for about 3 hours.

CD measurments

The PCMs were incorporated into a dismantled cuvettes with a pathlength of 0.1 mm (Hellma, Müllheim, Germany) and a total volume of 26 μL. All CD spectra were collected with the back face (metal/glass) of the PCM facing the

spectrometer detector. Approximately, 1.5×10^6 PCM substructures were in the optical path of the detector. CD spectra were collected using a commercial spectropolarimeter (JASCO J-715).

Protein adsorption

All solutions were used at a concentration of 1 mg/mL. The tryptophan solution was made up using milliQ water, and the protein solutions were made using a 10 mM Tris/HCl buffer at pH 7.5. The adsorption of proteins and tryptophan was done by incubating 30 μL of the solution on the PCM sample for 1 hour, after which the other half of the cuvette was carefully mounted on the PCM sample.

PCM surface regeneration

The PCM sample was used in multiple experiments. After each protein adsorption and measurement cycle, the sample was immersed in a sodium dodecyl sulphate detergent solution for 1 hour, followed by 2 % hellmanex solution and rinsed with milliQ water before and after each step. Finally, any remaining (organic) residue was removed in an oxygen plasma-cleaning unit for 30 min.

Chapter 3

Polystyrene Nanosphere Assembly For Metamaterial Fabrication

Polystyrene (PS) nanospheres (NS) have received increasing interest in relation to nanofabrication techniques due to the variety of available sizes and the possibility of forming closely packed monolayers. This allows for one of the few available routes towards the fabrication of metamaterials in a high-throughput way. Some of the fabricated structures are also chiral and can be either planar or 3-dimensional. The most interesting reported large-scale methods from closely packed PS NS monolayers include PCMs for surface enhanced IR absorption spectroscopy by nanospherical-lens UV lithography [62] or by a combination of holes produced by PS NS and glancing angle deposition [23], PCM with LSPR in the near- and mid-IR wavelength range [92] or a CD response in the visible wavelength range [86] by PS NS monolayers as mask for glancing angle deposition and 3-dimensional chiral metamaterials by PS NS monolayers as seeds for glancing angle deposition [84, 88, 93, 94].

However, the formation of these closely packed PS NS monolayers, which all of the fabrication techniques rely on, is not easy. Different approaches to form closely packed colloidal monolayers have been reported including spin coating [95], drop casting [96], electrostatic deposition [97], electrophoretic deposition [98] and Langmuir-Blodgett trough [99]. However, few methods are defect or domain free [100] and only include noise-aided self-assembly formation [101], merger of domains in closely packed monolayer by transferring it to a water surface [102] and spin coating while trapping the colloidals inside a polymer matrix [103].

In order to understand the mechanism and develop new ways to form perfect monolayers, the forces in between PS NS and between PS NS and substrates have been widely studied [12, 104, 105]. The potential between PS NS is described by the DLVO theory [106–108] and the self-assembly is generally driven by van der Waals forces (mainly hydrophobic effects) but requires a surface charge modification in order to disperse and remain stable on a water interface or remain stable in suspension. This induces a repulsive electrostatic force and an effective radius from possible counter ions (the debye radius) that both counteract the self-assembly. However, the major challenge is the diversity of PS surface modifications that does not allow for a universal route towards perfect monolayers. Hence the chemistry of a specific PS NS greatly affects the method parameters needed to form a perfect monolayer. The diameter of the PS NS also changes the balance between the attractive and repulsive forces and the assembly of closely packed monolayers with colloids of smaller diameter is exceedingly more difficult [109].

Different approaches towards forming closely packed PS NS monolayers have been attempted in this work. Furthermore, PCMs have been fabricated according to various previously reported PS NS techniques and other novel ones has been developed.

1 Self-Assembly of Closely Packed PS NS Monolayers

Spin Coating Method

The formation of large domains of closely packed monolayers was attempted through optimization of the spin coating process (Figure 3.1a). This involved multiple steps such as the initial spreading by slow spin speed, main spin coating at specific acceleration to a certain spin speed and finally a high spin speed to remove excess PS NS suspension from the edges of the substrate. Other parameters such as the solvent, PS NS concentration and spin time were equally important as the spin speed and acceleration and also had to be optimized. Water was determined to be the best solvent with a final PS NS concentration of 10 wt.%. The initial spread spin step was short (less than 10 seconds) to avoid significant evaporation. The duration of the main spin step had to be optimized to allow the solvent to complete evaporation. In the case of a 1 cm^2 substrate, approximately 120 seconds was sufficient, while still leaving the edges of the sample moist. The final step was short (1-3 seconds) and removed the solution at the edges.

Furthermore, the surface properties of the substrate and the diameter of the PS NS were also determined to be important. Hence the optimized parameters were only valid for PS NS with a diameter of 350 nm and a 1 cm^2

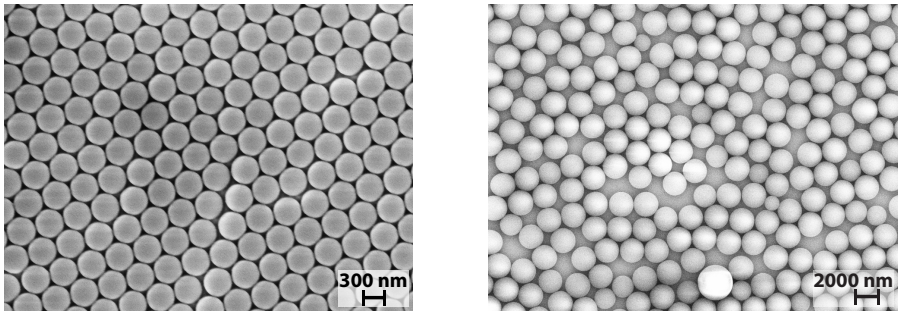

Figure 3.1: Spin coated monolayers of different sized PS NS, both spin coated with parameters optimized for only one of the sizes. (a) PS NS with a diameter of 350 nm in a closely packed monolayer as a result of highly optimized spin parameters. The samples are coated with 2 nm gold. (b) PS NS with a diameter of 1000 nm in a non closely packed monolayer as a result of no optimized spin parameters.

silicon or quartz substrate. However, when PS NS of a different diameter were used, all the parameters had to be re-optimized (Figure 3.1b). For this reason, other approaches to form closely packed monolayers, independent of the PS NS size, were attempted.

Spin Coating and Dipping

It has been reported that nearly infinitely large domains may be formed by spin coating a monolayer consisting of large closely packed domains and submerging the substrate into water [102]. If the surface energy of the substrate and PS NS monolayer is sufficiently low, the monolayer is released and will float on the water surface as a result of surface tension. The closely packed domains will then merge over time, resulting in a domain free monolayer. By dipping a new clean substrate under the monolayer and gently emerging it below the floating monolayer, it is transferred to the new substrate.

The monolayers formed by spin coating in this work (Figure 3.1a) are of equal quality as the one previously used to for the domain free monolayer [102]. When dipping the substrate into water, the monolayer peeled off and a monolayer with clear diffraction was observed on the water surface. However, a merger of the domains was never achieved no matter how long the monolayer was allowed to equilibrate on the water surface or how gently the floating monolayer was transferred to a new substrate. Experiments with transferring the floating monolayer to a hydrophilic substrate resulted in slightly improved monolayers due to the lack of a large water contact angle. Similarly, very gentle transfer of the monolayer by draining the water until the monolayer landed on a clean substrate also resulted in slightly improved

monolayers.

Nevertheless, a one domain closely packed monolayer was never achieved. Presumably, this is due to differences in surface properties of the PS NS used in this work and could result in more hydrophilic PS NS than the ones used to form the infinitely large domains.

PS NS with a 15 nm hydroxypropyl cellulose coating that turned the spheres hydrophobic when heated above 45 $^{\circ}C$ were also used. This prevented the PS NS from submerging into the water and forced them to remain on the water surface. Additionally, it had the benefit of leaving the PS NS surface uncharged. In this way very large domains were self-assembled. However, only PS NS with a large diameter were available during this work and closely packed monolayers consisting of larger PS NS are considerably easier to fabricate. Hence no further experiments with hydroxypropyl cellulose coated PS NS could be attempted.

Noise-Aided Larger Domain Formation

It has been reported that sound noise may be used to improve the domain size of slightly large PS NS spheres (368 and 530 nm) [101]. Similar sound noise might also be used to relax domains in monolayers floating on a water surface. Hence beakers with floating monolayers were left atop speakers emitting a broad spectrum of noise (white noise). Different time intervals and sound intensities were used, but an improvement of domain size was never observed. Ultrasound was also used, however, even very low levels would damage the floating monolayer.

Langmuir-Blodgett Method

Langmuir-blodgett is a well-known technique used to form monolayers on water surfaces. Hence it was hypothesized that this might also be useful for PS NS monolayer formation.

In order to keep the PS NS floating on the water surface, the solvent of the PS NS suspension was replaced with ethanol. The PS NS suspension was then gently added to the water surface. In total, approximately 100 μL was added to an area of approximately 120 cm^2.

At low area concentrations (no barrier compression) the PS NS were floating in a foam like way. During barrier compression, the PS NS would closely pack and form a more ordered layer with visible diffraction. However, at some point when the monolayer was completely compressed, double layer formations started to occur. This point was readily observable from the formation of a foam like layer on the water surface, but was difficult to monitor from the surface pressure. Furthermore, no improvement in domain size was observed, compared to the "spin coating and dipping" method.

Floating Perimeter Method

The most successful method used in this work was a floating perimeter method, that has never been reported before. It consisted of a Teflon plate with a hole in the middle. Differently shaped holes were used with the best shapes being round or polygonal. The Teflon plate was placed on a water surface in a petri dish. The monolayer was formed inside the Teflon perimeter on the water surface by slowly adding a PS NS suspension with 96% ethanol with a final concentration of 10 wt. %. As more suspension was added, a point was reached at which the PS NS spheres would form a closely packed monolayer. This was observable by the formation of a diffraction phenomenon. It was discovered that better results were obtained when stopping the addition of the suspension immediately after this point, even though the Teflon hole was only approximately 80 % filled with PS NS. After letting the ethanol evaporate and the monolayer equilibrate, draining and refilling the water in the petri dish could remove any submerged PS NS. Afterwards, a clean substrate was submerged and placed on a platform under water. The Teflon plate was then placed above this substrate and the water was very slowly drained until the closely packed PS NS monolayer landed on the substrate. Better results were obtained if the substrate was slightly tilted, allowing for water to rinse off. This method produced monolayers independently of the PS NS size or substrate properties. However, domains were always observed.

2 Self-assembled PS NS for PCM Fabrication

PS NS Monolayer Mask for E-beam Evaporation

E-beam evaporation through closely packed PS NS monolayers to fabricate large-scale planar chiral metamaterials has previously been reported [86, 92]. The lift-off process is often difficult for PS NS monolayers as the spheres stick to the surface very well. In this work, a new and efficient approach to achieve lift-off was developed.

After evaporation, the substrates were heated to approximately 90 $^{\circ}C$, close to the glass transition temperature of PS NS, and submerged in an MIBK/IPA (1:3) solution in an ultrasound bath. This readily removed any PS NS even when thick metal layers were deposited (Figure 3.2a). However, in order to fabricate any useful metamaterials, a one domain closely packed monolayer is required. As this was not achievable during this work, a large amount of defects were introduced into the fabricated metamaterials (Figure 3.2b). For this reason, the fabrication of chiral metamaterials by glancing angle deposition was never attempted.

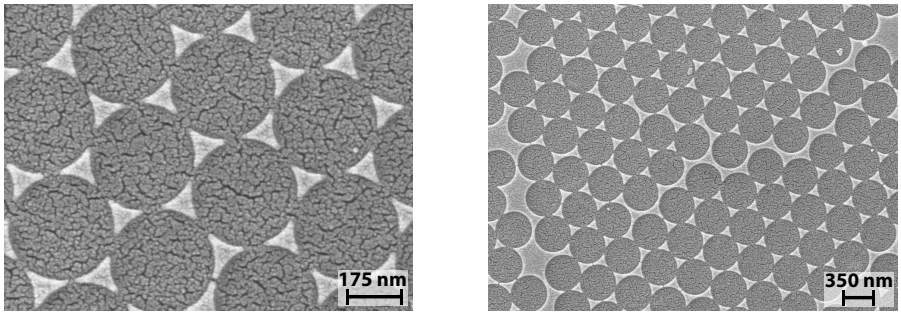

Figure 3.2: SEM picture of a closely packed PS NS monolayer used as mask for e-beam evaporation of 50 nm Au and a subsequent PS NS lift-off. The sample is coated with 2 nm Au. (a) The pattern from a perfect closely packed PS NS monolayer. (b) The pattern from a loosely packed PS NS monolayer.

PS NS Monolayer for UV Lithography

In opposition to using PS NS monolayers as a mask for glancing angle deposition, using PS NS as a nanolens does not require a perfect monolayer. The resulting metamaterial substructures will be similar, but the order will have the same quality as the monolayer. This method has previously been used in the fabrication of metamaterials with LSPR in the IR wavelength range [62]. However, smaller substructures yielding LSPR in the visible wavelength range have not yet been fabricated because PS NS with a minimum diameter of 750 nm were necessary in order to produce substructures other than holes.

In this work, it was possible to produce very small substructures with PS NS having a diameter of 600 nm by using a shorter wavelength light source of 185 nm (Figure 3.3). It was observed that very small structures could also be produced with large PS NS spheres (Figure 3.4).

By tilting the substrates 45° before exposure, elongated structures could be produced (Figure 3.5). This enabled the fabrication of complex chiral structures by having multiple exposure steps with off-set sample positions relative to the UV lamp, as was reported for large substructures [62]. However, the resulting features were not small enough to produce PCMs with LSPR in the 300-900 nm wavelength range (Table 2.1), used to measure the protein fingerprint by PCM based CD spectroscopy.

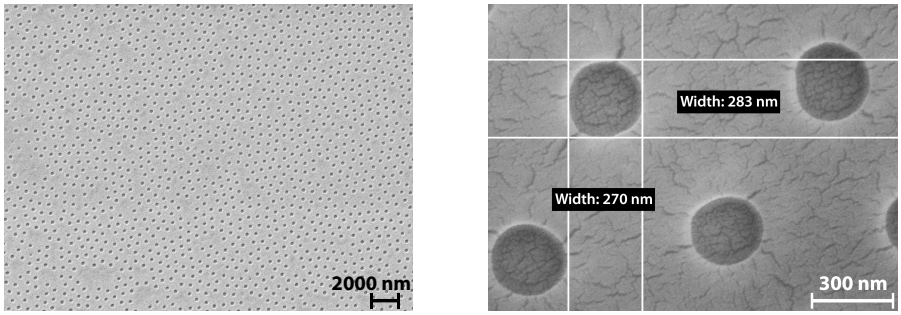

(a) (b)

Figure 3.3: SEM pictures of the developed pattern created in PMMA resist by UV lithography using a PS NS closely packed monolayer and subsequent PS NS lift-off. The sample is coated with 2 nm Au. (a) Developed substructure in PMMA next to a PS NS that was not removed during the lift-off to show the scale difference. (b) Close up of one of the created PMMA substructures.

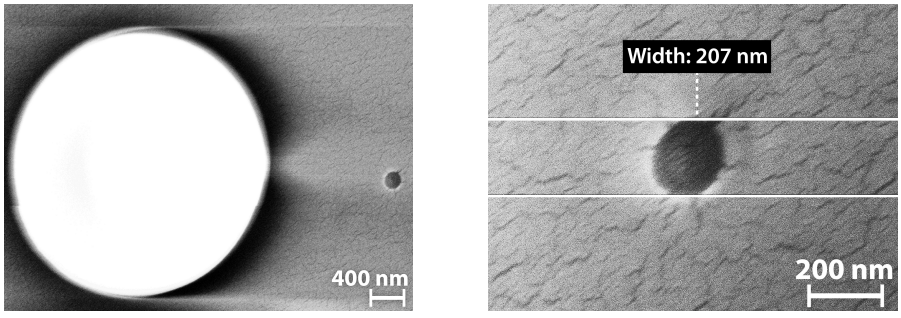

(a) (b)

Figure 3.4: SEM picture of the developed pattern created in PMMA resist by UV lithography using a PS NS closely packed monolayer and subsequent PS NS lift-off. One PS NS with diameter of 2000 nm was left on the surface for comparison to the developed pattern. The sample is coated with 2 nm Au. (a) Overview of the developed PMMA pattern. (b) Close up of one of the created PMMA substructures.

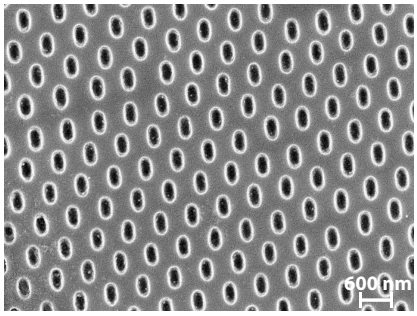

Figure 3.5: The developed pattern created in PMMA resist by UV lithography using a PS NS closely packed monolayer while tilting the sample at a 45° angle during exposure and subsequent PS NS lift-off. The sample is coated with 2 nm Au.

PS NS Mask For Gold Nanoparticle Annealing

As an alternative to metal deposition by traditional evaporation techniques that require high vacuum and are expensive, the annealing of Au nanoparticles was attempted. PS NS monolayers were used as a mask to produce a pattern of APTMS on the substrate. After removing the PS NS by use of a tape lift-off process, gold nanoparticles were incubated on the substrates for one hour. As gold nanoparticles would only stick to the surface coated with APTMS, a hole array was produced after rinsing the substrate (Figure 3.6). This allows for a cheap and easy way to fabricate metamaterials. By combining the aforementioned UV lithography process with PS NS as nanolenses, far more complex structures could be produced. However, no further attempts were performed, as the size of the features was too large to produce PCMs with LSPR in the necessary wavelength range.

Selective Etching by Hole Arrays Produced by PS NS UV Lithography

Monolayers of PS NS were used as previously described to fabricate a hole array in a PMMA photoresist by UV lithography. The PS NS were then removed by tape lift-off and the exposed PMMA was developed. By use of aqua regia (1:3) the underlying gold film was selectively etched in the developed PMMA holes (Figure 3.7). It was observed that the array consisted of holes with various sizes (Figure 3.7a) and very rough and non-uniform shapes (Figure 3.7b). It is likely that a less corrosive aqua regia solution might form more homogeneously sized holes, as the etch time could be longer and more controllable. However, the roughness of the holes is caused by the grain structure from the Au evaporation process and would have to be optimized.

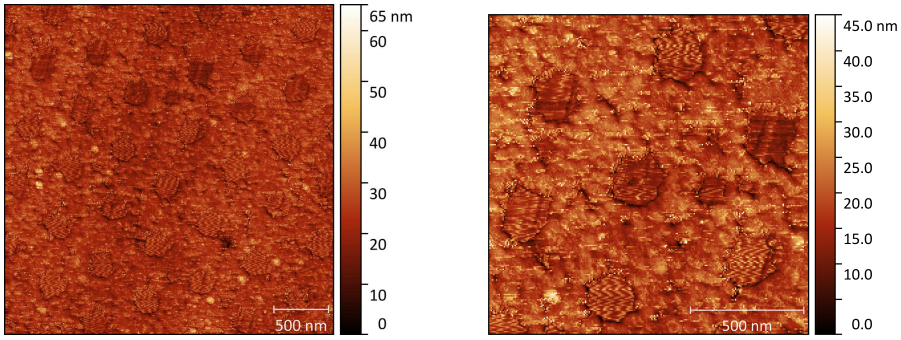

(a) **(b)**

Figure 3.6: (a) AFM measurement of the pattern fabricated using a PS NS monolayer as a mask for APTMS surface coating and subsequent incubating gold nanoparticles on the surface. The PS NS monolayer was then removed and the sample rinsed with milliQ water. (b) Close up of the pattern.

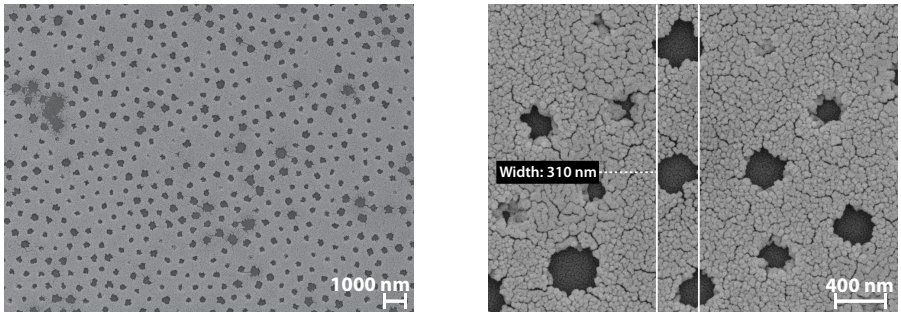

(a) **(b)**

Figure 3.7: SEM pictures of the pattern created in a gold film by selective etching using a closely packed PS NS monolayer to create a hole array by UV lithography in PMMA resist on top of the gold film and removing the PS NS to etch through the developed PMMA. The PMMA layer was then removed. (a) Overview of the pattern. (b) Close up of the pattern.

3 Conclusion

All of the studied PS NS techniques yield a possible route towards high-throughput PCM fabrication. The disadvantage is the need for a domain free closely packed monolayer. Many papers demonstrate techniques to achieve a defect free monolayer, however, it was not possible to reproduce the reported results. Some large domain closely packed monolayers were fabricated in this work, however it required much optimization.

Spin coating was a fast and efficient method for monolayer formation. The monolayers were of a good quality and many types of substrates could be used except for positively charged surfaces such as PMMA coated substrates as the PS NS often are stabilized by a negative or positive surface charge.

The spin coating and dipping method was slow but yielded the second best monolayers and could be used on all substrates.

White noise did not help relax domains in floating monolayers and required a long timescale.

The Langmuir-blodgett approach was very slow but yielded a good quality of monolayers.

The floating perimeter method was the best method as it was fast and produced some excellent monolayers. However, this method requires practice as the monolayer formation depends on the amount of solution added.

It is likely that none of the methods in this work yielded perfect closely packed monolayers as a result of the specific chemistry of the PS NS used for this study. In order to form defect free monolayers, the surface charges of the PS NS need to be highly optimized as these are responsible for the repulsive forces. If the surface charge is too high, more domains are formed in a way similar to what was observed in this work. If this is the main problem, a modulation of the surface charge could be attempted by changing the solution composition because only the submerged PS NS parts will be charged.

A domain free closely packed monolayer is required by the e-beam evaporation method and glancing angle deposition process as the resulting PCM geometry relies heavily on the monolayer quality. Using PS NS as lenses for UV lithography will not result in a perfect lattice if the monolayer is not perfect, but all the PCM substructures will be similar. When the distance between substructures is large enough, the LSPR is insensitive to periodicity because the distance between substructures is larger than the wavelength of the incident light. In this way, PS NS in non-perfect monolayers may be used to fabricate PCMs with UV lithography in a reproducible way. It was also demonstrated that the UV lithography technique could be combined with the deposition of Au NP to achieve PCMs without expensive high vacuum deposition methods. Furthermore, PS NS UV lithography also has potential

for selective etching that can yield a very fast way of PCM fabrication after careful optimization of the etching parameters.

Another challenge of all the PS NS techniques is the inherent relation between periodicity and structure size. To create smaller structures, smaller PS NS are needed and the periodicity will always be equal to the PS NS size. Furthermore, it is more difficult to form closely packed monolayers of smaller PS NS. $1\mu m$ PS NS monolayers as mask for glancing angle deposition will result in PCMs with a LSPR in the near- to mid- IR wavelength range [92]. Moreover, $750nm$ PS NS have been reported to produce PCMs with a CD response in the visible wavelength range by using the monolayers as mask for glancing angle deposition [86]. Furthermore, $500nm$ PS NS monolayers as seed for glancing angle deposition also produce PCMs with a CD response in the visible wavelength range [65]. Hence glancing angle methods may produce smaller structures by using smaller PS NS. However, it has been reported that PS NS smaller than $1\mu m$ were not applicable for producing PCMs by UV lithography and the $1\mu m$ PS NS resulted in PCMs with LSPR in the near- to mid-IR wavelength range [62].

This work succeeded in producing smaller structures by UV lithography based on PS NS lenses by using UV light with shorter wavelengths and smaller PS NS than what was previously reported [62]. By tilting the sample during exposure, features as low as 110 nm were produced which is slightly too large to yield LSPR in the visible wavelength range (Table 2.1). It was also observed that larger PS NS could also produce very small features by UV lithography, hence smaller PS NS would not necessarily result in significantly smaller features. However, problems with PS absorption might limit how much smaller the features produced by reducing the wavelength of the exposing light can be.

Another approach to achieve smaller features by PS NS UV lithography could be to use a multi-step exposure process. By moving the sample relative to the light source, the PS NS project the focused light onto different locations on the resist [62]. Hence certain areas can be exposed several times, while resist that was only exposed once or twice would not be sufficiently exposed to be developed. This may also be used to take advantage of the proximity effect and produce very low features, similar to what was demonstrated by EBL (Figure 2.4a).

It would also be interesting to produce two PCM samples with opposite handedness to probe how much the resulting CD response is affected by the random defects in the two samples.

4 Methods

Spin coating

All samples that were spin coated were done by adding an appropriate amount of PS NS diluted in milliQ water to a 10 wt. % concentration. The resulting closely packed monolayers were very insensitive to the amount of suspension added. However, the spin speed and acceleration was very important. For PS NS with a radius of 350 nm, a 3 step spin process was used: (1) A spreading phase with slow acceleration to spread the PS NS suspension on the substrate. 6 sec of 600 rpm with acceleration 100 rpm/s. (2) A main spin coating step to form closely packed monolayers. 120 sec of 2000 rpm with acceleration 200 rpm/s. (3) A final step to remove excess PS NS suspension at the sample edges. 3 sec of 3000 rpm with acceleration 1000 rpm/s. The substrates used were both quartz and silica.

Spin coating with dipping method

In the dipping methods the closely packed monolayers formed by spin coating were very carefully dipped into milliQ water. The monolayer then peeled off the substrate and was floating on the water surface. Small vibrations were then manually applied to form waves on the water surface after which the floating monolayer was allowed to regenerate for one hour to days. Finally, a pre-submerged clean substrate was emerged below the floating monolayer at a small tilt to allow water to rinse off the surface. This sample now had the monolayer on the surface and some water, that was allowed to dry at room temperature.

Noise-Aided larger domain formation

The noise-aided method was performed in the same way as the spin and dipping methods. However, the beaker of water was placed over a loudspeaker connected to a computer with a noise generator. Many different frequencies were used at a volume sufficient to see rippling on the water surface.

Langmuir-Blodgett method

Formation of closely packed monolayers by Langmuir-Blodgett with very slow perimeter movements was also attempted. Water in the PS NS suspension was substituted with ethanol by centrifuging the suspension at 2000 rpm for 15 min, discarding the water and dissolving the PS NS in 96 % ethanol to a final concentration of 10 wt. % An appropriate amount of this suspension was very slowly added to the water surface of the Langmuir-Blodgett trough in order to avoid mixing the water and PS NS suspension. The appropriate

amount of suspension was assessed by shining a strong light on the water surface at an angle, which would make visible a cloudy film on the water surface. When a coverage of about 70 % was reached, no more PS NS suspension was added after which, the ethanol was allowed to evaporate for one hour. The perimeters were then very slowly contracted. Even though a Wilhelmy Plate was used to measure the surface pressure, it was not sufficient as the formation of double layers were unmeasurable by the surface pressure plot. Hence constant inspection of the monolayer was needed with a strong flashlight to look for beginning diffraction patterns. These diffractions patterns were a sign of ordered monolayers and prompted the barriers to be stopped. Then the monolayer was left to stabilize for one hour, before the substrate was slowly pulled up, with or without barriers compressing.

Floating perimeter method

In the floating perimeter method a Teflon plate with a hole in was floating on a water surface. A 10 wt. % PS NS suspension in 96 % ethanol, prepared as described above, was slowly added to the water surface inside the hole. When the coverage was about 80 % a diffraction pattern was observed, prompting the stop of adding more PS NS suspension. The water was then drained and refilled several times to remove any PS NS that might have been dissolved in the water. This closely packed monolayer was then left to stabilize for one hour. Finally, the water was drained with the floating monolayer in the perimeter, standing over a pre-submerged substrate standing on a pillar with a slight tilt. The closely packed monolayer was in this way very gently transferred to this substrate.

PS NS mask for E-beam evaporation

Closely packed PS NS monolayers were used as mask for deposition of 3 nm Cr, used an adhesive layer, followed by deposition of 50 nm Au by e-beam evaporation in a Cryofox 600 explorer. After evaporation, the substrates were slightly heated to approximately 90 $^{\circ}C$, close to the glass transition temperature of PS NS, and submerged in a MIBK/IPA (1:3) solution in an ultrasound bath to lift-off the PS NS.

PS NS for UV lithography

100 nm of PMMA was spin coated on clean substrates. Onto these substrates a closely packed PS NS monolayer was formed by the "floating perimeter method" described above. This closely packed PS NS monolayer was used as lenses in a UV lithography process where only the focused light was sufficient to expose the PMMA. A standard UV tube was used for exposing the sample. The emission spectrum was recorded and showed two major peaks

at 185 nm and 253 nm. To avoid the formation of ozone the lamp was placed in an almost airtight box that was continuously purged with nitrogen. The substrate was in some cases put in an angle or off-set position, to produce different patterns. After exposure, the PS NS monolayer was removed by adhesive tape, as the PS NS would stick to the adhesive rather than the substrate when pulled off. The sample was then developed in MIBK/IPA (1:3) for one min and rinsed thoroughly in IPA.

PS NS mask for gold nanoparticle annealing

Closely packed PS NS monolayers were used as a mask to produce a pattern of APTMS on a silica substrate. After removing the PS NS by use of a tape lift-off process, gold nanoparticles with a 30 nm diameter were incubated for one hour on the substrate. The substrate was then rinsed in milliQ water and dried under a stream of nitrogen.

PS NS created resist pattern for selective etching

A closely packed PS NS monolayers were used as previously described to fabricate a hole array in a PMMA photoresist by UV lithography. The PS NS were then removed by tape lift-off and the exposed PMMA was developed. By use of aqua regia (1:3) the gold substrate was selectively etched in the developed PMMA holes. The substrate was then rinsed in milliQ water and dried by nitrogen blowing.

Chapter 4

Large-Scale Fabrication of Achiral Plasmonic Metamaterials With Giant Chiroptical Response

In recent years metamaterials have attracted a tremendous amount of attention owing to their unique properties enabling the fabrication and design of devices hitherto impossible. These properties have found implementations in various fields such as optics [110], improved photovoltaic devices [111], electronics [112], surface enhanced infrared spectroscopy [113], raman spectroscopy [114] as well as biosensors [115].

Planar chiral metamaterials (PCMs) have also attracted attention because of their negative refractive index [116, 117] and optical activity [118] such as circular dichroism (CD) [1]. Among other things, this makes them useful for the production of sensing devices for organic molecules and biomolecules [1]. Recently, the phenomena of the long proposed extrinsic chirality dating back to 1945 [119] have been observed experimentally with materials that are achiral [31]. These extrinsic chiral metamaterials (ECMs) demonstrate CD responses that are orders of magnitudes larger than their PCM counterpart [31]. ECMs typically consist of achiral subwavelength hole arrays where the chiroptical response originates from a large area excitation of surface plasmon polariton (SPP) waves. Compared to the localized surface plasmon resonance from PCMs, SPP waves from ECMs are extremely sensitive to the angle of incidence and less sensitive to structural imperfections [28]. Furthermore, ECMs are defined by having a zero response angle, which is the angle where the ECMs exhibit mirror symmetry and hence do not yield a CD response.

Though some PCMs show promise as they also yield huge CD responses through FANO resonance [120], the greatest advantage of ECMs is that sensing of biomolecules can be performed with only one sample in one experiment by inverting the tilt of the sample, whereas PCMs requires one samples of both enatiomeric structures and independent experiments with both samples.

To date only very few different ECMs other than hole arrays [28–30] and the original suggested U-shaped and split ring structures [31], have been investigated. These have been thoroughly studied [121–124] and other structures including theoretical suggestions are limited to plasma sphere arrays [33], gold dot arrays [34], gold square arrays [35], metal disk arrays [36], two layer hole arrays [37], polystyrene sphere templates for gold deposition [38] and structures formed by carbon nanotubes [39].

However, in order to be able to apply these metamaterials in sensing devices of organic molecules and biomolecules a reliable large area fabrication method is required. State of the art fabrication techniques are based on electron beam lithography or focused ion beam milling, which both are expensive and time consuming methods. Large-scale fabrication of PCMs have been attempted to some degree applying different approaches such as glancing angle deposition [88], scaffold ornamentation [25, 26], individual chiral nanoparticles [125], preassembled nanoparticles [24, 68, 126] and a variety of colloidal nanolithography techniques [23, 62, 92]. Compared to the above mentioned PCMs, the experimentally proven ECMs only comprise structures from polystyrene sphere templates for gold deposition [38], structures formed by carbon nanotubes [39] and larger U-shaped structures by nanoimprint lithography (NIL) [32] which have been scalably fabricated.

In the present work we present a novel route towards large-scale fabrication of ECMs and metamaterials in general. These structures have never been reported before and add to the scarce amount of experimentally investigated ECMs. Our fabrication approach is based on a two step thermal NIL process with subsequent glancing angle metal deposition. The master mold for the NIL was fabricated by anodic oxidation of an aluminum (Al) substrate, which previously has been demonstrated [40, 41]. During this process a disordered honeycomb structure is formed in the substrate. By controlling different parameters the interpore distance has been varied. ECMs with different interpore distance were investigated with CD spectroscopy and scanning electron microscopy (SEM). Furthermore, by altering the interpore distance and the glancing angle for metal deposition it was possible to tune the obtained CD signals from UV all the way to IR wavelengths. As a proof of concept, the resonance shifts of SPPs were studied upon interactions between a protein or a chiral organic molecule and the ECM surface.

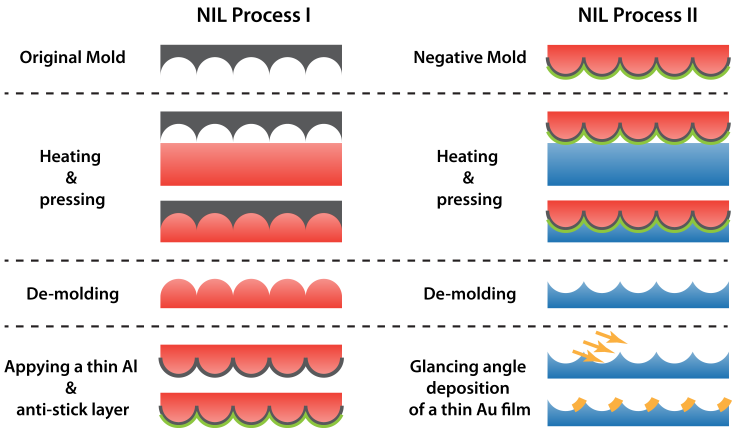

Figure 4.1: Schematical overview of the ECM fabrication process. First an original mold with a honeycomb structure is cast in a TOPAS polymer substrate. After de-molding a thin Al and anti-stick layer is applied to produce a negative mold. This negative mold is then cast in PMMA to produce the original honeycomb structure. This structure is used for initiation of glancing angle deposition of a 30 nm Au layer.

1 Fabrication and Characterization

The ECM fabrication process is illustrated schematically in Figure 4.1.

The original mold was fabricated by a self-ordering anodic oxidation of Al foils as described in a previous study [40]. In this process pores are produced in the Al surface with a honeycomb structure. However, the pattern is not perfect and several types of defects are present which are inevitably transferred to the final ECMs. By applying different acids and voltages in the anodic oxidation process, original molds with three different interpore distances (300 nm, 430 nm and 600 nm) have been prepared as previously described [41]. These served as master molds in the following NIL process (Figure 4.2a). The first imprints were cast in TOPAS polymer substrates. After de-molding the TOPAS structures were sputter coated with a thin Al film and subsequently an anti-stick monolayer was applied to produce negative molds (Figure 4.2b). The negative molds were then cast in PMMA polymer substrates (Figure 4.2c). The honeycomb pattern in the PMMA substrates served as the starting structure of the glancing angle deposition of Au films. By varying the deposition angle (50°, 60° and 70°), three different samples have been fabricated for each honeycomb interpore distance (Figure 4.2d-f).

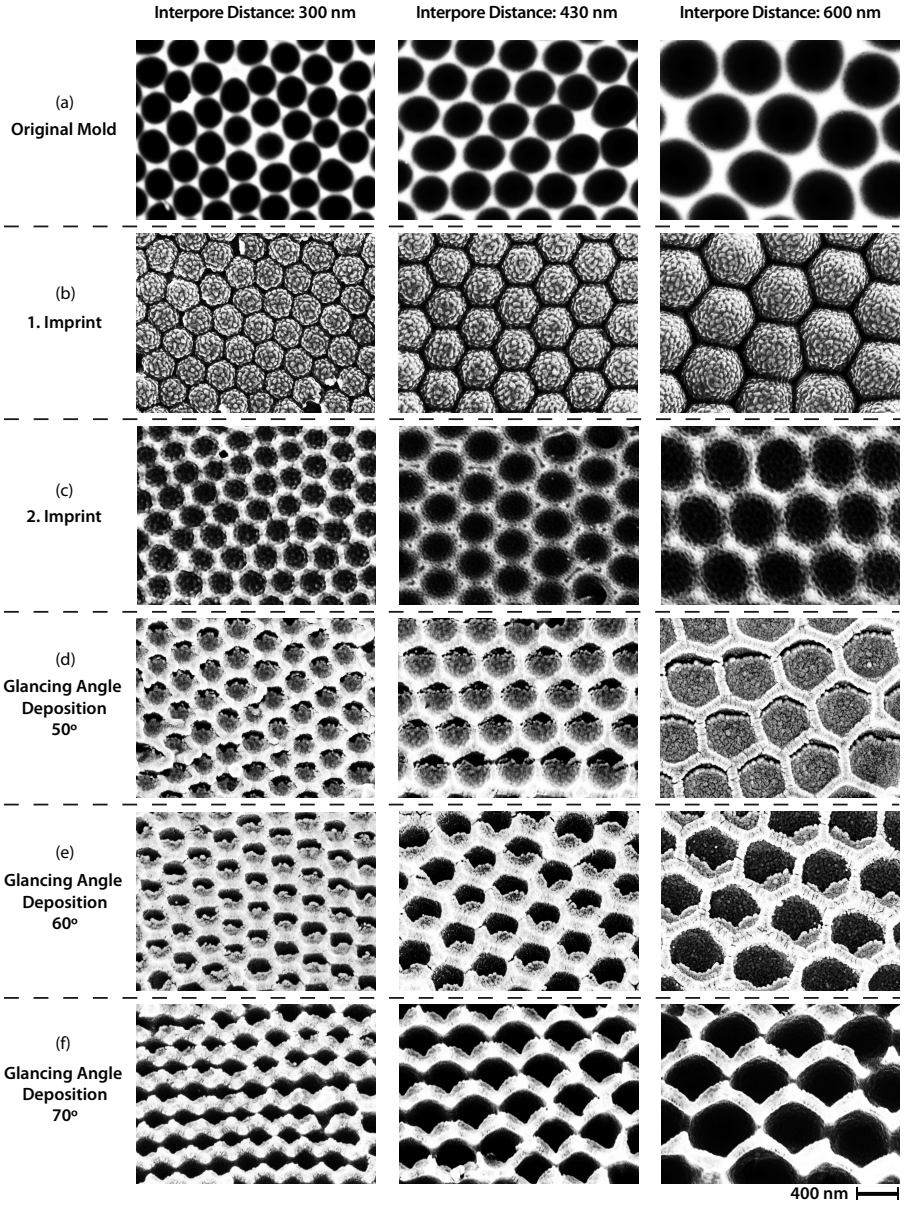

Figure 4.2: SEM pictures of (a) the original molds (b) 1. imprints with a thin Al layer (c) 2. imprints with a 2nm Au layer and (d-f) all the different ECMs produced by glancing angle deposition of 30 nm Au at 50°, 60° and 70°. The scale bar is shown in the bottom right corner.

In total, nine different samples have been prepared, each covering approximately $3cm^2$, together with three reference samples of a deposition angle of $0°$. Figure 4.3a shows a photograph of the samples prepared by a deposition angle of $60°$, the samples with 600 nm interpore distance show good diffraction (Figure 4.3b) while the samples with 430 nm interpore distance show moderate blue diffraction and the samples with 300 nm show no diffraction. However, the size of the samples are only limited by the size of the original molds, which were fabricated by another scalable technique, but the size of the samples was chosen as to be compatible with commercial dismantled cuvettes and only a small area of the sample are probed at any one time.

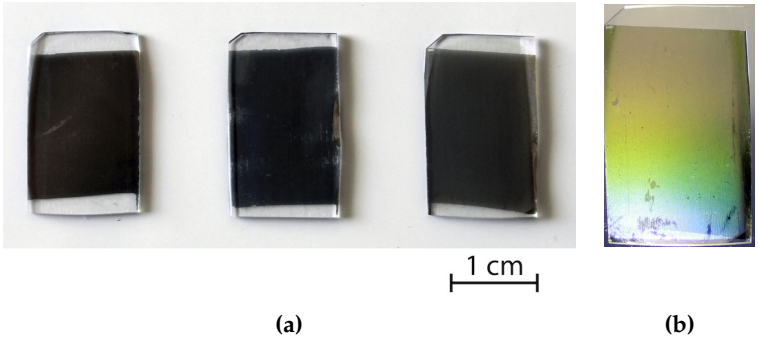

Figure 4.3: (a) Photography of the ECM samples prepared by a deposition angle of $60°$ and interpore distance of 300 nm, 430 nm and 600 nm from the left, respectively. The sizes were chosen as to be compatible with commercial dismantled cuvettes and only a small area of the sample are probed. (b) Photography of the sample prepared by a deposition angle of $60°$ and interpore distance of 600 nm with flashlight to illustrate the diffraction pattern (the scale bar does not apply to this photo).

The Extrinsic Chiral Metamaterial Criteria

A chiroptical response is only obtained from structures lacking mirror symmetry. As the unit structure of ECMs are not natively chiral, they rely greatly on the orientation of the sample with respect to the direction of the incident light causing a broken mirror symmetry. By careful design it is possible to design the ECM structure in such a way that no CD response is observed when the face of the ECM substrates are oriented perpendicular to the incident light. Hence a CD signal is only obtained when the sample is tilted out of one of the two angles θ and ϕ (Figure 4.4). This enables the investigation of the enantiomeric ECM structures (right-handed and left-handed structure) to be probed in the same experiment, by inverting the tilt of the ECM with respect to the normal ECM face angle.

The investigated ECMs have been designed in a way that it was possible to invert the CD signal by tilting the samples with respect to the θ angle

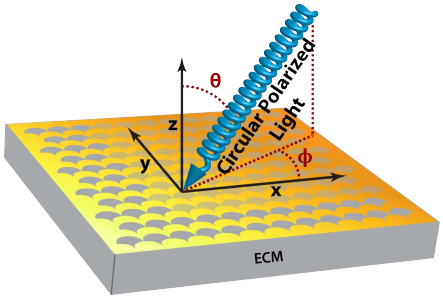

Figure 4.4: The two principle angles, θ and ϕ, of incident light with respect to the ECM structures.

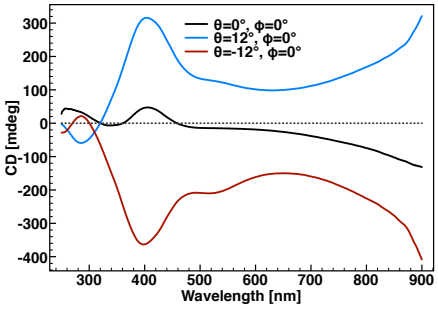

Figure 4.5: The resulting CD response from three ECM orientations ($\theta = 0°$,$\phi = 0°$), ($\theta = 12°$,$\phi = 0°$) and ($\theta = -12°$,$\phi = 0°$) of the ECM with 300 nm interpore distance and 60° deposition angle. It is evident that ($\theta = 0°$,$\phi = 0°$) shows no significant response, while the two other orientations yield an inverted line-shape.

while retaining a ϕ angle of 0° (Figure 4.5). The observed response from the bare sample at normal incident angle light of may have three different causes; 1) Various structural imperfections; 2) Spread in structure size; 3) The 3D nature of the ECM structure causing some intrinsic chirality. However, this CD response at $\phi = 0°$ has also been observed by ECMs produced with focused ion beam milling [28].

The ECM property that allows for the measurement of the enantiomeric structures from one sample, yields several advantages over PCMs in biosensor applications; 1) PCMs requires fabrication of the two enantiomeric samples, which increases the cost and the risk of imperfections. 2) With the use of PCMs it is necessary to perform two independent experiments, which is time-consuming and difficult to implement into a commercial product. 3) Since the CD response is concentration dependent, two independent PCM experiments are troublesome to interpret. All of these disadvantages with PCMs are totally avoided by the use of ECMs which are both cheaper, more reliable and only requires one experiment in biosensor applications.

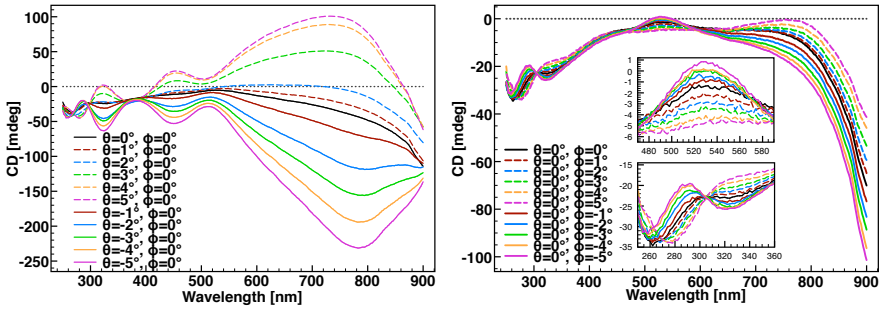

Figure 4.6: Angular scans and corresponding CD response from the ECM fabricated with 430 nm interpore distance and 50° glancing angle deposition. (a) Independent scan of the θ angle defined in Figure 4.4. (b) Independent scan of the ϕ angle defined in Figure 4.4.

Probing the Zero Response Angle

The zero response angle of the ECM with 450nm interpore distance and 50° glancing angle deposition was identified by scanning the θ and ϕ angles separately (Figure 4.6).

This ECM substrate was chosen as it exhibits more and stronger resonance modes than the other samples and will be used in most subsequent experiments. While the CD response was extremely sensitive towards angular rotation about the θ angle plane (Figure 4.6a), it exhibited a lower angular dependence towards the ϕ angle plane (Figure 4.6b).

Furthermore, it is evident from the angular scans (Figure 4.6) that the ECM has an intrinsic left-hand chirality. Hence the zero response angle is not identified by the lowest CD response but as the center of the enantiomeric signals. From the θ angle scan (Figure 4.6a), it appears as if $\theta = -1°$ and $\theta = +2°$ displays the least responses. Hence the θ angle resulting in minimum extrinsic chirality is between 0° and +1°. As virtually no difference in line-shape is observed between $\theta = 0°$ and $\theta = +1°$, $\theta = 0°$ was used as zero θ angle throughout the paper for convenience.

The two resonance modes located in the 260-360nm wavelength range of the ϕ angle scan (Figure 4.6b) indicate that $\phi = 0°$ to $\phi = -3°$ exhibits no extrinsic chirality. As virtually no difference in line-shape is observed between these angles, $\phi = 0°$ was used as zero response angle. Applying $\theta = 0°$ and $\phi = 0°$ as reference results in a more symmetrical angular scan (Figure 4.7) indicating the precision of the zero response angle determination.

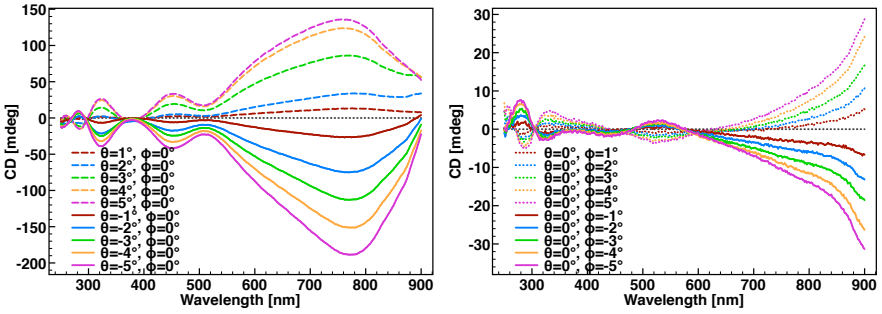

Figure 4.7: Angular scans with the intrinsic chirality subtracted. A much higher symmetrical CD response from the ECM enantiomers is observed compared to the angular scans in Figure 4.6. (a) Independent scan of the θ angle. (b) Independent scan of the ϕ angle.

Interpore Distance and Glancing Angle Deposition Dependence

Structures with 300, 430 and 600 nm interpore distances exhibited main plasmonic resonance ranges from $\sim 300 - 550$ nm, $\sim 450 - 800$ nm and above 900 nm, respectively (Figure 4.8).

Compared to the relative narrow linewidth of the CD response from ECMs comprised of hole arrays, the honeycomb ECMs exhibit a rather broad signal [28]. This is presumably related to the heterogeneity and 3D nature of the ECM structures which is less dominant in the hole arrays fabricated by focused ion beam lithography. In spite of this, the CD linewidth of the present ECMs are comparable to that of gammadion PCMs which has previously been used for biosensor applications [1]. Furthermore, compared to PCMs fabricated by another scalable technique [25], the CD linewidth of the honeycomb ECMs are more narrow. Hence the heterogeneity and 3D structure has not limited the use of the honeycomb ECMs for biosensing applications.

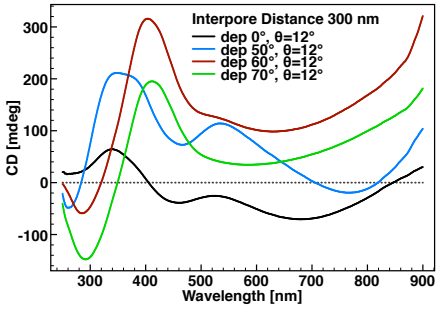

(a)

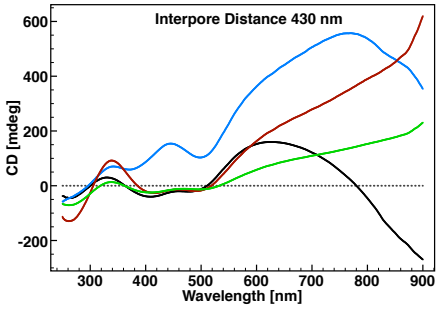

(b)

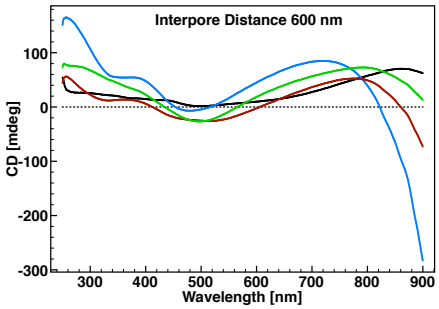

(c)

Figure 4.8: CD response from all the produced ECMs. (a) The CD response from the structures with 300 nm interpore distances. (b) The response from the structures with 430 nm interpore distances. (c) The response from the structures with 600 nm interpore distances. All measurements were recorded with an ECM orientation of $\theta = 12^{\circ}$ and $\phi = 0^{\circ}$.

While the interpore distance of the ECM array is the main factor in the position of the SPP resonance, the angle of the Au deposition has mainly an influence on the line-shape and number of resonance peaks (Figure 4.8). The samples prepared at 0° and 50° glancing angle deposition show a similar line-shape, as well as the samples prepared at 60° and 70°. This is reasonable as the angle deposition sensitivity, which determines the dependence of the resulting structure and the deposition angle, is very low at small angles but increases with large angles. The reason for this is found in the shadowing effect from the honeycomb starting structure. The glancing angle deposition is self-perpetuating at larger angles while small angles result only in minor shadowing effects. The samples prepared at 0° and 50°, in general, exhibit 3-4 distinct resonance peaks while the samples prepared at 60° and 70° only exhibit 2-3 distinct resonance peaks. This might be explained by the gold inside the hole arrays produced at 0° and 50° glancing angle deposition, resulting in a more complex 3D structure (Figure 4.2) and an extra origin of plasmonic resonance modes. The samples with 600 nm interpore distances had a main resonance wavelength above 900 nm (data not shown). These structures may find applications in other areas such as surface enhanced IR spectroscopy [127], THz generation [128] or THz-CD spectroscopy [129].

Scanning Angle Dependence and Intrinsic Spatial Structural Variations

As mentioned above, the plasmonic resonance wavelength and intensity depends on the orientation of the ECMs. Upon rotating the sample in the θ angle plane (Figure 4.9a) it is evident that the two distinct resonance modes in the near UV region merge upon increasing the θ angle from 10° to 20°. At $\theta = 30°$ this peak is blue-shifted. When the θ angle is increased to 40° and 50° the peak re-separates into two peaks. These changes may originate from the transition from a hole array towards a film with gratings upon increasing angles and subsequent larger backscattering. At $\theta = 60°$ the backscattering has increased significantly, resulting in a pronounced drop in CD response. Furthermore, the 770 nm plasmonic resonance mode does not show any angular dependence and remains located at the same wavelength.

From the ϕ angle scan (Figure 4.9b) it is evident that only plasmonic resonance modes in the infrared and UV wavelength range are induced. Upon increasing the ϕ angle, the resonance modes in the UV range intensifies and resonance wavelength changes occur. It is also noteworthy for other applications of the ECM, that a very strong resonance mode in the 900-1100 nm wavelength range has been identified in other measurements (data not shown) but is outside of the present measured range as it is not relevant to protein sensing using CD spectroscopy. As was the case with the θ angular scan, the CD response at a $\phi = 60°$ drops as a consequence of significantly increased backscattering.

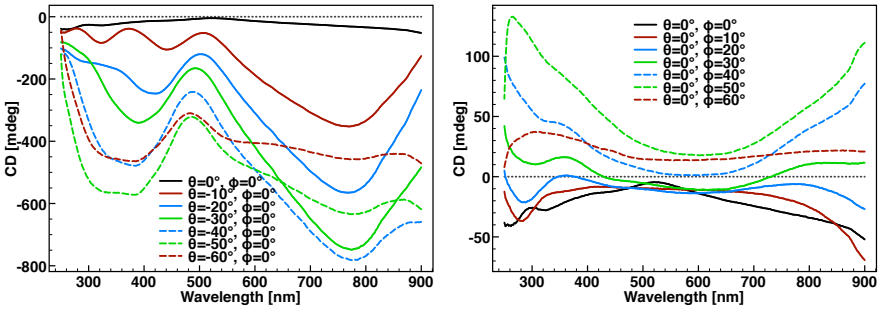

Figure 4.9: Angular scans with large angle increments and corresponding the CD response from the ECM fabricated with 430 nm interpore distance and 50° glancing angle deposition. (a) Independent scan of the θ angle. (b) Independent scan of the ϕ angle.

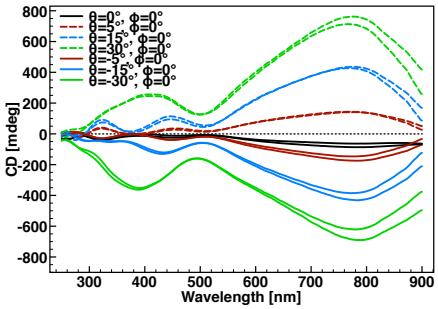

Figure 4.10: CD response from the ECM fabricated with 430 nm interpore distance and 50° glancing angle deposition in four different angle orientation and measured in two different positions 6 mm apart on the sample.

Typically, metamaterials are fabricated with a significantly smaller surface area than the beam profile used to probe the sample. However, the present ECMs are significantly larger, but with various structural imperfections. To validate the integrity of the sample fabricated with 430nm interpore distance and a glancing angle deposition of 50° was probed in two different positions over 6 mm apart. Minor differences were observed (Figure 4.10), indicating small structural differences. These differences are no larger than what has been reported for PCMs fabricated with e-beam lithography [1] or ECMs fabricated with ion beam milling [28] and most likely originate from structural imperfections. Another contributing factor might be that the ECM surface is much larger than the beam profile, hence the structures in the circumference of the beam profile may appear different from those substructures being completely probed. Beam profile induced imperfections are circumvented in usual fabrication techniques as the achievable sample area is much smaller than the beam profile.

2 Chiral Molecule Sensing

As a proof of concept, the sensing power of the honeycomb ECMs were investigated by monitoring the resonance shift upon adsorption of the chiral organic molecule cysteamine and the protein Cytochrom C. Cytochrome C acts as an electron shuttle and as a respiratory redox protein [130]. It also assists as an important mediator in the apoptotic pathways [130]. Due to a free surface accessible cysteine it is well known to readily adsorb onto gold surfaces and is often used to study electron transfer in cyclic voltammetry [131]. Cysteamine is the simplest stable aminothiol, hence it readily adsorbs onto gold surfaces and forms a self-assembled monolayer which is often used as the first layer in the functionalization of surfaces [132].

In all experiments the ECM fabricated with 430nm interpore distance and a glancing deposition angle of 50° was used as it displays a well defined response at ∼770 nm compared to the other structures, together with two minor distinct peaks at ∼440 nm and ∼330 nm. The resulting spectra are presented in Figure 4.11 and the corresponding shifts compared to the bare structure are summarized in Table 4.1.

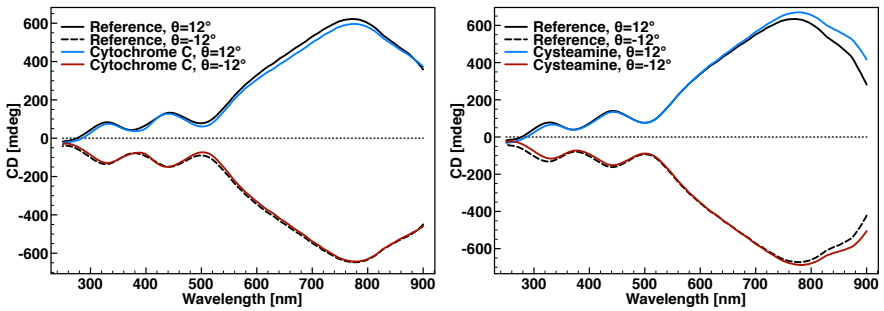

Figure 4.11: CD response from a bare ECM and with a molecule adsorbed on the surface. (a) CD response with and without Cytochrome C adsorbed on the ECM surface. (b) CD response with and without Cysteamine adsorbed on the ECM surface. All measurements were recorded with an ECM orientation of $\theta = 12°;\phi = 0°$ or $\theta = -12°;\phi = 0°$.

Table 4.1: Excitation shifts originating from different molecules

Molecule	$\triangle\lambda_{770nm}$ $(\theta_{12}/\theta_{-12})$	$\triangle\lambda_{440nm}$ $(\theta_{12}/\theta_{-12})$	$\triangle\lambda_{330nm}$ $(\theta_{12}/\theta_{-12})$
Cytochrome C	2/2 nm	-4/-4 nm	2/3 nm
Cysteamine	7/12 nm	2/2 nm	4/5 nm

A similar plasmonic resonance shift of the ∼770 nm mode upon adsorption of Cytochrome C was observed at different θ angles (Figure 4.12 and Table 4.2). This indicates that the sensitivity of the plasmonic resonance towards changes in local refractive index near the ECM surface is not effected by the θ angle. Only the ∼770 nm resonance mode was used in this analysis as the other modes change resonance as described above and as a result are incomparable.

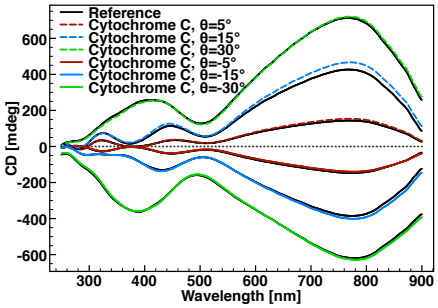

Figure 4.12: CD response from the ECM fabricated with 430 nm interpore distance and 50° glancing angle deposition in different angle orientation and measured with and without Cytochrome C adsorbed on the surface.

Table 4.2: Excitation shifts and dissymmetry factors of the plasmonic resonance at 770 nm at different θ angles, originating from adsorption of Cytochrome C on the ECM fabricated with 430nm interpore distance and a glancing angle deposition of 50°.

Angle	$\triangle\lambda_{770nm}$	$\triangle\triangle\lambda_{770nm}$
(θ_5/θ_{-5})	1.4/1.5 nm	0.1 nm
$(\theta_{15}/\theta_{-15})$	2.3/2.6 nm	0.3 nm
$(\theta_{30}/\theta_{-30})$	2.2/2.4 nm	0.2 nm

It has been demonstrated that the dissymmetry factor $(\triangle\triangle\lambda)$ of the shifts of the right- compared to the left-handed spectrum $(\triangle\triangle\lambda = \triangle\lambda_{Right} - \triangle\lambda_{Left})$ is an indication of an anisotropic adsorption (Table 4.3) [1]. Whereas a perfect isotropic adsorption would result in a $\triangle\triangle\lambda$ value of zero. Interestingly, the two molecules do not result in the same behavior in signal shifts. While Cytochrome C caused an essential non existing dissymmetry

Table 4.3: Dissymmetry factors, calculated from shifts in Table 4.1.

Molecule	$\triangle\triangle\lambda_{770nm}$	$\triangle\triangle\lambda_{440nm}$	$\triangle\triangle\lambda_{330nm}$
Cytochrome C	0 nm	0 nm	-1 nm
Cysteamine	-5 nm	0 nm	-1 nm

Table 4.4: Average shifts calculated from shifts in Table 4.1.

Molecule	$\triangle\lambda_{AV,330nm}$
Cytochrome C	2.5 nm
Cysteamine	4.5 nm

shift, Cysteamine exhibits a relatively large dissymmetry shift as indicated by the 770nm signal. This is coherent with other studies, demonstrating that Cysteamine forms a well-ordered layer on Au surfaces [133, 134]. Furthermore, it has been reported that Cytochrome C either adsorbs with the α-helix structure parallel to the Au surface [135] or that the protein instantly denaturates upon adsorption to the Au surface [136]. In either case this will result in an isotropic layer with respect to the incoming light, which is coherent with the obtained results.

The average extent of the two plasmonic enatiomer shifts at $(\triangle\lambda_{AV} = (\triangle\lambda_{Right} + \triangle\lambda_{Left})/2)$ gives an indication of the amount of molecules adsorbed on the gold surface of the metamaterial [1]. Instead of using the peak at 550 nm to determine the surface coverage as previously reported by PCMs [1], the peak at 330 nm has been used in this paper, since it is the peak located closest to the UV range (Table 4.4). From the data it is apparent that both Cytochrome C and Cysteamine do interact with the ECM gold surface. Compared to another study using PCMs, it is apparent that the $\triangle\lambda_{AV,330nm}$ of Cytochrome C and Cysteamine is comparable to the $\triangle\lambda_{AV,\sim 550nm}$ of the proteins resulting in the highest adsorption on a PCMs gold surface [1]. As the sensitivity of the ECM resonance mode at 330 nm is unknown the exact surface coverage cannot be determined. However, the sensitivity is not expected to deviate significantly from that observed with PCMs at 550 nm. Based on this both Cytochrome C and Cysteamine are adsorbed in picogram quantities on the ECM Au surface.

The current results demonstrate that proteins and chiral organic molecules in general readily adsorb onto the ECM surface. This demonstrates that the ECMs may be used for detection of proteins and chiral organic molecules in a label free way. Furthermore, the ease of Cysteamine adsorption on the ECM surface suggests that other molecules such as Ethanedithiol may be used to functionalize the ECM surface and provide the possibility to fabricate very sensitive sensor arrays.

3 Conclusions

In conclusion, a strong chiroptical response has been demonstrated from different achiral plasmonic hole arrays. The arrays were fabricated by a scaleable technique while retaining control and order of the resulting arrays. This sig-

nifies a substantial improvement to standard fabrication methods such as focused ion beam and electron beam lithography concerning cost and production time. Furthermore, the use of a small chiral organic molecule and a protein has been used as a proof of concept for the sensing of biological and chiral organic molecules in picogram quantities by CD spectroscopy. The response of the presented ECMs was tunable within the UVA and IR wavelengths, depending mainly on the interpore distance of the hole arrays. The deposition angle had an effect on the amount of resonance modes. Small glancing angle deposition resulted in complex ECM geometries and consequently more resonance modes were observed. The amount of modes are larger than has previously been reported for PCMs [1, 68, 126] and is a significant improvement, as more signals yield a more detailed protein fingerprint.

The enantiomeric form of the investigated ECMs were recorded by inverting the tilt of the same sample about the θ angle plane, effectively eliminating the disadvantages of PCMs having to fabricate two independent samples and conducting two separate experiments to probe the protein fingerprint. CD spectroscopy revealed that both Cytochrome C and Cysteamine readily adsorbed on the ECM gold surface, amounting to picogram quantities. Furthermore, the formation of a Cysteamine layer on the ECM gold surface suggests that similar organic molecules may be used to fabricate functionalized surfaces applicable for sensors with increased sensitivity or arrays hereof in a cheap and scaleable way.

4 Methods

Extrinsic chiral metamaterial fabrication

The original molds were prepared by anodic aluminum oxidation using an in house assembled anodization and wet-etching system. 99.98 % pure Al foils (Advent Research Materials Ltd. AL103310) were used as substrates after cleaning in an ultrasonic bath with a sequence of acetone, deionized water and methanol for 1 minute, respectively. In total three types of molds were prepared with different interpore distances, 300 nm, 430 nm and 600 nm. The substrate with 300nm interpore distance was prepared by anodization in 0.3 M oxalic acid solution at 140 V and with a solution temperature of 283 $\pm$ 0.5 K for 40 minutes. The substrate with 430 nm interpore distance was prepared by anodization in 1 M phosphoric acid solution at 180 V and with a solution temperature of 273 $\pm$ 0.5 K for 100 minutes. The substrate with 600nm interpore distance was prepared by anodization in 2 M citric acid solution at 285 V and with a solution temperature of 293 $\pm$ 0.5K for 20 minutes. More details on the fabrication of the original mold has been reported previously [40]. The original molds were used to make negative imprints by

thermal nanoimprint lithography using the EVG520HE semi-automated hot embossing system. This was done in TOPAS 5013L-10 substrates under vacuum with a stamping pressure of 1.25 bar and at 160 °C using the original molds. Next a 30nm film was sputter coated on the surface of the negative imprints. A monolayer of Trichloro(1H,1H,2H,2H-perfluorooctyl)silane (25*vol*% in toluene) was applied to the Al films by gas phase deposition for 1 h in a vacuum desiccator. These samples served as new molds for the second imprint in PMMA. The parameters of this imprint were similar to the once described above but were prepared at 120 °C. The negative molds were used several times without observable deterioration. The final ECMs were achieved by glancing angle deposition of 2nm Cr followed by 50nm Au at different deposition angles.

Scanning electron microscopy

SEM measurements of the ECM surfaces were done at high vacuum ($1 \cdot 10^{-6}$ mbar) and an electron high tension of 10 kV using a Zeiss 1540XB system and standard procedure. The samples were coated by 2 nm gold as to prevent a buildup of static charge.

CD spectroscopy measurements

The ECMs were compatible with commercial available liquid CD cells with a path length of 0.1 mm and a total volume of 50 μL. The CD spectra were collected in normal incident mode where the samples were parallel to the detector and in tilted configuration, where the samples were tilted by 12 °. CD spectra were collected using a commercial JASCO J-750 spectropolarimeter.

Adsorption of Cytochrome C and Cysteamine onto extrinsic chiral materials

Cytochrome C was adsorbed on the substrates by incubation of 50 μL protein solution ($1 mg \cdot ml^{-1}$) for 1 h. The Cysteamine was adsorbed by incubating 50 μL of solution (10mM) for 24 h. The Cysteamine solution was prepared with degassed milli-Q water and the Cytochrome C solution was prepared using 5 mM PBS buffer at pH 7.4.

Extrinsic chiral material surface regeneration

ECMs were reused several times and before each experiment the substrates were submerged for 2h in a sodium dodecyl sulphate solution, followed by a 30 min bath in a Hellmanex III solution at 37 °C. Finally the substrates were cleaned in an oxygen plasma-cleaning unit for 1 h. After each step the ECMs were rinsed with milli-Q water.

Chapter 5

A Computational Study of the Self-Assembly of the RFFFR Peptide

Self-assembled protein nanostructures have attracted much interest due to their involvement in more than 20 degenerative diseases such as Alzheimers, Parkinsons and Prion diseases [137, 138]. However, recent research has also been devoted to its applications such as nanomaterial engineering, nanolithography, regenerative medicine, biosensors, and drug delivery [52, 139–141].

Typically these model peptides originate from larger natural occurring peptides or proteins. One such example is the peptide LVFFA, derived from the β-amyloid peptide which then plays a crucial role in Alzheimers disease [48]. The LVFFA peptide was later modified towards the analogous diphenylalanine (FF). This peptide has been extensively studied and is known to self-assemble into a large variety of structures ranging from nanotubes [50], nanowires [49], films [49, 142], vertical aligned wires [142] and sponge-like structures [142] depending on pH conditions [143]. Recently, the related peptide triphenylalanine (FFF) was investigated which forms plate-like structures with lengths of several micrometers [144]. Furthermore, FFF forms nanospheres without any void space when the N-terminus is protected by a t-butyloxycarbonyl (t-Boc) group [52].

Even though the FF and FFF peptides are derived from the core recognition motif of the Alzheimer's β-amyloid peptide it is still debated whether they share any structural properties with the amyloid fibrils [50, 144, 145].

The self-assembly process is difficult to study experimentally, thus computational methods are an attractive approach to study self-assembly pro-

cesses [146]. The self-assembly process typically occurs on a timescale, which is outside the obtainable timescales for atomistic molecular dynamics (MD) and monte carlo simulations as well. In these cases coarse grained (CG) force fields represent an appealing alternative as the total amount of atoms, in general, is reduced by one third, allowing much larger systems and timescales to be simulated. The MARTINI CG force field [147] is amongst the most popular and versatile force fields. A number of complex molecules has been simulated, such as lipids [147], sterols [148], DNA [149], sugars [150], polymers [151], nanoparticles [152], proteins [153–155] and different solvents [147, 153, 156] as well.

The MARTINI CG force field [147] has some limitations compared to atomistic force fields. The structure of large biomolecules is not reproduced accurately over time in the standard version of the MARTINI force field [147]. Furthermore, the secondary structure has been fixed during the course of the simulation which significantly restricts the phenomena that can be studied. Additionally, the CG simulations yield less structural information than similar atomistic simulations as some atoms are not explicitly included. The latter limitation is circumvented in some CG models by using multiscaling, where parts of the simulation are in atomistic detail while the rest is represented by a CG model [157]. Another option is to translate the final CG structure into the equivalent atomistic structure and continue the simulation for a short period. Both options have been implemented in the MARTINI model [147], but it has been of limited use so far, due to the comprehensive workload required. However, a recent algorithm has made the implementation of the back-translation function more readily accessible [158]. See the Methods section for more information on the MARTINI force field.

The present work investigates, for the first time, the effects of modifying the FFF peptide to the amino acid sequence RFFFR. The motivation for the modification is to direct the self-assembly process towards nano-fibers, which may better resemble amyloid fibrils than the FF or FFF structures. The arginine residues are intended to restrict the interaction of Phe residues in one direction only.

1 In Depth Analysis of the RFFFR Fiber Formation

Peptide Self-Assembly

Snapshots of the CG self-assembly simulation at different time intervals are shown in Fig. 5.1a. Initially all peptides are randomly distributed in the simulation box. After 10 ns three small fiber segments with significant defects have been formed. 100 ns later, these smaller fibers self-assemble into one fiber with defects at the fiber ends. After 200 ns a continuous fiber has

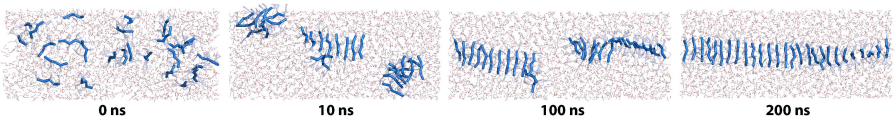

(a) Snapshots from the initial CG simulation

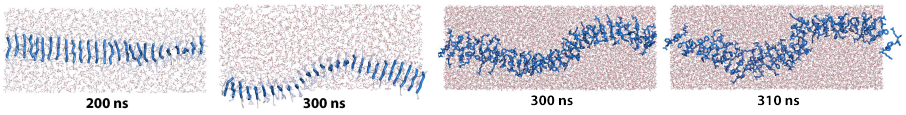

(b) Snapshots from the distance restraint CG simulation **(c)** Snapshots from the atomistic simulation

Figure 5.1: Water molecules and CG side chains are made transparent for simplicity sakes. (a) Snapshots from the initial 200 ns CG simulation where the self-assembly of the nano-fiber occurs. (b) Snapshots from the continued distance restraint 100 ns CG simulation where the cis-configuration of the peptide is prevented. (c) Snapshots from the 10 ns atomistic simulation.

been formed that spans the entire PBC. The peptides in the fiber from the initial CG simulation were mainly found to have an antiparallel configuration where Phe-2 is located in proximity to Phe-1 and Phe-3 of a neighboring peptide (Fig. 5.2a). However, some peptides adopt a cis-configuration for a short period of time during the initial CG simulation. Compared to atomistic simulations of the fiber, the amount of cis-configurations is found to be relatively high (data not shown).

For this reason the final configuration of the 200 ns long CG simulation was used as initial configuration for a 100 ns long distance restraint CG simulation (Fig. 5.1b) where the peptide cis-configuration was excluded. This resulted in a nearly defect free fiber where almost all peptides were oriented antiparallel.

To regain atomistic details, the final configuration of the 100 ns long distance restraint CG simulation was converted to an atomistic configuration and continued for 10 ns (Fig. 5.1c). During the simulation, the Phe residues assume distinct orientation modes at the expense of backbone-backbone angle distribution which becomes more disperse.

The Phenylalanine Cis-Configuration

The existence of cis-configurations in non Proline containing proteins is rather scarce [159]. However, a statistical investigation of the protein data bank reveal that the majority of cis-configured residues in non Proline containing proteins are involved in an interaction with an aromatic residue [160]. Hence we expect some Phe residues to assume a cis-configuration during the MD simulation.

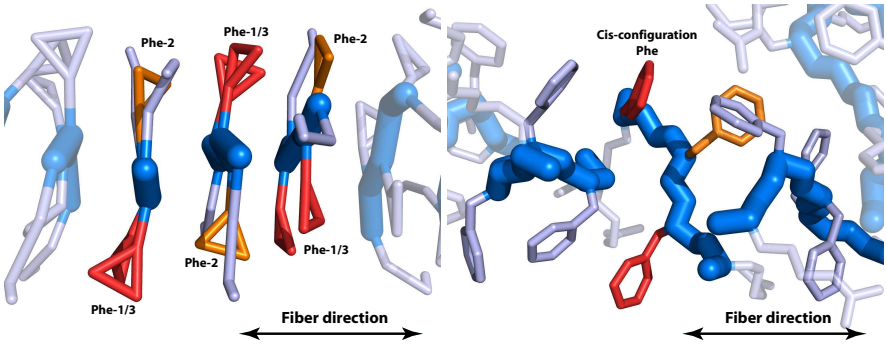

(a) Snapshot from the initial CG simulation

(b) Snapshot from the final atomistic simulation

Figure 5.2: Water molecules are removed in both snapshots while Phe-1 and Phe-3 residues has been highlighted in red and Phe-2 residues in orange. Hydrogen and oxygen atoms are removed in the atomistic snapshot. (a) Close-up snapshot from the initial CG simulation that illustrates the fiber configuration of three representative peptides in the CG simulations. It is apparent that peptides interact in an antiparallel mode as Phe-2 interact with Phe-1 and Phe-3 residues of other peptides. (b) Close-up snapshot from the atomistic simulation illustrating a peptide with a Phe residue in a cis-configuration. It is apparent that the backbone of the peptide with the cis-configurated Phe residue is not aligned with the residual peptides. Hence the cis-Phe residue is forced to assume a cis-configuration as it is too far away to interact with any other Phe residues.

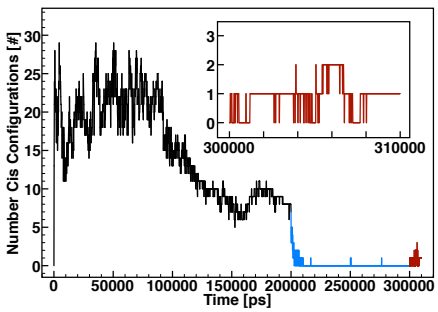

Figure 5.3: Number of Phe residues in a cis-configuration as a function of time over the three simulations; Initial CG simulation (black), CG simulation with distance restraints (blue) and atomistic simulation (red). For clarity a zoom in on the atomistic simulation is depicted in the insert.

Initially a high level of cis-peptide configurations is observed (Fig. 5.3). However, the amount of cis-configurations is reduced during the initial CG simulations, indicating that cis-configurations are important for the formation of the small initial segments while larger fibers are more stable without the cis-peptide configuration.

Another indication hereof is that the continuos fiber from the distance re-

strained CG simulation remains stable without the cis-peptide configuration (Fig. 5.3), hence they are not crucial for the stability of the fiber in the MARTINI model [147]. Furthermore, it is evident from the self-assembly, that the sum of the attractive intermolecular forces amounts to a larger force than the long range electrostatic repulsive forces of the peptides N-termini with a charge of +2. Hence it is likely that the attractive forces are also sufficiently strong to induce the cis-configuration in naturally occurring fibers.

Indications hereof are observed in the atomistic simulation where some peptides resume a cis-peptide configuration. This may be the result of the disperse backbone-backbone angle distribution as it causes some intermolecular Phe side chains to move apart and it becomes energetically favorable to interact with another Phe side chain in close proximity in the opposite direction (Fig. 5.2b). Hence the cis-configuration increases the stability of the fiber, but the net stability is presumably reduced by the increased disperse backbone-backbone angle distribution found during the atomistic simulation.

Structural Clusters

During the atomistic simulation a number of peptides adopt similar molecular structures. These structures were grouped together in clusters based on the single linkage method [161]. According to this method a structure belongs to a certain cluster if its RMSD compared to any other molecule in the cluster is smaller than a certain cut-off value. The center structures of the clusters found during the atomistic simulation using a cut-off of 0.5 Å are shown in Fig. 5.4. Furthermore, the occurrence and number of conformers belonging to each cluster is also listed in Fig. 5.4. Structural information of Arg residues were not included in the analysis as they had a high degree of conformational freedom.

Based on a Newman projection 27 main clusters should be present. However due to the influence of neighboring peptides in the fiber, a degeneracy of the peptide configuration is found, leading to the representation of only nine clusters in the stable fiber (Fig. 5.4). These correspond to 95.4 % of the structures any given peptide adopts during the simulation. The remaining structures are special structures such as the cis-configuration or short lived structures that peptides adopt for less than 50 ps during the simulation. It is noteworthy that nine major clusters were identified which implies a rather strict conformational flexibility of the single peptides in the fiber. Furthermore, very few different conformers participate in the clusters. On average a single conformer participates in 1.7 different clusters, indicating that few cluster transitions occur. The two largest clusters, cluster 3 and 4, constitute together 21 different peptides, hence most peptides adopt a structure belonging to one of these clusters during the simulation.

It should be mentioned that cluster 4 is different from the other clusters,

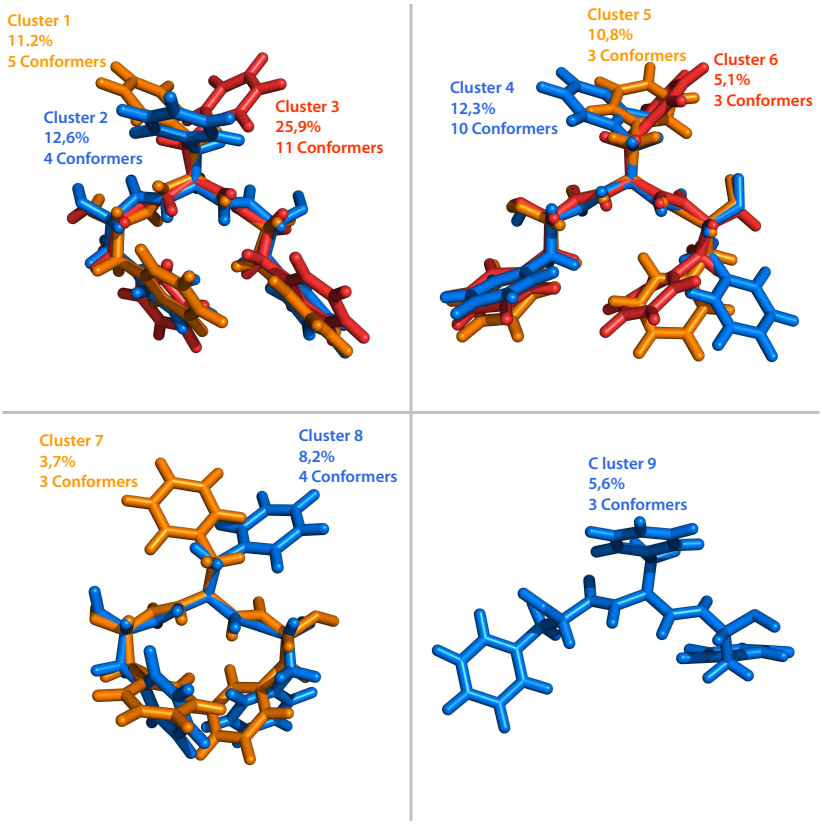

Figure 5.4: Overview of the center structure of the nine clusters found during the atomistic simulation. The total occurrence and number of conformers in each cluster are also listed.

as the Phe-3 residues assumed different orientations. These structures were considered as one single cluster as they had a large distance between the Phe-1 and Phe-3 residues in common, rendering π-stacking interactions negligible and hence had larger Phe side chain orientation fluctuations.

Secondary Structure

Usually secondary structure changes of large proteins require very long atomistic simulations in order to be reliable [162, 163]. For peptides, shorter time scales are sufficient to simulate the folding of a disordered structure into a near native structure [164, 165].

During the present atomistic simulation the secondary structure did not change significantly (Fig. 5.5). It was found that 80 % of the residues have random coil, 20 % beta-strand and occasionally assumed an alpha-helix like configuration. Compared to another atomistic simulation of initially pre-

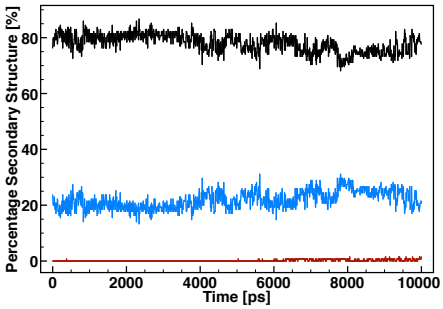

Figure 5.5: The peR$_{cen}$tage random coil (black), beta-strand (blues) and alpha-helix (red) secondary structure the peptides assume during the atomistic simulation as a function of time.

assembled FF and FFF structures, a beta-strand content of below half of what was determined in the current study, was reported [144]. However, experimental studies indicate that nanostructures self-assembled from the FF or FFF peptide consist of a high degree beta-sheet [50, 144]. Presumably this deviation is due to the limited simulation time and number of peptides in the simulation systems. It is likely that the same applies to the present study and a much higher amount of beta-strand content would be observed experimentally for the RFFFR peptide structures.

Hydrophobic Effects and H-bonds

The hydrophobic effect is a major driving force for association of apolar substances in aqueous solutions [166]. It can be enthalpy or entropy driven due to the exclusion of water molecules from the apolar surfaces [167]. As RFFFR consists of a hydrophilic shell and a hydrophobic core, peptide association is expected as a result of the hydrophobic effect. From the solvent accessible surface area (SASA) of the Phe residues as a function of time (Fig. 5.6a) it is apparent that it decreases drastically during the self-assembly and remains quite stable after equilibrium has been reached. This indicates that hydrophobic effects contributes to the self-assembly. A similar tendency and conclusion was reached in a MARTINI simulation study of the FFF peptide [51].

The stabilizing influence of hydrogen bonds in the resulting fibers has been studied by converting the CG system to atomistic details and performing a10 ns MD simulation with the OPLS-aa force field. To validate the obtained results, semi-empirical quantum mechanical calculations with MOPAC were compared to the OPLS-aa force field results. These simulations resulted in on an average 3.3 hydrogen bonds formed per peptide between two peptides (Fig. 5.6b). This is approximately 1.3$\times$ more hydrogen bonds than what was reported for FF [168]. Which leads to the conclusion that RFFFR fibers might be stabilized more by hydrogen bonds than FF structures. FF peptides

form simple head (NH_3^+) to tail (COO^-) hydrogen bonds while RFFFR form a relative elaborate network (Fig. 5.6b). A similar complex network was observed in another all atom simulation of FFF [144]. Concerning RFFFR, only 0.6 head to tail hydrogen bonds per peptide are formed while approximately 1 hydrogen bond is formed between Phe main chain to Phe main chain and Arg side chain to Arg main chain, respectively.

Being an amphiphile, RFFFR has more contact with water molecules than FF which forms more compact sheltered structures. For this reason a high amount of hydrogen bonds are also formed to water molecules (Fig. 5.6c). On average 16.4 hydrogen bonds per peptide are formed to water molecules, where hydrogen bonds to Arg main chain and side chain constitute by far the largest part. These bonds weaken the peptide-peptide hydrogen bonds as water competes for the hydrogen bond interaction. Furthermore, it is generally believed that supramolecular structures cannot be formed in water solely based on hydrogen bonds, on account of competitive hydrogen bond with water [169]. However, hydrophobic regions avert, to some extend, this competition and allows for the self-assembly based on hydrophobic effects and hydrogen bonds [170, 171]. The Phe residues in RFFFR may induce such a compartmentalization as indicated by the relative low water hydrogen bond competition of Phe residues (Fig. 5.6c). This also explains why far less peptide-water hydrogen bonds (0.5 per peptide) are observed in FF simulations, due to the lac of hydrophilic residues.

However, in depth analysis of the peptide-water hydrogen bonds, reveal that a large amount of these compose of peptide-water-peptide hydrogen bonds (Fig. 5.6d). These water mediated hydrogen bonds actually add to the stability of the fiber [172]. Each peptide forms 4.1 water mediated hydrogen bonds whereof 2.6, 0.9 and 0.6 water mediated hydrogen bonds are between Arg main chain, Arg side chain and Phe main chain, respectively. Hence Arg residues do not contribute significantly to the stability through peptide-peptide hydrogen bonds, but in return stabilizes the fiber through water mediated hydrogen bonds.

Compared to the MOPAC geometry optimized structures, supplied in section 2, the total amount of peptide-peptide hydrogen bonds are consistently low (Fig. 5.6b). In addition to the underestimation of the hydrogen bond strength of empirical force fields [173], this might imply that the OPLS-aa force field does not accurately account for hydrogen bonds. However, this is not expected to alter the obtained supramolecular fiber structures significantly, as indicated by the RMSD values obtained from the MOPAC calculations (data presented in section 2). Hence this deviation is expected to only increase the stability of the self-assembly compared to what is observed with the OPLS-aa force field.

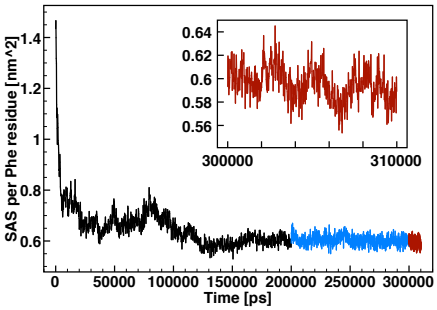

(a) SASA per Phe residue as a function of time. Initial CG simulation (black), CG simulation with distance restraints (blue) and atomistic simulation (red).

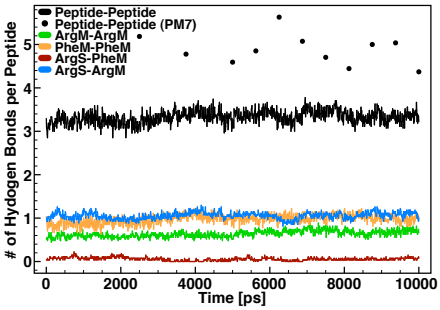

(b) Peptide-peptide hydrogen bonds as a function of time.

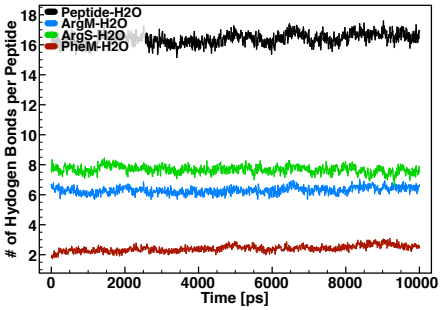

(c) Water-peptide hydrogen bonds as a function of time.

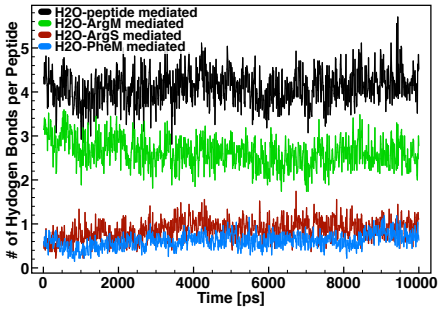

(d) Water mediated peptide-peptide hydrogen bonds as a function of time.

Figure 5.6: Overview of the hydrophobic effect as a function of time and hydrogen bonds as a function of time. A hydrogen bond is counted if the doner-acceptor distance is less than 0.35 nm and the hydrogen-donor-acceptor angle is greater than 150°. Where ArgM is Arg main chain; PheM is Phe main chain; ArgS is Arg side chain; PheS Phe side chain.

Phe-Phe π-Stacking

Hydrogen bonds are important to stability, but π-stacking might be even more important. These interactions are believed to play an important role in a wide range of phenomena including the stereo-chemistry of organic reactions [174], protein folding [175, 176], protein self-assembly [168, 177] and DNA and RNA base-pairing [178]. High level quantum mechanical calculations indicate that π-stacking energies are comparable to hydrogen bonds [179]. Since, more π-stacking interactions are observed than hydrogen bonds in the RFFFR fiber, π-stacking is expected to be the dominating stabilizing force in the resulting fiber assembly.

Standard empirical force fields, such as GROMOS, AMBER, CHARMM and OPLS-aa, account for π-stacking effects by modeling partial charges and

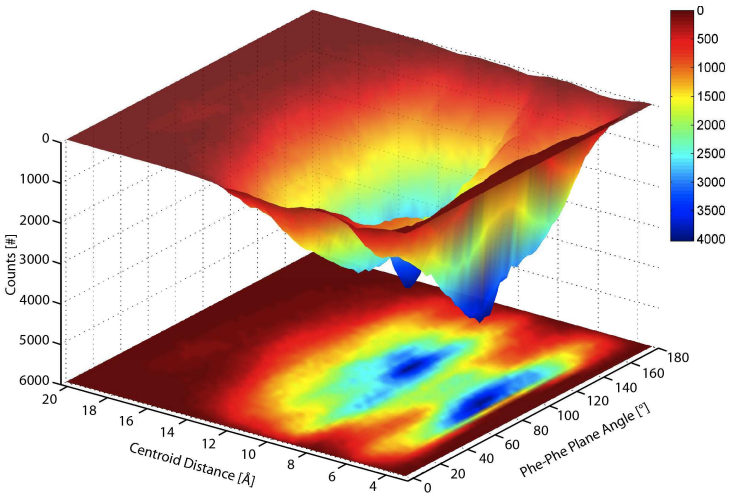

Figure 5.7: Intermolecular Phe-Phe plane angles versus centroid distance (R_{cen}) of the atomistic simulation. Data from the first nanosecond is not included.

the Lennard-Jones 12-6 potential function [180]. These force fields are rather limited by being completely devoid of any electronic structure, hence any charges are assigned to the nuclear center. Furthermore, since atomic charge is not an observable it is difficult to assign partial charges, but the force fields are parameterized to fit experimental or quantum mechanical calculated data. A recent benchmark of different force fields found that the OPLS-aa force field was amongst the most accurate force fields to account for non-bonded interactions such as π-stacking interactions [173]. Despite of the underestimated hydrogen bonds the OPLS-aa force field exceeded even DFT calculations [173]. Since no partial charges are used in aromatic amino acid residues in the MARTINI force field [147] no intermolecular Phe-Phe stacking mode is dominant during the present CG simulations.

It has been suggested that a small partial charge ($< \pm 0.153$), assigned to the C and H atoms belonging to Phe benzene rings, favors the parallel displaced (PD) stacking mode, while a high partial charge ($> \pm 0.3$) favors the T-shaped stacking mode [181]. The OPLS-aa force field applies a small partial charge (± 0.115), but the PD stacking mode was not found to be the preferred stacking mode during the simulation. Our findings conform with the majority of experimental and computational studies indicating that the T-shaped mode is more stable than the PD mode in proteins [182]. However, we also observe a more complex stacking behavior concerning the interplay between intra- and intermolecular π-stacking interactions. This may well be related to findings from a statistical investigation of the protein data bank that shows that over 80 % of the aromatic residues in the surveyed proteins

interact with more than one π-π pair, rendering an exact stacking model difficult to formulate [183].

The intermolecular Phe-Phe plane angles from neighboring Phe residues versus centroid distance (R_{cen}) is illustrated in Fig. 5.7. Two maxima are found at Phe-Phe plane angles of 87° and 100° and Phe-Phe separations of 5.5 and 10 , respectively. Thus the T-shaped mode (60-120°) is dominant, a hybrid mode (30-60° and 120-150°) in between the T-shaped and PD mode is common while the frequency of the PD mode (0-30° and 150-180°) is low. However, it is noteworthy that the Phe-Phe plane angles of the individual Phe pairs tend to remain stable during the atomistic simulation.

From Fig. 5.7 it is apparent that the R_{cen} may be as small as 4 in the PD stacking mode, while the R_{cen} between two Phe benzene rings in a T-shaped stacking mode may only come as close as 4.5 . This phenomenon is observed in other simulation studies of Phe stacking as well and is attributed to sterical hindrance [168, 176].

In the 6.8 $<R_{cen}<$8.7 range, the Phe-Phe plane angles are restricted to the T-shaped mode in the angle interval of 72-113°. Hence Phe ring pairs moving apart or closer need to adopt a T-shaped mode through this saddle point. The π-stacking interaction cut-off value of 7.5 , generally applied, is based on a statistical study of 505 non-homologous proteins from the protein data bank [176]. This cut-off value coincides with the saddle point found in the Phe-Phe interaction angle distribution plot (Fig. 5.7). The peptides with a Phe-Phe plane angle maximum of 100° and a separation distance of 10 shown in Fig. 5.7, preferentially adopt a perpendicular orientation towards each other. The maximum found at a separation distance of 4-5 , suggests a similar intermolecular π-stacking behavior of the RFFFR peptide compared to the FF and FFF peptide, as they too preferably assume T-shaped stacking modes [51, 144, 145, 168].

MOPAC geometry optimized structures conform with these results and only minor differences were observed in population distribution over the angle interval, see section 2. A very similar saddle point and the same maximum were obtained (Fig. 2S). A minor difference between minimum R_{cen} was discovered but this may be attributed the absence of PBC. It was also observed that the propensity for Phe residues to assume a T-shape stacking mode is slightly overestimated in the OPLS-aa force field compared to MOPAC calculations.

Concerning intramolecular π-stacking interactions it is found that the R_{cen} between Phe-1/Phe-3 and Phe-2 internally in the peptides are larger than the cut-off length, rendering these interactions negligible (Fig. 5.8a). Hence the two distinct modes found in the angle distribution analysis are a consequence of the energetically favorable peptide configurations previously discussed. However, it is noteworthy that no direct transitions between the two modes are observed, indicating that a large energy barrier exists between these two

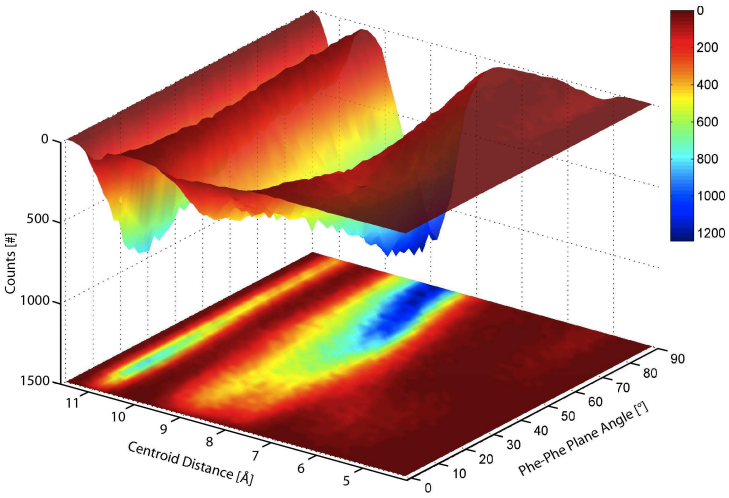

(a) Intramolecular Phe-Phe benzene angles between Phe-2 and Phe-1 or Phe-3 residues only versus centroid distance (R_{cen}) of the atomistic simulation.

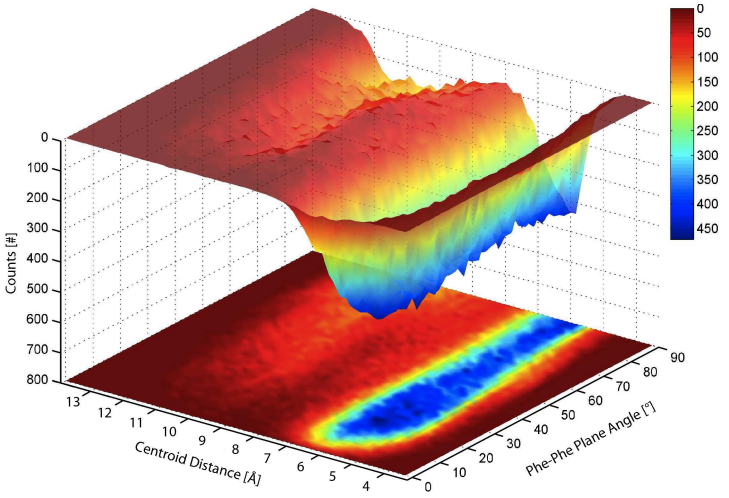

(b) Intramolecular Phe-Phe benzene angles between Phe-1 and Phe-3 residues only versus centroid distance (R_{cen}) of the atomistic simulation.

Figure 5.8: Intramolecular Phe-Phe benzene angle distributions from the atomistic simulation. Data from the first nanosecond is not included.

different peptide configurations.

The intramolecular Phe-Phe angle distribution of Phe-1 and Phe-3 residues is found to slightly favor the PD π-stacking mode, but a quite even distribu-

tion across all three regions (0-30°, 30-60° and 60-90°) is found (Fig. 5.8b) which is coherent with the cluster analysis (Fig. 5.4). This indicates that the Phe side chains have a sufficient high flexibility to enable them to assume an intermolecular T-shaped stacking mode. Whereas intramolecular Phe residues do not favor any specific stacking mode in RFFFR, the T-shaped mode is dominant both inter- and intramolecular in FF and FFF peptide structures [51, 144, 145, 168]. This difference arises from the design of RFFFR, as Phe residues may only interact in one direction, rendering it geometrically impossible that both inter- and intramolecular Phe residues stack in the T-shaped mode. Furthermore, the intermolecular Phe residues are able to move closer than intramolecular Phe residues (evident from Fig. 5.7 compared to Fig. 5.8b). Hence π-stacking interactions are stronger for inter- than intramolecular Phe residues, which may explain why intramolecular Phe residues adjust their stacking mode in such a way that the intermolecular Phe residues are able to stack in a T-shaped mode.

Within the limitations imposed to the simulations and static fixation of parameters relevant to the interactions, it is shown that intramolecular Phe-Phe stacking orientation do not contribute the stability of the fiber. Had the opposite been the case, the fiber may not have remained stable during the final atomistic simulation or the MOPAC geometry optimization. However, a somewhat over exaggerated, due to the missing PBC, average Cα RMSD value of 2.68 Åwas found, indicating that the two models produce relative comparable results, see section 2. Reference simulations where PBC were unimportant, resulted in an average Cα RMSD value of 1.31 Åindicating the high accuracy of the OPLS-aa force field.

For more details and discussion on the comparison to the semi-empirical quantum mechanical calculations with MOPAC, see section 2.

Critical Fiber Concentration

The critical fiber concentration of RFFFR was determined from a series of self-assembly MD simulations. Starting with randomly positioned peptides a number of simulations with the same amount of peptides, but at different concentrations, were performed to monitor if fibers or smaller segments thereof were formed. Several, factors such as pH, temperature and simulation system size also influences the critical fiber concentration, which was not investigated in the present study.

An overview of the performed simulations is given in Table 5.1. The simulations with peptide concentrations of 120 mM and 170 mM resulted in continuous fibers rapidly.

At a peptide concentration of 100 mM, the peptides assembled into fiber segments and in some cases a single fiber with disconnected ends was formed. As it might have been a matter of time before these fibers assembled into one

continuous fiber, the simulations were extended to 1 μs, after which continuous fibers assembled in 2 out of 7 simulations. The extended timescale and the low ratio of simulations where fibers assembled, indicates that 100 mM is close to the critical fiber concentration.

The simulations with peptide concentration of 70 mM and 20 mM did not form single or continues fibers, not even on a 1 μs timescale. Instead the peptides assembled into many small fiber or micelle like structures, indicating that these are below the critical fiber concentration. Hence it is likely that under these simulation conditions the critical fiber concentration of RFFFR is between 70 mM and 100 mM.

Table 5.1: Overview of simulations performed to investigate at which peptide concentrations fibers self-assemble from initial randomly positioned peptides. All simulations contain the same amount of peptides.

Concentration (mM)	Fibers/Simulations	Durations (ns)
170	1/1	200
120	1/1	200
100	2/7	1000
70	0/5	1000
20	0/1	200

To verify the results an additional series of simulations was performed where the single continuous fiber from the simulation of the peptide concentration 120 mM was inserted into a larger simulation box yielding a peptide concentration of 100 mM and 70 mM. An overview of these simulations is illustrated in Table 5.2.

It is apparent that the fiber remains stable in all simulations at 100 mM peptide concentration but disassembles in all simulations at 70 mM peptide concentration. Hence these results are coherent with the conclusion from the self-assembly simulation series and the critical fiber concentration is found to be in between 70 mM and 100 mM.

Table 5.2: Overview of simulations performed where the single continues fiber from the simulation with 120 mM were inserted into bigger simulation boxes in order to verify that the the critical fiber concentration is between 70 mM and 100 mM.

Concentration (mM)	Fiber Remained Stable	Durations (ns)
100	5/5	200
70	0/5	200

2 Semi-Empirical Quantum Mechanical Validation

The results obtained from the all atom MD simulation with the OPLS-aa force fields were compared to results obtained by a semi-empirical quantum mechanical (SQM) approach. The MOPAC package [184] developed by Stewart was used as the implemented module MOZYME [185] allows for the calculation of more than 1000 atoms, which is the approximate limit of standard SQM calculations. However, MOZYME [185] utilizes a localized molecular orbital method that allows for processing a system of 15,000 atoms in a very fast timescale compared to other solutions. The newest MOPAC method, PM7 [186], is additionally well known for its very high accuracy that borders DFT-D calculations [186–188].

The OPLS-aa snapshots that was geometry optimized with MOPAC was as follows (starting from the beginning of the OPLS-aa simulation): 2500 ps, 3750 ps, 5000 ps, 5625 ps, 6250 ps, 6875 ps, 7500 ps, 8125 ps, 8750 ps, 9375 ps and 10,000 ps. Explicit solvent from the MD snapshots were removed and solvent effects were accounted for by the COSMO implicit water model [189] with a dielectric constant of 78.4. The geometry optimization convergence criterion was set to a maximum gradient of 10.0 kcal/mol/Å, after which a second calculation was performed with a convergence criterion of 5.0 kcal/mol/Å. Finally a single SCF calculation was performed to correct any error in heat of formation.

As PBC are not possible to implement with the SQM approach, on larger systems with many charges, a second simulation series was performed. This series was performed in the same way as described above, but with frozen alpha carbon atoms of the arginine residues in the peptides constituting the ends of the fiber, enforcing the fiber to remain in a stretched configuration. This series will be denoted the, restricted MOPAC calculations, henceforth.

RMSD of the Calculations

Since no PBC were implemented during the MOPAC calculations a large structural difference was expected compared to the MD simulation snapshots calculated with the OPLS-aa force field. The MOPAC calculations mimic a free fiber with a finite length in solution, while the OPLS-aa simulations mimic a continues infinite fiber in solution. As indicated by the RMSD values (Fig. 5.9a), the RMSD values were found to fluctuate a lot. This fluctuate is related to the contraption and expansion of the fiber with finite length calculated by MOPAC, while the continues fiber remain rather the same length during the MD simulation. This effect was circumvented in the restricted MOPAC calculations and yielded much more stable and in general much lower RMSD values (Fig. 5.9b).

As a reference, four peptides in the fiber from the OPLS-aa simulation

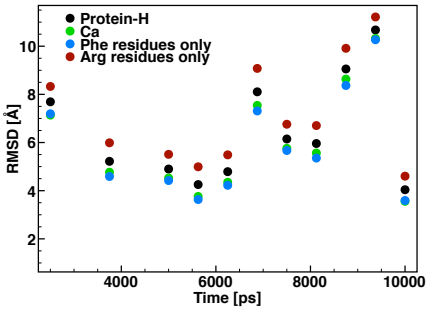

(a) RMSD values of OPLS-aa snapshots compared to the MOPAC geometry optimized snapshots.

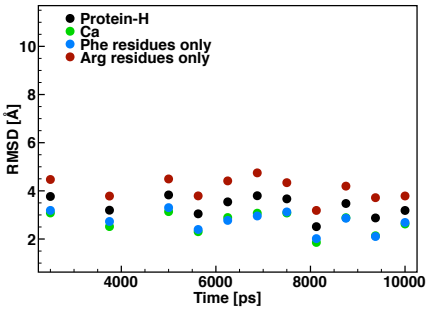

(b) RMSD values of OPLS-aa snapshots compared to the restricted MOPAC geometry optimized snapshots.

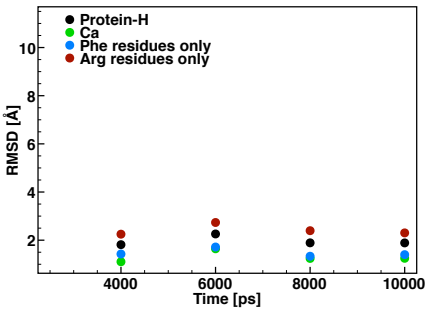

(c) RMSD values of OPLS-aa snapshots, from a simulation with four peptides in a big simulation box, compared to the restricted MOPAC geometry optimized snapshots.

Figure 5.9: Overview of the RMSD values of different groups from the OPLS-aa snapshots compared to the MOPAC geometry optimized snapshots. (Black: All atoms without hydrogen atoms, green: All alpha carbon atoms, blue: All atoms in the phenylalanine residues, red: All atoms in the arginine residues).

were cut out and inserted into a large simulation box (10 nm x 10 nm x 10 nm) after which the box was filled with water. This configuration was energy minimized and served as starting point in a 10 ns long MD simulation performed with the OPLS-aa force field using the same parameters as the main OPLS-aa simulations. This small fiber segment would never interact significantly with its periodic mirror counterpart due to the large simulation box. MOPAC calculations were performed on selected snapshot of this simulation. This resulted in low RMSD values between the OPLS-aa snapshots and the MOPAC geometry optimized snapshots (Fig. 5.9c).

Comparing the RMSD values of the simulation series (Fig. 5.9) it is apparent that the MOPAC calculations deviate a lot from the OPLS-aa calculation. However, the restricted MOPAC calculations yield some low RMSD values, indicating that the large values of the MOPAC calculations is likely to originate form the missing PBC. Hence the Phe-Phe configuration data from the MOPAC calculations apply to another situation than the one in the OPLS-aa MD simulation. The restricted MOPAC calculation has an average RMSD (Protein-H) value of 3.35 Åcompared to the OPLS-aa calculations. As the average RMSD (Protein-H) value of the reference simulation with four peptides is 1.96 Å, the restricted MOPAC calculations are acceptable considering the imposed imitation of PBC.

The average Ca RMSD values of the MOPAC, restricted MOPAC and small four peptide MOPAC calculations are 5.99 Å, 2.68 Åand 1.31 Å, respectively. A CHARMM simulation study [190] of eight different proteins showed average RMSD (Ca) values (compared to the crystal structure) in the range of 1.06 Å- 3.58 Å. The same eight proteins had average RMSD (Ca) values ranging from 3.16 - 4.15 Åwhen the MARTINI force field was used [191]. Reports of RMSD values from other studies using different all-atom force fields (AMBER, CHARMM, GROMOS, OPLS-aa) range from 0.94 - 4 Å [192, 193]. Considering this the obtained OPLS-aa results are in very good agreement with the restricted MOPAC calculations.

Interestingly, the Phe residues obtain the lowest RMSD values of all the analyzed groups (Fig. 5.9). Only the Ca group from the calculations of the small simulation consisting of four peptides obtain a lower RMSD than the Phe residues groups. Hence the OPLS-aa Phe configurations are in very good agreement with the configurations obtained by MOPAC. The RMSD values of the Ca atoms are only marginal higher than the RMSD values for Phe residues, which means that the secondary structure is not expected to be significant different. In all simulation series, arginine residues yield the highest RMSD value, which is not surprisingly as this group is the most flexible group. It could also be an indication of a discrepancy between the two water models used, as implicit solvent was used in the MOPAC calculations while explicit solvent was used in the OPLS-aa calculations.

Table 5.3: Overview of the peR_{cen}tage population of three stacking modes, parallel, semi-parallel and T-shaped found from the calculation series performed with MOPAC, restricted MOPAC and OPLS-aa of the selected snapshots. The population it only determined for intermolecular Phe pairs with a R_{cen} less than 7 Å.

0Å$\leqslant R_{cen} \leqslant$ 7.0Å	MOPAC	Restricted MOPAC	OPLS-aa
Parallel stacking mode	18.1%	18.6%	20.1%
Hybrid stacking mode	33.7%	35.4%	20.4%
T-shaped stacking mode	48.2%	46.0%	59.5%

Table 5.4: Overview of the peR_{cen}tage population of three stacking modes, parallel, semi-parallel and T-shaped found from the calculation series performed with MOPAC, restricted MOPAC and OPLS-aa of the selected snapshots. The population it only determined for intermolecular Phe pairs with a R_{cen} greater than 7 Åand less than 14 Å.

7Å$\leqslant R_{cen} \leqslant$ 14.0Å	MOPAC	Restricted MOPAC	OPLS-aa
Parallel stacking mode	14.6%	13.3%	14.0%
Hybrid stacking mode	37.7%	37.5%	34.6%
T-shaped stacking mode	47.7%	49.2%	51.4%

Intermolecular Phe-Phe Plane Angle Distribution

It is noteworthy that the intermolecular Phe-Phe plane angle distributions in (Fig. 5.10), was calculated based on all Phe-Phe interactions within 1.4 nm. Hence the results are not directly comparable to Fig. 5.7, where only the Phe-Phe interactions of neighbour peptides were included in the analysis.

From Fig. 5.10, it is apparent that Phe residues preferably stack in the T-shaped mode in both MOPAC calculations and the OPLS-aa calculations. Furthermore, all calculations result in a saddle-point at approximately 7 Åthat is close to the before mentioned limit (7.5 Å) where Phe-Phe stacking is pertinent. Hence both methods are equally accurate in determining the cut-off value, even when simulated under different situations. The small discrepancy between the experimental value and the simulated might be explained by the fact that 7.5 Åwas determined from an investigation of the protein data bank [176]. Hence the analysis was based on intramolecular interactions rather than intermolecular interactions, which is the case in this study.

Overall the surface-shapes are very comparable witsplicedh only few discrepancies. In the R_{cen} area where Phe-Phe stacking is pertinent ($R_{cen} < 7.5$ Å), it is apparent that the Phe side-chains may approach each other more in both MOPAC calculations than in the OPLS-aa calculations. From the MOPAC calculations the closest observed R_{cen} was 3.41 Å, in the restricted MOPAC calculations the smallest observed R_{cen} was 3.58 Å, while it was 3.97 Åduring the OPLS-aa calculations. A similar tendency is observed for Phe residues that stack in a T-shape mode, though they in general are further apart by a

small measure, due to steric hindrance (Fig. 5.10). It is likely that this difference is related to the absence of PBC in the MOPAC calculations, however it does not explain the discrepancy between the restricted MOPAC calculations and the OPLS-aa calculations. Hence a minor inconsistency might be introduced by the OPLS-aa force field compared to MOPAC.

In the range 0 Å< R_{cen} < 7.0 Åof the Phe-Phe plane angle distribution, a more narrow distinct local maximum is observed for both MOPAC calculation series compared to the OPLS-aa calculations (Fig. 5.10). However, a larger population of Phe-Phe residues are found to be in a T-shaped stacking mode in the OPLS-aa calculations (Table 5.3). Though the restrictive angle range of the T-shaped mode in the MOPAC calculations seems rather imposed, Table 5.3 might imply that the propensity for Phe residues to stack in a T-shaped mode might be somewhat exaggerated in the OPLS-aa force field.

Above the R_{cen} where Phe-Phe stacking is pertinent, the Phe-Phe plane angle distribution populate a slightly broader angle range in the MOPAC calculations compared to the restricted MOPAC calculations and even more so, compared to the OPLS-aa calculations (Table 5.4). This may be related to the absence of PBC in the MOPAC calculations or an effect from the potential energy surface related to the specific force fields. However, the models conform rather well, which is an indication of the similarity in the peptide configurations rather than a similar π stacking configuration.

Intramolecular Phe-Phe Plane Angle Distribution

The intramolecular Phe-Phe plane angle distributions in Fig. 5.11 were calculated by the same method as Fig. 5.8. Hence the results are directly comparable, but for simplicity and to ensure that the observed MOPAC results are not a consequence of selecting specific snapshots, the analysis was also conducted on the same OPLS-aa snapshots.

As was the case with the thorough investigation in Fig. 5.8, the amount of Phe-Phe interaction in the range where π-π stacking is pertinent is very low compared to the amount of interactions above this range. The data set in Fig. 5.11 is too low to obtain a detailed overview of the Phe-Phe plane angle distribution in the range within 0-7.5 Å.

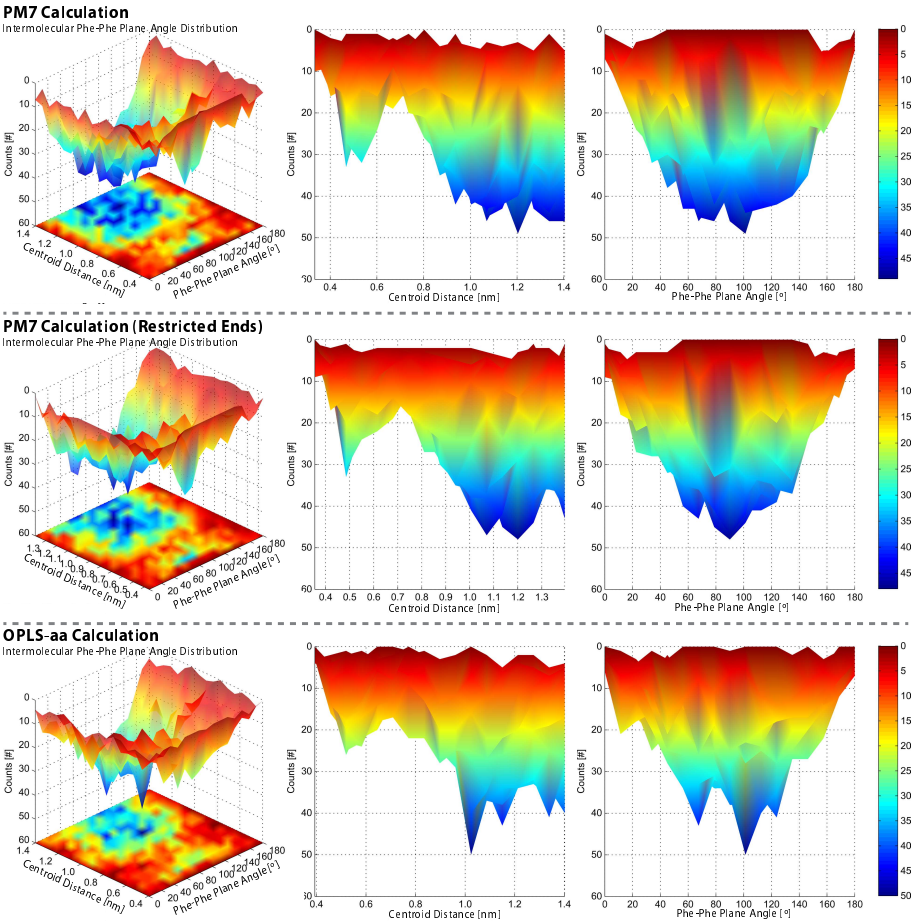

Figure 5.10: Intermolecular Phe-Phe plane angle distributions versus centroid distance (R_{cen}) determined from MOPAC, restricted MOPAC and OPLS-aa calculations of selected snapshots from a 10 ns long MD simulations performed with the OPLS-aa force field. π-π stacking with a R_{cen} above 7.5 Åis negligible, hence maximums above this distance yields information of the peptide configurations rather than π-π stacking.

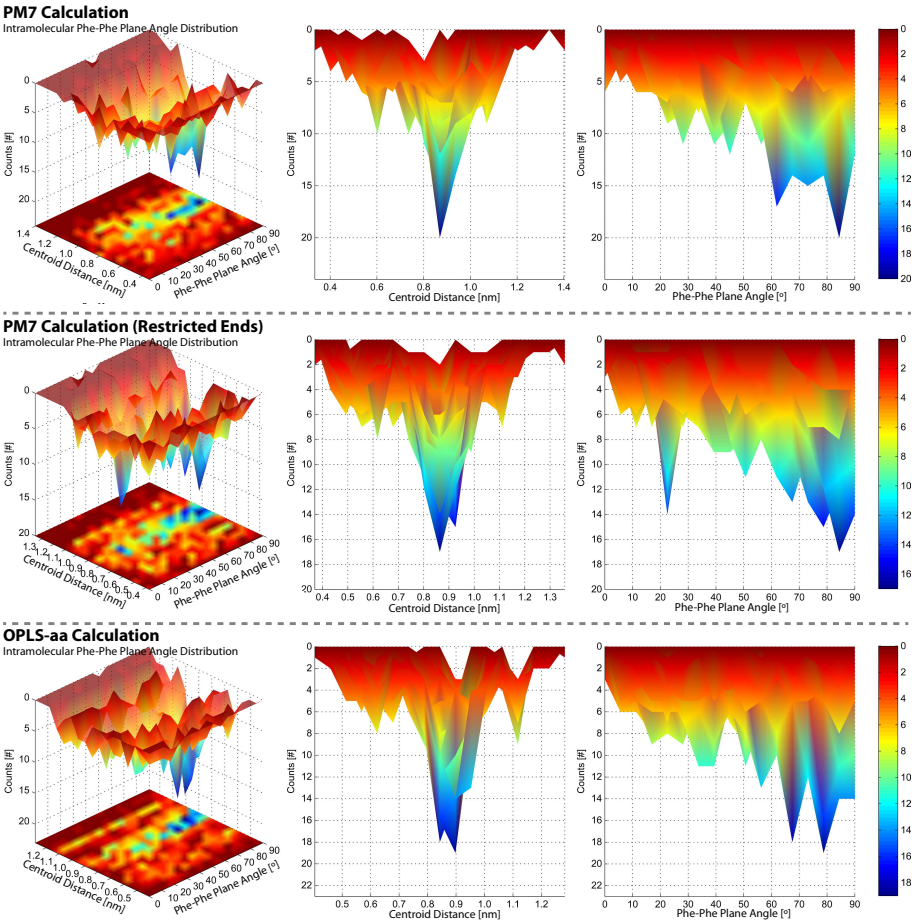

Figure 5.11: Intramolecular Phe-Phe plane angle distributions versus centroid distance (R_{cen}) determined from MOPAC, restricted MOPAC and OPLS-aa calculations of selected snapshots from a 10 ns long MD simulations performed with the OPLS-aa force field. π-π stacking with a R_{cen} above 7.5 Åis negligible, hence maximums above this distance yields information of the peptide configurations rather than π-π stacking.

However, some minor peaks appear all over the angle range (0-90°), indicating the no preferable stacking mode exists in the R_{cen} range of 0 - 7.5 Å. In all calculations the minor peaks are centered on approximately 6 Å.

Above the R_{cen} where π-π stacking is pertinent the Phe residues preferably stack in a T-shaped mode with a R_{cen} of approximately 9 Åin all calculations. However, in Fig. 5.8 a larger population of Phe pairs were found to stack in a parallel mode with a separation of 11 Å. This configuration is eliminated during MOPAC global geometry optimization, while it appears in both the restricted MOPAC and OPLS-aa calculation series. As was the case in Fig. 5.8, this mode is very restricted to a Phe-Phe separation of 11 Åin the restricted MOPAC and OPLS-aa calculation with very little R_{cen} flexibility and few transition possibilities. Due to the absence of this configuration in the MOPAC calculation, it is likely that the configuration is linked to a stretched fiber. This seems likely, as Phe residues in a peptide in a stretched fiber would need to spread wider (a larger intermolecular Phe pair separation would render the interactions negligible). Furthermore, it is know from Fig. 5.8 that this configuration originates from Phe-2 in relation to Phe-1 and Phe-3 and not from Phe-1 in relation to Phe-3. Hence the Phe residues in the configuration point in opposite directions and would yield a wider peptide.

Opposed to the analysis in Fig. 5.8, no favored stacking mode is observed at a R_{cen} of 11 Å. It is possible that this is due to the limited data-set. Or it could be a random consequence of the selected snapshots missing this configuration. However it is noteworthy that an extra major local maximum is observed in the restricted MOPAC calculation series with an Phe-Phe plane angle of 22° and a R_{cen} of 9 Å. This maximum was not observed in any other analysis. The origin of this mode is unknown but it is possible that it is the missing maximum at 20° and a R_{cen} of 11 Åfrom Fig. 5.8, that has shifted due to the allowance of the Phe-Phe pairs to move closer. However the mode is very distinct and seems very restrictive, indicating a very fixed peptide configuration.

3 Other Peptides That Assemble Into Amyloid Fibrils

Prior to the results obtained in the above presented publication [194], a virtual screening approach has been performed in order to identify possible candidates for further detailed computational and experimental studies. The starting point for this virtual screening has been the basis of other already published results such as the self-assembled structures and MD simulations of FF and FFF peptides [49, 52, 142–144] and the virtual screening of all tripeptides for hydrogel self-assembly [195].

The screening for potential short peptides that self-assembled into amy-

loid fibers included: QFFQ, FFFD, RFFR, QFFFQ, RFFFE and RFFFR. The potential was assessed based on a 100 ns long MD simulation trajectory performed with the MARTINI force field. According to the simulations, all peptides formed amyloid like fibers except FFFD, which formed micell like structures (Figure 5.12). However, the initial simulation box was cubic with dimensions only chosen so as to satisfy a constant peptide/water ratio in all simulations. Hence some simulation boxes might restrain a perfect fiber formation. That is likely to be the case for the simulations of QFFQ, RFFR and RFFFE. It is also noteworthy that the following conclusion was based on a single simulation for each peptide and is hence not a comprehensive investigation, but a short initial screen of the fiber formation potential.

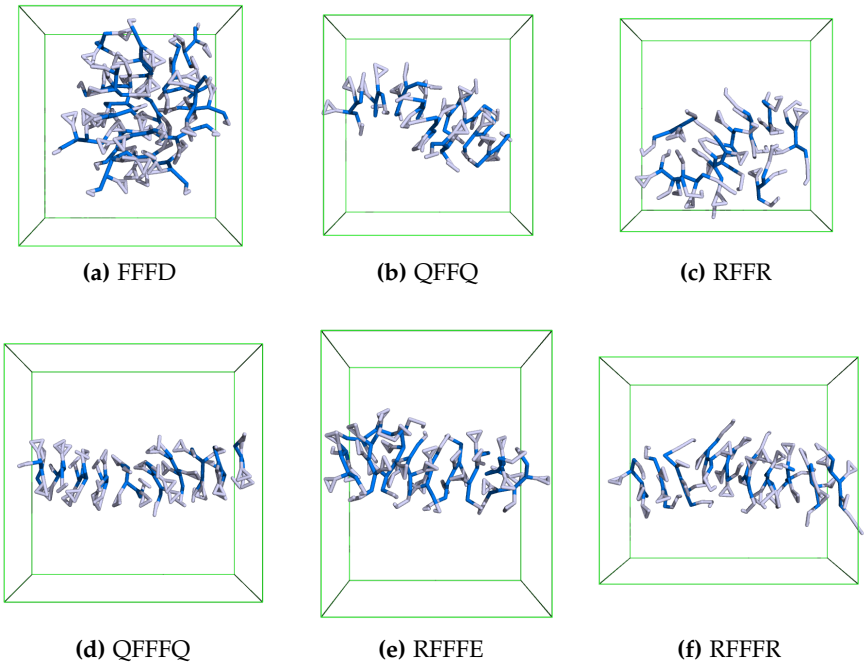

(a) FFFD **(b)** QFFQ **(c)** RFFR

(d) QFFFQ **(e)** RFFFE **(f)** RFFFR

Figure 5.12: Final snapshot of a 100 ns long CG MD simulation performed with the MARTINI force field and polarized CG water model. Water molecules have been made transparent for simplicity, dark blue represents the peptide backbone, light blue is the peptide side chains and green is the simulation box. (a) The FFFD peptide. (b) The QFFQ peptide. (c) The RFFR peptide. (d) The QFFFQ peptide. (e) The RFFFE peptide. (f) The RFFFR peptide.

QFFFQ and RFFFR both formed the most ordered fibers and on the shortest time scale (>10 ns). In spite of this, RFFFR was chosen as the peptide with the greatest propensity to amyloid formation as the Arg side chain is positively charged and hence able to better shield the hydrophobic fiber core from water exposure.

4 Design of a Simulation Box with Walls

Other results that are worthy to mention and were obtained prior to the above presented publication [194] include the design of a CG MD simulation wall. This was required to study the self-assembly process of the RFFFR peptides into single continuous fibers in one direction. Initial simulations without walls had chaotic fiber networks not suitable for analysis or visualising the self-assembly. As walls have never been parameterised in the MARTINI force field, different approaches for implementation of walls in the XY-plane were attempted.

GROMACS walls

Though this is the native GROMACS method for implementing walls, it requires a large amount of parameterizing to fit with CG MARTINI simulations. The walls may consist of an arbitrary atom type, however, the LJ potential and density needs to be modified. Furthermore, it only offers the option of adding one or two walls, hence the fiber formation may proceed in a 2D way. Due to these limitations, only a few attempts with GROMACS walls were performed. The wall consisted of MARTINI pseudoatoms (beads) similar to unpolarized CG water molecules with a density of 12 atoms/nm^2 (dense wall as one bead has a radius of 0.21 nm and corresponds to four water molecules).

As the wall was constructed of water like molecules, it was expected that the interaction with the peptides would be rather inert and only gently push the peptides away when they came very close. Instead it is apparent that the peptides are strongly attracted to the wall (Figure 5.13a). Most likely this is the well know phenomenon of protein adsorption onto interfaces due to a decrease in conformational entropy compared to that of the native conformation [196].

Hence the atoms of the wall are stationary and act as a solid interface. For this reason, thoroughly parametrisation of the LJ potential is necessary in which case a wall consisting of moving atoms might be easier to construct.

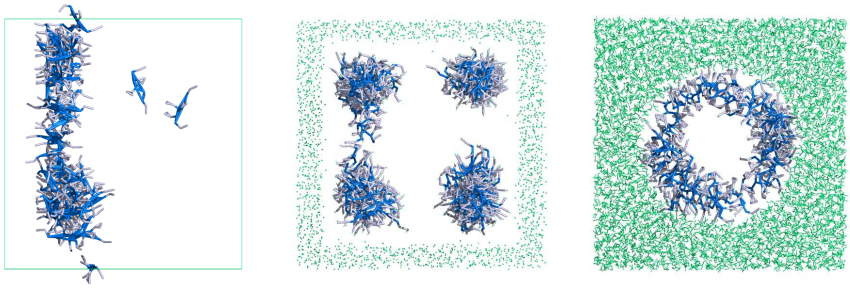

(a) GROMACS implicit wall, 160ns. **(b)** Position restrained water wall, 10ns. **(c)** Circular position restrained water wall, 74ns.

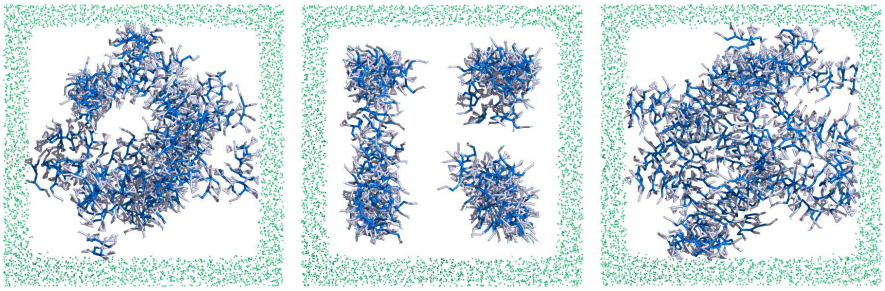

(d) Charged position restrained wall, 9ns. **(e)** Wall with modified LJ potential, 10ns. **(f)** Wall with user-specified table potential, 10ns.

Figure 5.13: Final snapshots of CG MD simulations with different walls and RFFFR peptides that forms fibers performed with the MARTINI force field and polarized CG water model. Water molecules have been made transparent for simplicity, dark blue represents the peptide backbone, light blue is the peptide side chains and green represent the wall or wall atoms. (a) 160 ns long simulation with GROMACS wall consisting of implicit atoms. (b) 10 ns long simulation with position restrained water wall. (c) 74 ns long simulation with circular position restrained water wall. (d) 9 ns long simulation with charged position restrained wall. (e) 10 ns long simulation with a wall consisting of atoms having a modified LJ potential. (f) 10 ns long simulation with wall consisting of atoms having a user-specified table potential.

Position restrained water walls

The simplest of the tested wall types consisted of moving CG water molecules which were position restrained in the simulation box edges to form a wall. This allows for the wall molecules to move, while still remain within the vicinity of the wall boundaries. Hence when peptides try to push the water molecules away from their proximate restrained position, an opposite force is exerted onto the water molecules, which then functions as a wall.

In total eight attempts were performed with varying position restrain strength. Some walls were constructed of CG water beads, while others consisted of polarized CG water molecules. Furthermore some attempts were

restricted in all directions, while others were only restricted in the X and Y direction, allowing for a semiisotropic environment. Though these wall molecules were moving and interacted with other beads in a similar way as ordinary water molecules an entropic effect was still observed (Figure 5.13b). Even weak restrictions resulted in an interface effect.

Circular walls

In an attempt to diminish the entropic effect, circular XY plane position restrained water walls were constructed. It was hoped that the reduced contact area between peptides and the wall in a circular wall, compared to in a square wall, would result in a diminished entropic effect. However this was not the case. In total three attempts with varying cell diameters, leading to varying attractive forces, were performed. In all simulations spiralling fibers along the walls were formed (Figure 5.13c).

Charged water walls

Another wall type consisted of XY plane position restrained charged non-polarized CG water beads. As the PME algorithm was used, the repulsive electrostatic force between the wall and the peptides would decrease reciprocally. In this way, it was the hope that the attractive entropic effect would be counteracted by an equally strong repulsive force from a partial wall charge. In total 26 attempts with varying partial charges were performed. However, it was observed that the magnitude of the partial charge only determined a distance to a perimeter where the two opposing forces were equal. The fibers would be spatially limited to stay at the border of the perimeter as repulsive forces from the wall dominated outside and attractive entropically effects dominated inside the perimeter (Figure 5.13d).

C6C12 potential modified walls

A more sophisticated wall type was constructed of XY plane position restrained CG beads with user-designed non-bonded parameters. Similar to the charged wall, the aim was to model a counteracting repulsive force, that would be equal to the attractive entropically effect. In total nine attempts were performed with varying sigma and epsilon values for the LJ 12-6 potential $(V(r))$ as a function of the interatomic distance (r).

$$V(r) = 4\varepsilon \left[\left(\frac{\sigma}{r}\right)^{12} - \left(\frac{\sigma}{r}\right)^{6} \right]$$

However, due to the limited range of repulsive van der Waals forces, these attempts resulted in a similar effect as with a charged wall. A perimeter was created where the fibers were not allowed outside with varying strictness, depending on the sigma and epsilon values (Figure 5.13e).

Table-specified potential walls

The most advanced way of constructing the wall was through user-specified non-bonded tabulated potentials. This allows the user to modify and exactly specify the potential at any given distance between two specific atom types. In total three such attempts were performed with varying table potentials between the wall atoms and the peptide. The table potentials were designed to assert a repulsive force to the peptides with different strengths. Regarding other molecules in the simulation, the wall interacted as if it consisted of water. Two of the simulations resulted in the fibers being pushed a distance away from the wall. However, inside this perimeter, no attractive force from an entropical effect was observed. Hence the peptides were able to move freely. The last simulation resulted in a near perfect wall where the peptides were able to move freely all over the simulation box expect through the wall (Figure 5.13f). It was observed that some fiber ends were slightly attracted to the wall, indicating that the repulsive force should be increased by a very small amount.

Adjusted simulation box size

Though the table-specified potential wall was well parametrized, it was decided to use another method to ensure RFFFR fiber formation in only one direction. An explicit wall requires a large simulation box which results in an exponential amount of atoms to be calculated. Hence this is very computationally exhausting.

To omit this problem several simulations were performed to determine the relation between the amount of peptides and the length of the formed equilibrated RFFFR fiber. Afterwards it was observed that a single fiber would form, spanning through the PBC in one direction only, if the simulation box and amount of peptides was fitted. All simulations in the publicised material mentioned above were performed based on this principle.

5 Conclusion

The RFFFR peptide was designed to form nano-fibers and the self-assembly potential has been investigated through a combination of CG-, atomistic MD simulations and semi-empirical quantum mechanical calculations. Arg residues were designed to restrict the interactions of Phe-Phe in one direction and ensure solubility. Thereby the self-assembly of the peptide preferred fiber formation over random aggregation as has been reported for FF and FFF peptides [49, 52, 142–144].

Above a critical fiber concentration determined to be in the interval of 70 mM - 100 mM, the peptides assemble into fibers according to a three-step

process. Initially randomly dispersed peptides aggregate into small clusters, as these grow larger, they assume small fiber segment structures. These small fibers grow into one large fiber spanning the PBC.

Hydrophobic effects might play an important role in the self-assembly and the final fiber is found to be stabilized by a large amount of intermolecular and water mediated hydrogen bonds. However, the amount is rather underestimated compared to semi-empirical quantum mechanical calculations, indicating that hydrogen bonds might play an even larger role.

π-stacking interactions between Phe residues are also found to be important for the self-assembly process. Intermolecular Phe residues favorably stack in a distinct T-shaped mode, while intramolecular Phe residues, within the range where π-stacking is pertinent, are found to stack in no distinct mode. Semi-empirical quantum mechanical calculations verified these results with only minor differences between the OPLS-aa and PM7 calculations. Among the most significant deviations were a slightly increased propensity for Phe residues to assume T-shaped stacking modes.

As π-stacking has been proven to promote amyloid formation and is believed to be the most important factor, the RFFFR peptide has proven to be a novel suitable model system for investigation of the formation, stability and disassembly of amyloids as well [197–200]. Furthermore, the structure formed by RFFFR has unique properties that can be exploited in other applications such as biological nanowires with conductive properties facilitated through charge transport between overlapping delocalized aromatic π-orbitals as well.

6 Methods

The MARTINI CG force field [147] used in the present study, joins in general four heavy atoms into one CG spheres/bead. Each bead is assigned the united properties of the enclosed atoms, substantially reducing the amount of interactions to be calculated. In this model, the protein backbone is represented by a single bead while the individual amino acid side chains are represented by one or more beads, depending on the amino acid. Non-bonded interactions in the MARTINI force field are parameterized from experimental data such as the partitioning free energies between amino acid side chains and the oil/water interface. The bonded interactions in the MARTINI force field are determined from the distribution of bond lengths, angles and dihedral angles derived from protein structures from the Protein Data Bank and comparison with atomistic force fields.

The initial self-assembly is simulated with the MARTINI force field [147] succeeded by a distance restrained MARTINI simulation. This final structure is back-transformed into an atomistic structure. Starting from this struc-

ture a 20 ns atomistic simulation is performed with the OPLS-aa force field [173, 201, 202]. From the atomistic simulation, structural information of the peptide and the π-stacking interaction of phenylalanine (Phe) residues have been extracted. Furthermore, a series of CG simulations are performed to determine the minimum peptide concentration necessary to form a single stable nano-fiber.

All simulations were performed with GROMACS v.4.6 [203]. The initial RFFFR structure was created and geometry optimized for an extended strand structure within YASARA [204]. The resulting structure was converted to a MARTINI CG peptide (Fig. 5.14) using the martinize.py v.2.4 script.

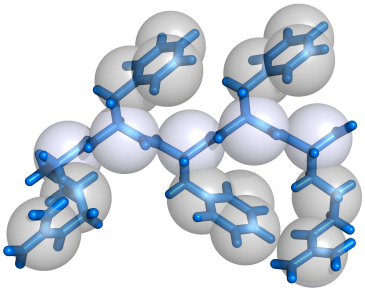

Figure 5.14: Atomistic structure of the peptide (RFFFR), created in YASARA (blue) and the corresponding MARTINI structure. In The MARTINI model amino acid backbones are represented by one bead (white), while side chains of arginine and phenylalanine have two and three bead, respectively (gray).

The initial MD configuration was constructed by adding 27 CG peptides at random positions in a box with dimensions 12nm x 5nm x 5 nm (x,y,z). Water was then added at any sterically allowed position, amounting to 2149 MARTINI polarized water molecules. After each modification, a steepest decent minimization with 10.000 steps was used to minimize the potential energy of the system.

Using time steps of 20 fs, an isotropic simulation of 200 ns was performed with the MARTINI force field v.2.2P [147]. The final configuration was used in a 100 ns continued distance restrained CG simulation where the Phe residues were locked in a trans-configuration, due to a observed very slow equilibration of the cis-trans configuration. The initial velocities were adopted from the last frame of the 200 ns long CG simulation.

The final CG structure from the distance restrained simulation was converted to an atomistic structure using the Backward script [158]. Water was removed in order to center the fiber in the simulation box, after which 8517 SPC water molecules, 108 chloride ions and 54 sodium ions were added to ensure system charge neutrality. Then an energy minimization was performed with a steepest decent minimization with 100.000 steps. This was

followed by a 100 ps long semi-isotropic simulation with the OPLS-aa force field [173, 201, 202] to equilibrate the system. The resulting structure was used in a 10 ns long isotropic simulation performed with the OPLS-aa force field with time steps of 1 fs.

The initial velocities of the first CG and atomistic simulations were assigned a Maxwell distribution at 323 K and 300 K, respectively. During the CG simulations the temperature and pressure were kept constant at 323 K and 1.013 bar with the v-rescale [205] and berendsen [206] algorithm, respectively. The elevated temperature was adopted in order to prevent the system from getting trapped in a local conformational energy minima during the self-assembly. The atomistic simulation was kept at 300 K and 1.013 bar with the Nose-Hoover [207] and Parrinello-Rahman [208] algorithm, respectively. This close to room temperature was adopted as the elevated temperature was no longer needed. In both the CG and atomistic simulations periodic boundary conditions (PBC) were applied in all directions and electrostatic interactions were calculated by the particle mesh ewald [209] (PME) algorithm with a real space cut-off at 1.5 nm in the CG simulations and 1 nm in the atomistic simulation.

Selected snapshots from the all atom simulation were geometry optimized by semi-empirical quantum mechanical (SQM) calculations using the MOPAC [184] package. The MOPAC package [184] developed by Stewart was used as the implemented module MOZYME [184] allows for the calculation of more than 1000 atoms, which is the approximate limit of standard SQM calculations. However, MOZYME [184] utilizes a localized molecular orbital method that allows for processing a system of 15,000 atoms in a very fast timescale compared to other solutions. The newest MOPAC version allows for the use of the new PM7 [186] method which is additionally well known for its very high accuracy that borders DFT-D calculations [186, 187, 210].

The OPLS-aa snapshots that was geometry optimized with PM7 [186] was as follows (starting from the beginning of the OPLS-aa simulation): 2500 ps, 3750 ps, 5000 ps, 5625 ps, 6250 ps, 6875 ps, 7500 ps, 8125 ps, 8750 ps, 9375 ps and 10,000 ps. Explicit solvent from the MD snapshots were removed and solvent effects were accounted for by the COSMO implicit water model [189] with a dielectric constant of 78.4. The geometry optimization convergence criterion was set to a maximum gradient of 10.0 kcal/mol/Å, after which a second calculation was performed with a convergence criterion of 5.0 kcal/mol/Å. Finally a single SCF calculation was performed to correct any error in heat of formation.

As PBC are not possible to implement with the SQM approach, on larger systems with many charges, a second simulation series was performed. This series was performed in the same way as described above, but with frozen alpha carbon atoms of the arginine residues in the peptides constituting the ends of the fiber, enforcing the fiber to remain in a stretched configuration.

This series will be denoted the "restricted PM7 calculations" henceforth. As a reference a 10 ns all atom MD simulation was performed containing only four peptides in a large simulation box. Hence PBC were not important during this simulation and subsequent PM7 calculations yielded relatively low RMSD values.

Additionally, a series of CG simulations with varying peptide concentrations were performed to determine the minimum concentration at which peptides assembled into stable fibers. These simulations were all carried out with the same parameters as the non-distance restrained CG simulation. To improve validity of the results, more simulations were performed with concentrations close to the critical fiber concentration. The simulations had different initial velocities in order to cover a wider conformational space. Furthermore, the critical fiber concentration was confirmed in another MD simulation series where a stable fiber was inserted into a simulation box corresponding to the concentrations above and below the critical fiber concentration. In this way it was possible to study fiber stability or disassembly.

Simulation time of CG and atomistic simulations do not scale 1:1 and a direct translation is often difficult. The MARTINI time compared to atomistic time is in general scaled by a factor of 4 [148, 211], but several other factors have been reported earlier [212, 213]. For this reason actual simulation rather than effective time has been used throughout this paper.

Chapter 6

The Physical Properties and Self-Assembly Potential of the RFFFR Peptide

The ability of natural proteins to form supramolecular structures [214] has been known for a long time to be responsible for many biological functions such as S-layer proteins that cover the outer cell membrane of some organisms [215]. Peptides are also known to self-assemble in nature and apart from other structures [216, 217] can form amyloid fibers related to natural biological functions [218, 219] or several human disorders [137, 138]. Recently, the self-assembly of designer peptides has also attracted a tremendous interest owing to their ability to form supramolecular structures with high bio-compatibility, chemical diversity and potential solubility in aqueous solutions [220–222]. The applications of the formed structures are numerous and include carrier-mediated drug delivery [223–226], tissue engineering [227], antimicrobial agents [228], fluorescent probes [229], energy storage [230], biomineralization [231], membrane protein stabilization [232] and bioinspired electronics such as field-effect transistors [233], microprobes [234], microarrays [234], biosensing devices [235], diodes [236] and nanotubes as conductive wires [234, 237].

As self-assembling peptides are mainly known from amyloid fibers, these peptides are often used as scaffold to develop designer peptides. One scaffold that has been widely used is the core sequence of the Amyloid beta peptide (Aβ), β(16-20) KLVFF [48] or Aβ(17-21) LVFFA [238]. Due to the presence of the FF motif in both sequences and the identification of aromatic residues as having the highest propensity to cause amyloid formation [239], the peptides FF have been extensively studied by many groups [50, 142]. Later the FFF

peptide was also studied [144]. However, neither peptide forms amyloid fibers, but a variety of other structures. Instead, peptides that form amyloid fibers or fibers are often peptide amphiphiles or peptides with alternating hydrophobic and hydrophilic amino acids.

Fibers of peptides have attracted interest for many applications owing to the ease of synthesis, high biocompatibility and biodegradability [240–242]. This includes biomedical applications such as drug-delivery systems [243], analyte detection [244], biomarker sensing [245], tissue engineering [246], immune response modulators [247] and cell fate controller [248]. Fibers of peptides also demonstrate potential for electronic devices as it allows for significant downscaling of the sizes of circuit components compared to what is possible with traditional inorganic semi-conductor technology [249]. Furthermore, peptide self-assembled fibers may also be applicable in material science due to their unique mechanical silk-like properties [250, 251].

Recently the self-assembly of the RFFFR peptide was investigated by coarse grained molecular dynamics (MD) simulations, atomistic MD simulations and semi-empirical calculations that indicated an amyloid fiber formation [194]. The motivation for the modification of the FF and FFF peptide is to direct the self-assembly process towards nano-fibers rather than the more random aggregated structures of FF or FFF. The arginine residues are intended to restrict the interaction of Phe residues in one direction only while the unprotected N- and C-termini ensures an anti parallel configuration by inducing a neutral C-terminus. In this way the charge of the neighboring peptides are not proximate, ensuring that the attractive effects are sufficiently strong for self-assembly. While the attractive effects may be dominated by "tugging in" of hydrophobic residues, computational data further suggests that the RFFFR amyloid fiber is stabilized by $\pi - \pi$ stacking interactions and a complex hydrogen bond network.

In this paper we report the synthesis and experimental data of the self-assembly of RFFFR. The self-assembly is investigated with different biophysical methods such as spectroscopy methods, atomic force microscopy (AFM) and scanning electron microscopy (SEM). These measurements indicate that the structure of the amyloid fibers fit very well with the *in silico* data of another study [194]. However, it is observed that the peptides not only form 1 dimensional fibers as predicted by simulations, but form more complex 3 dimensional fiber entangled structures in solution instead. The applications of these structures as molecular conductive wires or drug-delivery system is demonstrated, but applications may extend to material science, tissue engineering, advanced nanomaterial fabrication and encapsulation of biomolecules with purpose to stabilize/preserve their function.

1 The self-assembly process

The self-assembly of the RFFFR peptides was investigated in milliQ water and PBS solutions with different concentrations, but the results were not significant different as the self-assembly is not solely governed by electrostatic interactions. To enable comparison with physiological conditions the following results in this paper are obtained by use of 1X PBS at pH 7.4. As the pH is far below the pKa values of the Arg side chains and termini, Arg and the N-terminus are positively charged while the C-terminus is negatively charged.

It was observed that the RFFFR peptides assemble into fibers that curl together and form spheres (Figure 6.1 and Figure 6.2a). Upon dilution be-

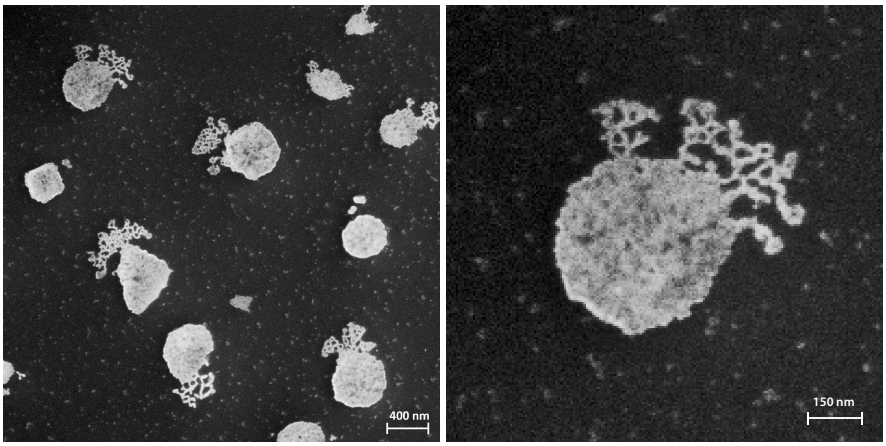

Figure 6.1: SEM measurements of (a) RFFFR fibers untangling from spheres adsorbed on a silicon surface. (b) closeup of Figure 6.1a.

low the critical fiber concentration (approximately 5mM) the fibers begin to untangle (Figure 6.1 and Figure 6.2b). When the fibers have totally untangled (Figure 6.2c and Figure 6.3), a dissolution process begins (Figure 6.2d-f). These results are in agreement with the fluorescent anistropy measurements, discussed later, and it is therefor likely that the observed AFM measurements are not a surface induced effect or that some other peptide structure existed which did not bind to the AFM surface. It is also unlikely that the rinsing of the AFM surface, after incubation of the peptide solution, removed any peptide structures as all peptide structures are tightly bound by electrostatic interactions to the surface. Furthermore, the short environmental change in buffer during rinsing of the sample is very short and induced configurational changes in the assembled structures are very slow, hence it is unlikely to effects what was observed with AFM.

The obtained sphere-like RFFFR structures are unique from almost any other self-assembled peptide structure, as the peptides form a structure (fibers) that again forms a structure (spheres). Typically, peptides form a structure comprised of the individual peptides which is also true for the closely related FFF peptide, that forms plate-like structures in aqueous solution [51] and sphere-like structures in chloroform [252]. These peptides aggregate in a more random way as to minimize solvent exposure and to maximize attractive forces, which is why the RFFFR peptide was designed with Arg residues in each terminus to intentionally force the self-assembly in one direction only. The observed entanglement of the fibers into sphere-like structures must then be an indication that the Arg residues are not completely sufficient to limit the self-assembly to only one direction.

The size of the spheres greatly depends on the peptide concentration above the critical fiber concentration. Hence the time it takes for the fibers to untangle also varies. The reason for the fiber entanglement may be to further decrease the water accessible surface of phenylalanine residues. This is indicated by the uniform shape of the spheres in the SEM measurements, as any water inside the spheres would have evaporated under the high vacuum conditions and deformed the spheres. Other studies of fibers that form complex structures report of microhydrogels that binds water in the interior [253]. The difference likely originates from the hydrophobicity level of the respective peptides. Hence it is possible that the compactness of RFFFR spheres may be controlled by reducing the polarity of the solvent or by reducing the stabilizing forces of hydrogen bonds and that RFFFR hydrogels or untangled fibers may be obtained under different conditions.

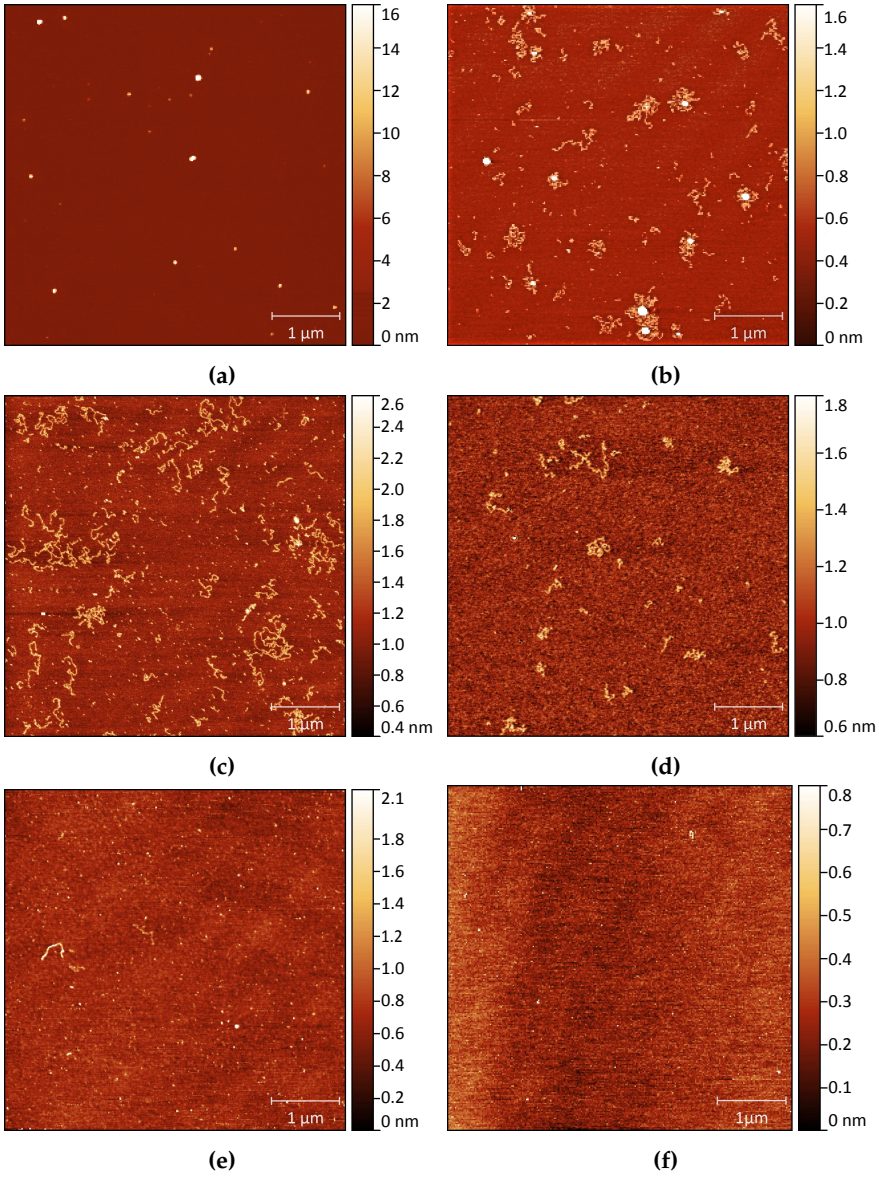

Figure 6.2: AFM measurements of 10mM RFFFR solution diluted to 1mM and measured at different time intervals. (a) 0 min. (b) 30 min. (c) 60 min. (d) 120 min. (e) 240 min. (f) 480 min.

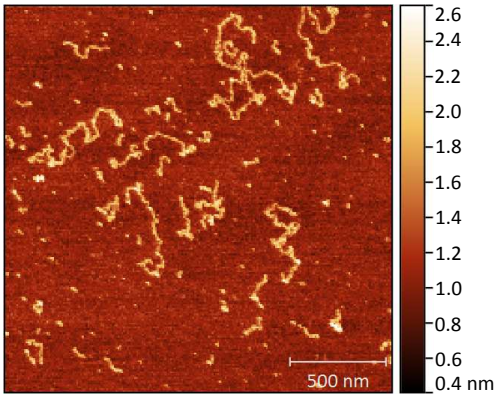

Figure 6.3: Closeup of Figure 6.2c.

The height profile from the AFM measurements of the individual fibers (Figure 6.4b) suggest a fiber height of 0.6-1.2 nm. This approximately coincides with the 0.8-2.4 nm reported earlier in a computational study of the self-assembly process (Figure 6.4a) [194]. The deviation is likely to originate from the environmental difference as the AFM measurements were performed on "dry" fibers with the arginine side chains attracted to the mica surface, while the simulations were performed in solution. Furthermore, the antiparallel assembly of the peptides, may cause the fibers to adsorb with the shorter width perpendicular to the mica surface, as only half of the positively charged arginine residues are in contact with the negatively charged mica surface otherwise. Hence the height difference between the height measured with AFM and predicted in the computational study [194] is sufficiently small, that it verifies a similar self-assembly. This demonstrates the potential of designing self-assembling peptides and predicting the resulting structure by the coarse grained MARTINI model [147] and the new PM7 [186] semi-empirical approach.

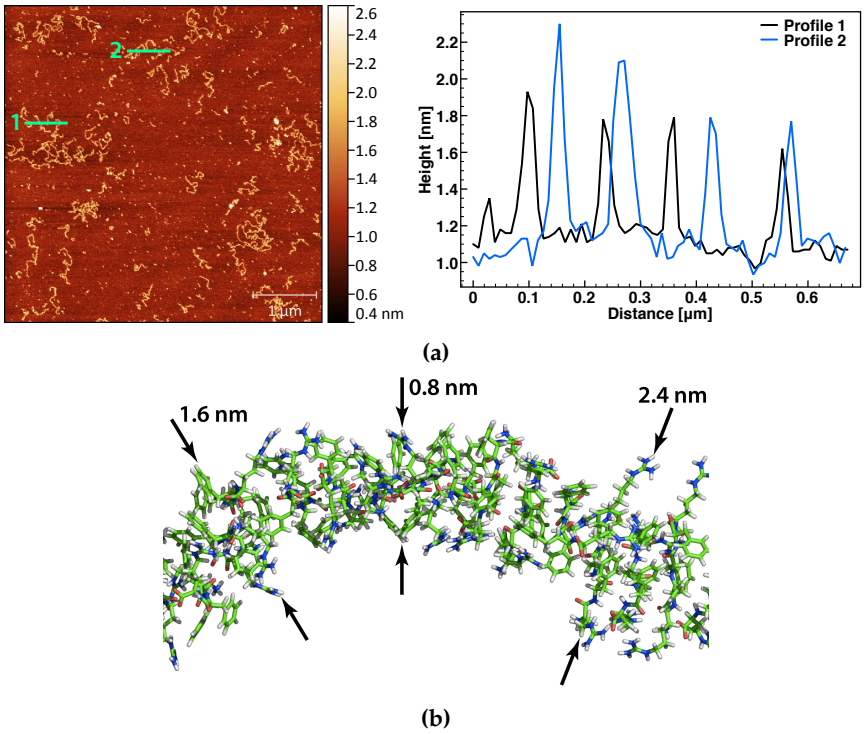

Figure 6.4: Comparison of measured and calculated fiber width. (a) Two height profiles of the RFFFR fibers and their position on the AFM measurement (Figure 6.2c) indicated by the green lines. (b) Theoretical fiber width of the fiber self-assembled in a previously reported molecular dynamics study [194].

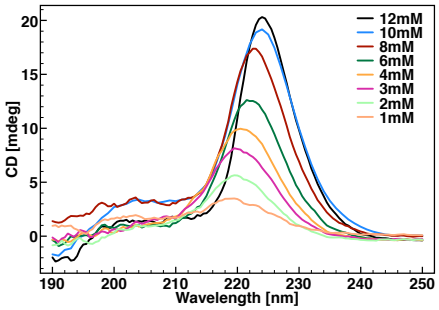

Figure 6.5: CD spectroscopy recorded from 190-250 nm with different RFFFR peptide concentrations.

The stabilizing forces of the RFFFR fibers

Most self-assemblies are driven by hydrophobic effects or electrostatic forces, however, the stabilizing intramolecular forces are equally important. Many structures are stabilized by hydrogen bonds between β-sheets and a recent trend is to use $\pi - \pi$ stacking in guided assembly [249, 254].

CD spectroscopy measurements did not show any signals that could be related to a beta sheet structure (Figure 6.5). This is likely because of the small size of the peptides, the low solution concentration and the very compact form of spheres. Instead spectra are dominated by a single peak with a maximum located in the range of 219-224 nm depending on the peptide concentration. These peaks arise from either $n \rightarrow \pi^*$ or $\pi \rightarrow \pi^*$ transitions.

However, the assignment is not unambiguous as $\pi \rightarrow \pi^*$ is often observed as a sharp strong peak at around 197-200 nm, while the $n \rightarrow \pi^*$ is the lowest energy amide band typically observed in the 210-230 nm range as a lower broader peak [255]. Spectra conforming to this have been reported for Aβ inspired peptides [256, 257].

The observed peaks of RFFFR are located in the range where $n \rightarrow \pi^*$ transitions typically occur and are relatively broad. However, very similar CD spectra of other short self-assembling peptides and other aromatic systems have been observed before and assigned $\pi \rightarrow \pi^*$ transitions [258–262]. Furthermore, the peak position is red-shifted as a function of higher peptide concentrations. Though the peak position is sensitive towards secondary structure changes and β-sheet bending, it is more likely an effect of the increase in sphere size, similar to the one observed when substituting an organic solvent with water [263]. Due to the sphere formation by the "tugging in" effect of phenylalanine residues, it is likely that the $\pi \rightarrow \pi^*$ transition becomes more stable, resulting in a lower transition energy. A $n \rightarrow \pi^*$ transition is expected to blue-shift with increased sphere size, as the possibility for the lone pair electrons in the ground n state to form hydrogen bonds to other

peptide groups increases. Hence the fibers are stabilized by $\pi - \pi$ stacking as previously suggested by computational data [194].

To study the structure of the fibers and secondary structure of the composing peptides, Thioflavin T (ThT) was used as a fluorescent probe. ThT almost exclusively binds to β-sheet rich amyloid structures with aromatic-hydrophobic grooves that span more than four consecutive β-strands [264–267]. Upon binding the ThT fluorescent properties change significantly with a huge increase in quantum yield, emission and excitation shift which is why it is one of the most widely used probes for staining and identifying amyloid structures [268].

Fluorescence spectroscopy measurements revealed an emission peak at 435 nm was observed when the ThT solution was excited at 353 nm (Figure 6.6a). Upon addition of RFFFR spheres/fibers, the 435 nm emission peak disappeared (Figure 6.6a). Instead the emission peak had shifted to 485 nm when excited with 440 nm, which was not observed for the pure ThT solution. As previously reported, this is proof of a β-sheet rich amyloid structure in solution [264–268] even though the CD measurements did not yield any secondary structure information. Furthermore, it is likely that the observed structures seen in the AFM experiment are not the result of surface induced assembly.

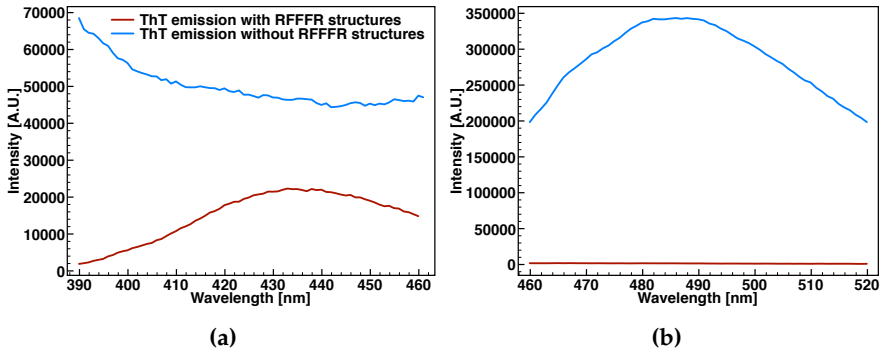

Figure 6.6: Fluorescence spectroscopy spectra of ThT with RFFFR self-assembled structures (blue line) and without RFFFR self-assembled structures (red line). (a) Recorded spectra in the interval 390-460 nm with 353 nm excitation. (b) Recorded spectra in the interval 460-520 nm with 440 nm excitation.

Fluorescence anisotropy spectroscopy was measured with use of Phe residues over time with the same diluted RFFFR solution as was used for the AFM measurements, resulting in slow untangling of the fibers and subsequent dissolution (Figure 6.7). In contrary to what is expected of a dissolution process, the anisotropy increases over time. Typically this would have been explained by Phe residues that moved more freely in fiber and sphere structures than in solution, however this is not likely in this case as the self-assembly is the result of Phe "tuggin in" effects, hydrogen bonds and $\pi - \pi$ stacking. Instead it can be explained by the previously computational study of the RFFFR fibers, where the phenylalanine residues assumed strict Phe-Phe configurations as a result of π-stacking [194]. This study further discovered by atomistic and semi-empirical quantum mechanical calculations that the Phe-Phe residues assume a T-shape π-stacking configuration [194]. As HomoFRET [269, 270] is known to occur between Trp residues [271] it is possible that energy is transferred from one phenylalanine residue to another perpendicular phenylalanine residue, explaining why the anisotropy behaves opposite of what is expected. Hence it is believed that the increase in anisotropy when spheres/fibers dissolve is indicative of a T-shaped π-stacking configuration which is in good agreement with high level computational calculations of the fibers [194].

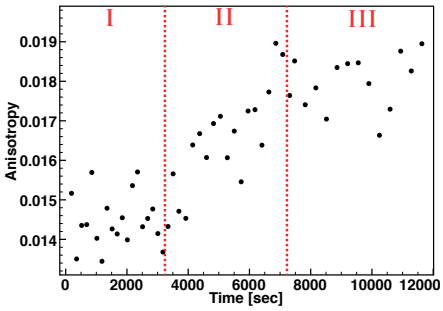

Figure 6.7: Fluorescence anisotropy over time of the same 10mM RFFFR peptide solution that was diluted to 1mM and used for the AFM measurements (Figure 6.2). In time interval I the spheres are untangling. In time interval II the spheres are totally untangled and the fibers are dissolving. In time interval III the fibers have totally dissolved.

2 Applications of the RFFFR Structures

Molecular electronics

Molecular electronics is necessary for continued development of more powerful computers as it renders it possible for down-scaling electrical components, reduce fabrication cost, avoid poisons in the fabrication process and allow for diverse functions by tuning of the chemical properties. In this field DNA has attracted a tremendous amount of interest due to the self-assembly properties and size, however it is difficult to probe the conductive properties [272]. The conductive properties of some proteins, however, have been known for a long time, which has been explained by various theories such as ionic transport [273], proton transport [274] or tightly bound oriented ice-like water molecules around the protein [275]. However, in order to be applicable in solid-state electronic devices the proteins need to be conductive in a "dry" state (electron transport) [276]. While most proteins are considered electrical insulators [237, 277, 278], some are known to be very efficient electron transporters [279–281]. Today, two prevailing mechanisms responsible for the electron transfer, coherent tunneling [276, 279, 282] and charge hopping [276, 283] exists, which may also occur concurrently.

Amide to amide groups are considered hopping sites and hydrogen bond networks aid in this coupling [281, 284]. Furthermore, aromatic amino acids also facilitate hopping sites through the delocalized π orbitals [285]. Hence it is very likely that RFFFR will exhibit strong electron transport abilities through Arg-Arg, Arg-Phe and Phe-Phe hopping sites enhanced by the previously reported complex hydrogen network [194]. Kelvin probe force microscopy (KPFM) measurements of the fibers entangled into large spheres (Figure 6.8a) were used to measure the surface potential difference (Figure 6.8b). Very small surface potential differences, below 2 mV, between the gold substrate and RFFFR spheres were measured (Figure 6.9), which might indicate a strong conductivity. Furthermore, no charging effect was observed during the SEM measurements (Figure 6.1) as is characteristic for insulating materials. Similar, conductivity in peptide structures induced by stabilized by intermolecular $\pi - \pi$ stacking have previously been reported [234, 237, 254]. KPFM have also previously been used to prove that peptide nanodots of FF peptides can store charges [286].

It is expected that untangled fibers have relatively higher conductivity than the spheres, as the $\pi - \pi$ stacking interaction and hydrogen bond network is more elaborate when it is connected in only one direction. It is also unlikely that the conductivity observed in the KPFM measurements is related to ionic or water effects as any water bound by the spheres would have evaporated and deformed the spheres in the high vacuum environment of the SEM measurements. Hence it is likely that the untangled fibers are conductive in

a "dry" state and have applications in solid-state electronic devices.

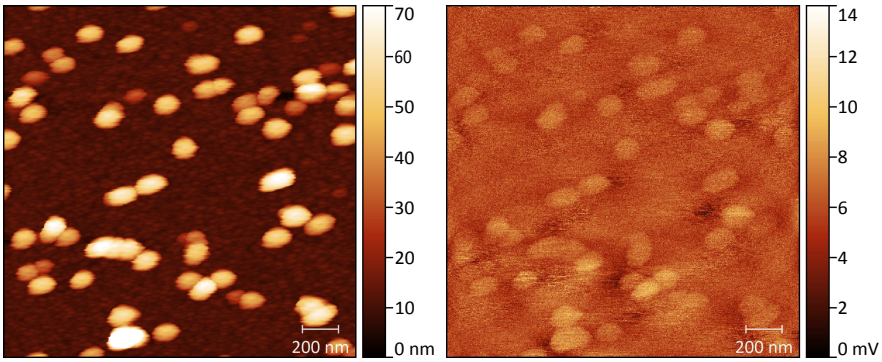

Figure 6.8: AFM and subsequent KPFM measurement of RFFFR spheres on a 40 nm thick gold layer. (a) The topology measurements. (b) The surface potential.

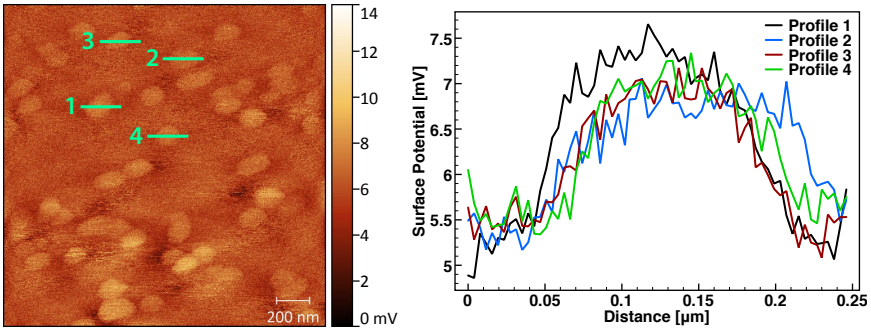

Figure 6.9: Four surface potential profiles and their position on the KPFM measurement (Figure 6.8) indicated by the green lines.

Drug delivery system

Self-assembled amyloid fibril networks or microgels from peptides have previously been suggested as potential drug-delivery systems [253, 287, 288]. The reported RFFFR spheres and fibers may also be used for such applications. As the spheres form due to a tugging in effect of the phenylalanine residues to minimize water exposure, it is likely that hydrophobic drugs, resulting in low potency, could be incorporated into the fibers or spheres allowing for a much higher potency. This also enables a controlled longterm release of drugs with a short life time, that limits the use of many drugs, as the fibers untangle and dissolve and the drug is slowly released (Figure

6.1). The release period may be optimized through the sphere size, simply by assembly at different peptide concentrations. No differences in sphere untanglement time at very low pH conditions (approximately pH 2), similar to those in the stomach, and normal physiological conditions were observed. This might indicate that the structures could be used for peroral medication. Furthermore, if the sphere surfaces were to be functionalized with molecules having affinity towards specific targets, the encapsulated drugs would have an increased selectivity and potential side-effects would be diminished.

3 RFFFR as Model System for ECM Based Sensing

In addition to the above presented results, experiments with the sensing of the RFFFR structures were also attempted based on the ECM samples described in Chapter 4.

Amyloid diseases are particularly difficult to diagnose since it requires direct verification of the specific protein rather than the presence of a biomarker [45, 46]. However, proper diagnosis is imperative as many of the diseases are treatable but require very type specific therapy that often is intensive or invasive [45–47]. However, recently the special sensitivity of chiral metamaterials towards β-sheet rich proteins has lead to the hypothesis that these sensors might be particularly suitable for detection of amyloid structures and could serve as a diagnosis method [1].

To probe the possibility of using ECM based CD spectroscopy to diagnose amyloid related diseases, the RFFFR peptide was probed as a model amyloid system. RFFFR spheres (peptide concentration of 20 mM) were adsorbed on the ECM surface of the sample prepared by an interpore distance of 430 nm and glancing angle deposition of 60°. The resulting CD responses indicate large mode shifts (Figure 6.10) compared to the shifts induced by other proteins adsorbed on PCMs reported by others [1], the PCM in this work (Figure 2.5) and on an another ECM sample (Figure 4.11).

The mode shifts are summarized in Table 6.1 and it is evident that the RFFFR peptide spheres induced no dissymmetry factor ($\triangle\triangle\lambda = \triangle\lambda_{righthanded} - \triangle\lambda_{lefthanded}$). Hence no protein fingerprint is observed. This can be explained by the isotropic way in which the spheres are configured and adsorb on the ECM surface.

Table 6.1: Mode shifts originating from adsorption of RFFFR spheres.

$\triangle\lambda_{489nm}$ $(\theta_{12}/\theta_{-12})$	$\triangle\lambda_{413nm}$ $(\theta_{12}/\theta_{-12})$	$\triangle\lambda_{338nm}$ $(\theta_{12}/\theta_{-12})$
7/7 nm	3/3 nm	0/0 nm

When free fibers (20 mM stock solution diluted to 0.1 mM) were adsorbed on the ECM surface, no shifts were observed. This is likely due to the very

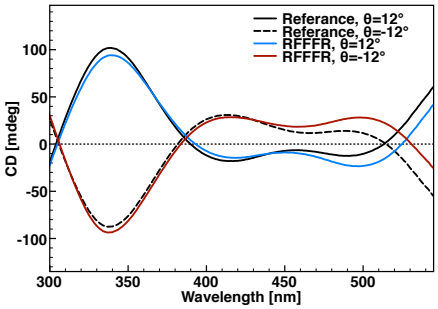

Figure 6.10: CD response of the ECM sample produced with a interpore distance of 430 nm and glancing angle deposition of 60° with no biomolecules adsorbed on the surface and with the RFFFR entangled fiber structures (20 mM) adsorbed on the surface. All measurements were recorded with an ECM orientation of $\theta = 12°$ or $\theta = -12°$ while $\phi = 0°$ in both configurations.

low concentration and small size of the peptides. However, as large shifts were observed for the spheres, it is likely that large amyloid fibers consisting of fibrils will adsorb in an anisotropic way and induce a significant protein fingerprint. Hence ECM based sensor systems can be used to diagnose some amyloid diseases by ultra sensitive detection of the specific protein related to a disease.

4 Conclusion

The self-assembly of the peptide RFFFR into fibers, as previously suggested, has been experimentally confirmed. The fibers have the same dimensions, within statistical error, as those determined by computational calculations, indicating the same configuration as predicted. It was observed that the fibers get entangled into spheres, possibly to further reduce the solvent accessible area of phenylalanine residues. When these spheres were diluted below a critical fiber concentration, the fibers untangled and dissolved after some time.

The spheres and fibers were observed to readily bind ThT, resulting in a significant increase in quantum yield, excitation and emission shift of ThT, proving the presence of amyloid structure. CD spectroscopy measurements were not indicative of any secondary structure but were dominated by electronic transitions originating from $\pi - \pi$ stacking interactions as predicted by previously reported computational calculations [194]. These computational calculations also indicated a very favorably T-shaped stacking mode, explaining why an increase in fluorescence anisotropy was observed during fiber dissolution in the present experimental study.

KPFM measurements were performed on self-assembled "dry" fibers/sphe-

res, indicating a very high conductivity comparable to that of gold. It is expected that the untangled fibers are more conductive than the spheres as the fibers have a more dense $\pi - \pi$ stacking and hydrogen bond network in the fiber direction compared to the environment in the sphere where $\pi - \pi$ stacking and hydrogen bonds may be formed in all directions. These spheres contain no water as they remained intact during SEM measurements and did not show any charging effects. Hence the conductivity presumably originates from charge-hopping and overlapping delocalized aromatic π-orbitals as well. This allows the RFFFR fibers to be applicable in novel bioinspired solid-state electronic devices.

The spheres untangle and dissolve into small fibers when diluted below the critical fiber concentration. Hence the spheres likely have potential as a drug-delivery system. The high pH stability of the spheres indicates that it may be a candidate for a peroral drug-delivery system.

5 Methods

RFFFR peptide synthesis. RFFFR was synthesized by solid-phase peptide synthesis techniques. Standard 9-fluorenyl- methyloxycarbonyl (Fmoc)-protecting group and activation by 2-(1H-benzotriazol-1-yl)-1,1,3,3-tetramethyluronium hexa- fluorophosphate (HBTU) chemistry was used. The peptide was synthesized both manually and using a fully automated peptide synthesizer Activotec P-11 (ActivotecSPP, Cambridge, UK). After the final cleavage from the resin the product was precipitated with ice-cold diethylether. The precipitate was centrifuged down and resuspended in ice-cold diethylether, this step was repeated 5 times with no resuspension the last time after which the pellet was frozen in liquid nitrogen and freeze-dried. The lyophilized peptide was then dissolved in 5% acetic acid and frozen in liquid nitrogen and freeze-dried, this process was repeated once. The lyophilized peptide was then dissolved in 0.1% hydrochloric acid and frozen in liquid nitrogen and freeze-dried, this process was repeated three twice.

Some lyophilized peptide was analyzed by reverse-phase high-performance liquid chromatography (RP-HPLC) UltiMate 3000 Standard LC Systems (Dionex, California, USA) using a C18 semi-preparative column (Phenomenex, California, USA), for 60 min with a flow rate of 1 mL/min. A mobile phase of water with 0.1% TFA was used. Sample elution was monitored using a UV-VIS detector operating at 214, 240 and 260 nm. The peptide crude was found to be over 90% pure, hence no further purification steps were taken.

RFFFR peptide solution preparation. All protein solutions were prepared in 1x PBS buffer with pH 7.4. The exact concentrations were determined by lambert-beers law using a thermo scientific UV-VIS spectrophotometer (VWK International UV1 v4.60, West Chester, PA). As RFFFR contains no

amino acids suitable for absorption of 280 nm light, the recently developed protocol for concentration determination by absorption of 205 nm light [289], was used with a calculated $\epsilon_{205} = 39620 M^{-1} cm - 1$.

Atomic force microscopy. AFM imaging of the untanglement of the RFFFR fibers were done at different time intervals (0min, 30min, 60min, 120min and 240min) after a 10 mM peptide solution in 1x PBS buffer (stored over night at room temperature) was diluted to 1mM peptide concentration. 30 μL solution of the diluted stock solution was placed on a freshly cleaved mica surface at the above specified time intervals and incubated for 10 min. After incubation, the mica surface was rinsed in 1 mL milliQ water three times before it was blow dried under a stream of dry nitrogen. The AFM measurements were performed with a Ntegra Aura (NT-MDT, Zelenograd, Russia) operating in tapping mode using OMCL-AC240TS cantilevers (Olympus, Japan). The data were analyzed using freeware image processing software Gwyddion.

Thioflavin T fluorescence and fluorescence anisotropy spectroscopy. Fluorescence characterization of the ThT binding to RFFFR fiber spheres was carried out using a RTC 2000 PTI spectrofluorimeter (PTI photon technology international, New Jersey, USA) at room temperature. Spectra in the range of 390-460 nm and 460-520 nm were acquired with an excitation of 353 and 440 nm, respectively, from 36 μM ThT in 1x PBS buffer and 36 μM ThT incubated with 10 mM RFFFR for 1h in 1x PBS buffer.

The same 10 mM peptide stock solution (stored over night at room temperature) that was diluted to 1 mM, used for the AFM measurements, was used to measure fluorescence anisotropy over time. Phenylalanine residues in RFFFR were used as fluorescent probe and an excitation and emission maxima of 260 and 284 nm were determined and used, respectively. A RTC 2000 PTI spectrofluorimeter in a L-shaped configuration with motorized polarizers was used to record the G-factor and subsequent anisotropy with 3 min intervals for 195 min at room temperature. The G-factor measurements lasted 10 sec each and the anisotropy measurements lasted 20 sec each. When measurements were not performed, the beam was blanked. The anisotropy calculations were performed in the PTI FeliX32 software using the formula:

$$r = \frac{I_{VV} - G I_{VH}}{I_{VV} + 2G I_{VH}}$$

where G is the correction factor:

$$G = \frac{I_{HV}}{I_{HH}}$$

Both experiments used slit widths of 5 nm and a quartz cuvette with path length of 0.2 cm.

Circular dichroism spectroscopy. CD spectra were obtained of a peptide stock solution diluted to specific peptide concentrations (1 mM, 2 mM, 3 mM, 4 mM, 6 mM, 8 mM, 10 mM and 12mM) in 1x PBS buffer and stored

over night at room temperature before the measurements using a J-715 spectropolarimeter (Jasco Inc, Pennsylvania, USA). Spectra were recorded from 190 to 250 nm with 1 nm step, 1nm bandwidth and 2 sec collection time per step, taking 20 averages at room temperature. A 0.1 mm quartz cuvette was used.

Kelvin-Probe force microscopy. KPFM was used to generate a 2-dimensional surface potential map of fibers entangled into spheres and adsorbed onto a 40 nm thick gold film. The substrates were prepared by sputter coating of 40 nm gold onto a Si wafer and the fiber/spheres were adsorbed on the substrate by incubating 50 μL of 25 mM peptide solution in 1x PBS buffer on the surface for 1 hour. The samples were investigated using an Ntegra Aura setup (NT-MDT, Zelenograd, Russia) in Kelvin Probe mode and Platinum-Iridium coated NSG01/Pt cantilevers (NT-MDT, Zelenograd, Russia). The sample was mounted on a sample holder with a metal spring in order to electrically connect the sample surface to the AFM ground, which is required for KPFM measurements. The measurements were carried out in a two-pass lift mode, where every line is scanned twice. In the first pass the topography of the sample is measured in AFM mode. In the second pass the recorded topography is used to keep the cantilever tip at a fixed predefined distance of 10 nm to the sample, while measuring the surface potential.

Scanning electron microscopy. SEM measurements were done at high vacuum ($1 \cdot 10^{-6}$ mbar) and an electron high tension of 15 kV using a Zeiss 1540XB system (Carl Zeiss, Jena, Germany) and standard procedure. The substrates were prepared by sputter coating of 40 nm gold onto a Si wafer and the fiber/spheres were adsorbed on the substrate by diluting a 25 mM peptide solution in 1x PBS buffer to 1 mM incubating 50 μL of the diluted solution on the surface for 15 min.

Chapter 7

Overall Discussion

The general purpose of this Ph.D. study was to develop plasmonic chiral metamaterials for biomolecule sensing based on CD spectroscopy. Initial metamaterials consisting of gammadion structures were fabricated by EBL as this is one of the standard "top-down" approaches (Chapter 2).

One of the produced PCMs samples covered a large area and consisted of different substructures due to a drifting stigma in the EBL process. Typically, metamaterials consist of only one substructure per sample as this enables comparison with theoretical calculations and makes it easier to relate an observation with a specific structure [1, 28, 61, 75]. However, since the LSPR wavelength depends greatly on the shape of the substructures, a high amount of CD modes compared to other reported chiral metamaterials (Table 2.3) and the ECMs reported in this work (Chapter 4) were observed. These modes originate from the optical excitation of LSPR in the gold metamaterial. Hence the observed modes from the PCM sample in this work are the sum of the LSPR wavelengths originating from the different substructures on the same sample. As the gammadion structure has been reported to result in four LSPR modes [1], the remaining four modes observed from the complex sample in this work must originate from the other structures on the sample.

Moreover, samples with diversity in substructure geometry or size usually display a broadening of the LSPR [290, 291] that generally reduces the biosensing capabilities [292]. However, no such broadening was observed from the PCM in this work as all of the CD modes were very distinct and had spectral linewidths comparable to those reported for gammadions [1]. Presumably, this is because the gradual deformations happened in abrupt laps, causing no closely related substructures and with no overlapping of LSPR wavelengths. Exactly how many different substructures were present on the sample or distribution thereof is difficult to estimate as many different substructures in between the gammadion and N-shape existed.

In traditional CD spectroscopy the analyte of interest is directly probed, but metamaterial based CD spectroscopy relies on the changes induced by the analyte on the LSPR modes. As the LSPR wavelength location is very sensitive towards changes in the dielectric constant from analytes, it enables detection of analytes in the picogram range whereas traditional CD spectroscopy is limited to probing analytes in the microgram range [1]. The disadvantage of metamaterial based CD spectroscopy compared to traditional CD spectroscopy is that it is unable to determine the precise and quantitative secondary structure composition of proteins. Furthermore, it is only capable of distinguishing protein fingerprints of proteins with a high content of β-sheet secondary structure.

When an analyte of interest is adsorbed on the metamaterial surface, not all LSPR wavelength modes are affected in the same way. This gives rise to a specific fingerprint used to identify the analyte [1]. Hence it is important to have sufficient modes to distinguish between similar proteins. As it was previously observed that proteins with similar secondary structure composition could result in very different fingerprints [1], the fingerprint is likely also related to the overall conformation. Furthermore, proteins with different conformation could have parts of the fingerprint that were indistinguishable [1]. Hence a fingerprint based on three modes, as previously reported for the gammadions [1], is likely not sufficient for an accurate assignment in all situations. This would particularly be a problem when closely related proteins, with almost identical secondary structure and conformation, need to be distinguished. In this regard, the many substructures on the sample produced in this work would help to better differentiate proteins compared to the previously reported gammadions [1].

Because the fingerprint is based on very small wavelength shifts, the intensity of the modes is also important. It was possible that the many different substructures on the same sample in this work would decrease the intensity of the modes, as fewer substructures would contribute to the respective modes. However, relative to the much lower area of the PCM in this work compared to the reported 25 times larger area of the gammadions [1], the CD intensity of the modes was almost comparable to the most intense CD mode obtained with the gammadion structure [1]. The extent of the shifts induced by different proteins adsorbed on the PCM surface is a measure of the sensitivity. Since the shifts observed from the PCM in this work (Table 2.4) are comparable to those previously observed by gammadions [1], the sensitivity is also similar. For these reasons, if the substructures are carefully designed, more substructures on the same sample yield a more complex protein fingerprint compared to other PCMs and thus a more accurate sensing device. However, as the mirror image PCM sample could not be produced in this work, a true protein fingerprint was not achievable as it is based on more dissymetry factors ($\triangle\triangle\lambda = \triangle\lambda_{righthanded} - \triangle\lambda_{lefthanded}$) which are a

measure of the difference in the shift between two mirror image CD modes from PCMs with opposite handedness. Hence the only disadvantage of having more substructures on the same sample is the increased complexity in creating two exactly similar PCM samples with opposite handedness.

To obtain a scalable way to fabricate PCM, different PS NS monolayer methods were investigated (Chapter 3). However, compared to the table of smallest structural features required to yield LSPR in the visible wavelength range (Table 2.1), the PS NS methods could not produce sufficiently small features. Some possible solutions to improve the methods are mentioned in Chapter 3. However, another more interesting solution could be to apply the methods to the fabrication of ECMs. The results in this work indicate that ECMs generally produce LSPR in the visible wavelength range from larger feature sizes compared to their PCM counterparts. While PCMs require a feature size of about 80 nm, the ECMs in this work have larger features and even samples with 600 nm periodicity yielded distinct CD responses in the visible range (Chapter 4). Similar ECM hole arrays with a diameter as large as 250 nm and a periodicity of 530 nm have been reported to yield a distinct CD response in the visible range [28]. Such hole arrays with diameters as small as 200 nm could easily be fabricated during this work by PS NS UV lithography. Furthermore, this approach could also be used to fabricate more complex hole arrays. The disadvantage of these PS NS methods may be that the monolayers have to be perfect, as ECMs are not allowed to have an intrinsic chiral hole array. Furthermore, mainly planar ECM structures can be produced by PS NS lithography compared to the 3D ECM structures reported in this work.

The major problem of PCM sensing is that two exact PCM samples are required with opposite handedness. Even reported structures that are fabricated with EBL or FIB milling have structural imperfections resulting in different CD responses from mirror image structures [1, 28]. Furthermore, in order to obtain the protein fingerprint by PCM based CD spectroscopy, a reference measurement and a measurement with a protein of interest adsorbed on the PCM sample are required for each mirror image PCM structure [1]. Hence it is difficult to distinguish if the minor CD mode shifts are related to differences in the PCM substructure properties, differences in the adsorption experiments or an actual protein fingerprint. In efforts to avoid this problem, different ECM samples were fabricated (Chapter 4) that only exhibit an induced chirality when the sample is probed at a non-normal angle of incidence. Hence both enantiomeric structures can be realized with the same sample by inverting the tilt of the sample. This allows for very reliable protein fingerprint measurements and an easy implementation into commercial devices compared to the previously reported PCM based sensing [1].

Another advantage of the ECMs fabricated in this work was the diversity of achievable substructures and the scalability of the ECM fabrication

process. Metamaterials with LSPR in the visible wavelength range generally require very small features that are mainly obtainable by EBL or FIB milling (Table 2.1). These methods are generally time-consuming, expensive and not suited for high throughput production. Hence only very small metamaterial areas fabricated by these methods have previously been reported (Table 2.2). This generally limits the implementation of metamaterials to academic research rather than implementation into consumer devices. Compared to the reported areas of PCMs (Table 2.2) and the PCM sample with the largest area prepared in this work ($1 \times 1mm^2$) which required 12 hours writing in the EBL system, ECMs were produced in arbitrary sizes in 2 hours by using the novel approach developed in this work.

Regarding reproducibility, other samples produced by high throughput techniques such as the spiral structures created by glancing angle deposition [88] produced samples with opposite handedness that exhibit very imperfect mirror image CD responses. Similar scaffold ornamentation of ZnO nanopillars displays some large differences between mirror image structures [25]. Even chiral nanoparticles do not result in an exact mirror image CD response when the mirror image sample is probed [24, 125]. Furthermore, it is likely that all PS NS methods will also result in very different PCM samples, as each sample requires a new monolayer that will never be exactly alike or defect free. Hence it is difficult to integrate metamaterials, fabricated by most high throughput methods, into commercial devices as each sample would require calibration because no samples are similar. However, the ECMs in this work were produced by a novel combination of thermal nanoimprint and glancing angle deposition (Chapter 4). Because the master mold does not deteriorate in the process, it can be used infinite times to produce the same sample over and over again. In this way, each sample will yield the same CD response that only has to be calibrated once.

Features as small as 31 nm were achieved by using the proximity effect in the EBL process while only larger features were produced by the novel method for ECM fabrication. However, the ECM fabrication method is still capable of producing small features if the parameters of the anodic oxidation process, used for fabricating the master mold, is optimized for smaller interpore distances and deeper holes.

PCM sensing is based on localized surface plasmons and ECM sensing is based on surface plasmon polaritons [28]. This explains many of the observed differences between the PCMs and ECMs fabricated in this work. For instance, localized surface plasmons are generally only sensitive towards the local geometry of areas comparable or smaller than the operating wavelength, while surface plasmon polariton are sensitive to large areas. This is why PCMs are insensitive to the angle of incident light. Another difference is the sensing distance (the distance from the metamaterial surface where the plasmonic effect is sensitive to changes in the dielectric constant). Localized sur-

face plasmons are limited to a 10-50 nm range [89–91], but surface plasmon polaritons are a coupling between surface plasmons in the metal and electromagnetic waves in the dielectric medium which can extend much further. For a gold/water interface, electromagnetic waves have a decay length of approximately 150-400 nm in the measured CD wavelength range [293, 294]. For this reason, the produced ECMs should be far more sensitive than PCMs in general. However, The protein fingerprint was only obtainable for proteins that were adsorbed as an isotropic layer. Hence proteins in a solution will not yield any fingerprint and the longer sensing distance of ECMs are therefore not applicable. However, if an ECM was developed that consisted of layered metal films, a significant improved sensitivity might be observed as the surface plasmon polariton would be able to "sense" proteins adsorbed on other metal layers as well.

While the ECMs did not show improved sensing sensitivity compared to the PCMs in this work, both structures are equally sensitive as the previously reported gammadion PCMs [1]. These materials are capable of sensing proteins in the picogram quantity by using CD spectroscopy [1]. Even though this is termed ultra sensitive [1], classical metamaterial LSPR shift based sensing is far more sensitive and capable of detecting even single molecules [17]. The advantage of chiral metamaterial sensing is that a protein fingerprint is acquired by label-free means. Standard LSPR shift based sensing can also be label-free [17] however it is impossible to determine which molecule causes a certain shift without functionalizing the metamaterial surface. Hence it is doubtful that standard functionalized metamaterials can be used more than once and they require an array of functional sensors to be sensitive to more than one molecule, whereas chiral metamaterials can identify many different molecules by label-free means. The special sensitivity of chiral metamaterials towards β-sheet rich proteins has spawned the hypothesis that these sensors might be particularly suitable for the detection of amyloid structures [1].

To verify this postulation, a peptide that forms amyloid fibers was developed and studied by computational means (Chapter 5). The simulations confirmed that the peptide indeed formed amyloid fibers with β-sheet secondary structure. The peptide was also studied empirically and the amyloid formation was confirmed by specific fluorescent probes and AFM measurements (Chapter 6). Although many atomistic details from the simulation could explain different empirically observed results, the empirical self-assembly was more advanced as the fibers entangled into spheres. When diluted below the critical fiber concentration, the spheres untangled into free fibers which then slowly dissolved. Even though the MARTINI force field generally produces some very realistic results [195], the failure to predict the fiber entanglement is likely related to the starting conditions.

Hence in order to simulate the self-assembly of fibers that entangle into spheres, many more peptides in the same simulation box might be necessary.

Such MD simulations with the MARTINI force field have previously been reported for the related FF and FFF peptides, consisting of systems with 600 peptides [51, 168]. These simulations have lead to self-assembled spheres, vesicles and tube structures. However, the major difference between these simulations and the RFFFR simulations is that the FF and FFF structures are formed from the individual peptides whereas the RFFFR spheres consist of entangled fibers consisting of RFFFR peptides. Furthermore, the fiber should not be able to span through the PBC as continuous fibers need to make a fiber break, which results in an energy barrier, before initiation of sphere formation is possible. Hence a much larger simulation box is required to first form fibers that do not pass through the PBC and consequently will entangle into a sphere.

While CG force fields such as MARTINI may enable the simulation of such large systems, the paradigm of atomistic simulations is that they are limited to either a large system with a timescale too short to predict any natural self-assembly phenomena or a small system that often does not represent the complexity of reality but has a long timescale [295]. Hence a sufficient large atomistic RFFFR system that would be able to form spheres, would likely be too computationally exhaustive and require supercomputers. Furthermore, this would also make semi-empirical quantum mechanical simulations impossible as the PM7 force field [186], which is perhaps the best semi-empirical force field for large systems, is limited to systems consisting of less than 15,000 atoms. Hence a large quantity of structural information would be lost as only the MARTINI force fields would be applicable.

An example of such information could be the observed cis-configuration of the phenylalanine side chains in the RFFFR peptides during the self-assembly (Chapter 5). Initially, very high amounts of cis-configurations were being observed, hence a modified force field was developed to restrict this configuration as it was believed to be an artefact (Figure 5.3). Later, the same phenomena have been observed in MARTINI simulations of larger proteins and removed by similar methods as it was once again believed to be an artefact [296]. However, when the RFFFR peptide simulations were converted to atomistic detail, these cis-configurations reappeared at limited levels (Figure 5.3). Hence it is likely that the cis-configuration is a natural phenomenon in short peptides that is even observed in some larger proteins, especially for aromatic residues [160]. However, these findings would not have been observed had atomistic simulations over sufficiently long timescales not been feasible.

Furthermore, the cis-configuration explains why the fibers are able to form solid spheres. As the spheres are solid, the fiber needs to be very flexible especially near the center of the sphere where the peptides need to be able to adopt very large backbone-backbone tilts. However $\pi - \pi$ stacking only occurs at a very limited range [176] and therefore a large backbone-backbone

tilt would break the interaction resulting in an increase in potential energy or steric hindrance. These effects are reduced if the phenylalanine side chains are allowed to assume a cis-configuration, enabling the fibers to entangle into spheres.

The ability of the fibers to entangle into spheres is important for the metamaterial based CD methods as the peptide structure is adsorbed in an isotropic manner on the metamaterial surfaces. Consequently, a protein fingerprint was not obtainable from the spheres by PCM or ECM based CD spectroscopy. Even when free fibers (spheres diluted below the critical fiber concentration) were adsorbed on the ECM surface, no shift or protein fingerprint was observed. The lack of a distinct protein fingerprint is likely related to the small size of the peptides and the very low peptide concentration needed to form free fibers (0.1 mM in this experiment).

The sphere structures did induce huge CD wavelength shifts. These remarkably large shifts were caused by the larger size of the spheres compared to normal proteins, as the shift is induced by a change in dielectric constant in the vicinity of an ECM surface. This surface area is defined by the decay length of the surface polaritons for ECMs, and can extend to 150-400 nm in the measured CD wavelength range for a gold/water interface. In this regard, the experiments confirmed that large peptide structures yield large shifts. Hence it is likely that the typically large assembly of amyloid fibers consisting of smaller fibrils will adsorb in an anisotropic manner and cause a significant protein fingerprint, enabling the detection of proteins in very small amounts. For these reasons, ECM and PCM based sensing methods are very efficient sensor systems for amyloid structures and might be used for diagnosis of some amyloid related diseases at an early stage.

Chapter 8

References

References

[1] E. Hendry, T. Carpy, J. Johnston, M. Popland, R. V. Mikhaylovskiy, A. J. Lapthorn, S. M. Kelly, L. D. Barron, N. Gadegaard, and M. Kadodwala. Ultrasensitive detection and characterization of biomolecules using superchiral fields. *Nature Nanotechnology*, 5(2):783–787, 2010.

[2] Morten Slyngborg, Esben Skovsen, and Peter Fojan. An investigation of the interaction between melittin and a model lipid bilayer. *Journal of Self-Assembly and Molecular Electronics*, 2(1):53–76, 2014.

[3] Mingqian Zhang, Shile Feng, Lei Wang, and Yongmei Zheng. Lotus effect in wetting and self-cleaning. *Biotribology*, 5:31–43, 2016.

[4] Yang Zhao, Changquan Qiu, Xuesong Li, Ardcharaporn Vararattanavech, Wenming Shen, Jaume Torres, Claus Hélix-Nielsen, Rong Wang, Xiao Hu, Anthony G. Fane, and Chuyang Y. Tang. Synthesis of robust and high-performance aquaporin-based biomimetic membranes by interfacial polymerization-membrane preparation and {RO} performance characterization. *Journal of Membrane Science*, 423-424:422–428, 2012.

[5] Thomas Taubner, Dmitriy Korobkin, Yaroslav Urzhumov, Gennady Shvets, and Rainer Hillenbrand. Near-field microscopy through a sic superlens. *Science*, 313(5793):1595–1595, 2006.

[6] Satoshi Kawata, Yasushi Inouye, and Prabhat Verma. Plasmonics for near-field nano-imaging and superlensing. *Nat Photon*, 3(7):388–394, 2009.

[7] A. N. Lagarkov and V. N. Kissel. Near-perfect imaging in a focusing system based on a left-handed-material plate. *Phys. Rev. Lett.*, 92(7):077401, 2004.

[8] D. Schurig, J. J. Mock, B. J. Justice, S. A. Cummer, J. B. Pendry, A. F. Starr, and D. R Smith. Metamaterial electromagnetic cloak at microwave frequencies. *Science*, 314(5801):977–980, 2006.

[9] Zhong Lei Mei and Tie Jun Cui. Experimental realization of a broadband bend structure using gradient index metamaterials. *Opt. Express*, 17(20):18354–18363, 2009.

[10] J. B. Pendry, A. J. Holden, D. J. Robbins, and W. J. Stewart. Magnetism from conductors and enhanced nonlinear phenomena. *IEEE Transactions on Microwave Theory and Techniques*, 47(11):2075–2084, 1999.

[11] Yang Liu, Yitung Chen, Jichun Li, Tzu chen Hung, and Jianping Li. Study of energy absorption on solar cell using metamaterials. *Solar Energy*, 86(5):1586–1599, 2012.

[12] Hou-Tong Chen, Willie J. Padilla, Joshua M. O. Zide, Arthur C. Gossard, Antoinette J. Taylor, and Richard D. Averitt. Active terahertz metamaterial devices. *Nature*, 444(7119):597–600, 2006.

[13] Ryan A. Stevenson, Adam H. Bily, David Cure, Mohsen Sazegar, and Nathan Kundtz. Rethinking wireless communications: Advanced antenna design using lcd technology. *SID Symposium Digest of Technical Papers*, 46(1):827–830, 2015.

[14] Y. M. Madany. Design and analysis of multiband annular slot antenna with metamaterial array structure for intelligent transportation communication systems. In *Antennas and Propagation Society International Symposium (APSURSI), 2013 IEEE*, pages 1798–1799, 2013.

[15] Jin-Woo Kim, Ekaterina I. Galanzha, Evgeny V. Shashkov, Hyung-Mo Moon, and Vladimir P. Zharov. Golden carbon nanotubes as multimodal photoacoustic and photothermal high-contrast molecular agents. *Nat Nano*, 4(10):688–694, 2009.

[16] Juan Yguerabide and Evangelina E. Yguerabide. Light-scattering submicroscopic particles as highly fluorescent analogs and their use as tracer labels in clinical and biological applications: I. theory. *Analytical Biochemistry*, 262(2):137–156, 1998.

[17] V. G. Kravets, F. Schedin, R. Jalil, L. Britnell, R. V. Gorbachev, D. Ansell, B. Thackray, K. S. Novoselov, A. K. Geim, A. V. Kabashin, and A. N. Grigorenko. Singular phase nano-optics in plasmonic metamaterials for label-free single-molecule detection. *Nat Mater*, 12(4):304–309, 2013.

[18] Jian Feng Li, Yi Fan Huang, Yong Ding, Zhi Lin Yang, Song Bo Li, Xiao Shun Zhou, Feng Ru Fan, Wei Zhang, Zhi You Zhou, WuDe Yin, Bin Ren, Zhong Lin Wang, and Zhong Qun Tian. Shell-isolated nanoparticle-enhanced raman spectroscopy. *Nature*, 464(7287):392–395, 2010.

[19] Mustafa S. Yavuz, Yiyun Cheng, Jingyi Chen, Claire M. Cobley, Qiang Zhang, Matthew Rycenga, Jingwei Xie, Chulhong Kim, Kwang H. Song, Andrea G. Schwartz, Lihong V. Wang, and Younan Xia. Gold nanocages covered by smart polymers for controlled release with near-infrared light. *Nat Mater*, 8(12):935–939, 2009.

[20] Xiaohua Huang, Ivan H. El-Sayed, Wei Qian, and Mostafa A. El-Sayed. Cancer cell imaging and photothermal therapy in the near-infrared region by using gold nanorods. *Journal of the American Chemical Society*, 128(6):2115–2120, 2006.

[21] Mark L. Brongersma. Introductory lecture: nanoplasmonics. *Faraday Discuss.*, 178(0):9–36, 2015.

[22] K. Lance Kelly, Eduardo Coronado, Lin Lin Zhao, , and George C. Schatz. The optical properties of metal nanoparticles : the influence of size, shape, and dielectric environment. *The Journal of Physical Chemistry B*, 107(3):668–677, 2003.

[23] Stefano Cataldo, Jun Zhao, Frank Neubrech, Bettina Frank, Chunjie Zhang, Paul V. Braun, and Harald Giessen. Hole-mask colloidal nanolithography for large-area low-cost metamaterials and antenna-assisted surface-enhanced infrared absorption substrates. *ACS Nano*, 6(1):979–985, 2012.

[24] Xibo Shen, Ana Asenjo-Garcia, Qing Liu, Qiao Jiang, F. Javier García de Abajo, Na Liu, and Baoquan Ding. Three-dimensional plasmonic chiral tetramers assembled by dna origami. *Nano Letters*, 13(5):2128–2133, 2013.

[25] Bongjun Yeom, Huanan Zhang, Hui Zhang, Jai Il Park, Kyoungwon Kim, Alexander O. Govorov, and Nicholas A. Kotov. Chiral plasmonic nanostructures on achiral nanopillars. *Nano Letters*, 13(11):5277–5283, 2013.

[26] Robert Schreiber, Jaekwon Do, Eva-Maria Roller, Tao Zhang, Verena J. Schuller, Philipp C. Nickels, Jochen Feldmann, and Tim Liedl. Hierarchical assembly of metal nanoparticles, quantum dots and organic dyes using dna origami scaffolds. *Nature Nanotechnology*, 9(1):74–78, 2014.

[27] Norma J Greenfield. Using circular dichroism spectra to estimate protein secondary structure. *Nat Protoc*, 1(6):2876–2890, 2006.

[28] Ben M. Maoz, Assaf Ben Moshe, Daniel Vestler, Omri Bar-Elli, and Gil Markovich. Chiroptical effects in planar achiral plasmonic oriented nanohole arrays. *Nano Letters*, 12(5):2357–2361, 2012.

[29] Xavier Zambrana-Puyalto, Xavier Vidal, and Gabriel Molina-Terriza. Angular momentum-induced circular dichroism in non-chiral nanostructures. *Nat Commun*, 5, 2014.

[30] Oriol Arteaga, Ben M. Maoz, Shane Nichols, Gil Markovich, and Bart Kahr. Complete polarimetry on the asymmetric transmission through subwavelength hole arrays. *Opt. Express*, 22(11):13719–13732, 2014.

[31] E. Plum, X.-X. Liu, V. A. Fedotov, Y. Chen, D. P. Tsai, and N. I. Zheludev. Metamaterials: Optical activity without chirality. *Phys. Rev. Lett.*, 102(11):113902, 2009.

[32] Thomas W. H. Oates, Timur Shaykhutdinov, Tolga Wagner, Andreas Furchner, and Karsten Hinrichs. Gyrotropy in achiral materials: the coupled oscillator model. *Advanced Materials*, 26(42):7197–7201, 2014.

[33] Vassilios Yannopapas. Circular dichroism in planar nonchiral plasmonic metamaterials. *Opt. Lett.*, 34(5):632–634, 2009.

[34] Amr Shaltout, Jingjing Liu, Vladimir M. Shalaev, and Alexander V. Kildishev. Optically active metasurface with non-chiral plasmonic nanoantennas. *Nano Letters*, 14(8):4426–4431, 2014.

[35] Shun Hashiyada, Tetsuya Narushima, and Hiromi Okamoto. Local optical activity in achiral two-dimensional gold nanostructures. *The Journal of Physical Chemistry C*, 118(38):22229–22233, 2014.

[36] Sergey S. Kruk, Christian Helgert, Manuel Decker, Isabelle Staude, Christoph Menzel, Christoph Etrich, Carsten Rockstuhl, Chennupati Jagadish, Thomas Pertsch, Dragomir N. Neshev, and Yuri S. Kivshar. Optical metamaterials with quasicrystalline symmetry: Symmetry-induced optical isotropy. *Phys. Rev. B*, 88(20):201404–201409, 2013.

[37] Mohamed Boutria, Rachid Oussaid, Daniel Van Labeke, and Fadi Issam Baida. Tunable artificial chirality with extraordinary transmission metamaterials. *Phys. Rev. B*, 86(15):155428–155435, 2012.

[38] Alessandro Belardini, Alessio Benedetti, Marco Centini, Grigore Leahu, Francesco Mura, Simona Sennato, Concita Sibilia, Valentina Robbiano, Maria Caterina Giordano, Christian Martella, Davide Comoretto, and

Francesco Buatier de Mongeot. Second harmonic generation circular dichroism from self-ordered hybrid plasmonic photonic nanosurfaces. *Advanced Optical Materials*, 2(3):208–213, 2014.

[39] A. Yokoyama, M. Yoshida, A. Ishii, and Y. K. Kato. Giant circular dichroism in individual carbon nanotubes induced by extrinsic chirality. *Phys. Rev. X*, 4(1):11005–11011, 2014.

[40] Yao-Chung Tsao, Thomas Søndergaard, Esben Skovsen, Leonid Gurevich, Kjeld Pedersen, and Thomas Garm Pedersen. Pore size dependence of diffuse light scattering from anodized aluminum solar cell backside reflectors. *Opt. Express*, 21(S1):A84–A95, 2013.

[41] Yao-Chung Tsao, Christian Fisker, and Thomas Garm Pedersen. Nanoimprinted backside reflectors for a-si:h thin-film solar cells: Critical role of absorber front textures. *Opt. Express*, 22(S3):A651–A662, 2014.

[42] Nazrin Kooy, Khairudin Mohamed, Lee Tze Pin, and Ooi Su Guan. A review of roll-to-roll nanoimprint lithography. *Nanoscale Research Letters*, 9(1):320, 2014.

[43] Stephen Y. Chou, Peter R. Krauss, and Preston J. Renstrom. Nanoimprint lithography. *Journal of Vacuum Science & Technology B*, 14(6):4129–4133, 1996.

[44] M. Häffner, A. Heeren, M. Fleischer, D.P. Kern, G. Schmidt, and L.W. Molenkamp. Simple high resolution nanoimprint-lithography. *Microelectronic Engineering*, 84(5–8), 2007.

[45] Nelson Leung, Samih H. Nasr, and Sanjeev Sethi. How i treat amyloidosis: the importance of accurate diagnosis and amyloid typing. *Blood*, 120(16):3206–3213, 2012.

[46] Raymond L. Comenzo. How i treat amyloidosis. *Blood*, 114(15):3147–3157, 2009.

[47] M. Ankarcrona, B. Winblad, C. Monteiro, C. Fearns, E. T. Powers, J. Johansson, G. T. Westermark, J. Presto, B-G. Ericzon, and J. W. Kelly. Current and future treatment of amyloid diseases. *Journal of Internal Medicine*, pages 1365–2796, 2016.

[48] Claudio Sotoa, Mark S. Kindyc, Marc Baumannb, and Blas Frangione. Inhibition of alzheimer's amyloidosis by peptides that prevent β-sheet conformation. *Biochemical and Biophysical Research Communications*, 226(3):672–680, 1996.

[49] Tae Hee Han, Won Jun Lee, Duck Hyun Lee, Ji Eun Kim, Eun-Young Choi, and Sang Ouk Kim. Peptide/graphene hybrid assembly into core/shell nanowires. *Advanced Materials*, 22(18):2060–2064, 2010.

[50] Meital Reches and Ehud Gazit. Casting metal nanowires within discrete self-assembled peptide nanotubes. *Science*, 300(5619):625–627, 2003.

[51] Cong Guo, Yin Luo, Ruhong Zhou, and Guanghong Wei. Triphenylalanine peptides self-assemble into nanospheres and nanorods that are different from the nanovesicles and nanotubes formed by diphenylalanine peptides. *Nanoscale*, 6(5):2800–2811, 2014.

[52] Tae Hee Han, Taedong Ok, Jangbae Kim, Dong Ok Shin, Hyotcherl Ihee, Hee-Seung Lee, and Sang Ouk Kim. Bionanosphere lithography via hierarchical peptide self-assembly of aromatic triphenylalanine. *Small*, 6(8):945–951, 2003.

[53] L. Pasteur. Recherches sur les relations qui peuvent exister entre la forme cristalline et la composition chimique, et le sens de la polarisation rotatoire. *Ann. Chim. Phys.*, 24(3):442–459, 1848.

[54] W.T. Baron Kelvin. Baltimore lectures on molecular dynamics and the wave theory of light. Lecture, 1904.

[55] Assaf Ben Moshe, Daniel Szwarcman, and Gil Markovich. Size dependence of chiroptical activity in colloidal quantum dots. *ACS Nano*, 5(11):9034–9043, 2011.

[56] Cyrille Gautier, , and Thomas Bürgi*. Chiral n-isobutyryl-cysteine protected gold nanoparticles: Preparation, size selection, and optical activity in the uv-vis and infrared. *Journal of the American Chemical Society*, 128(34):11079–11087, 2006.

[57] Yee-Hsiung Chen, Jen Tsi Yang, and Hugo M. Martinez. Determination of the secondary structures of proteins by circular dichroism and optical rotatory dispersion. *Biochemistry*, 11(22):4120–4131, 1972.

[58] Lien Ai Nguyen, Hua He, and Chuong Pham-Huy. Chiral drugs: An overview. *Int J Biomed Sci*, 2(2):85–100, 2006.

[59] A. S. Schwanecke, A. Krasavin, D. M. Bagnall, A. Potts, A. V. Zayats, and N. I. Zheludev. Broken time reversal of light interaction with planar chiral nanostructures. *Phys. Rev. Lett.*, 91(24):247404–247408, 2003.

[60] Yiqiao Tang and Adam E. Cohen. Optical chirality and its interaction with matter. *Phys. Rev. Lett.*, 104(16):163901–163905, 2010.

[61] M. Decker, M. W. Klein, M. Wegener, and S. Linden. Circular dichroism of planar chiral magnetic metamaterials. *Opt. Lett.*, 32(7):856–858, 2007.

[62] Yun-Chorng Chang, Sih-Chen Lu, Hsin-Chan Chung, Shih-Ming Wang, Tzung-Da Tsai, and Tzung-Fang Guo. High-throughput nanofabrication of infra-red and chiral metamaterials using nanospherical-lens lithography. *Scientific Reports*, 3:3339–3346, 2013.

[63] V. K. Valev, J. J. Baumberg, B. De Clercq, N. Braz, X. Zheng, E. J. Osley, S. Vandendriessche, M. Hojeij, C. Blejean, J. Mertens, C. G. Biris, V. Volskiy, M. Ameloot, Y. Ekinci, G. A. E. Vandenbosch, P. A. Warburton, V. V. Moshchalkov, N. C. Panoiu, and T. Verbiest. Nonlinear superchiral meta-surfaces: Tuning chirality and disentangling non-reciprocity at the nanoscale. *Advanced Materials*, 26(26):4074–4081, 2014.

[64] Lei Kang, Shoufeng Lan, Yonghao Cui, Sean P. Rodrigues, Yongmin Liu, Douglas H. Werner, and Wenshan Cai. An active metamaterial platform for chiral responsive optoelectronics. *Advanced Materials*, 27(29):4377–4383, 2015.

[65] Yizhuo He, Keelan Lawrence, Whitney Ingram, and Yiping Zhao. Circular dichroism based refractive index sensing using chiral metamaterials. *Chem. Commun.*, 52(10):2047–2050, 2016.

[66] G. Raschke, S. Kowarik, T. Franzl, C. Sönnichsen, T. A. Klar, J. Feldmann, A. Nichtl, , and K. Kürzinger. Biomolecular recognition based on single gold nanoparticle light scattering. *Nano Letters*, 3(7):935–938, 2003.

[67] Tomas Rindzevicius, Yury Alaverdyan, Andreas Dahlin, Fredrik Höök, Duncan S. Sutherland, , and Mikael Käll. Plasmonic sensing characteristics of single nanometric holes. *Nano Letters*, 5(11):2335–2339, 2005.

[68] S. Chen, M Svedendahl, M Käll, L Gunnarsson, and A Dmitriev. Ultrahigh sensitivity made simple: nanoplasmonic label-free biosensing with an extremely low limit-of-detection for bacterial and cancer diagnostics. *Nanotechnology*, 20(43):434015–434024, 2009.

[69] Joana Rafaela Lara Guerreiro, Maj Frederiksen, Vladimir E. Bochenkov, Victor De Freitas, Maria Goreti Ferreira Sales, and Duncan Steward Sutherland. Multifunctional biosensor based on localized surface plasmon resonance for monitoring small molecule-protein interaction. *ACS Nano*, 8(8):7958–7967, 2014.

[70] érôme Martin, Julien Proust, Davy Gérard, and Jérôme Plain. Localized surface plasmon resonances in the ultraviolet from large scale nanostructured aluminum films. *Opt. Mater. Express*, 3(7):954–959, 2013.

[71] Xinlong Xu, Bo Peng, Dehui Li, Jun Zhang, Lai Mun Wong, Qing Zhang, Shijie Wang, and Qihua Xiong. Flexible visible-infrared metamaterials and their applications in highly sensitive chemical and biological sensing. *Nano Letters*, 11(8):3232–3238, 2011.

[72] George H. Chan, Jing Zhao, Erin M. Hicks, George C. Schatz, , and Richard P. Van Duyne. Plasmonic properties of copper nanoparticles fabricated by nanosphere lithography. *Nano Letters*, 7(7):1947–1952, 2007.

[73] J. Zhang, C. Cao, X. Xu, C. Liow, S. Li, P.-H. Tan, and Q. Xiong. Tailoring plasmonic metamaterials for dna molecular logic gates. *ArXiv e-prints*, 2013.

[74] Xibo Shen, Ana Asenjo-Garcia, Qing Liu, Qiao Jiang, F. Javier García de Abajo, Na Liu, and Baoquan Ding. Three-dimensional plasmonic chiral tetramers assembled by dna origami. *Nano Letters*, 13(5):2128–2133, 2013.

[75] Wensheng Gao, Ching Yan Ng, Ho Ming Leung, Yunhui Li, Hong Chen, and Wing Yim Tam. Circular dichroism in single-layered gold sawtooth gratings. *J. Opt. Soc. Am. B*, 29(11):3021–3026, 2012.

[76] Shumei Chen, Franziska Zeuner, Martin Weismann, Bernhard Reineke, Guixin Li, Ventsislav Kolev Valev, Kok Wai Cheah, Nicolae Coriolan Panoiu, Thomas Zentgraf, and Shuang Zhang. Giant nonlinear optical activity of achiral origin in planar metasurfaces with quadratic and cubic nonlinearities. *Advanced Materials*, 28(15):1521–4095, 2016.

[77] Justyna K. Gansel, Michael Thiel, Michael S. Rill, Manuel Decker, Klaus Bade, Volker Saile, Georg von Freymann, Stefan Linden, and Martin Wegener. Gold helix photonic metamaterial as broadband circular polarizer. *Science*, 325(5947):1513–1515, 2009.

[78] Vitor R. Manfrinato, Lihua Zhang, Dong Su, Huigao Duan, Richard G. Hobbs, Eric A. Stach, and Karl K. Berggren. Resolution limits of electron-beam lithography toward the atomic scale. *Nano Letters*, 13(4):1555–1558, 2013.

[79] J. Gierak, A. Madouri, A.L. Biance, E. Bourhis, G. Patriarche, C. Ulysse, D. Lucot, X. Lafosse, L. Auvray, L. Bruchhaus, and R. Jede. Sub-5 nm fib direct patterning of nanodevices. *Microelectronic Engineering*, 84(5-8):779–783, 2007.

[80] Nassir Mojarad, Jens Gobrecht, and Yasin Ekinci. Beyond euv lithography: a comparative study of efficient photoresists performance. *Scientific Reports*, 5:9235–9242, 2015.

[81] Bruno Gompf, Julia Braun, Thomas Weiss, Harald Giessen, Martin Dressel, and Uwe Hübner. Periodic nanostructures: Spatial dispersion mimics chirality. *Phys. Rev. Lett.*, 106(18):185501, 2011.

[82] Oriol Arteaga, Jordi Sancho-Parramon, Shane Nichols, Ben M. Maoz, Adolf Canillas, Salvador Bosch, Gil Markovich, and Bart Kahr. Relation between 2d/3d chirality and the appearance of chiroptical effects in real nanostructures. *Opt. Express*, 24(3):2242–2252, 2016.

[83] Wei Li, Zachary J. Coppens, Lucas V. Besteiro, Wenyi Wang, Alexander O. Govorov, and Jason Valentine. Circularly polarized light detection with hot electrons in chiral plasmonic metamaterials. *Nat Commun*, 6, 2015.

[84] Yidong Hou, Shuhong Li, Yarong Su, Xia Huang, Yu Liu, Li Huang, Yin Yu, Fuhua Gao, Zhiyou Zhang, and Jinglei Du. Design and fabrication of three-dimensional chiral nanostructures based on stepwise glancing angle deposition technology. *Langmuir*, 29(3):867–872, 2013.

[85] Maxim V. Gorkunov, Vladimir E. Dmitrienko, Alexander A. Ezhov, Vladimir V. Artemov, and Oleg Y. Rogov. Implications of the causality principle for ultra chiral metamaterials. *Scientific Reports*, 5:9273–9278, 2015.

[86] Shiwei Xie, Jinzhe Yang, Xiao Xiao, Yidong Hou, Jinglei Du, Lin Pang, Xie Li, and Fuhua Gao. Scalable fabrication of quasi-three-dimensional chiral plasmonic oligomers based on stepwise colloid sphere lithography technology. *Nanoscale Research Letters*, 10:393–402, 2015.

[87] Xinghui Yin, Martin Schäferling, Ann-Katrin U. Michel, Andreas Tittl, Matthias Wuttig, Thomas Taubner, and Harald Giessen. Active chiral plasmonics. *Nano Letters*, 15(7):4255–4260, 2015.

[88] Johnson Haobijam Singh, Greshma Nair, Arijit Ghosh, and Ambarish Ghosh. Wafer scale fabrication of porous three-dimensional plasmonic metamaterials for the visible region: chiral and beyond. *Nanoscale*, 5(16):7224–7228, 2013.

[89] Matthew E. Stewart, Christopher R. Anderton, Lucas B. Thompson, Joana Maria, Stephen K. Gray, John A. Rogers, , and Ralph G. Nuzzo. Nanostructured plasmonic sensors. *Chemical Reviews*, 108(2):494–521, 2008.

[90] Michelle Duval Malinsky, K. Lance Kelly, George C. Schatz, , and Richard P. Van Duyne. Chain length dependence and sensing capabilities of the localized surface plasmon resonance of silver nanoparti-

cles chemically modified with alkanethiol self-assembled monolayers. *Journal of the American Chemical Society*, 123(7):1471–1482, 2001.

[91] Li-Wei Nien, Jia-Han Li, and Chun-Hway Hsueh. Optimized sensitivity and electric field enhancement by controlling localized surface plasmon resonances for bowtie nanoring nanoantenna arrays. *Plasmonics*, 10(3):553–561, 2015.

[92] Alex Nemiroski, Mathieu Gonidec, Jerome M. Fox, Philip Jean-Remy, Evan Turnage, and George M. Whitesides. Engineering shadows to fabricate optical metasurfaces. *ACS Nano*, 8(11):11061–11070, 2014.

[93] Y.-P. Zhao, D.-X. Ye, Pei-I Wang, G.-C. Wang, and T.-M. Lu. Fabrication of si nanocolumns and si square spirals on self-assembled monolayer colloid substrates. *International Journal of Nanoscience*, 1(1):87, 2002.

[94] George K. Larsen, Yizhuo He, Whitney Ingram, and Yiping Zhao. Hidden chirality in superficially racemic patchy silver films. *Nano Letters*, 13(12):6228–6232, 2013.

[95] G. Arutinov, S. B. Brichkin, and V. F. Razumov. Self-assembling of polystyrene microsphere monolayers by spin-coating. *Nanotechnologies in Russia*, 5(1):67–72, 2010.

[96] Peter A. Kralchevsky and Kuniaki Nagayama. Capillary forces between colloidal particles. *Langmuir*, 10(1):23–36, 1994.

[97] Xun Zhang, Junhu Zhang, Difu Zhu, Xiao Li, Xuemin Zhang, Tieqiang Wang, and Bai Yang. A universal approach to fabricate ordered colloidal crystals arrays based on electrostatic self-assembly. *Langmuir*, 26(23):17936–17942, 2010.

[98] Ke-Qin Zhang and Xiang Y. Liu. In situ observation of colloidal monolayer nucleation driven by an alternating electric field. *Nature*, 429(2004):739–743, 6993.

[99] Karl-Ulrich Fulda and Bernd Tieke. Langmuir films of monodisperse 0.5 μm spherical polymer particles with a hydrophobic core and a hydrophilic shell. *Advanced Materials*, 6(4):288–290, 1994.

[100] Nicolas Vogel, Clemens K. Weiss, and Katharina Landfester. From soft to hard: the generation of functional and complex colloidal monolayers for nanolithography". *Soft Matter*, 8(15):4044–4061, 2012.

[101] Worawut Khunsin, Andreas Amann, Gudrun Kocher-Oberlehner, Sergei G. Romanov, Saroj Pullteap, Han Cheng Seat, Eoin P. O'Reilly,

Rudolf Zentel, and Clivia M. Sotomayor Torres. Noise-assisted crystallization of opal films. *Advanced Functional Materials*, 22(9):1812–1821, 2012.

[102] H. Li, J. Low, K. S. Brown, and N. Wu. Large-area well-ordered nanodot array pattern fabricated with self-assembled nanosphere template. *IEEE Sensors Journal*, 8(6):880–884, 2008.

[103] Peng Jiang, , and Michael J. McFarland. Large-scale fabrication of wafer-size colloidal crystals, macroporous polymers and nanocomposites by spin-coating. *Journal of the American Chemical Society*, 126(42):13778–13786, 2004.

[104] D.M. Schaefer, M. Carpenter, R. Reifenberger, L.P. Demejo, and D.S. Rimai. Surface force interactions between micrometer-size polystyrene spheres and silicon substrates using atomic force techniques. *Journal of Adhesion Science and Technology*, 8(3):197–/210, 1994.

[105] B. Gady, , R. Reifenberger*, D. S. Rimai, , and L. P. DeMejo. Contact electrification and the interaction force between a micrometer-size polystyrene sphere and a graphite surface. *Langmuir*, 13(9):2533/–2537, 1997.

[106] B. Derjaguin. A theory of interaction of particles in presence of electric double layers and the stability of lyophobe colloids and disperse systems. *Progress in Surface Science*, 43(1):1–14, 1993.

[107] B. Derjaguin and L. Landau. Theory of the stability of strongly charged lyophobic sols and of the adhesion of strongly charged particles in solutions of electrolytes. *Progress in Surface Science*, 43(1):30–59, 1993.

[108] E. J. W. Verwey and J. T. G. Overbeek. *Theory of stability of lyophobic colloids : the interaction of sol particles having an electric double layer*. Elsevier, New York, 1948.

[109] Yudi Guo, Dongyan Tang, Yunchen Du, and Binbin Liu. Controlled fabrication of hexagonally close-packed langmuir–blodgett silica particulate monolayers from binary surfactant and solvent systems. *Langmuir*, 29(9):2849–2858, 2013.

[110] Jason Valentine, Shuang Zhang, Thomas Zentgraf, Erick Ulin-Avila, Dentcho A. Genov, Guy Bartal, and Xiang Zhang. Three-dimensional optical metamaterial with a negative refractive index. *Nature*, 455(7211):376–379, 2008.

[111] Harry A. Atwater and Albert Polman. Plasmonics for improved photovoltaic devices. *Nature Materials*, 9(3):205–213, 2010.

[112] Rashid Zia, Jon A. Schuller, Anu Chandran, and Mark L. Brongersma. Plasmonics: the next chip-scale technology. *Materials Today*, 9(7–8):20–27, 2006.

[113] Martina Abb, Yudong Wang, Nikitas Papasimakis, C. H. de Groot, and Otto L. Muskens. Surface-enhanced infrared spectroscopy using metal oxide plasmonic antenna arrays. *Nano Letters*, 14(1):346–352, 2014.

[114] Paul Kühler, Max Weber, and Theobald Lohmüller. Plasmonic nanoantenna arrays for surface-enhanced raman spectroscopy of lipid molecules embedded in a bilayer membrane. *ACS Applied Materials & Interfaces*, 6(12):8947–8952, 2014.

[115] Ahmet A. Yanik, Min Huang, Osami Kamohara, Alp Artar, Thomas W. Geisbert, John H. Connor, and Hatice Altug. An optofluidic nanoplasmonic biosensor for direct detection of live viruses from biological media. *Nano Letters*, 10(12):4962–4969, 2010.

[116] J. B. Pendry. A chiral route to negative refraction. *Science*, 306(5700):1353–1355, 2004.

[117] Shuang Zhang, Yong-Shik Park, Jensen Li, Xinchao Lu, Weili Zhang, and Xiang Zhang. Negative refractive index in chiral metamaterials. *Phys. Rev. Lett.*, 102(2):023901, 2009.

[118] Kirsty Hannam, David A. Powell, Ilya V. Shadrivov, and Yuri S. Kivshar. Broadband chiral metamaterials with large optical activity. *Phys. Rev. B*, 89(12):125105, 2014.

[119] C.W. Bunn, editor. *Chemical Crystallography*. Oxford University Press, New York, 1945.

[120] Shuai Zu, Yanjun Bao, and Zheyu Fang. Planar plasmonic chiral nanostructures. *Nanoscale*, 8(7):3900–3905, 2016.

[121] C. Feng, Z.B. Wang, S. Lee, J. Jiao, and L. Li. Giant circular dichroism in extrinsic chiral metamaterials excited by off-normal incident laser beams. *Optics Communications*, 285(10):2750–2754, 2012.

[122] J. H. Shi, Z. Zhu, H. F. Ma, W. X. Jiang, and T. J. Cui. Tunable symmetric and asymmetric resonances in an asymmetrical split-ring metamaterial. *Journal of Applied Physics*, 112(7), 2012.

[123] Feng Wang, Zhengping Wang, and Jinhui Shi. Theoretical study of high-q fano resonance and extrinsic chirality in an ultrathin babinet-inverted metasurface. *Journal of Applied Physics*, 116(15), 2014.

[124] Ivana Sersic, Marie Anne van de Haar, Felipe Bernal Arango, and A. Femius Koenderink. Ubiquity of optical activity in planar metamaterial scatterers. *Phys. Rev. Lett.*, 108(22):223903, 2012.

[125] Yunlong Zhou, Ming Yang, Kai Sun, Zhiyong Tang, and Nicholas A. Kotov. Similar topological origin of chiral centers in organic and nanoscale inorganic structures: Effect of stabilizer chirality on optical isomerism and growth of cdte nanocrystals. *Journal of the American Chemical Society*, 132(17):6006–6013, 2010.

[126] Zhiyuan Fan and Alexander O. Govorov. Plasmonic circular dichroism of chiral metal nanoparticle assemblies. *Nano Letters*, 10(7):2580–2587, 2010.

[127] Yongqian Li, Lei Su, Chen Shou, Chunmeng Yu, Jinjun Deng, and Yu Fang. Surface-enhanced molecular spectroscopy (sems) based on perfect-absorber metamaterials in the mid-infrared. *Scientific Reports*, 3(2865), 2013.

[128] Liang Luo, Ioannis Chatzakis, Jigang Wang, Fabian B. P Niesler ., Martin Wegener, Thomas Koschny, and Costas M. Soukoulis. Broadband terahertz generation from metamaterials. *Nature Communications*, 5, 2014.

[129] Jun-Ho Choi and Minhaeng Cho. Terahertz chiroptical spectroscopy of an alfa-helical polypeptide: A molecular dynamics simulation study. *The Journal of Physical Chemistry B*, 118(45):12837–12843, 2014.

[130] Xuesong Liu, Caryn Naekyung Kim, Jie Yang, Ronald Jemmerson, and Xiaodong Wang. Induction of apoptotic program in cell-free extracts: Requirement for datp and cytochrome c. *Cell*, 86(1):147–157, 1996.

[131] Haiying Liu, Hiromichi Yamamoto, Jianjun Wei, and David H. Waldeck. Control of the electron transfer rate between cytochrome c and gold electrodes by the manipulation of the electrode's hydrogen bonding character. *Langmuir*, 19(6):2378–2387, 2003.

[132] Reza Karimi Shervedani, Anahita Farahbakhsh, and Mojtaba Bagherzadeh. Functionalization of gold cysteamine self-assembled monolayer with ethylenediaminetetraacetic acid as a novel nanosensor. *Analytica Chimica Acta*, 587(2):254–262, 2007.

[133] Mikael Wirde, Ulrik Gelius, and Leif Nyholm. Self-assembled monolayers of cystamine and cysteamine on gold studied by xps and voltammetry. *Langmuir*, 15(19):6370–6378, 1999.

[134] Reza Karimi Shervedani, Mojtaba Bagherzadeh, and Seyed Ahmad Mozaffari. Determination of dopamine in the presence of high concentration of ascorbic acid by using gold cysteamine self-assembled monolayers as a nanosensor. *Sensors and Actuators B: Chemical*, 115(2):614–621, 2006.

[135] Shourui Lin, Xiue Jiang, Lixu Wang, Guihua Li, and Liping Guo. Adsorption orientation of horse heart cytochrome c on a bare gold electrode hampers its electron transfer. *The Journal of Physical Chemistry C*, 116(1):637–642, 2012.

[136] Yanxiu Zhou, Tsutomu Nagaoka, and Guoyi Zhu. Electrochemical studies of cytochrome c disulfide at gold electrodes. *Biophysical Chemistry*, 79(1):55–62, 1999.

[137] G. Bhak, Y.J. Choe, and S. R. Paik. Mechanism of amyloidogenesis: nucleation-dependent fibrillation versus double-concerted fibrillation. *BMP reports*, 42(9):541–551, 2009.

[138] M. Stefani and C. M. Dobson. Protein aggregation and aggregate toxicity: new insights into protein folding, misfolding diseases and biological evolution. *Journal of Molecular Medicine*, 81(11):678–699, 2003.

[139] Ehud Gazit. Self-assembled peptide nanostructures: the design of molecular building blocks and their technological utilization. *Chemical Society Reviews*, 36:1263–1269, 2007.

[140] Lei Liu, Katerina Busuttil, Shuai Zhang, Yanliang Yang, Chen Wang, Flemming Besenbachera, and Mingdong Dong. The role of self-assembling polypeptides in building nanomaterials. *Physical Chemistry Chemical Physics*, 13:17435–17444, 2011.

[141] José V. González-Aramundiz, María V. Lozano, Ana Sousa-Herves, Eduardo Fernandez-Megia, and Noemi Csaba. Polypeptides and polyaminoacids in drug delivery. *Expert Opinion on Drug Delivery*, 9(2):183–201, 2012.

[142] Mohtadin Hashemi, Peter Fojan, and Leonid Gurevich. The many faces of diphenylalanine. *Journal of Self-Assembly and Molecular Electronics*, 1(2):195–208, 2013.

[143] Xuehai Yan, Pengli Zhu, and Junbai Li. Self-assembly and application of diphenylalanine-based nanostructures. *Chemical Society Reviews*, 39:1877–1890, 2010.

[144] Phanourios Tamamis, Lihi Adler-Abramovich, Meital Reches, Karen Marshall, Pawel Sikorski, Louise Serpell, and Ehud Gazit. Self-assembly of phenylalanine oligopeptides: Insights from experiments and simulations. *Biophysical Journal*, 96(12):5020–5029, 2009.

[145] Carl Henrik Görbitz. Nanotube formation by hydrophobic dipeptides. *Chemistry - A European Journal*, 7(23):5153–5159, 2001.

[146] Naresh Thota, Zhonglin Luo, Zhongqiao Hu, and Jianwen Jiang. Self-assembly of amphiphilic peptide $(af)_6h_5k_15$: Coarse-grained molecular dynamics simulation. *Journal of Physical Chemistry B*, 117(33):9690–9698, 2013.

[147] Siewert J. Marrink, Alex H. de Vries, and Alan E. Mark. Coarse grained model for semiquantitative lipid simulations. *Journal of Physical Chemistry B*, 108(2):750–760, 2004.

[148] Siewert J. Marrink, H. Jelger Risselada, Serge Yefimov, D. Peter Tieleman, and Alex H. de Vries. The martini force field: Coarse grained model for biomolecular simulations. *J. Phys. Chem. B*, 111(27):7812–7824, 2007.

[149] Josephine Corsi, Robert W. Hawtin, Oscar Ces, George S. Attard, and Syma Khalid. Dna lipoplexes: Formation of the inverse hexagonal phase observed by coarse-grained molecular dynamics simulation. *Langmuir*, 26(14):12119–12125, 2010.

[150] Cesar A. López, Andrzej J. Rzepiela, Alex H. de Vries, Lubbert Dijkhuizen, Philippe H. Hünenberger, and Siewert J. Marrink. Martini coarse-grained force field: Extension to carbohydrates. *Journal of Chemical Theory and Computation*, 5(12):3195–3210, 2009.

[151] Hwankyu Lee, Alex H. de Vries, Siewert J. Marrink, and Richard W. Pastor. A coarse-grained model for polyethylene oxide and polyethylene glycol: Conformation and hydrodynamics. *The Journal of Physical Chemistry B*, 113(40):13186–13194, 2009.

[152] Jirasak Wong-Ekkabut, Svetlana Baoukina, Wannapong Triampo, I-Ming Tang, Peter D. Tieleman, and Luca Monticelli. Computer simulation study of fullerene translocation through lipid membranes. *Nat Nano*, 3(6):363–368, 2008.

[153] Siewert J. Marrink and D. Peter Tieleman. Perspective on the martini model. *Chemical Society Reviews*, 42:6801–6822, 2013.

[154] Jesper Sørensen, Xavier Periole, Katrine K. Skeby, Siewert J. Marrink, and Birgit Schiøtt. Protofibrillar assembly toward the formation of amyloid fibrils. *Biophysical Chemistry*, 2(19):2385–2390, 2011.

[155] Marc Baaden and Siewert J Marrink. Coarse-grain modelling of protein-protein interactions. *Structural Biology*, 23(6):878–886, 2013.

[156] Khongvit Prasitnok and Mark R. Wilson. A coarse-grained model for polyethylene glycol in bulk water and at a water/air interface. *Physical Chemistry Chemical Physics*, 15(40):17093–17104, 2013.

[157] Andrzej J. Rzepiela, Martti Louhivuori, Christine Peter, and Siewert J. Marrink. Hybrid simulations: combining atomistic and coarse-grained force fields using virtual sites. *Physical Chemistry Chemical Physics*, 13(22):10437–10448, 2011.

[158] Tsjerk A. Wassenaar, Kristyna Pluhackova, Rainer A. Böckmann, Siewert J. Marrink, and D. Peter Tieleman. Going backward: A flexible geometric approach to reverse transformation from coarse grained to atomistic models. *Journal of Chemical Theory and Computation*, 10(2):676–690, 2014.

[159] G.N. Ramachandran and Alok K. Mitra. An explanation for the rare occurrence of cis peptide units in proteins and polypeptides. *Journal of Molecular Biology*, 107(1):85–92, 1976.

[160] Andreas Jabs, Manfred S Weiss, and Rolf Hilgenfeld. Non-proline cis peptide bonds in proteins. *Journal of Molecular Biology*, 286(1):291–304, 1999.

[161] R. Sibson. Slink: An optimally efficient algorithm for the single-link cluster method. *The Computer Journal*, 16(1):30–34, 1973.

[162] David E. Shaw, Paul Maragakis, Kresten Lindorff-Larsen, Stefano Piana, Ron O. Dror, Michael P. Eastwood, Joseph A. Bank, John M. Jumper, John K. Salmon, Yibing Shan, and Willy Wriggers. Atomic-level characterization of the structural dynamics of proteins. *Science*, 330(6002):341–346, 2010.

[163] Peter L. Freddolino, Feng Liu, Martin Gruebele, and Klaus Schulten. Ten-microsecond molecular dynamics simulation of a fast-folding ww domain. *Biophysical Journal*, 94(10):L75–L77, 2008.

[164] Shibasish Chowdhury, Mathew C. Lee, Guoming Xiong, and Yong Duan. Ab initio folding simulation of the trp-cage mini-protein approaches nmr resolution. *Journal of Molecular Biology*, 327(3):711–717, 2003.

[165] Carlos Simmerling, Bentley Strockbine, and Adrian E. Roitberg. All-atom structure prediction and folding simulations of a stable protein. *Journal of the American Chemical Society*, 124(38):11256–11259, 2002.

[166] David Chandler. Interfaces and the driving force of hydrophobic assembly. *Nature*, 437:640–647, 2005.

[167] Adam Biela, Nader N. Nasief, Michael Betz, Andreas Heine, David Hangauer, and Gerhard Klebe. Dissecting the hydrophobic effect on the molecular level: The role of water, enthalpy, and entropy in ligand binding to thermolysin. *Angewandte Chemie International Edition*, 52(6):1822–1828, 2013.

[168] Cong Guo, Yin Luo, Ruhong Zhou, and Guanghong Wei. Probing the self-assembly mechanism of diphenylalanine-based peptide nanovesicles and nanotubes. *Nano*, 6(5):3907–3918, 2012.

[169] G.A. Jeffrey, editor. *An Introduction to Hydrogen Bonding*. Oxford University Press, Oxford, 1997.

[170] G.D. Fasman, editor. *Prediction of Protein Structure and the Principles of Protein Conformation*. Plenum, New York, 1990.

[171] Hicham Fenniri, Packiarajan Mathivanan, Kenrick L. Vidale, Debra M. Sherman, Klaas Hallenga, Karl V. Wood, and Joseph G. Stowell. Hydrogen bonds and salt bridges across protein-protein interfaces. *Journal of the American Chemical Society*, 123(16):3854–3855, 2001.

[172] D Xu, C J Tsai, and R Nussinov. Hydrogen bonds and salt bridges across protein-protein interfaces. *Protein Engineering*, 10(9):999–1012, 1997.

[173] Robert S. Paton and Jonathan M. Goodman. Hydrogen bonding and π-stacking: How reliable are force fields? a critical evaluation of force field descriptions of nonbonded interactions. *Journal of Chemical Information and Modeling*, 49(4):944–955, 2009.

[174] David A. Evans, Kevin T. Chapman, Deborah Tan Hung, and Alan T. Kawaguchi. Transition state pi-solvation by aromatic rings: An electronic contribution to diels-alder reaction diastereoselectivity. *Angewandte Chemie International Edition in English*, 26(11):1184–1186, 1987.

[175] Jiří Vondrášk, Lada Bendová, Vojtěch Klusák, and Pavel Hobza. Unexpectedly strong energy stabilization inside the hydrophobic core of small protein rubredoxin mediated by aromatic residues: Correlated ab initio quantum chemical calculations. *Journal of the American Chemical Society*, 127(8):2615–2619, 2005.

[176] Georgia B. McGaughey, Marc Gagné, and Anthony K. Rappé. pi-stacking interactions. alive and well in proteins. *The Journal of Biological Chemistry*, 273(25):15458–15463, 1998.

[177] Darshan Ranganathan, V. Haridas, R. Gilardi, and Isabella L. Karle. Self-assembling aromatic-bridged serine-based cyclodepsipeptides (serinophanes): A demonstration of tubular structures formed through aromatic pi-pi interactions. *Journal of the American Chemical Society*, 120(42):10793–10800, 1998.

[178] C. A. Hunter. Aromatic interactions in proteins, dna and synthetic receptors. *Philosophical Transactions: Physical Sciences and Engineering*, 345(1674):77–85, 1993.

[179] Petr Jurečka and Pavel Hobza. True stabilization energies for the optimal planar hydrogen-bonded and stacked structures of guanine· · ·cytosine, adenine· · ·thymine, and their 9- and 1-methyl derivatives: Complete basis set calculations at the mp2 and ccsd(t) levels and comparison with experiment. *Journal of the American Chemical Society*, 125(50):15608–15613, 2003.

[180] Gianni Chessari, Christopher A. Hunter, Caroline M. R. Low, Martin J. Packer, Jeremy G. Vinter, and Cristiano Zonta. An evaluation of force-field treatments of aromatic interactions. *Chemistry A European Journal*, 8(13):2860–2867, 2002.

[181] S. Sun and E. R. Bernstein. Aromatic van der waals clusters:? structure and nonrigidity. *Journal of Physical Chemistry*, 100(32):13348–13366, 1996.

[182] Christophe Chipot, Richard Jaffe, Bernard Maigret, David A. Pearlman, and Peter A. Kollman. Benzene dimer:? a good model for $\pi - \pi$ interactions in proteins? a comparison between the benzene and the toluene dimers in the gas phase and in an aqueous solution. *J. Am. Chem. Soc.*, 118(45):11217–11224, 1996.

[183] S. K. Burley and G. A. Petsko. Aromatic-aromatic interaction: a mechanism of protein structure stabilization. *Science*, 229(4708):23–28, 1985.

[184] J. J. P. Stewart. "mopac", 2012. http://openmopac.net.

[185] J. J. P. Stewart. "mozyme". http://www.openmopac.net/MOZYME_literature.html.

[186] J. J. P. Stewart. Optimization of parameters for semiempirical methods vi: more modifications to the nddo approximations and re-optimization of parameters. *Journal of Molecular Modeling*, 19(1):1–32, 2013.

[187] Martin Korth, Michal Pitoáňk, Jan Řezáč, and Pavel Hobza. A transferable h-bonding correction for semiempirical quantum-chemical methods. *Journal of Chemical Theory and Computation*, 6(1):344–352, 2010.

[188] Nusret Duygu Yilmazer and Martin Korth. Enhanced semiempirical qm methods for biomolecular interactions. *Computational and Structural Biotechnology Journal*, 13:169–175, 2015.

[189] A. Klamt and G. Schuurmann. Cosmo: a new approach to dielectric screening in solvents with explicit expressions for the screening energy and its gradient. *J. Chem. Soc., Perkin Trans. 2*, pages 799–805, 1993.

[190] Michael Feig. Is alanine dipeptide a good model for representing the torsional preferences of protein backbones? *Journal of Chemical Theory and Computation*, 4(9):1555–1564, 2008.

[191] Junfeng Gu, Fang Bai, Honglin Li, and Xicheng Wang. A generic force field for protein coarse-grained molecular dynamics simulation. *Int J Mol Sci.*, 13(11):14451–14469, 2012.

[192] Daniel J. Price and Charles L. Brooks. Modern protein force fields behave comparably in molecular dynamics simulations. *Journal of Computational Chemistry*, 23(11):1045–1057, 2002.

[193] Ligabue-Braun R, Sachett LG, Pol-Fachin L, and Verli H. The calcium goes meow: Effects of ions and glycosylation on fel d 1, the major cat allergen. *PLoS ONE*, 10(7), 2015.

[194] Morten Slyngborg and Peter Fojan. A computational study of the self-assembly of the rfffr peptide. *Phys. Chem. Chem. Phys.*, 17(44):30023–30036, 2015.

[195] Pim W. J. M. Frederix, Gary G. Scott, Yousef M. Abul-Haija, Daniela Kalafatovic, Charalampos G. Pappas, Nadeem Javid, Neil T. Hunt, Rein V. Ulijn, and Tell Tuttle. Exploring the sequence space for (tri-)peptide self-assembly to design and discover new hydrogels. *Nat Chem*, 7(1):30–37, 2015.

[196] Willem Norde. Driving forces for protein adsorption at solid surfaces. *Macromolecular Symposia*, 103(1):5–18, 1996.

[197] Ehud Gazit. Mechanisms of amyloid fibril self-assembly and inhibition. model short peptides as a key research tool. *FEBS Journal*, 272(23):5971–5978, 2005.

[198] David Zanuy and Ruth Nussinov. The sequence dependence of fiber organization. a comparative molecular dynamics study of the islet amyloid polypeptide segments 22-27 and 22-29. *Journal of Molecular Biology*, 329(3):565–584, 2003.

[199] Amedeo Caflisch. Computational models for the prediction of polypeptide aggregation propensity. *Current Opinion in Chemical Biology*, 10(5):437–444, 2006.

[200] Amol P. Pawara, Kateri F. DuBay, Jesús Zurdo, Fabrizio Chiti, Michele Vendruscolo, and Christopher M. Dobson. Prediction of aggregation-prone and aggregation-susceptible regions in proteins associated with neurodegenerative diseases. *Journal of Molecular Biology*, 350(2):379–392, 2005.

[201] William L. Jorgensen and Julian. Tirado-Rives. The opls [optimized potentials for liquid simulations] potential functions for proteins, energy minimizations for crystals of cyclic peptides and crambin. *Journal of the American Chemical Society*, 110(6):1657–1666, 1988.

[202] George A. Kaminski and Richard A. Friesner. Evaluation and reparametrization of the opls-aa force field for proteins via comparison with accurate quantum chemical calculations on peptides. *Journal of Physical Chemistry B*, 105(28):6474–6487, 2001.

[203] Sander Pronk, Szilárd Páll, Roland Schulz, Per Larsson, Pär Bjelkmar, Rossen Apostolov, Michael R. Shirts, Jeremy C. Smith, Peter M. Kasson, David van der Spoel, Berk Hess, and Erik Lindahl. Gromacs 4.5: a high-throughput and highly parallel open source molecular simulation toolkit. *Bioinformatics*, 29(7):845–854, 2013.

[204] Elmar Krieger, Günther Koraimann, and Gert Vriend. Increasing the precision of comparative models with yasara nova - a self-parameterizing force field. *Proteins: Structure, Function, and Bioinformatics*, 47(3):393–402, 2002.

[205] Giovanni Bussi, Davide Donadio, and Michele Parrinello. Canonical sampling through velocity rescaling. *The Journal of Chemical Physics*, 126(1):–, 2007.

[206] H. J. C. Berendsen, J. P. M. Postma, W. F. van Gunsteren, A. DiNola, and J. R. Haak. Molecular dynamics with coupling to an external bath. *The Journal of Chemical Physics*, 81(8):3684–3690, 1984.

[207] Ailan Cheng and Kenneth M. Merz. Application of the nosé-hoover chain algorithm to the study of protein dynamics. *The Journal of Physical Chemistry*, 100(5):1927–1937, 1996.

[208] M. Parrinello and A. Rahman. Canonical sampling through velocity rescaling. *Journal of Applied Physics*, 52(12):7182–7190, 1981.

[209] Ulrich Essmann, Lalith Perera, Max L. Berkowitz, Tom Darden, Hsing Lee, and Lee G. Pedersen. A smooth particle mesh ewald method. *The Journal of Chemical Physics*, 103(19):8577–8593, 1995.

[210] Nusret Duygu Yilmazer and Martin Korth. Enhanced semiempirical {QM} methods for biomolecular interactions. *Computational and Structural Biotechnology Journal*, 13:169–175, 2015.

[211] David Van Der Spoel, Erik Lindahl, Berk Hess, Gerrit Groenhof, Alan E. Mark, and Herman J. C. Berendsen. Fast, flexible, and free. *J. Comput. Chem.*, 26(16):1701–1718, 2005.

[212] Riccardo Baron, Alex H. de Vries, Philippe H. Hünenberger, and Wilfred F. van Gunsteren. Comparison of atomic-level and coarse-grained models for liquid hydrocarbons from molecular dynamics configurational entropy estimates. *J. Phys. Chem. B*, 110(16):8464–8473, 2006.

[213] Riccardo Baron, Alex H. de Vries, Philippe H. Hünenberger, and Wilfred F. van Gunsteren. Configurational entropies of lipids in pure and mixed bilayers from atomic-level and coarse-grained molecular dynamics simulations. *J. Phys. Chem. B*, 110(31):15602–15614, 2006.

[214] Bas J. G. E. Pieters, Mark B. van Eldijk, Roeland J. M. Nolte, and Jasmin Mecinovic. Natural supramolecular protein assemblies. *Chem. Soc. Rev.*, 45(1):24–39, 2016.

[215] Uwe B Sleytr and Terry J Beveridge. Bacterial s-layers. *Trends in Microbiology*, 7(6):253–260, 1999.

[216] Markus B. Linder. Hydrophobins: Proteins that self assemble at interfaces. *Current Opinion in Colloid & Interface Science*, 14(5):1359–0294, 2009.

[217] Mauricio Comas-Garcia, Rees F. Garmann, Surendra W. Singaram, Avinoam Ben-Shaul, Charles M. Knobler, and William M. Gelbart. Characterization of viral capsid protein self-assembly around short single-stranded rna. *The Journal of Physical Chemistry B*, 118(27):7510–7519, 2014.

[218] Vassiliki A. Iconomidou and Stavros J. Hamodrakas. Natural protective amyloids. *Current Protein and Peptide Science*, 9(3):291–309, 2008.

[219] Samir K. Maji, Marilyn H. Perrin, Michael R. Sawaya, Sebastian Jessberger, Krishna Vadodaria, Robert A. Rissman, Praful S. Singru, K. Peter R. Nilsson, Rozalyn Simon, David Schubert, David Eisenberg, Jean Rivier, Paul Sawchenko, Wylie Vale, and Roland Riek. Functional amyloids as natural storage of peptide hormones in pituitary secretory granules. *Science*, 325(5938):328–332, 2009.

[220] Dindyal Mandal, Amir Nasrolahi Shirazi, and Keykavous Parang. Self-assembly of peptides to nanostructures. *Org. Biomol. Chem.*, 12(22):3544–3561, 2014.

[221] Roberto de la Rica and Hiroshi Matsui. Applications of peptide and protein-based materials in bionanotechnology. *Chem. Soc. Rev.*, 39(9):3499–3509, 2010.

[222] Mischa Zelzer and Rein V. Ulijn. Next-generation peptide nanomaterials: molecular networks, interfaces and supramolecular functionality. *Chem. Soc. Rev.*, 39(9):3351–3357, 2010.

[223] Robert J. Mart, Rachel D. Osborne, Molly M. Stevens, and Rein V. Ulijn. Peptide-based stimuli-responsive biomaterials. *Soft Matter*, 2(10):822–835, 2006.

[224] Maurizio Prato, Kostas Kostarelos, and Alberto Bianco. Functionalized carbon nanotubes in drug design and discovery. *Accounts of Chemical Research*, 41(1):60–68, 2008.

[225] Tom O. McDonald, Honglei Qu, Brian R. Saunders, and Rein V. Ulijn. Branched peptide actuators for enzyme responsive hydrogel particles. *Soft Matter*, 5(8):1728–1734, 2009.

[226] Paul D. Thornton, Robert J. Mart, Simon J. Webb, and Rein V. Ulijn. Enzyme-responsive hydrogel particles for the controlled release of proteins: designing peptide actuators to match payload. *Soft Matter*, 4(4):821–827, 2008.

[227] Tzu-Yun Cheng, Ming-Hong Chen, Wen-Han Chang, Ming-Yuan Huang, and Tzu-Wei Wang. Neural stem cells encapsulated in a functionalized self-assembling peptide hydrogel for brain tissue engineering. *Biomaterials*, 34(8):2005–2016, 2013.

[228] Maryam M. Javadpour, , and Mary D. Barkley. Self-assembly of designed antimicrobial peptides in solution and micelles. *Biochemistry*, 36(31):9540–9549, 1997.

[229] Ying Zhao, Tianjiao Ji, Hai Wang, Suping Li, Yuliang Zhao, and Guangjun Nie. Self-assembled peptide nanoparticles as tumor microenvironment activatable probes for tumor targeting and imaging. *Journal of Controlled Release*, 177:11–19, 2014.

[230] Lihi Adler-Abramovich, Daniel Aronov, Peter Beker, Maya Yevnin, Shiri Stempler, Ludmila Buzhansky, Gil Rosenman, and Ehud Gazit. Self-assembled arrays of peptide nanotubes by vapour deposition. *Nat Nano*, 4(12):849–854, 2009.

[231] David L. Masica, Sarah B. Schrier, Elizabeth A. Specht, and Jeffrey J. Gray. De novo design of peptide-calcite biomineralization systems. *Journal of the American Chemical Society*, 132(35):12252–12262, 2010.

[232] Soren Roi Midtgaard, Martin Cramer Pedersen, Jacob Judas Kain Kirkensgaard, Kasper Kildegaard Sorensen, Kell Mortensen, Knud J. Jensen, and Lise Arleth. Self-assembling peptides form nanodiscs that stabilize membrane proteins. *Soft Matter*, 10(5):738–752, 2014.

[233] Rohan J. Kumar, James M. MacDonald, Th. Birendra Singh, Lynne J. Waddington, and Andrew B. Holmes. Hierarchical self-assembly of semiconductor functionalized peptide α-helices and optoelectronic properties. *Journal of the American Chemical Society*, 133(22):8564–8573, 2011.

[234] Jaime Castillo, Simone Tanzi, Maria Dimaki, and Winnie Svendsen. Manipulation of self-assembly amyloid peptide nanotubes by dielectrophoresis. *ELECTROPHORESIS*, 29(24):5026–5032, 2008.

[235] Roberto de la Rica, Christophe Pejoux, Cesar Fernandez-Sanchez, Antonio Baldi, and Hiroshi Matsui. Peptide-nanotube biochips for label-free detection of multiple pathogens. *Small*, 6(10):1092–1095, 2010.

[236] John D. Tovar. Supramolecular construction of optoelectronic biomaterials. *Accounts of Chemical Research*, 46(7):1527–1537, 2013.

[237] Nurit Ashkenasy, W. Seth Horne, and M. Reza Ghadiri. Design of self-assembling peptide nanotubes with delocalized electronic states. *Small*, 2(1):99–102, 2006.

[238] William P. Esler, Evelyn R. Stimson, Joseph R. Ghilardi, Yi-An Lu, Arthur M. Felix, Harry V. Vinters, Patrick W. Mantyh, Jonathan P. Lee, , and John E. Maggio. Point substitution in the central hydrophobic cluster of a human β-amyloid congener disrupts peptide folding and abolishes plaque competence. *Biochemistry*, 35(44):13914–13921, 1996.

[239] Amol P. Pawar, Kateri F. DuBay, Jesús Zurdo, Fabrizio Chiti, Michele Vendruscolo, and Christopher M. Dobson. Prediction of aggregation-prone and aggregation-susceptible regions in proteins associated with neurodegenerative diseases. *Journal of Molecular Biology*, 350(2):379–392, 2005.

[240] Rein V. Ulijn and Andrew M. Smith. Designing peptide based nanomaterials. *Chem. Soc. Rev.*, 37(4):664–675, 2008.

[241] Claudia Tomasini and Nicola Castellucci. Peptides and peptidomimetics that behave as low molecular weight gelators. *Chem. Soc. Rev.*, 42(1):156–172, 2013.

[242] Yong-beom Lim, Kyung-Soo Moon, and Myongsoo Lee. Recent advances in functional supramolecular nanostructures assembled from bioactive building blocks. *Chem. Soc. Rev.*, 38(4):925–934, 2009.

[243] Fan Zhao, Man Lung Ma, and Bing Xu. Molecular hydrogels of therapeutic agents. *Chem. Soc. Rev.*, 38(4):883–891, 2009.

[244] Chunhua Ren, Jianwu Zhang, Minsheng Chen, and Zhimou Yang. Self-assembling small molecules for the detection of important analytes. *Chem. Soc. Rev.*, 43(21):7257–7266, 2014.

[245] Masato Ikeda, Tatsuya Tanida, Tatsuyuki Yoshii, Kazuya Kurotani, Shoji Onogi, Kenji Urayama, and Itaru Hamachi. Installing logic-gate responses to a variety of biological substances in supramolecular hydrogel-enzyme hybrids. *Nat Chem*, 6(6):511–518, 2014.

[246] Fabrizio Gelain, Akihiro Horii, and Shuguang Zhang. Designer self-assembling peptide scaffolds for 3-d tissue cell cultures and regenerative medicine. *Macromolecular Bioscience*, 7(5):544–551, 2007.

[247] Gregory A. Hudalla, Tao Sun, Joshua Z. Gasiorowski, Huifang Han, Ye F. Tian, Anita S. Chong, and Joel H. Collier. Gradated assembly of multiple proteins into supramolecular nanomaterials. *Nat Mater*, 13(8):829–836, 2014.

[248] Yi Kuang and Bing Xu. Disruption of the dynamics of microtubules and selective inhibition of glioblastoma cells by nanofibers of small hydrophobic molecules. *Angewandte Chemie International Edition*, 52(27):6944–6948, 2013.

[249] Herdeline Ann M. Ardo na and John D. Tovar. Peptide pi-electron conjugates: Organic electronics for biology? *Bioconjugate Chemistry*, 26(12):2290–2302, 2015.

[250] Daniel J. Rubin, Hadi T. Nia, Thierry Desire, Peter Q. Nguyen, Michael Gevelber, Christine Ortiz, and Neel S. Joshi. Mechanical reinforcement of polymeric fibers through peptide nanotube incorporation. *Biomacromolecules*, 14(10):3370–3375, 2013.

[251] Tuomas P. J. Knowles and Markus J. Buehler. Nanomechanics of functional and pathological amyloid materials. *Nat Nano*, 6(8):469–479, 2011.

[252] Amir Handelman, Natalia Kuritz, Amir Natan, and Gil Rosenman. Reconstructive phase transition in ultrashort peptide nanostructures and induced visible photoluminescence. *Langmuir*, 32(12):2847–2862, 2016.

[253] Ulyana Shimanovich, Igor Efimov, Thomas O. Mason, Patrick Flagmeier, Alexander K. Buell, Aharon Gedanken, Sara Linse, Karin S. Åkerfeldt, Christopher M. Dobson, David A. Weitz, and Tuomas P. J. Knowles. Protein microgels from amyloid fibril networks. *ACS Nano*, 9(1):43–51, 2015.

[254] Haixia Xu, Apurba K. Das, Masaki Horie, Majeed S. Shaik, Andrew M. Smith, Yi Luo, Xiaofeng Lu, Richard Collins, Steven Y. Liem, Aimin Song, Paul L. A. Popelier, Michael L. Turner, Ping Xiao, Ian A. Kinloch, and Rein V. Ulijn. An investigation of the conductivity of peptide nanotube networks prepared by enzyme-triggered self-assembly. *Nanoscale*, 2(6):960–966, 2010.

[255] M. Gupta, A. Bagaria, A. Mishra, P. Mathur, A. Basu, S. Ramakumar, and V.S. Chauhan. Self-assembly of a dipeptide- containing conformationally restricted dehydrophenylalanine residue to form ordered nanotubes. *Advanced Materials*, 19(6):858–861, 2007.

[256] Marta J. Krysmann, Valeria Castelletto, Antonios Kelarakis, Ian W. Hamley, Rohan A. Hule, and Darrin J. Pochan. Self-assembly and hydrogelation of an amyloid peptide fragment. *Biochemistry*, 47(16):4597–4605, 2008.

[257] Amir Handelman, Amir Natan, and Gil Rosenman. Structural and optical properties of short peptides: nanotubes-to-nanofibers phase transformation. *Journal of Peptide Science*, 20(7):487–493, 2014.

[258] Silvia Marchesan, Christopher D. Easton, Firdawosia Kushkaki, Lynne Waddington, and Patrick G. Hartley. Tripeptide self-assembled hydrogels: unexpected twists of chirality. *Chem. Commun.*, 48(16):2195–2197, 2012.

[259] Silvia Marchesan, Yue Qu, Lynne J. Waddington, Christopher D. Easton, Veronica Glattauer, Trevor J. Lithgow, Keith M. McLean, John S. Forsythe, and Patrick G. Hartley. Self-assembly of ciprofloxacin and a tripeptide into an antimicrobial nanostructured hydrogel. *Biomaterials*, 34(14):3678–3687, 2013.

[260] S. Marchesan, K. E. Styan, C. D. Easton, L. Waddington, and A. V. Vargiu. Higher and lower supramolecular orders for the design of self-assembled heterochiral tripeptide hydrogel biomaterials. *J. Mater. Chem. B*, 3(41):8123–8132, 2015.

[261] Jadwiga Frelek, Wojciech J. Szczepek, Stephan Neubrech, Bernd Schultheis, Joachim Brechtel, and Hans-Georg Kuball. Chiroptical properties of cisoid enones from circular dichroism (cd) and anisotropic

circular dichroism (acd) spectroscopy. *Chemistry - A European Journal*, 8(8):1899–1907, 2002.

[262] Valeria Castelletto, Ge Cheng, Steve Furzeland, Derek Atkins, and Ian W. Hamley. Control of strand registry by attachment of peg chains to amyloid peptides influences nanostructure. *Soft Matter*, 8(20):5434–5438, 2012.

[263] Eigil B. Nielsen and John A. Schellman. The absorption spectra of simple amides and peptides. *The Journal of Physical Chemistry*, 71(7):2297–2304, 1967.

[264] Nadine D. Younan and John H. Viles. A comparison of three fluorophores for the detection of amyloid fibers and prefibrillar oligomeric assemblies. tht (thioflavin t); ans (1-anilinonaphthalene-8-sulfonic acid); and bisans (4,4-dianilino-1,1-binaphthyl-5,5-disulfonic acid). *Biochemistry*, 54(28):4297–4306, 2015.

[265] Adam L. Cloe, Joseph P. R. O. Orgel, Joseph R. Sachleben, Robert Tycko, and Stephen C. Meredith. The japanese mutant aβ ($\triangle$e22-aβ1-39) forms fibrils instantaneously, with low-thioflavin t fluorescence: Seeding of wild-type aβ1-40 into atypical fibrils by $\triangle$e22-aβ1-39. *Biochemistry*, 50(12):2026–2039, 2011.

[266] Matthew Biancalana, Koki Makabe, Akiko Koide, and Shohei Koide. Molecular mechanism of thioflavin-t binding to the surface of beta-rich peptide self-assemblies. *Journal of Molecular Biology*, 385(4):1052–1063, 2009.

[267] Chun Wu, Matthew Biancalana, Shohei Koide, and Joan-Emma Shea. Binding modes of thioflavin-t to the single-layer β-sheet of the peptide self-assembly mimics. *Journal of Molecular Biology*, 394(4):627–633, 2009.

[268] Matthew Biancalana and Shohei Koide. Molecular mechanism of thioflavin-t binding to amyloid fibrils. *Biochimica et biophysica acta*, 1804(7):1405–1412, 2010.

[269] Fiona T. S. Chan, Clemens F. Kaminski, and Gabriele S. Kaminski Schierle. Homofret fluorescence anisotropy imaging as a tool to study molecular self-assembly in live cells. *ChemPhysChem*, 12(3):500–509, 2011.

[270] Laurens H. Lindenburg, Mantas Malisauskas, Tari Sips, Lisanne van Oppen, Sjors P. W. Wijnands, Stan F. J. van de Graaf, and Maarten Merkx. Quantifying stickiness: Thermodynamic characterization of intramolecular domain interactions to guide the design of forster resonance energy transfer sensors. *Biochemistry*, 53(40):6370–6381, 2014.

[271] Pierre D. J. Moens, Michael K. Helms, and David M. Jameson. Detection of tryptophan to tryptophan energy transfer in proteins. *The Protein Journal*, 23(1):79–83, 2004.

[272] Gideon I. Livshits, Avigail Stern, Dvir Rotem, Natalia Borovok, Gennady Eidelshtein, Agostino Migliore, Erika Penzo, Shalom J. Wind, Rosa Di Felice, Spiros S. Skourtis, Juan Carlos Cuevas, Leonid Gurevich, Alexander B. Kotlyar, and Danny Porath. Long-range charge transport in single g-quadruplex dna molecules. *Nat Nano*, 9(12):1040–1046, 2014.

[273] Barnett Rosenberg. Electrical conductivity of proteins. *Nature*, 193(4813):364–365, 1962.

[274] M. H. Cardew and D. D. Eley. The semiconductivity of organic substances. part 3.-haemoglobin and some amino acids. *Discuss. Faraday Soc.*, 27(0):115–128, 1959.

[275] G King and J.A Medley. D.c. conduction in swollen polar polymers. i. electrolysis of the keratin-water system. *Journal of Colloid Science*, 4(1):1–7, 1949.

[276] Izhar Ron, Israel Pecht, Mordechai Sheves, and David Cahen. Proteins as solid-state electronic conductors. *Accounts of Chemical Research*, 43(7):945–953, 2010.

[277] Charlotte A. E. Hauser and Shuguang Zhang. Nanotechnology: Peptides as biological semiconductors. *Nature*, 468(7323):516–517, 2010.

[278] X. Mu noz Berbel, F.J. Mu noz, N. Vigués, and J. Mas. On-chip impedance measurements to monitor biofilm formation in the drinking water distribution network. *Sensors and Actuators B: Chemical*, 118(1-2):129–134, 2006.

[279] R.A. Marcus and Norman Sutin. Electron transfers in chemistry and biology. *Biochimica et Biophysica Acta (BBA) - Reviews on Bioenergetics*, 811(3):265–322, 1985.

[280] Winkler J. R., Di Bilio Angel J., Farrow N. A., Richards J. H., and Gray H. B. Electron tunneling in biological molecules. *Pure and Applied Chemistry*, 71(9):1753–1764, 1999.

[281] Heinz-Bernhard Kraatz, Irene Bediako-Amoa, Samuel H. Gyepi-Garbrah, , and Todd C. Sutherland. Electron transfer through h-bonded peptide assemblies. *The Journal of Physical Chemistry B*, 108(52):20164–20172, 2004.

[282] Michael N. Paddon-Row. Superexchange-mediated charge separation and charge recombination in covalently linked donor-bridge-acceptor systems. *Australian Journal of Chemistry*, 56(8):729–748, 2003.

[283] J. Jortner, M. Bixon, T. Langenbacher, and M. E. Michel-Beyerle. Charge transfer and transport in dna. *Proc. Natl. Acad. Sci. U.S.A.*, 95(22):12759–12765, 1998.

[284] Tomoyuki Morita, , and Shunsaku Kimura. Long-range electron transfer over 4 nm governed by an inelastic hopping mechanism in self-assembled monolayers of helical peptides. *Journal of the American Chemical Society*, 125(29):8732–8733, 2003.

[285] Mohammad R. Seyedsayamdost, Jianming Xie, Clement T. Y. Chan, Peter G. Schultz, , and JoAnne Stubbe. Site-specific insertion of 3-aminotyrosine into subunit a2 of e. coli ribonucleotide reductase: Direct evidence for involvement of y730 and y731 in radical propagation. *Journal of the American Chemical Society*, 129(48):15060–15071, 2007.

[286] Nadav Amdursky, Gil Shalev, Amir Handelman, Simon Litsyn, Amir Natan, Yakov Roizin, Yossi Rosenwaks, Daniel Szwarcman, and Gil Rosenman. Bioorganic nanodots for non-volatile memory devices. *APL Mater.*, 1(6):062104, 2013.

[287] Senthil T. Kumar, Jessica Meinhardt, Ann-Kathrin Fuchs, Tobias Aumüler, Jörg Leppert, Berthold Büchele, Uwe Knüpfer, Ramadurai Ramachandran, Jay Kant Yadav, Erik Prell, Isabel Morgado, Oliver Ohlenschläger, Uwe Horn, Thomas Simmet, Matthias Görlach, and Marcus Fändrich. Structure and biomedical applications of amyloid oligomer nanoparticles. *ACS Nano*, 8(11):11042–11052, 2014.

[288] V. Castelletto, J. E. McKendrick, I. W. Hamley, U. Olsson, and C. Cenker. Pegylated amyloid peptide nanocontainer delivery and release system. *Langmuir*, 26(14):11624–11627, 2010.

[289] Nicholas J Anthis and G Marius Clore. Sequence-specific determination of protein and peptide concentrations by absorbance at 205 nm. *Protein Science : A Publication of the Protein Society*, 22(6):851–858, 2013.

[290] Emiko Kazuma and Tetsu Tatsuma. Localized surface plasmon resonance sensors based on wavelength-tunable spectral dips. *Nanoscale*, 6(4):2397–2405, 2014.

[291] H. Yockell-Leliévre, F. Lussier, and J.-F. Masson. Influence of the particle shape and density of self-assembled gold nanoparticle sensors on lspr and sers. *The Journal of Physical Chemistry C*, 119(51):28577–28585, 2015.

[292] Jeffrey N. Anker, W. Paige Hall, Olga Lyandres, Nilam C. Shah, Jing Zhao, and Richard P. Van Duyne. Biosensing with plasmonic nanosensors. *Nat Mater*, 7(6):442–453, 2008.

[293] Yichen Zhang, Christophe Arnold, Peter Offermans, and Jaime Gómez Rivas. Surface wave sensors based on nanometric layers of strongly absorbing materials. *Opt. Express*, 20(9):9431–9441, 2012.

[294] Katherine A. Willets and Richard P. Van Duyne. Localized surface plasmon resonance spectroscopy and sensing. *Annual Review of Physical Chemistry*, 58(1):267–297, 2007.

[295] Ron Elber. Long-timescale simulation methods. *Current Opinion in Structural Biology*, 15(2):151–156, 2005.

[296] Florian A. Herzog, Lukas Braun, Ingmar Schoen, and Viola Vogel. Improved side chain dynamics in martini simulations of protein–lipid interfaces. *Journal of Chemical Theory and Computation*, 12(5):2446–2458, 2016.

Part II

Papers

Paper A

Phys. Chem. Chem. Phys., 17, 30023-30036, 2015

PCCP

PAPER

Cite this: *Phys. Chem. Chem. Phys.*, 2015, **17**, 30023

A computational study of the self-assembly of the RFFFR peptide

Morten Slyngborg and Peter Fojan*

The β-amyloid peptide sequence, LVFFA, inspired the investigation of the fiber formation potential of the RFFFR peptide. The self-assembly was studied *in silico* by coarse grained-, atomistic molecular dynamics simulations and semi-empirical quantum mechanical calculations. The fiber formation was found to occur according to a three step process starting with the emergence of small aggregates that join together and form fiber segments that eventually form one continuous fiber. From a series of simulations the critical fiber concentration was determined to be in the interval between 70 mM and 100 mM. To obtain more structural information of the stable fiber, the final coarse grained configuration was backtransformed to atomistic detail. Based on this structure a 10 ns atomistic simulation was performed, which suggests that the fiber is stabilized by hydrogen bonds and water mediated hydrogen bonds. These stabilizing bonds are, however, reduced by competitive protein–water hydrogen bonds. Hence, π-stacking is suspected to play a larger role in fiber stabilization. The π-stacking of inter-molecular Phe residues are found to favor a T-shaped stacking mode, while intramolecular π-stacking interactions assume a broad variety of modes from the parallel displaced mode to the T-shaped stacking mode and modes in between, with equal probability. Selected snapshots from the atomistic simulation were geometry optimized using semi-empirical quantum mechanical methods to validate the fiber stability and π-stacking configuration. An average Cα-RMSD was determined to be 2.68 Å. These findings indicate that the fiber may be used as a novel model system for the study of amyloid fibers or self-assembled conductive biowires, respectively.

Received 6th March 2015,
Accepted 16th October 2015

DOI: 10.1039/c5cp01324k

www.rsc.org/pccp

1 Introduction

Self-assembled protein nanostructures have attracted much interest due to their involvement in more than 20 degenerative diseases such as Alzheimer's, Parkinson's and Prion diseases.[1,2] However, recent research has also been devoted to their applications in nanomaterial engineering, nanolithography, regenerative medicine, biosensors, and drug delivery.[3–6]

Typically these model peptides originate from larger naturally occurring peptides or proteins. One such example is the LVFFA peptide, derived from the β-amyloid peptide which then plays a crucial role in Alzheimer's disease.[7] The LVFFA peptide was later modified to the analogous diphenylalanine (FF). This peptide has been extensively studied and is known to self-assemble into a large variety of structures ranging from nanotubes,[8] nanowires,[9] films,[9,10] vertical aligned wires[10] and sponge-like structures[10] depending on pH conditions.[11] Recently, the related peptide triphenylalanine (FFF) was investigated which forms plate-like structures with lengths of several micrometers.[12] Furthermore, FFF forms nanospheres without any void space when the N-terminus is protected by a *t*-butyloxycarbonyl (*t*-Boc) group.[4]

Even though the FF and FFF peptides are derived from the core recognition motif of the Alzheimer's β-amyloid peptide it is still debated whether they share any structural properties with the amyloid fibrils.[8,12,13]

The self-assembly process is difficult to study experimentally, thus computational methods are an attractive approach to study self-assembly processes.[14] The self-assembly process typically occurs on a timescale, which is outside the obtainable timescales for atomistic molecular dynamics (MD) and Monte Carlo simulations as well. In these cases coarse grained (CG) force fields represent an appealing alternative as the total amount of atoms, in general, is reduced by one third, allowing much larger systems and timescales to be simulated. The MARTINI CG force field[15] is amongst the most well-known and versatile force fields. A number of complex molecules have been simulated, such as lipids,[15] sterols,[16] DNA,[17] sugars,[18] polymers,[19] nanoparticles,[20] proteins[21–23] as well as different solvents.[15,21,24]

The MARTINI CG force field[15] has some limitations compared to atomistic force fields. The structure of large biomolecules is not reproduced accurately over time in the standard version of the MARTINI force field.[15] Furthermore, the secondary structure

Department of Physics and Nanotechnology, Aalborg University, 9220 Aalborg St, Denmark. E-mail: fp@nano.aau.dk

This journal is © the Owner Societies 2015

has been fixed during the course of the simulation, which significantly restricts the phenomena that can be studied. Additionally, the CG simulations yield less structural information than similar atomistic simulations as some atoms are not explicitly included. The latter limitation is circumvented in some CG models by using multiscaling, where parts of the simulation are in atomistic detail while the rest is represented by a CG model.[25] Another option is to translate the final CG structure into the equivalent atomistic structure and continue the simulation for a short period. Both options have been implemented in the MARTINI model,[15] but it has been of limited use so far, due to the comprehensive workload required. However, a recent algorithm has made the implementation of the back-translation function more readily accessible.[26]

The present study investigates, for the first time, the effects of modifying the FFF peptide to the amino acid sequence RFFFR. The motivation for the modification is to direct the self-assembly process towards nano-fibers, which may better resemble amyloid fibrils than the FF or FFF structures. The arginine residues are intended to restrict the interaction of Phe residues in one direction only.

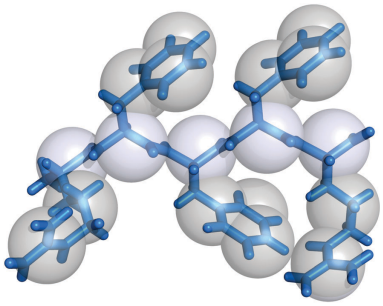

Fig. 1 Atomistic structure of the peptide (RFFFR), created in YASARA (blue) and the corresponding MARTINI structure. In the MARTINI model amino acid backbones are represented by one bead (white), while side chains of arginine and phenylalanine have two and three beads, respectively (gray).

2 Methods

The MARTINI CG force field[15] used in the present study joins in general four heavy atoms into one CG spheres/bead. Each bead is assigned the united properties of the enclosed atoms, substantially reducing the amount of interactions to be calculated. In this model, the protein backbone is represented by a single bead while the individual amino acid side chains are represented by one or more beads, depending on the amino acid. Non-bonded interactions in the MARTINI force field are parameterized from experimental data such as the partitioning free energies between amino acid side chains and the oil/water interface. The bonded interactions in the MARTINI force field are determined from the distribution of bond lengths, angles and dihedral angles derived from protein structures from the Protein Data Bank and comparison with atomistic force fields.

The initial self-assembly is simulated using the MARTINI force field[15] succeeded by a distance restrained MARTINI simulation. This final structure is back-transformed into an atomistic structure. Starting from this structure a 20 ns atomistic simulation is performed using the OPLS-aa force field.[27–29] From the atomistic simulation, structural information of the peptide and the π-stacking interaction of phenylalanine (Phe) residues have been extracted. Furthermore, a series of CG simulations are performed to determine the minimum peptide concentration necessary to form a single stable nano-fiber.

All simulations were performed using GROMACS v.4.6.[30] The initial RFFFR structure was created and geometry optimized for an extended strand structure within YASARA[31] The resulting structure was converted to a MARTINI CG peptide (Fig. 1) using the martinize.py v.2.4 script. The initial MD configuration was constructed by adding 27 CG peptides at random positions in a box with dimensions 12 nm $\times$ 5 nm $\times$ 5 nm (x, y, z). Water was then added at any sterically allowed position, amounting to 2149 MARTINI polarized water molecules. After each modification, a steepest decent minimization with 10 000 steps was used to minimize the potential energy of the system.

Using time steps of 20 fs, a 200 ns isotropic simulation was performed using the MARTINI force field v.2.2P.[15] The final configuration was used in a 100 ns continued distance restrained CG simulation where the Phe residues were locked in *trans*-configuration, since a very slow equilibration of the *cis–trans* configuration was observed. The initial velocities were adopted from the last frame of the 200 ns long CG simulation.

The final CG structure from the distance restrained simulation was converted to an atomistic structure using the Backward script.[26] Water was removed in order to center the fiber in the simulation box, after which 8517 SPC water molecules, 108 chloride ions and 54 sodium ions were added to ensure system charge neutrality. Then energy minimization was performed by a steepest decent minimization with 100 000 steps. This was followed by a 100 ps long semi-isotropic simulation using the OPLS-aa force field[27–29] to equilibrate the system. The resulting structure was used in a 10 ns long isotropic simulation performed using the OPLS-aa force field with time steps of 1 fs.

The initial velocities of the first CG and atomistic simulations were assigned a Maxwell distribution at 323 K and 300 K, respectively. During the CG simulations the temperature and pressure were kept constant at 323 K and 1.013 bar with the v-rescale[32] and Berendsen[33] algorithm, respectively. The elevated temperature was adopted in order to prevent the system from getting trapped in local conformational energy minima during self-assembly. The atomistic simulation was kept at 300 K and 1.013 bar using the Nosé–Hoover[34] and

 This journal is © the Owner Societies 2015

Parrinello–Rahman[35] algorithm, respectively. This close to room temperature was adopted as the elevated temperature was no longer needed. In both the CG and atomistic simulations periodic boundary conditions (PBC) were applied in all directions and electrostatic interactions were calculated by the particle mesh Ewald[36] (PME) algorithm with a real space cut-off at 1.5 nm in the CG simulations and 1 nm in the atomistic simulation.

Selected snapshots from the all atom simulation were geometry optimized by semi-empirical quantum mechanical (SQM) calculations using the MOPAC[37] package. The MOPAC package[37] developed by Stewart was used as the implemented module MOZYME[37] allows for the calculation of more than 1000 atoms, which is the approximate limit of standard SQM calculations. However, MOZYME[37] utilizes a localized molecular orbital method that allows for processing a system of 15 000 atoms in a very fast timescale compared to other solutions. The newest MOPAC version allows for the use of the new PM7[38] method which is additionally well known for its very high accuracy that borders DFT-D calculations.[38–40]

The OPLS-aa snapshots that were geometry optimized with PM7[38] are as follows (starting from the beginning of the OPLS-aa simulation): 2500 ps, 3750 ps, 5000 ps, 5625 ps, 6250 ps, 6875 ps, 7500 ps, 8125 ps, 8750 ps, 9375 ps and 10 000 ps. Explicit solvent from the MD snapshots was removed and solvent effects were accounted for by the COSMO implicit water model[41] with a dielectric constant of 78.4. The geometry optimization convergence criterion was set to a maximum gradient of 10.0 kcal mol^{-1} $Å^{-1}$, after which a second calculation was performed with a convergence criterion of 5.0 kcal mol^{-1} $Å^{-1}$. Finally a single SCF calculation was performed to correct any error in heat of formation.

As PBC are not possible to implement with the SQM approach, on larger systems with many charges, a second simulation series was performed. This series was performed in the same way as described above, but with frozen alpha carbon atoms of the arginine residues in the peptides constituting the ends of the fiber, enforcing the fiber to remain in a stretched configuration. This series will be denoted as the restricted PM7 calculations henceforth. As a reference a 10 ns all atom MD simulation was performed containing only four peptides in a large simulation box. Hence PBC were not important during this simulation and subsequent PM7 calculations yielded relatively low RMSD values.

Additionally, a series of CG simulations with varying peptide concentrations were performed to determine the minimum concentration at which peptides assembled into stable fibers. These simulations were all carried out with the same parameters as the non-distance restrained CG simulation. To improve validity of the results, more simulations were performed with concentrations close to the critical fiber concentration. The simulations had different initial velocities in order to cover a wider conformational space. Furthermore, the critical fiber concentration was confirmed in another MD simulation series where a stable fiber was inserted into a simulation box corresponding to the concentrations above and below the critical fiber concentration. In this way it was possible to study fiber stability or disassembly.

Simulation time of CG and atomistic simulations do not scale 1 : 1 and a direct translation is often difficult. The MARTINI time compared to atomistic time is in general scaled by a factor of 4,[16,42] but several other factors have been reported earlier.[43,44] For this reason actual simulation rather than effective time has been used throughout this paper.

3 Results and discussion

3.1 Peptide self-assembly

Snapshots of the CG self-assembly simulation at different time intervals are shown in Fig. 2a. Initially all peptides are randomly distributed in the simulation box. After 10 ns three small fiber segments with significant defects were formed. 100 ns later, these smaller fibers self-assemble into one fiber with defects at the fiber ends. After 200 ns a continuous fiber was formed that spans the entire PBC. The peptides in the fiber from the initial CG simulation were mainly found to have an antiparallel configuration where Phe-2 is located in proximity to Phe-1 and Phe-3 of a neighboring peptide (Fig. 3a). However, some peptides

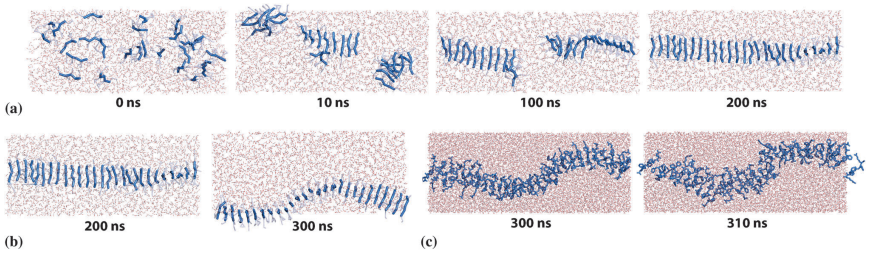

Fig. 2 Water molecules and CG side chains are made transparent for the sake of simplicity. (a) Snapshots from the initial 200 ns CG simulation where the self-assembly of the nano-fiber occurs. (b) Snapshots from the continued distance restraint 100 ns CG simulation where the *cis*-configuration of the peptide is prevented. (c) Snapshots from the 10 ns atomistic simulation.

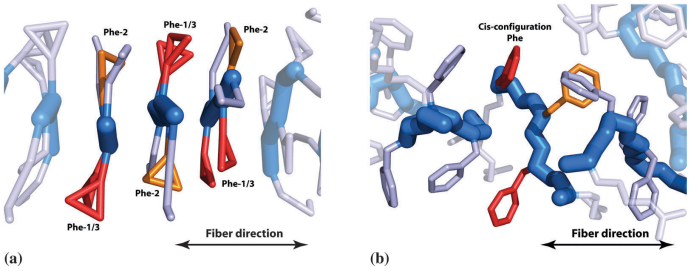

Fig. 3 Water molecules are removed in both snapshots while Phe-1 and Phe-3 residues have been highlighted in red and Phe-2 residues in orange. Hydrogen and oxygen atoms are removed in the atomistic snapshot. (a) Close-up snapshot from the initial CG simulation that illustrates the fiber configuration of three representative peptides in the CG simulations. It is apparent that peptides interact in an antiparallel mode as Phe-2 interacts with Phe-1 and Phe-3 residues of other peptides. (b) Close-up snapshot from the atomistic simulation illustrating a peptide with a Phe residue in *cis*-configuration. It is apparent that the backbone of the peptide with the *cis*-configurated Phe residue is not aligned with the residual peptides. Hence the *cis*-Phe residue is forced to assume *cis*-configuration as it is too far away to interact with any other Phe residues.

adopt a *cis*-configuration for a short period of time during the initial CG simulation. Compared to atomistic simulations of the fiber, the amount of *cis*-configurations is found to be relatively high (data not shown).

For this reason the final configuration of the 200 ns long CG simulation was used as the initial configuration for a 100 ns long distance restraint CG simulation (Fig. 2b) where the peptide *cis*-configuration was excluded. This resulted in a nearly defect free fiber where almost all peptides were oriented antiparallel.

To regain atomistic details, the final configuration of the 100 ns long distance restraint CG simulation was converted to an atomistic configuration and continued for 10 ns (Fig. 2c). During simulation, the Phe residues assume distinct orientation modes at the expense of backbone–backbone angle distribution which becomes more disperse.

3.2 The phenylalanine *cis*-configuration

The existence of *cis*-configurations in non-proline containing proteins is rather scarce.[45] However, a statistical investigation of the protein data bank reveals that the majority of *cis*-configured residues in non-proline containing proteins are involved in an interaction with an aromatic residue.[46] Hence we expect some Phe residues to assume a *cis*-configuration during the MD simulation.

Initially a high level of *cis*-peptide configurations is observed (Fig. 4). However, the amount of *cis*-configurations is reduced during the initial CG simulations, indicating that *cis*-configurations are important for the formation of small initial segments while larger fibers are more stable without the *cis*-peptide configuration.

Another indication hereof is that the continuous fiber from the distance restrained CG simulation remains stable without *cis*-peptide configuration (Fig. 4), hence they are not crucial for the stability of the fiber in the MARTINI model.[15] Furthermore, it is evident from the self-assembly that the sum of attractive intermolecular forces amounts to a larger force than the long range electrostatic repulsive forces of the N-termini of peptides

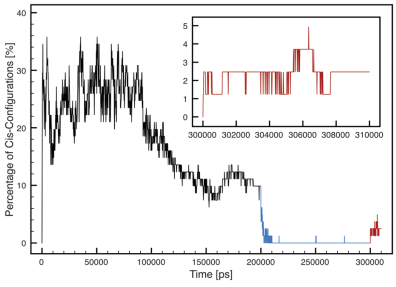

Fig. 4 Number of Phe residues in *cis*-configuration as a function of time over three simulations; initial CG simulation (black), CG simulation with distance restraints (blue) and atomistic simulation (red). For clarity a zoom-in of the atomistic simulation is depicted in the insert.

with a charge of +2. Hence it is likely that the attractive forces are also sufficiently strong to induce *cis*-configuration in naturally occurring fibers.

Indications hereof are observed in the atomistic simulation where some peptides resume *cis*-peptide configuration. This may be the result of the disperse backbone–backbone angle distribution as it causes some intermolecular Phe side chains to move apart and it becomes energetically favorable to interact with another Phe side chain in close proximity in the opposite direction (Fig. 3b). Hence *cis*-configuration increases the stability of the fiber, but the net stability is presumably reduced by the increased disperse backbone–backbone angle distribution found during atomistic simulation.

3.3 Structural clusters

During the atomistic simulation a number of peptides adopt similar molecular structures. These structures were grouped

 This journal is © the Owner Societies 2015

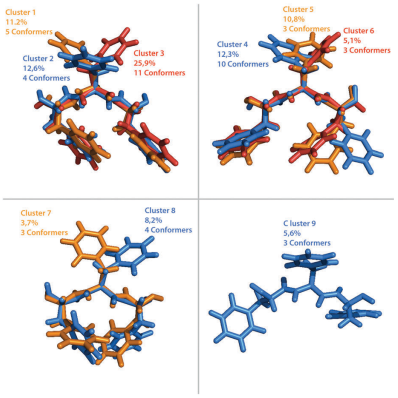

Fig. 5 Overview of the center structure of the nine clusters found during the atomistic simulation. The total occurrence and the number of conformers in each cluster are also listed.

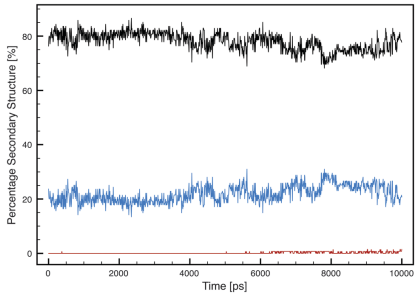

Fig. 6 The percentage random coil (black), beta-strand (blues) and alpha-helix (red) secondary structure of the peptides are assumed during the atomistic simulation as a function of time.

together in clusters based on the single linkage method.[47] According to this method a structure belongs to a certain cluster if its RMSD compared to any other molecule in the cluster is smaller than a certain cut-off value. The center structures of the clusters found during the atomistic simulation using a cut-off of 0.5 Å are shown in Fig. 5. Furthermore, the occurrence and number of conformers belonging to each cluster is also listed in Fig. 5. Structural information of Arg residues was not included in the analysis as they had a high degree of conformational freedom.

Based on the Newman projection 27 main clusters should be present. However due to the influence of neighboring peptides in the fiber, a degeneracy of peptide configuration is found, leading to the representation of only nine clusters in the stable fiber (Fig. 5). These correspond to 95.4% of the structures any given peptide adopts during the simulation. The remaining structures are special structures such as *cis*-configuration or short lived structures that peptides adopt for less than 50 ps during the simulation. It is noteworthy that nine major clusters were identified, which implies a rather strict conformational flexibility of the single peptides in the fiber. Furthermore, very few different conformers participate in the clusters. On average a single conformer participates in 1.7 different clusters, indicating that few cluster transitions occur. The two largest clusters, cluster 3 and 4, constitute together 21 different peptides, hence most peptides adopt a structure belonging to one of these clusters during the simulation.

It should be mentioned that cluster 4 is different from other clusters, as the Phe-3 residues assume different orientations. These structures were considered as one single cluster as they had a large distance between the Phe-1 and Phe-3 residues in common, rendering π-stacking interactions negligible and hence had larger Phe side chain orientation fluctuations.

3.4 Secondary structure

Usually secondary structure changes of large proteins require very long atomistic simulations in order to be reliable.[48,49] For peptides, shorter time scales are sufficient to simulate the folding of a disordered structure into a near native structure.[50,51]

During the present atomistic simulation the secondary structure did not change significantly (Fig. 6). It was found that 80% of the residues had random coil, 20% beta-strand and occasionally assumed an alpha-helix like configuration. Compared to another atomistic simulation of initially pre-assembled FF and FFF structures, a beta-strand content of below half of what was determined in the current study, was reported.[12] However, experimental studies indicate that nanostructures self-assembled from the FF or FFF peptide consist of a high degree beta-sheet.[8,12] Presumably this deviation is due to the limited simulation time and number of peptides in the simulation systems. It is likely that the same applies to the present study and a much higher amount of beta-strand content would be observed experimentally for the RFFFR peptide structures.

3.5 Hydrophobic effects and H-bonds

The hydrophobic effect is a major driving force for the association of apolar substances in aqueous solutions.[52] It can be enthalpy or entropy driven due to the exclusion of water molecules from the apolar surfaces.[53] As RFFFR consists of a hydrophilic shell and a hydrophobic core, peptide association is expected as a result of the hydrophobic effect. From the solvent accessible surface area (SASA) of the Phe residues as a function of time (Fig. 7a) it is apparent that it decreases drastically during the self-assembly and remains quite stable after equilibrium has been reached. This indicates that hydrophobic effects contribute to self-assembly. A similar tendency and conclusion were reached in a MARTINI simulation study of the FFF peptide.[54]

The stabilizing influence of hydrogen bonds in the resulting fibers has been studied by converting the CG system into

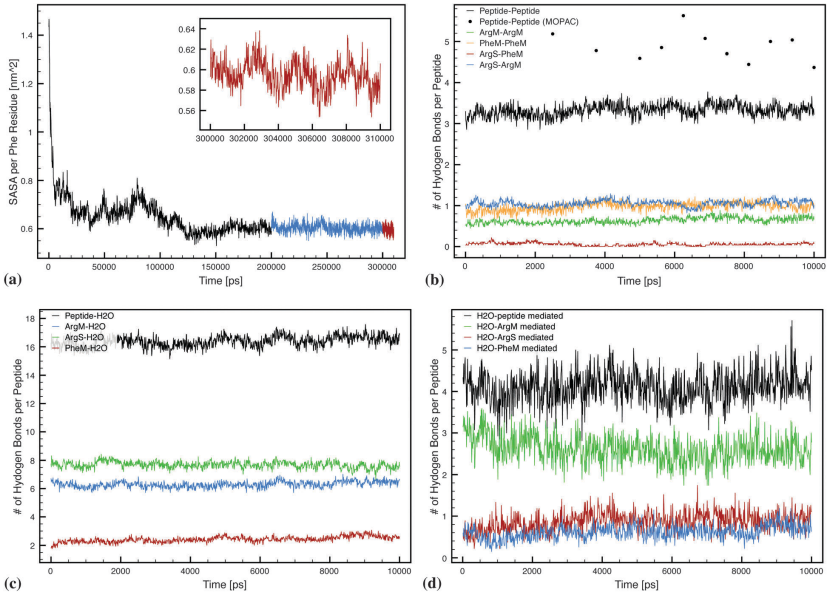

Fig. 7 Overview of the hydrophobic effect as a function of time and hydrogen bonds as a function of time. A hydrogen bond is counted if the donor–acceptor distance is less than 0.35 nm and the hydrogen-donor–acceptor angle is greater than 150° where ArgM is the Arg main chain; PheM is the Phe main chain; ArgS is the Arg side chain; PheS is the Phe side chain. (a) SASA per Phe residue as a function of time. Initial CG simulation (black), CG simulation with distance restraints (blue) and atomistic simulation (red). (b) Peptide–peptide hydrogen bonds as a function of time. (c) Water–peptide hydrogen bonds as a function of time. (d) Water mediated peptide–peptide hydrogen bonds as a function of time.

atomistic structures and performing a 10 ns MD simulation using the OPLS-aa force field. To validate the obtained results, semi-empirical quantum mechanical calculations using PM7 (Section 3.7) were compared to the OPLS-aa force field results. These simulations resulted in on an average 3.3 hydrogen bonds formed per peptide between two peptides (Fig. 7b). This is approximately 1.3 times more hydrogen bonds than what was reported for FF,[55] which leads to the conclusion that RFFFR fibers might be stabilized more by hydrogen bonds than FF structures. FF peptides form simple head (NH_3^+) to tail (COO^-) hydrogen bonds while RFFFR forms a relative elaborate network (Fig. 7b). A similar complex network was observed in another all atom simulation of FFF.[12] Concerning RFFFR, only 0.6 head to tail hydrogen bonds per peptide are formed while approximately 1 hydrogen bond is formed between the Phe main chain to the Phe main chain and the Arg side chain to the Arg main chain, respectively.

Being an amphiphile, RFFFR has more contact with water molecules than FF which forms more compact sheltered structures. For this reason a high amount of hydrogen bonds are also formed in water molecules (Fig. 7c). On average 16.4 hydrogen bonds per peptide are formed in water molecules, where hydrogen bonds to the Arg main chain and the side chain constitute by far the largest part. These bonds weaken the peptide–peptide hydrogen bonds as water competes for the hydrogen bond interaction. Furthermore, it is generally believed that supramolecular structures cannot be formed in water solely based on hydrogen bonds, on account of competitive hydrogen bond with water.[56] However, hydrophobic regions avert, to some extent, this competition and allows for the self-assembly based on hydrophobic effects and hydrogen bonds.[57,58] The Phe residues in RFFFR may induce such compartmentalization as indicated by the relatively low water hydrogen bond competition of Phe residues (Fig. 7c). This also explains why far less peptide–water hydrogen bonds (0.5 per peptide) are observed in FF simulations, due to the lack of hydrophilic residues.

However, in depth analysis of the peptide–water hydrogen bonds reveals that a large amount of these composed of peptide–water–peptide hydrogen bonds (Fig. 7d). These water mediated hydrogen bonds actually add to the stability of the fiber.[59] Each peptide forms 4.1 water mediated hydrogen bonds whereof 2.6, 0.9 and 0.6 water mediated hydrogen bonds are between the Arg main chain, theArg side chain and the Phe main chain, respectively. Hence Arg residues do not contribute

 This journal is © the Owner Societies 2015

significantly to the stability through peptide–peptide hydrogen bonds, but in return stabilizes the fiber through water mediated hydrogen bonds.

Compared to the PM7 geometry optimized structures, the total amount of peptide–peptide hydrogen bonds is consistently low (Fig. 7b). In addition to the underestimation of the hydrogen bond strength of empirical force fields,[29] this might imply that the OPLS-aa force field does not accurately account for hydrogen bonds. However, this is not expected to alter the obtained supramolecular fiber structures significantly, as indicated by the RMSD values obtained from the PM7 calculations (see Section 3.7). Hence this deviation is expected to only increase the stability of the self-assembly compared to what is observed using the OPLS-aa force field.

3.6 Phe–Phe π-stacking

Hydrogen bonds are important for stability, but π-stacking might be even more important. These interactions are believed to play an important role in a wide range of phenomena including the stereo-chemistry of organic reactions,[60] protein folding,[61,62] protein self-assembly[55,63] and DNA and RNA base-pairing.[64] High level quantum mechanical calculations indicate that π-stacking energies are comparable to hydrogen bonds.[65] Since more π-stacking interactions are observed than hydrogen bonds in the RFFFR fiber, π-stacking is expected to be the dominating stabilizing force in the resulting fiber assembly.

Standard empirical force fields, such as GROMOS, AMBER, CHARMM and OPLS-aa, account for π-stacking effects by modeling partial charges and the Lennard-Jones 12-6 potential function.[66] These force fields are rather limited by being completely devoid of any electronic structure, hence any charges are assigned to the nuclear center. Furthermore, since atomic charge is not an observable it is difficult to assign partial charges, but the force fields are parameterized to fit experimental or quantum mechanical calculated data. A recent benchmark of different force fields found that the OPLS-aa force field was amongst the most accurate force fields to account for non-bonded interactions such as π-stacking interactions.[29] Despite the underestimated hydrogen bonds the OPLS-aa force field exceeded even DFT calculations.[29] Since no partial charges are used in aromatic amino acid residues in the MARTINI force field[15] no intermolecular Phe–Phe stacking mode is dominant during the present CG simulations.

It has been suggested that a small partial charge ($< \pm 0.153$), assigned to the C and H atoms belonging to Phe benzene rings, favors the parallel displaced (PD) stacking mode, while a high partial charge ($> \pm 0.3$) favors the T-shaped stacking mode.[67] The OPLS-aa force field applies a small partial charge (± 0.115), but the PD stacking mode was not found to be the preferred stacking mode during the simulation. Our findings conform with the majority of experimental and computational studies indicating that the T-shaped mode is more stable than the PD mode in proteins.[68] However, we also observe a more complex stacking behavior concerning the interplay between intra- and intermolecular π-stacking interactions. This may well be related to findings from a statistical investigation of the protein data bank that shows that over 80% of the aromatic residues in the surveyed proteins interact with more than one π–π pair, rendering an exact stacking model difficult to formulate.[69]

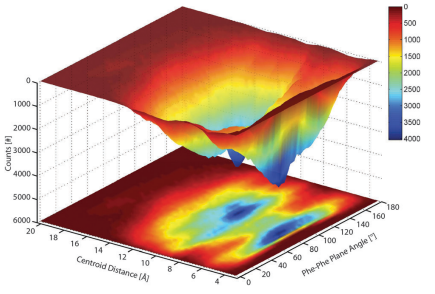

Fig. 8 Intermolecular Phe–Phe plane angles *versus* centroid distance (R_{cen}) of the atomistic simulation. Data from the first nanosecond are not included.

The intermolecular Phe–Phe plane angles from neighboring Phe residues *versus* centroid distance (R_{cen}) are illustrated in Fig. 8. Two maxima are found at Phe–Phe plane angles of 87° and 100° and Phe–Phe separations of 5.5 Å and 10 Å, respectively. Thus the T-shaped mode (60–120°) is dominant, a hybrid mode (30–60° and 120–150°) in between the T-shaped and PD mode is common while the frequency of the PD mode (0–30° and 150–180°) is low. However, it is noteworthy that the Phe–Phe plane angles of the individual Phe pairs tend to remain stable during the atomistic simulation.

From Fig. 8 it is apparent that R_{cen} may be as small as 4 Å in the PD stacking mode, while R_{cen} between two Phe benzene rings in a T-shaped stacking mode may only come as close as 4.5 Å. This phenomenon is also observed in other simulation studies of Phe stacking and is attributed to sterical hindrance.[55,62]

In the 6.8 Å $< R_{cen} <$ 8.7 Å range, the Phe–Phe plane angles are restricted to the T-shaped mode in the angle interval of 72–113°. Hence Phe ring pairs moving apart or closer need to adopt a T-shaped mode through this saddle point. The π-stacking interaction cut-off value of 7.5 Å, generally applied, is based on a statistical study of 505 non-homologous proteins from the protein data bank.[62] This cut-off value coincides with the saddle point found in the Phe–Phe interaction angle distribution plot (Fig. 8). The peptides with a Phe–Phe plane angle maximum of 100° and a separation distance of 10 Å shown in Fig. 8, preferentially adopt a perpendicular orientation towards each other. The maximum found at a separation distance of 4–5 Å, suggests a similar intermolecular π-stacking behavior of the RFFFR peptide compared to the FF and FFF peptides, as they too preferably assume T-shaped stacking modes.[12,13,54,55]

PM7 geometry optimized structures conform with these results and only minor differences were observed in population distribution over the angle interval (see Section 3.7). A very similar saddle point and the same maximum were obtained (Fig. 11).

A minor difference between minimum R_{cen} was discovered but this may be attributed to the absence of PBC. It was also observed that the propensity for Phe residues to assume a T-shape stacking mode is slightly overestimated in the OPLS-aa force field compared to PM7 calculations.

Concerning intramolecular π-stacking interactions it is found that R_{cen} between Phe-1/Phe-3 and Phe-2 internally in the peptides are larger than the cut-off length, rendering these interactions negligible (Fig. 9a). Hence the two distinct modes found in the angle distribution analysis are a consequence of the energetically favorable peptide configurations discussed previously. However, it is noteworthy that no direct transitions between the two modes are observed, indicating that a large energy barrier exists between these two different peptide configurations.

The intramolecular Phe–Phe angle distribution of Phe-1 and Phe-3 residues is found to slightly favor the PD π-stacking mode, but a quite even distribution across all three regions (0–30°, 30–60° and 60–90°) is found (Fig. 9b) which is coherent with the cluster analysis (Fig. 5). This indicates that the Phe side chains have a sufficient high flexibility to enable them to assume an intermolecular T-shaped stacking mode. Whereas intramolecular Phe residues do not favor any specific stacking mode in RFFFR, the T-shaped mode is dominant both inter- and intramolecular in FF and FFF peptide structures.[12,13,54,55] This difference arises from the design of RFFFR, as Phe residues may only interact in one direction, making it geometrically impossible for both inter- and intramolecular Phe residues to stack in the T-shaped mode. Furthermore, the intermolecular Phe residues are able to move closer than intramolecular Phe residues (evident from Fig. 8 compared to Fig. 9b). Hence π-stacking interactions are stronger for inter-molecular Phe residues compared to intramolecular Phe residues, which may explain why intramolecular Phe residues adjust their stacking mode in such a way that the intermolecular Phe residues are able to stack in a T-shaped mode.

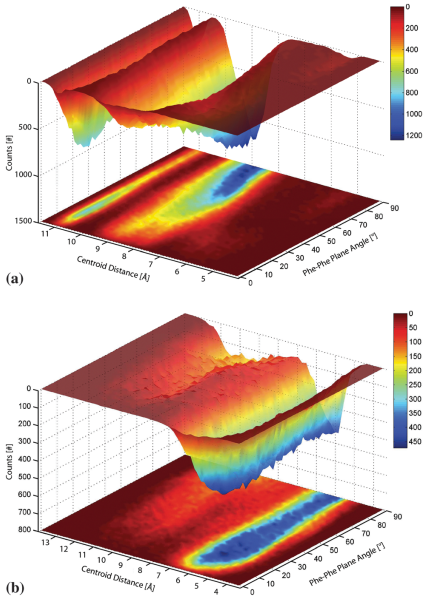

Fig. 9 Intramolecular Phe–Phe benzene angle distributions from the atomistic simulation. Data from the first nanosecond are not included. (a) Intramolecular Phe–Phe benzene angles between Phe-2 and Phe-1 or Phe-3 residues only *versus* centroid distance (R_{cen}) of the atomistic simulation. (b) Intramolecular Phe–Phe benzene angles between Phe-1 and Phe-3 residues only *versus* centroid distance (R_{cen}) of the atomistic simulation.

Within the limitations imposed to the simulations and static fixation of parameters relevant to the interactions, it is shown that intramolecular Phe–Phe stacking orientation does not contribute the stability of the fiber. Had it been the opposite case, the fiber may not have remained stable during the final atomistic simulation or the PM7 geometry optimization. However, a somewhat over exaggerated, due to the missing PBC, average Cα RMSD value of 2.68 Å was found, indicating that the two models produce relatively comparable results (see Section 3.7). Reference simulations where PBC were unimportant resulted in an average Cα RMSD value of 1.31 Å indicating the high accuracy of the OPLS-aa force field.

3.7 Semi-empirical quantum mechanical calculations

Root mean square deviation of different calculations. Since no PBC were implemented during the PM7 calculations a large structural difference was expected compared to the MD simulation snapshots calculated using the OPLS-aa force field. The PM7 calculations mimic a free fiber with a finite length in solution, while the OPLS-aa simulations mimic a continuous infinite fiber in solution. As indicated by the RMSD values (Fig. 10a), the RMSD values were found to fluctuate a lot. This fluctuation is related to the contraption and expansion of the fiber with a finite length calculated by PM7, while the continuous fiber remains maintains the same length during the MD simulation. This effect was circumvented in the restricted PM7 calculations and yielded much more stable and in general much lower RMSD values (Fig. 10b).

As a reference, four peptides in the fiber from the OPLS-aa simulation were cut out and inserted into a large simulation box (10 nm × 10 nm × 10 nm) after which the box was filled with water. This configuration was energy minimized and served as the starting point in a 10 ns long MD simulation performed using the OPLS-aa force field and the same parameters as the OPLS-aa simulations described in the paper. This small fiber segment would never interact significantly with its periodic mirror counterpart due to the large simulation box. PM7 calculations were performed on the selected snapshot of this simulation. This resulted in low RMSD values between

 This journal is © the Owner Societies 2015

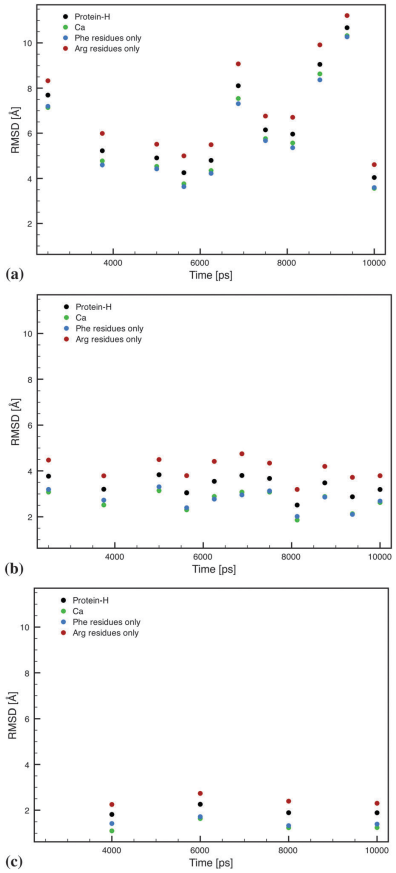

Fig. 10 Overview of the RMSD values of the OPLS-aa snapshots compared to the PM7 geometry optimized counterpart. (a) RMSD values of OPLS-aa snapshots compared to the PM7 geometry optimized snapshots. (b) RMSD values of OPLS-aa snapshots compared to the restricted PM7 geometry optimized snapshots. (c) RMSD values of OPLS-aa snapshots, from a simulation with four peptides in a big simulation box, compared to the comparable PM7 geometry optimized snapshots.

the OPLS-aa snapshots and the PM7 geometry optimized snapshots (Fig. 10c).

Comparing the RMSD values of the simulation series (Fig. 10) it is apparent that the PM7 calculations deviate a lot from the OPLS-aa calculation. However, the restricted PM7 calculations yield some low RMSD values, indicating that the large values of the PM7 calculations likely originate due to the missing PBC. Hence the Phe–Phe configuration data from the PM7 calculations apply to another situation than the one in the OPLS-aa MD simulation. The restricted PM7 calculations have an average RMSD (protein-H) value of 3.35 Å compared to the OPLS-aa calculations. As the average RMSD (protein-H) value of the reference simulation with four peptides is 1.96 Å, the restricted PM7 calculations are acceptable considering the imposed imitation of PBC.

The average Ca RMSD values of the PM7, restricted PM7 and small four peptide PM7 calculations are 5.99 Å, 2.68 Å and 1.31 Å, respectively. A CHARMM simulation study[70] of eight different proteins showed average RMSD (Ca) values (compared to the crystal structure) in the range of 1.06–3.58 Å. The same eight proteins had average RMSD (Ca) values ranging from 3.16–4.15 Å when the MARTINI force field was used.[71] Reports of RMSD values from other studies using different all-atom force fields (AMBER, CHARMM, GROMOS, OPLS-aa) range from 0.94 to 4 Å.[72,73] Considering this the obtained OPLS-aa results are in very good agreement with the restricted PM7 calculations.

Interestingly, the Phe residues obtain the lowest RMSD values of all the analyzed groups (Fig. 10). Only the Ca group from the calculations of the small simulation consisting of four peptides obtain a lower RMSD than the Phe residue groups. Hence the OPLS-aa Phe configurations are in very good agreement with the configurations obtained by PM7. The RMSD values of the Ca atoms are only marginally higher than the RMSD values for Phe residues, which means that the secondary structure is not expected to be significantly different. In all simulation series, arginine residues yield the highest RMSD value, which is not surprising as this group is the most flexible group. It could also be an indication of a discrepancy between the two water models used, as implicit solvent was used in the PM7 calculations while explicit solvent was used in the OPLS-aa calculations.

Intermolecular Phe–Phe plane angle distribution. It is noteworthy that the intermolecular Phe–Phe plane angle distributions in Fig. 11, were calculated based on all Phe–Phe interactions within 1.4 nm. Hence the results are not directly comparable to Fig. 8, where only the Phe–Phe interactions of neighbor peptides were included in the analysis.

From Fig. 11, it is apparent that Phe residues preferably stack in the T-shaped mode in both the PM7 calculation series and the OPLS-aa calculations. Furthermore, all calculations result in a saddle-point at approximately 7 Å that is close to the before mentioned limit (7.5 Å) where Phe–Phe stacking is pertinent. Hence both methods are equally accurate in determining the cut-off value, even when simulated under different conditions. The small discrepancy between the experimental value and the simulated one might be explained by the fact that 7.5 Å was determined from an investigation of the protein data bank.[62] Hence the analysis was based on intramolecular interactions rather than intermolecular interactions, which is the case in this study.

Overall the surface-shapes are very comparable with only few discrepancies. In the R_{cen} area where Phe–Phe stacking is

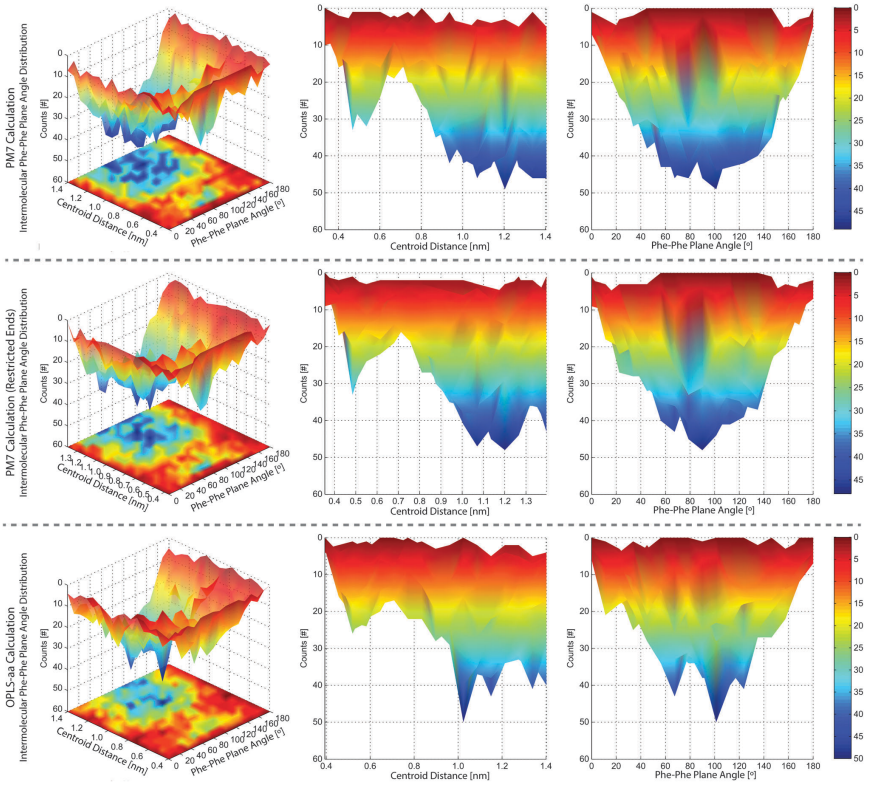

Fig. 11 Intermolecular Phe–Phe plane angle distributions *versus* centroid distance (R_{cen}) determined from PM7, restricted PM7 and OPLS-aa calculations of selected snapshots from a 10 ns long MD simulations performed using the OPLS-aa force field. π–π stacking with a R_{cen} of above 7.5 Å is negligible, hence maxima above this distance yield information of the peptide configurations rather than π–π stacking.

pertinent (R_{cen} < 7.5 Å), it is apparent that the Phe side-chains may approach each other more in both PM7 calculation series than in the OPLS-aa calculations. From the PM7 calculations the closest observed R_{cen} was 3.41 Å, in the restricted PM7 calculations the smallest observed R_{cen} was 3.58 Å, while it was 3.97 Å during the OPLS-aa calculations. A similar tendency is observed for Phe residues that stack in a T-shape mode, though they in general are farther apart by a small measure, due to steric hindrance (Fig. 11). It is likely that this difference is related to the absence of PBC in the PM7 calculations, however it does not explain the discrepancy between the restricted PM7 calculations and the OPLS-aa calculations. Hence a minor inconsistency might be introduced by the OPLS-aa force field compared to the PM7 method.

In the range 0 Å < R_{cen} < 7.0 Å of the Phe–Phe plane angle distribution, a more narrow distinct local maximum is observed for both PM7 calculation series compared to the OPLS-aa calculations (Fig. 11). However, a larger population of Phe–Phe residues are found to be in a T-shaped stacking mode in the OPLS-aa calculations (Table 1). Though the restrictive angle range of the T-shaped mode in the PM7 calculations seems rather imposed, Table 1 might imply that the propensity for Phe residues to stack in a T-shaped mode might be slightly exaggerated in the OPLS-aa force field.

Above R_{cen} where Phe–Phe stacking is pertinent, the Phe–Phe plane angle distribution populates a slightly broader angle range in the PM7 calculations compared to the restricted PM7 calculations and even more so, compared to the OPLS-aa

 This journal is © the Owner Societies 2015

Table 1 Overview of the percentage population of three stacking modes, parallel, semi-parallel and T-shaped found from the calculation series performed using PM7, restricted PM7 and OPLS-aa of the selected snapshots. The population is only determined for intermolecular Phe pairs with a R_{cen} less than 7 Å

0 Å < R_{cen} < 7.0 Å	PM7 (%)	Restricted PM7 (%)	OPLS-aa (%)
Parallel stacking mode	18.1	18.6	20.1
Hybrid stacking mode	33.7	35.4	20.4
T-shaped stacking mode	48.2	46.0	59.5

Table 2 Overview of the percentage population of three stacking modes, parallel, semi-parallel and T-shaped found from the calculation series performed using PM7, restricted PM7 and OPLS-aa of the selected snapshots. The population is only determined for intermolecular Phe pairs with a R_{cen} greater than 7 Å and less than 14 Å

7 Å < R_{cen} < 14.0 Å	PM7 (%)	Restricted PM7 (%)	OPLS-aa (%)
Parallel stacking mode	14.6	13.3	14.0
Hybrid stacking mode	37.7	37.5	34.6
T-shaped stacking mode	47.7	49.2	51.4

calculations (Table 2). This may be related to the absence of PBC in the PM7 calculations or an effect from the potential energy surface related to the specific force fields. However, the models conform rather well, which is an indication of the similarity in the peptide configurations rather than a similar π stacking configuration.

Intramolecular Phe–Phe plane angle distribution. The intramolecular Phe–Phe plane angle distributions in Fig. 12 were calculated using the same method as in Fig. 9. Hence the results are directly comparable, but for simplicity and to ensure that the observed PM7 results are not a consequence of selecting specific snapshots, the analysis was also conducted on the same OPLS-aa snapshots.

As was the case with the thorough investigation in Fig. 9, the amount of Phe–Phe interaction in the range where π–π stacking is pertinent is very low compared to the amount of interactions above this range. The data set in Fig. 12 is too low to obtain a detailed overview of the Phe–Phe plane angle distribution in the range within 0–7.5 Å. However, some minor peaks appear all over the angle range (0–90°), indicating that no preferable stacking mode exists in the R_{cen} range of 0–7.5 Å. In all calculations the minor peaks are centered on approximately 6 Å.

Above R_{cen} where π–π stacking is pertinent the Phe residues preferably stack in a T-shaped mode with a R_{cen} of approximately 9 Å in all calculations. However, in Fig. 9 a larger population of Phe pairs was found to stack in a parallel mode with a separation of 11 Å. This configuration is eliminated during PM7 global geometry optimization, while it appears in both the restricted PM7 and OPLS-aa calculation series. As was the case in Fig. 9, this mode is very restricted to a Phe–Phe separation of 11 Å in the restricted PM7 and OPLS-aa calculation with very little R_{cen} flexibility and a few transition possibilities. Due to the absence of this configuration in the PM7 calculation series, it is likely that the configuration is linked to a stretched fiber. This seems likely, as Phe residues in a peptide in a stretched fiber would need to spread wider (a larger intermolecular Phe pair separation would make the interactions negligible). Furthermore, it is know from Fig. 9 that this configuration originates from Phe-2 in relation to Phe-1 and Phe-3 and not from Phe-1 in relation to Phe-3. Hence the Phe residues in the configuration point in the opposite directions and would yield a wider peptide.

Contrary to the analysis in Fig. 9, no favored stacking mode is observed at a R_{cen} of 11 Å. It is possible that this is due to the limited data-set or it could be a random consequence of the selected snapshots missing this configuration. However, it is noteworthy that an extra major local maximum is observed in the restricted PM7 calculation series with an Phe–Phe plane angle of 22° and a R_{cen} of 9 Å. This maximum was not observed in any other analysis. The origin of this mode is unknown but it is possible that it is the missing maximum at 20° and a R_{cen} of 11 Å from Fig. 9a, which has shifted by allowing the Phe–Phe pairs to move closer. However the mode is very distinct and seems very restrictive indicating a very fixed peptide configuration.

3.8 Critical fiber concentration

The critical fiber concentration of RFFFR was determined from a series of self-assembly MD simulations. Starting with randomly positioned peptides a number of simulations with the same amount of peptides, but at different concentrations, were performed to monitor if fibers or smaller segments thereof were formed. Several factors such as pH, temperature and the simulation system size also influence the critical fiber concentration, which is not investigated in the present study.

An overview of the performed simulations is given in Table 3. The simulations with peptide concentrations of 120 mM and 170 mM resulted in continuous fibers rapidly.

At a peptide concentration of 100 mM, the peptides assembled into fiber segments and in some cases a single fiber with disconnected ends was formed. As it might have been a matter of time before these fibers assembled into one continuous fiber, the simulations were extended to 1 μs, after which continuous fibers assembled in 2 out of 7 simulations. The extended timescale and the low ratio of simulations, where fibers assemble, indicate that 100 mM is close to the critical fiber concentration.

The simulations with a peptide concentration of 70 mM and 20 mM did not form single or continuous fibers, not even on a 1 μs timescale. Instead the peptides assembled into many small fiber or micelle like structures, indicating that these are below the critical fiber concentration. Hence it is likely that under these simulation conditions the critical fiber concentration of RFFFR is between 70 mM and 100 mM.

To verify the results an additional series of simulations was performed where the single continuous fiber from the simulation of the peptide concentration 120 mM was inserted into a larger simulation box yielding a peptide concentration of 100 mM and 70 mM. An overview of these simulations is illustrated in Table 4.

It is apparent that the fiber remains stable in all simulations at 100 mM peptide concentration but disassembles in all

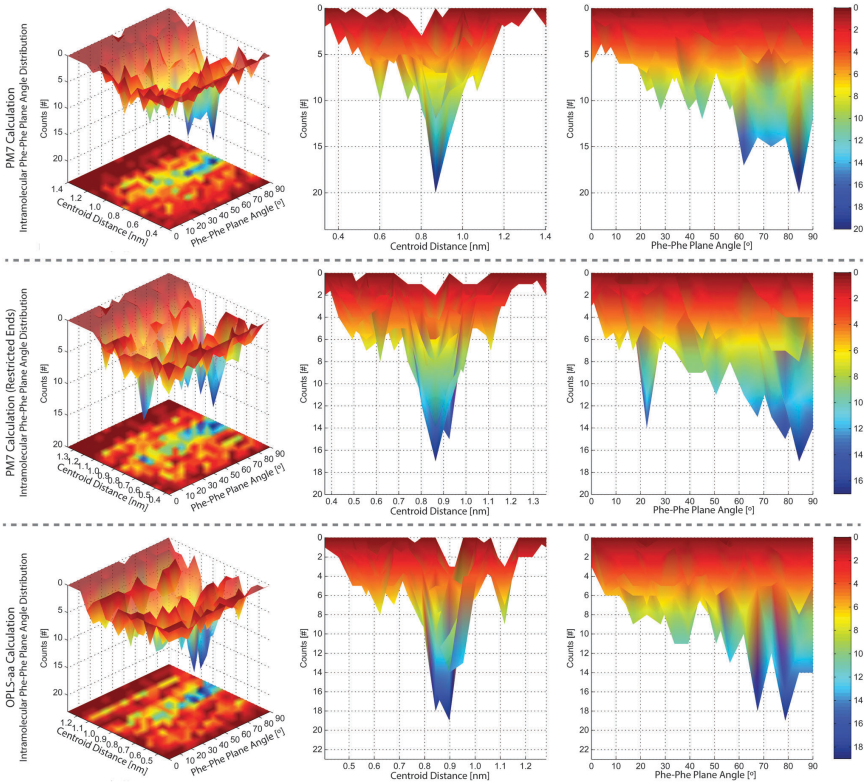

Fig. 12 Intramolecular Phe–Phe plane angle distributions *versus* centroid distance (R_{cen}) determined from PM7, restricted PM7 and OPLS-aa calculations of selected snapshots from a 10 ns long MD simulations performed using the OPLS-aa force field. π–π stacking with a R_{cen} of above 7.5 Å is negligible, hence maxima above this distance yield information of the peptide configurations rather than π–π stacking.

Table 3 Overview of simulations performed to investigate at what peptide concentrations fibers self-assemble from initial randomly positioned peptides. All simulations contain the same amount of peptides

Concentration (mM)	Fibers/simulations	Durations (ns)
170	1/1	200
120	1/1	200
100	2/7	1000
70	0/5	1000
20	0/1	200

Table 4 Overview of simulations performed where the single continuous fiber from the simulation with 120 mM was inserted into bigger simulation boxes in order to verify that the critical fiber concentration is between 70 mM and 100 mM

Concentration (mM)	Fiber remained stable	Durations (ns)
100	5/5	200
70	0/5	200

simulations at 70 mM peptide concentration. Hence these results are coherent with the conclusion from the self-assembly simulation series and the critical fiber concentration is found to be in between 70 mM and 100 mM.

4 Conclusions

The RFFFR peptide was designed to form nano-fibers and the self-assembly potential has been investigated through a combination of CG-, atomistic MD simulations and semi-empirical

 This journal is © the Owner Societies 2015

quantum mechanical calculations. Arg residues were designed to restrict the interactions of Phe–Phe in one direction and ensure solubility. Thereby the self-assembly of the peptide preferred fiber formation over random aggregation as has been reported for FF and FFF peptides.[4,9–12]

Above a critical fiber concentration determined to be in the interval of 70–100 mM, the peptides assemble into fibers according to a three-step process. Initially randomly dispersed peptides aggregate into small clusters, as these grow larger, they assume small fiber segment structures. These small fibers grow into one large fiber spanning the PBC.

Hydrophobic effects might play an important role in the self-assembly and the final fiber is found to be stabilized by a large amount of intermolecular and water mediated hydrogen bonds. However, the amount is rather underestimated compared to semi-empirical quantum mechanical calculations, indicating that hydrogen bonds might play an even larger role.

π-Stacking interactions between Phe residues are also found to be important for the self-assembly process. Intermolecular Phe residues favorably stack in a distinct T-shaped mode, while intramolecular Phe residues, within the range where π-stacking is pertinent, are found to stack in no distinct mode. Semi-empirical quantum mechanical calculations verified these results with only minor differences between the OPLS-aa and PM7 calculations. Among the most significant deviations were a slightly increased propensity for Phe residues to assume T-shaped stacking modes.

As π-stacking has been proven to promote amyloid formation and is believed to be the most important factor, the RFFFR peptide has proven to be a novel suitable model system for investigation of the formation, stability and disassembly of amyloids as well.[74–77] Furthermore, the structure formed by RFFFR has unique properties that can be exploited in other applications such as biological nanowires with conductive properties facilitated through charge transport between overlapping delocalized aromatic π-orbitals as well.

References

1 G. Bhak, Y. Choe and S. R. Paik, *BMB Rep.*, 2009, **42**, 541–551.
2 M. Stefani and C. M. Dobson, *J. Mol. Med.*, 2003, **81**, 678–699.
3 E. Gazit, *Chem. Soc. Rev.*, 2007, **36**, 1263–1269.
4 T. H. Han, T. Ok, J. Kim, D. O. Shin, H. Ihee, H.-S. Lee and S. O. Kim, *Small*, 2003, **6**, 945–951.
5 L. Liu, K. Busuttil, S. Zhang, Y. Yang, C. Wang, F. Besenbachera and M. Dong, *Phys. Chem. Chem. Phys.*, 2011, **13**, 17435–17444.
6 J. V. González-Aramundiz, M. V. Lozano, A. Sousa-Herves, E. Fernandez-Megia and N. Csaba, *Expert Opin. Drug Delivery*, 2012, **9**, 183–201.
7 C. Sotoa, M. S. Kindyc, M. Baumannb and B. Frangione, *Biochem. Biophys. Res. Commun.*, 1996, **226**, 672–680.
8 M. Reches and E. Gazit, *Science*, 2003, **300**, 625–627.
9 T. H. Han, W. J. Lee, D. H. Lee, J. E. Kim, E.-Y. Choi and S. O. Kim, *Adv. Mater.*, 2010, **22**, 2060–2064.
10 M. Hashemi, P. Fojan and L. Gurevich, *J. Self-Assem. Mol. Electron.*, 2013, **1**, 195–208.
11 X. Yan, P. Zhu and J. Li, *Chem. Soc. Rev.*, 2010, **39**, 1877–1890.
12 P. Tamamis, L. Adler-Abramovich, M. Reches, K. Marshall, P. Sikorski, L. Serpell and E. Gazit, *Biophys. J.*, 2009, **96**, 5020–5029.
13 C. H. Görbitz, *Chem. – Eur. J.*, 2001, **7**, 5153–5159.
14 N. Thota, Z. Luo, Z. Hu and J. Jiang, *J. Phys. Chem. B*, 2013, **117**, 9690–9698.
15 S. J. Marrink, A. H. de Vries and A. E. Mark, *J. Phys. Chem. B*, 2004, **108**, 750–760.
16 S. J. Marrink, H. J. Risselada, S. Yefimov, D. P. Tieleman and A. H. de Vries, *J. Phys. Chem. B*, 2007, **111**, 7812–7824.
17 J. Corsi, R. W. Hawtin, O. Ces, G. S. Attard and S. Khalid, *Langmuir*, 2010, **26**, 12119–12125.
18 C. A. López, A. J. Rzepiela, A. H. de Vries, L. Dijkhuizen, P. H. Hünenberger and S. J. Marrink, *J. Chem. Theory Comput.*, 2009, **5**, 3195–3210.
19 H. Lee, A. H. de Vries, S. J. Marrink and R. W. Pastor, *J. Phys. Chem. B*, 2009, **113**, 13186–13194.
20 J. Wong-Ekkabut, S. Baoukina, W. Triampo, I.-M. Tang, P. D. Tieleman and L. Monticelli, *Nat. Nanotechnol.*, 2008, **3**, 363–368.
21 S. J. Marrink and D. P. Tieleman, *Chem. Soc. Rev.*, 2013, **42**, 6801–6822.
22 J. Sørensen, X. Periole, K. K. Skeby, S. J. Marrink and B. Schiøtt, *J. Phys. Chem. Lett.*, 2011, **2**, 2385–2390.
23 M. Baaden and S. J. Marrink, *Curr. Opin. Struct. Biol.*, 2013, **23**, 878–886.
24 K. Prasitnok and M. R. Wilson, *Phys. Chem. Chem. Phys.*, 2013, **15**, 17093–17104.
25 A. J. Rzepiela, M. Louhivuori, C. Peter and S. J. Marrink, *Phys. Chem. Chem. Phys.*, 2011, **13**, 10437–10448.
26 T. A. Wassenaar, K. Pluhackova, R. A. Böckmann, S. J. Marrink and D. P. Tieleman, *J. Chem. Theory Comput.*, 2014, **10**, 676–690.
27 W. L. Jorgensen and J. Tirado-Rives, *J. Am. Chem. Soc.*, 1988, **110**, 1657–1666.
28 G. A. Kaminski and R. A. Friesner, *J. Phys. Chem. B*, 2001, **105**, 6474–6487.
29 R. S. Paton and J. M. Goodman, *J. Chem. Inf. Model.*, 2009, **49**, 944–955.
30 S. Pronk, S. Páll, R. Schulz, P. Larsson, P. Bjelkmar, R. Apostolov, M. R. Shirts, J. C. Smith, P. M. Kasson, D. van der Spoel, B. Hess and E. Lindahl, *Bioinformatics*, 2013, **29**, 845–854.
31 E. Krieger, G. Koraimann and G. Vriend, *Proteins: Struct., Funct., Bioinf.*, 2002, **47**, 393–402.
32 G. Bussi, D. Donadio and M. Parrinello, *J. Chem. Phys.*, 2007, **126**, DOI: 10.1063/1.2408420.
33 H. J. C. Berendsen, J. P. M. Postma, W. F. van Gunsteren, A. DiNola and J. R. Haak, *J. Chem. Phys.*, 1984, **81**, 3684–3690.
34 A. Cheng and K. M. Merz, *J. Phys. Chem.*, 1996, **100**, 1927–1937.

35 M. Parrinello and A. Rahman, *J. Appl. Phys.*, 1981, **52**, 7182–7190.
36 U. Essmann, L. Perera, M. L. Berkowitz, T. Darden, H. Lee and L. G. Pedersen, *J. Chem. Phys.*, 1995, **103**, 8577–8593.
37 J. J. P. Stewart, *MOPAC*, 2012, http://openmopac.net.
38 J. J. P. Stewart, *J. Mol. Model.*, 2013, **19**, 1–32.
39 M. Korth, M. Pitoáňk, J. Řezáč and P. Hobza, *J. Chem. Theory Comput.*, 2010, **6**, 344–352.
40 N. D. Yilmazer and M. Korth, *Comput. Struct. Biotechnol. J.*, 2015, **13**, 169–175.
41 A. Klamt and G. Schuurmann, *J. Chem. Soc., Perkin Trans. 2*, 1993, 799–805.
42 D. V. D. Spoel, E. Lindahl, B. Hess, G. Groenhof, A. E. Mark and H. J. C. Berendsen, *J. Comput. Chem.*, 2005, **26**, 1701–1718.
43 R. Baron, A. H. de Vries, P. H. Hnenberger and W. F. van Gunsteren, *J. Phys. Chem. B*, 2006, **110**, 8464–8473.
44 R. Baron, A. H. de Vries, P. H. Hnenberger and W. F. van Gunsteren, *J. Phys. Chem. B*, 2006, **110**, 15602–15614.
45 G. Ramachandran and A. K. Mitra, *J. Mol. Biol.*, 1976, **107**, 85–92.
46 A. Jabs, M. S. Weiss and R. Hilgenfeld, *J. Mol. Biol.*, 1999, **286**, 291–304.
47 R. Sibson, *Comput. J.*, 1973, **16**, 30–34.
48 D. E. Shaw, P. Maragakis, K. Lindorff-Larsen, S. Piana, R. O. Dror, M. P. Eastwood, J. A. Bank, J. M. Jumper, J. K. Salmon, Y. Shan and W. Wriggers, *Science*, 2010, **330**, 341–346.
49 P. L. Freddolino, F. Liu, M. Gruebele and K. Schulten, *Biophys. J.*, 2008, **94**, L75–L77.
50 S. Chowdhury, M. C. Lee, G. Xiong and Y. Duan, *J. Mol. Biol.*, 2003, **327**, 711–717.
51 C. Simmerling, B. Strockbine and A. E. Roitberg, *J. Am. Chem. Soc.*, 2002, **124**, 11256–11259.
52 D. Chandler, *Nature*, 2005, **437**, 640–647.
53 A. Biela, N. N. Nasief, M. Betz, A. Heine, D. Hangauer and G. Klebe, *Angew. Chem., Int. Ed.*, 2013, **52**, 1822–1828.
54 C. Guo, Y. Luo, R. Zhou and G. Wei, *Nanoscale*, 2014, **6**, 2800–2811.
55 C. Guo, Y. Luo, R. Zhou and G. Wei, *ACS Nano*, 2012, **6**, 3907–3918.
56 *An Introduction to Hydrogen Bonding*, ed. G. Jeffrey, Oxford University Press, Oxford, 1997.
57 *Prediction of Protein Structure and the Principles of Protein Conformation*, ed. G. Fasman, Plenum, New York, 1990.
58 H. Fenniri, P. Mathivanan, K. L. Vidale, D. M. Sherman, K. Hallenga, K. V. Wood and J. G. Stowell, *J. Am. Chem. Soc.*, 2001, **123**, 3854–3855.
59 D. Xu, C. J. Tsai and R. Nussinov, *Protein Eng.*, 1997, **10**, 999–1012.
60 D. A. Evans, K. T. Chapman, D. T. Hung and A. T. Kawaguchi, *Angew. Chem., Int. Ed. Engl.*, 1987, **26**, 1184–1186.
61 J. Vondrek, L. Bendov, V. Klusk and P. Hobza, *J. Am. Chem. Soc.*, 2005, **127**, 2615–2619.
62 G. B. McGaughey, M. Gagné and A. K. Rappé, *J. Biol. Chem.*, 1998, **273**, 15458–15463.
63 D. Ranganathan, V. Haridas, R. Gilardi and I. L. Karle, *J. Am. Chem. Soc.*, 1998, **120**, 10793–10800.
64 C. A. Hunter, *Philos. Trans. R. Soc., A*, 1993, **345**, 77–85.
65 P. Jureka and P. Hobza, *J. Am. Chem. Soc.*, 2003, **125**, 15608–15613.
66 G. Chessari, C. A. Hunter, C. M. R. Low, M. J. Packer, J. G. Vinter and C. Zonta, *Chem. – Eur. J.*, 2002, **8**, 2860–2867.
67 S. Sun and E. R. Bernstein, *J. Phys. Chem.*, 1996, **100**, 13348–13366.
68 C. Chipot, R. Jaffe, B. Maigret, D. A. Pearlman and P. A. Kollman, *J. Am. Chem. Soc.*, 1996, **118**, 11217–11224.
69 S. K. Burley and G. A. Petsko, *Science*, 1985, **229**, 23–28.
70 M. Feig, *J. Chem. Theory Comput.*, 2008, **4**, 1555–1564.
71 J. Gu, F. Bai, H. Li and X. Wang, *Int. J. Mol. Sci.*, 2012, **13**, 14451–14469.
72 D. J. Price and C. L. Brooks, *J. Comput. Chem.*, 2002, **23**, 1045–1057.
73 R. Ligabue-Braun, L. Guimarães Sachett, L. Pol-Fachin and H. Verli, *PLoS ONE*, 2015, **10**, DOI: 10.1371/journal.pone.0132311.
74 E. Gazit, *FEBS J.*, 2005, **272**, 5971–5978.
75 D. Zanuy and R. Nussinov, *J. Mol. Biol.*, 2003, **329**, 565–584.
76 A. Caflisch, *Curr. Opin. Chem. Biol.*, 2006, **10**, 437–444.
77 A. P. Pawara, K. F. DuBay, J. Zurdo, F. Chiti, M. Vendruscolo and C. M. Dobson, *J. Mol. Biol.*, 2005, **350**, 379–392.

 This journal is © the Owner Societies 2015

Paper B

Beilstein Journal of Nanotechnology, 7, 914-925, 2016

BEILSTEIN JOURNAL OF NANOTECHNOLOGY

Large-scale fabrication of achiral plasmonic metamaterials with giant chiroptical response

Morten Slyngborg, Yao-Chung Tsao and Peter Fojan*

Full Research Paper

Open Access

Address:
Department of Physics and Nanotechnology, Aalborg University, Skjernvej 4A, 9220 Aalborg East, Denmark

Email:
Peter Fojan* - fp@nano.aau.dk

* Corresponding author

Keywords:
biomolecule sensing; extrinsic chiral metamaterials; scalable fabrication

Beilstein J. Nanotechnol. **2016,** *7,* 914–925.
doi:10.3762/bjnano.7.83

Received: 01 April 2016
Accepted: 09 June 2016
Published: 24 June 2016

Associate Editor: A. J. Meixner

© 2016 Slyngborg et al.; licensee Beilstein-Institut.
License and terms: see end of document.

Abstract

A variety of extrinsic chiral metamaterials were fabricated by a combination of self-ordering anodic oxidation of aluminum foil, nanoimprint lithography and glancing angle deposition. All of these techniques are scalable and pose a significant improvement to standard metamaterial fabrication techniques. Different interpore distances and glancing angle depositions enable the plasmonic resonance wavelength to be tunable in the range from UVA to IR. These extrinsic chiral metamaterials only exhibit significant chiroptical response at non-normal angles of incidence. This intrinsic property enables the probing of both enantoimeric structures on the same sample, by inverting the tilt of the sample relative to the normal angle. In biosensor applications this allows for more precise, cheap and commercialized devices. As a proof of concept two different molecules were used to probe the sensitivity of the metamaterials. These proved the applicability to sense proteins through non-specific adsorption on the metamaterial surface or through functionalized surfaces to increase the sensing sensitivity. Besides increasing the sensing sensitivity, these metamaterials may also be commercialized and find applications in surface-enhanced IR spectroscopy, terahertz generation and terahertz circular dichroism spectroscopy.

Introduction

In recent years metamaterials have attracted a tremendous amount of attention owing to their unique properties enabling the fabrication and design of devices hitherto impossible. These properties have found implementations in various fields such as optics [1], improved photovoltaic devices [2], electronics [3], surface-enhanced infrared spectroscopy [4], Raman spectroscopy [5] and biosensors [6].

Planar chiral metamaterials (PCMs) have also attracted attention because of their negative refractive index [7,8] and optical activity [9] such as circular dichroism (CD) [10]. Among other things, this makes them useful for the production of sensing devices for organic molecules and biomolecules [10]. Recently, the phenomena of the long proposed extrinsic chirality dating back to 1945 [11] have been observed experimentally with ma-

terials that are achiral [12]. These extrinsic chiral metamaterials (ECMs) demonstrate CD responses that are orders of magnitudes larger than their PCM counterpart [12]. ECMs typically consist of achiral subwavelength hole arrays where the chiroptical response originates from a large area excitation of surface plasmon polariton (SPP) waves. Compared to the localized surface plasmon resonance from PCMs, SPP waves from ECMs are extremely sensitive to the angle of incidence and less sensitive to structural imperfections [13]. Furthermore, ECMs are defined by having a zero response angle, which is the angle where the ECMs exhibit mirror symmetry and hence do not yield a CD response. Though some PCMs show promise as they also yield huge CD responses through FANO resonance [14], the greatest advantage of ECMs is that sensing of biomolecules can be performed with only one sample in one experiment by inverting the tilt of the sample, whereas PCMs requires one samples of both enatiomeric structures and independent experiments with both samples.

To date, only very few different ECMs other than hole arrays [13,15,16] and the original suggested U-shaped and split ring structures [12], have been investigated. These have been thoroughly studied [17-20] and other structures including theoretical suggestions are limited to plasma sphere arrays [21], gold dot arrays [22], gold square arrays [23], metal disk arrays [24], two layer hole arrays [25], polystyrene sphere templates for gold deposition [26] and structures formed by carbon nanotubes [27].

However, in order to be able to apply these metamaterials in sensing devices of organic molecules and biomolecules a reliable large-area fabrication method is required. State-of-the-art fabrication techniques are based on electron beam lithography or focused ion beam milling, which both are expensive and time consuming methods. Large-scale fabrication of PCMs have been attempted to some degree applying different approaches such as glancing angle deposition [28], scaffold ornamentation [29,30], individual chiral nanoparticles [31], preassembled nanoparticles [32-34] and a variety of colloidal nanolithography techniques [35-37]. Compared to the above mentioned PCMs, the experimentally proven ECMs only comprise structures from polystyrene sphere templates for gold deposition [26], structures formed by carbon nanotubes [27] and larger U-shaped structures by nanoimprint lithography (NIL) [38] which have been scalably fabricated.

In the present work we present a novel route towards the large-scale fabrication of ECMs and metamaterials in general. These structures have never been reported before and add to the scarce amount of experimentally investigated ECMs. Our fabrication approach is based on a two-step thermal NIL process with subsequent glancing angle metal deposition. The master mold for the NIL was fabricated by anodic oxidation of an aluminum (Al) substrate, which has been demonstrated previously [39,40]. During this process a disordered honeycomb structure is formed in the substrate. By controlling different parameters the interpore distance has been varied. ECMs with different interpore distance were investigated with CD spectroscopy and scanning electron microscopy (SEM). Furthermore, by altering the interpore distance and the glancing angle for metal deposition it was possible to tune the obtained CD signals from UV all the way to IR wavelengths. As a proof of concept, the resonance shifts of SPPs were studied upon interactions between a protein or a chiral organic molecule and the ECM surface.

Results and Discussion

The ECM fabrication process is illustrated schematically in Figure 1. The original mold was fabricated by a self-ordering anodic oxidation of Al foils as described in a previous study [39]. In this process pores are produced in the Al surface with a honeycomb structure. However, the pattern is not perfect and several types of defects are present, which are inevitably transferred to the final ECMs. By applying different acids and voltages in the anodic oxidation process, original molds with three different interpore distances (300, 430 and 600 nm) have been prepared as previously described [40]. These served as master molds in the following NIL process (Figure 2a).

The first imprints were cast in TOPAS polymer substrates. After de-molding the TOPAS structures were sputter-coated with a thin Al film and subsequently an anti-stick monolayer was applied to produce negative molds (Figure 2b). The negative molds were then cast in PMMA polymer substrates (Figure 2c). The honeycomb pattern in the PMMA substrates served as the starting structure of the glancing angle deposition of Au films. By varying the deposition angle (50, 60 and 70°), three different samples have been fabricated for each honeycomb interpore distance (Figure 2d–f).

In total, nine different samples have been prepared, each covering approximately 3 cm^2, together with three reference samples of a deposition angle of 0°. Figure 3a shows a photograph of the samples prepared at a deposition angle of 60°, the samples with 600 nm interpore distance show good diffraction (Figure 3b) while the samples with 430 nm interpore distance show moderate blue diffraction and the samples with 300 nm show no diffraction. However, the size of the samples are only limited by the size of the original molds, which were fabricated by another scalable technique, but the size of the samples was chosen to be compatible with commercial dismantled cuvettes and only a small area of the sample are probed at any given time.

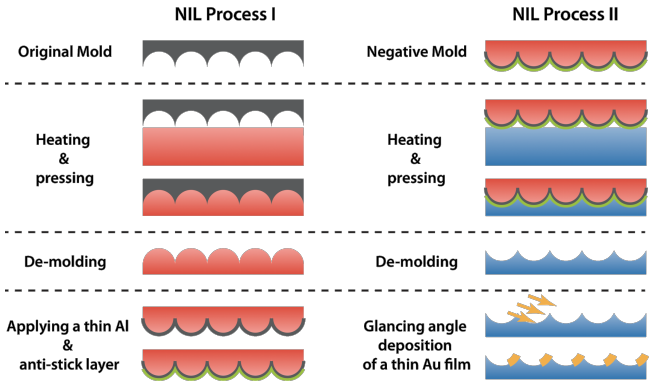

Figure 1: Schematical overview of the ECM fabrication process. First an original mold with a honeycomb structure is cast in a TOPAS polymer substrate. After de-molding a thin Al and anti-stick layer is applied to produce a negative mold. This negative mold is then cast in PMMA to produce the original honeycomb structure. This structure is used for initiation of glancing angle deposition of a 30 nm Au layer.

The criteria for extrinsic chiral metamaterials

A chiroptical response is only obtained from structures lacking mirror symmetry. As the unit structures of ECMs are not natively chiral, they rely greatly on the orientation of the sample with respect to the direction of the incident light causing a broken mirror symmetry. By careful design it is possible to design the ECM structure in such a way that no CD response is observed when the face of the ECM substrates are oriented perpendicular to the incident light. Hence a CD signal is only obtained when the sample is tilted out of one of the two angles θ and ϕ (Figure 4).

This enables the investigation of the enantiomeric ECM structures (right-handed and left-handed structure) to be probed in the same experiment, by inverting the tilt of the ECM with respect to the normal ECM face angle. The investigated ECMs have been designed in a way that it was possible to invert the CD signal by tilting the samples with respect to the θ angle while retaining a ϕ angle of 0° (Figure 5). The observed response from the bare sample when irradiated with light at a normal incident angle may have three different causes: 1) various structural imperfections, 2) a spread in structure size, 3) the 3D nature of the ECM structure causing some intrinsic chirality. However, this CD response at $\phi = 0°$ has also been observed by ECMs produced with focused ion beam milling [13].

The ECM property that allows for the measurement of the enantiomeric structures from one sample, yields several advantages over PCMs in biosensor applications: 1) PCMs require fabrication of the two enantiomeric samples, which increases the cost and the risk of imperfections. 2) With the use of PCMs it is necessary to perform two independent experiments, which is time-consuming and difficult to implement into a commercial product. 3) Since the CD response is concentration-dependent, two independent PCM experiments are troublesome to interpret. All of these disadvantages with PCMs are totally avoided by the use of ECMs, which are both cheaper, more reliable and only require one experiment in biosensor applications.

Probing the zero-response angle

The zero-response angle of the ECM with 450 nm interpore distance and 50° glancing angle deposition was identified by scanning the θ and ϕ angles separately (Figure 6). This ECM substrate was chosen as it exhibits more and stronger resonance modes than the other samples and will be used in most subsequent experiments. While the CD response was extremely sensitive towards angular rotation about the θ angle plane (Figure 6a), it exhibited a lower angular dependence on the ϕ angle plane (Figure 6b).

Furthermore, it is evident from the angular scans (Figure 6) that the ECM has an intrinsic left-hand chirality. Hence, the zero-response angle is not identified by the lowest CD response but as the center of the enantiomeric signals. From the θ angle scan (Figure 6a), it appears as if $\theta = -1°$ and $\theta = +2°$ display the least response. Hence, the θ angle resulting in minimum extrinsic chirality is between 0° and +1°. As virtually no difference in

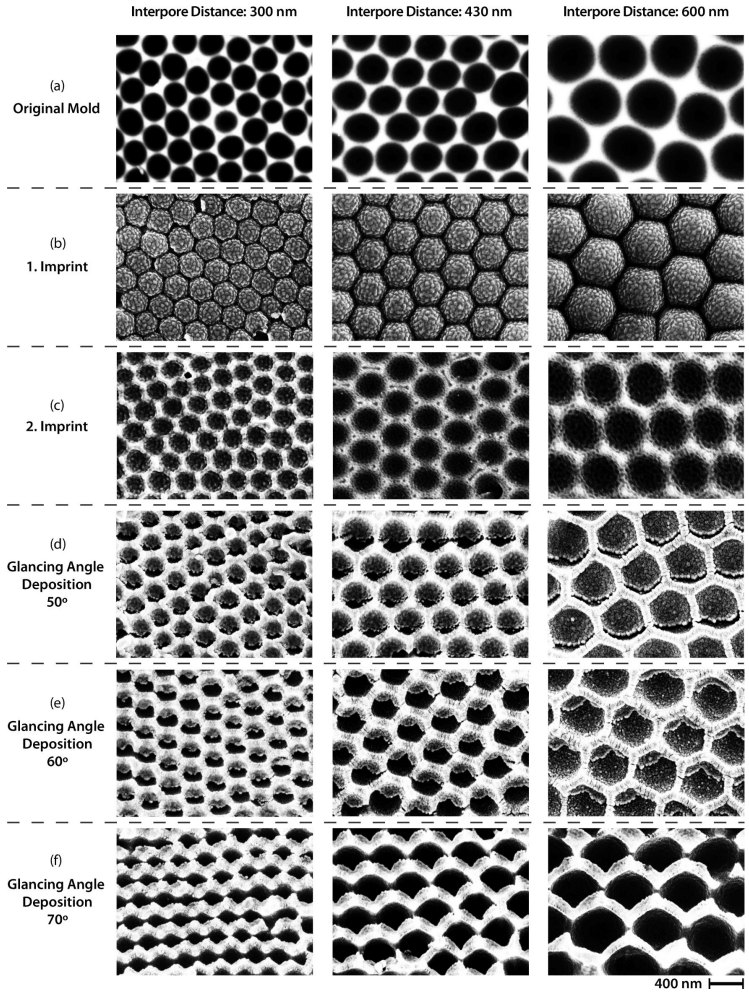

Figure 2: SEM pictures of (a) the original molds (b) 1. imprints with a thin Al layer (c) 2. imprints with a 2 nm Au layer and (d–f) all the different ECMs produced by glancing angle deposition of 30 nm Au at 50, 60 and 70°. The scale bar is shown in the bottom right corner.

line shape is observed between $\theta = 0°$ and $\theta = +1°$, $\theta = 0°$ was used as zero-θ-angle throughout the paper for the sake of convenience.

The two resonance modes located in the wavelength range of 260–360 nm of the ϕ angle scan (Figure 6b) indicate that $\phi = 0°$ to $\phi = -3°$ exhibits no extrinsic chirality. As virtually no difference in line shape is observed between these angles, $\phi = 0°$ was used as zero-response angle. Applying $\theta = 0°$ and $\phi = 0°$ as reference results in a more symmetrical angular scan (Figure 7) indicating the precision of the determination of the zero-response angle.

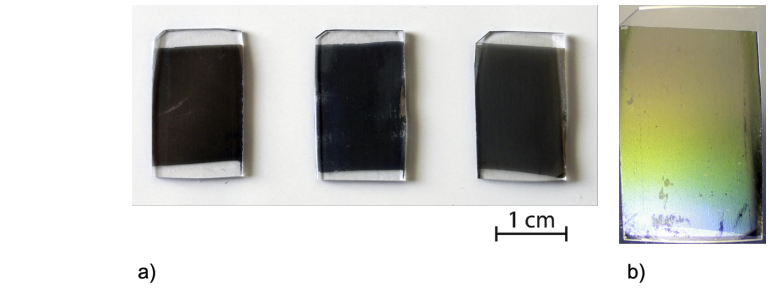

Figure 3: (a) Photography of the ECM samples prepared at a deposition angle of 60° and interpore distance of 300, 430 and 600 nm from the left, respectively. The sizes were chosen as to be compatible with commercial dismantled cuvettes and only a small area of the sample is probed.
(b) Photography of the sample prepared by a deposition angle of 60° and interpore distance of 600 nm with flashlight to illustrate the diffraction pattern (the scale bar does not apply to this photo).

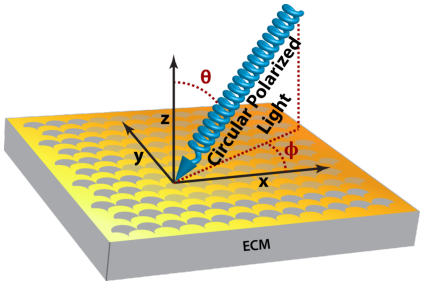

Figure 4: The two principle angles, θ and ϕ, of incident light with respect to the ECM structures.

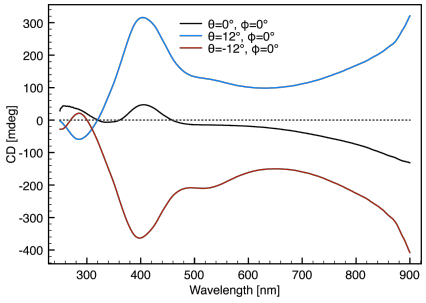

Figure 5: The resulting CD response from three ECM orientations (θ = 0°, ϕ = 0°), (θ = 12°, ϕ = 0°) and (θ = −12°, ϕ = 0°) of the ECM with 300 nm interpore distance and 60° deposition angle. It is evident that (θ = 0°, ϕ = 0°) shows no significant response, while the two other orientations yield inverted line shapes.

Influence of interpore distance and glancing angle deposition

Structures with interpore distances of 300, 430 and 600 nm exhibited main plasmonic resonance ranges of about 300–550 nm, 450–800 nm and above 900 nm (Figure 8).

Compared to the relatively narrow linewidth of the CD response from ECMs comprised of hole arrays, the honeycomb ECMs exhibit a rather broad signal [13]. This is presumably related to the heterogeneity and 3D nature of the ECM structures, which is less dominant in the hole arrays fabricated by focused ion beam lithography. In spite of this, the CD linewidths of the present ECMs are comparable to those of gammadion PCMs, which have been previously used for biosensor applications [10]. Furthermore, compared to PCMs fabricated by another scalable technique [29], the CD linewidths of the honeycomb ECMs are more narrow. Hence the heterogeneity and 3D structure has not limited the use of the honeycomb ECMs for biosensing applications.

While the interpore distance of the ECM array is the main factor in the position of the SPP resonance, the angle of the Au deposition has mainly an influence on the line shape and the number of resonance peaks (Figure 8). The samples prepared at 0 and 50° glancing angle deposition show a similar line shape, as well as the samples prepared at 60 and 70°. This is reasonable as the angle deposition sensitivity, which determines the dependence of the resulting structure on the deposition angle, is very low at small angles but increases with large angles. The reason for this is found in the shadowing effect of the honeycomb structure. The glancing angle deposition is self-perpetuating at larger angles while small angles result only in minor shadowing effects. The samples prepared at 0 and 50°, in general, exhibit three to four distinct resonance peaks while the

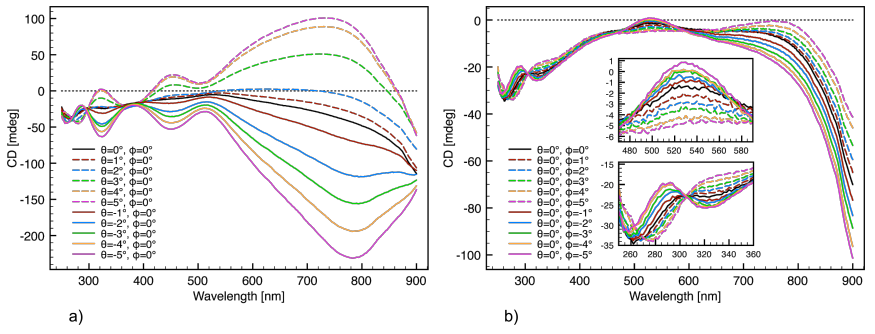

Figure 6: Angular scans and corresponding CD response from the ECM fabricated with 430 nm interpore distance and 50° glancing angle deposition. (a) Independent scan of the θ angle defined in Figure 4. (b) Independent scan of the ϕ angle defined in Figure 4.

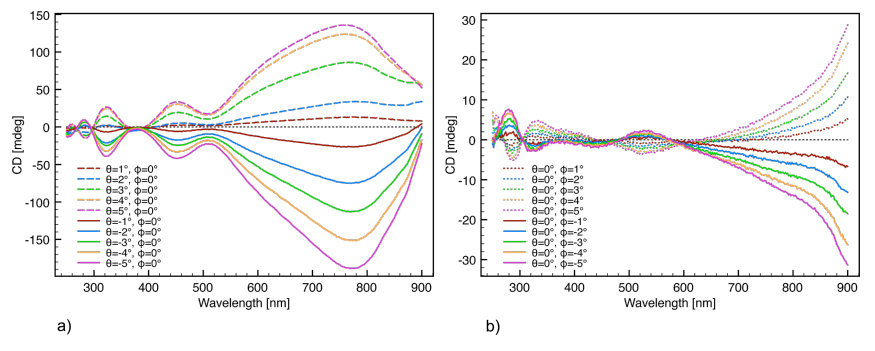

Figure 7: Angular scans with the intrinsic chirality subtracted. A much higher symmetrical CD response from the ECM enantiomers is observed compared to the angular scans in Figure 6. (a) Independent scan of the θ angle. (b) Independent scan of the ϕ angle.

samples prepared at 60 and 70° only exhibit two to three distinct resonance peaks. This might be explained by the gold inside the hole arrays produced at 0 and 50° glancing angle deposition, resulting in a more complex 3D structure (Figure 2) and an additional origin of plasmonic resonance modes. The samples with 600 nm interpore distances had a main resonance wavelength above 900 nm (data not shown). These structures may find applications in other areas such as surface enhanced IR spectroscopy [41], terahertz generation [42] or THz-CD spectroscopy [43].

Influence of the scanning angle and of intrinsic spatial structural variations

As mentioned above, the plasmonic resonance wavelength and intensity depends on the orientation of the ECMs. Upon rotating the sample in the θ angle plane (Figure 9a) it is evident that the two distinct resonance modes in the near-UV region merge upon increasing the θ angle from 10 to 20°. At θ = 30° this peak is blue-shifted. When the θ angle is increased to 40 and 50° the peak re-separates into two peaks. These changes may originate from the transition from a hole array towards a film with gratings upon increasing angles and subsequent larger backscattering. At θ = 60° the backscattering has increased significantly, resulting in a pronounced drop in CD response. Furthermore, the 770 nm plasmonic resonance mode does not show any angular dependence and remains located at the same wavelength.

From the ϕ angle scan (Figure 9b) it is evident that only plasmonic resonance modes in the infrared and UV range are in-

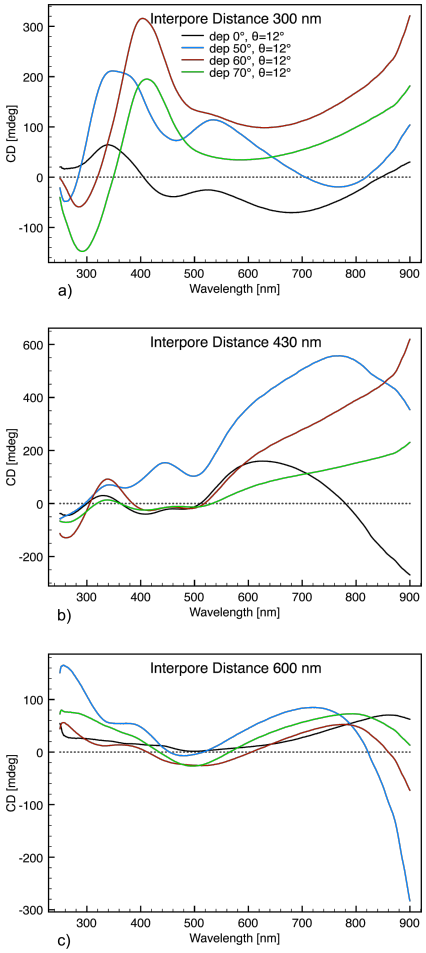

Figure 8: CD response from all the produced ECMs. (a) The CD response from the structures with 300 nm interpore distances. (b) The response from the structures with 430 nm interpore distances. (c) The response from the structures with 600 nm interpore distances. All measurements were recorded with an ECM orientation of θ = 12° and ϕ = 0°.

duced. Upon increasing the ϕ angle, the resonance modes in the UV range intensifies and changes of the resonance wavelengths occur. It is also noteworthy for other applications of the ECM, that a very strong resonance mode in the range of 900–1100 nm has been identified in other measurements (data not shown) but is outside of the measured range presented here as it is not relevant to protein sensing using CD spectroscopy. Similar to the θ angular scan, the CD response at a ϕ = 60° drops as a consequence of significantly increased backscattering.

Typically, metamaterials are fabricated with a significantly smaller surface area than the beam profile used to probe the sample. However, the present ECMs are significantly larger, but with various structural imperfections. To validate the integrity of the sample fabricated with 430 nm interpore distance and a glancing angle deposition of 50° was probed in two different positions over 6 mm apart. Minor differences were observed (Figure 10), indicating small structural differences.

These differences are no larger than what has been reported for PCMs fabricated with e-beam lithography [10] or ECMs fabricated with ion beam milling [13] and most likely originate from structural imperfections. Another contributing factor might be that the ECM surface is much larger than the beam profile, hence the structures in the circumference of the beam profile may appear different from those substructures being completely probed. Beam profile induced imperfections are circumvented in usual fabrication techniques as the achievable sample area is much smaller than the beam profile.

Sensing of chiral molecules

As a proof of concept, the sensing power of the honeycomb ECMs were investigated by monitoring the resonance shift upon adsorption of the chiral organic molecule cysteamine and the protein cytochrome c. cytochrome c acts as an electron shuttle and as a respiratory redox protein [44]. It also assists as an important mediator in the apoptotic pathways [44]. Due to a free surface-accessible cysteine it is well known to readily adsorb onto gold surfaces and is often used to study electron transfer in cyclic voltammetry [45]. Cysteamine is the simplest stable aminothiol, hence it readily adsorbs onto gold surfaces and forms a self-assembled monolayer which is often used as the first layer in the functionalization of surfaces [46].

In all experiments the ECM fabricated with 430 nm interpore distance and a glancing deposition angle of 50° was used as it displays a well-defined response at ca. 770 nm compared to the other structures, together with two minor distinct peaks at ca. 440 nm and ca. 330 nm. The resulting spectra are presented in Figure 11 and the corresponding shifts compared to the bare structure are summarized in Table 1.

A similar plasmonic resonance shift of the resonance mode around 770 nm upon adsorption of cytochrome c was observed at different θ angles (Figure 12 and Table 2). This indicates that the sensitivity of the plasmonic resonance towards changes in

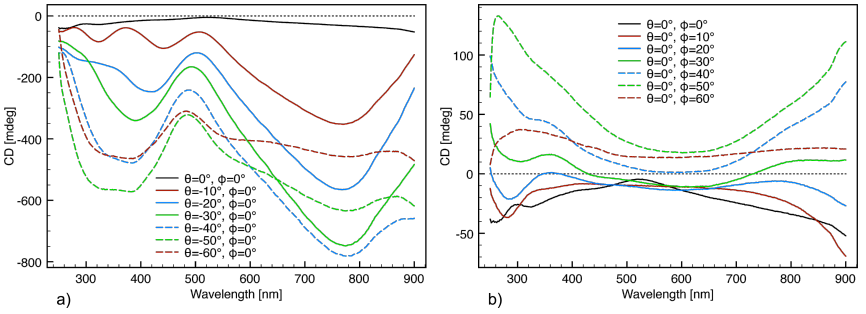

Figure 9: Angular scans with large angle increments and corresponding the CD response from the ECM fabricated with 430 nm interpore distance and 50° glancing angle deposition. (a) Independent scan of the θ angle. (b) Independent scan of the ϕ angle.

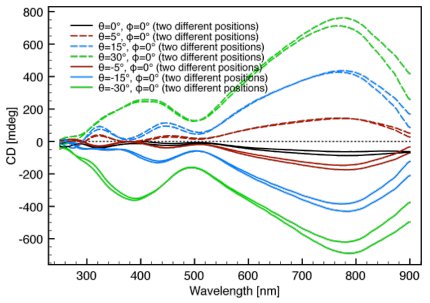

Figure 10: CD response from the ECM fabricated with 430 nm interpore distance and 50° glancing angle deposition in four different angle orientation and measured in two different positions 6 mm apart on the sample.

the local refractive index near the ECM surface is not effected by the θ angle. Only the resonance mode around 770 nm was used in this analysis as the resonances of the other modes are altered as described above and as a result are incomparable.

It has been demonstrated that the dissymmetry factor [10] (ΔΔλ) of the shifts of the right-handed spectrum compared to the left-handed spectrum ($\Delta\Delta\lambda = \Delta\lambda_{right} - \Delta\lambda_{left}$) is an indication of an anisotropic adsorption (Table 3) [10]. Whereas a perfect isotropic adsorption would result in a ΔΔλ value of zero. Interestingly, the adsorption of the two molecules does not result in the same behavior in signal shifts. While the adsorption of cytochrome c did not result in a measurable dissymmetry shift, the adsorption of cysteamine caused a relatively large dissymmetry shift as indicated by the 770 nm signal. This

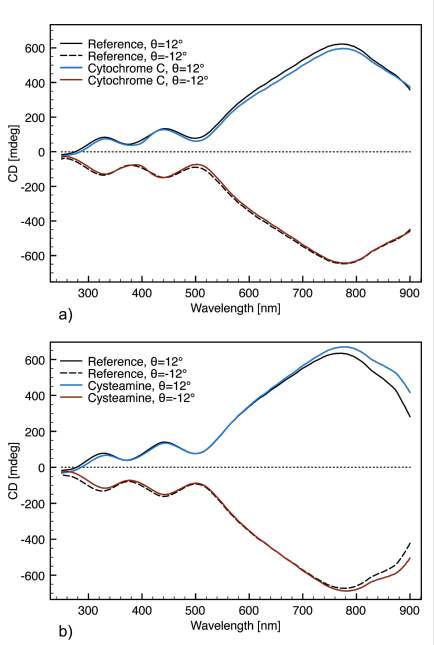

Figure 11: CD response from a bare ECM and with a molecule adsorbed on the surface. (a) CD response with and without cytochrome c adsorbed on the ECM surface. (b) CD response with and without Cysteamine adsorbed on the ECM surface. All measurements were recorded with an ECM orientation of θ = 12°; ϕ = 0° or θ = −12°; ϕ = 0°.

Table 1: Excitation shifts originating from different molecules.

molecule	$\Delta\lambda_{770\ nm}$ (θ_{12}/θ_{-12})	$\Delta\lambda_{440\ nm}$ (θ_{12}/θ_{-12})	$\Delta\lambda_{330\ nm}$ (θ_{12}/θ_{-12})
cytochrome c	2/2 nm	−4/−4 nm	2/3 nm
cysteamine	7/12 nm	2/2 nm	4/5 nm

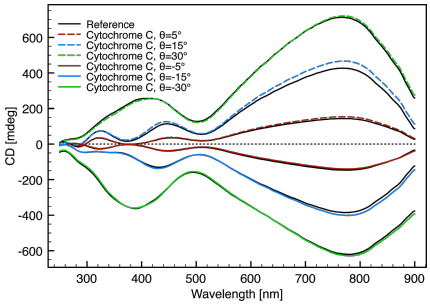

Figure 12: CD response from the ECM fabricated with 430 nm interpore distance and 50° glancing angle deposition with different angle orientation and measured with and without cytochrome c adsorbed on the surface.

Table 2: Excitation shifts and dissymmetry factors of the plasmonic resonance at 770 nm at different θ angles, originating from adsorption of cytochrome c on the ECM fabricated with 430 nm interpore distance and a glancing angle deposition of 50°.

angle	$\Delta\lambda_{770\ nm}$	$\Delta\Delta\lambda_{770\ nm}$
(θ_5/θ_{-5})	1.4/1.5 nm	0.1 nm
(θ_{15}/θ_{-15})	2.3/2.6 nm	0.3 nm
(θ_{30}/θ_{-30})	2.2/2.4 nm	0.2 nm

Table 3: Dissymmetry factors, calculated from the shifts given in Table 1.

molecule	$\Delta\Delta\lambda_{770\ nm}$	$\Delta\Delta\lambda_{440\ nm}$	$\Delta\Delta\lambda_{330\ nm}$
cytochrome c	0 nm	0 nm	−1 nm
cysteamine	−5 nm	0 nm	−1 nm

is coherent with other studies, demonstrating that cysteamine forms a well-ordered layer on Au surfaces [47,48]. Furthermore, it has been reported that cytochrome c either adsorbs with the α-helix structure parallel to the Au surface [49] or that the protein instantly denaturates upon adsorption to the Au surface [50]. In either case this will result in an isotropic layer with respect to the incoming light, which is coherent with the obtained results.

The average extent of the two plasmonic enantiomer shifts ($\Delta\lambda_{av} = (\Delta\lambda_{right} + \Delta\lambda_{left})/2$ gives an indication of the amount of molecules adsorbed on the gold surface of the metamaterial [10]. Instead of using the peak at 550 nm to determine the surface coverage as previously reported by PCMs [10], the peak at 330 nm has been used in this paper, since it is the peak located closest to the UV range (Table 4).

Table 4: Average shifts calculated from the shifts given in Table 1.

molecule	$\Delta\lambda_{AV,330nm}$
cytochrome c	2.5 nm
cysteamine	4.5 nm

From the data it is apparent that both cytochrome c and cysteamine do interact with the ECM gold surface. Compared to another study using PCMs, it is apparent that the $\Delta\lambda_{AV,330nm}$ of cytochrome c and cysteamine is comparable to the $\Delta\lambda_{AV,\approx 550nm}$ of the proteins resulting from the highest adsorption on a PCMs gold surface [10]. As the sensitivity of the ECM resonance mode at 330 nm is unknown the exact surface coverage cannot be determined. However, the sensitivity is not expected to deviate significantly from that observed with PCMs at 550 nm. Based on this both cytochrome c and cysteamine are adsorbed in picogram quantities on the ECM Au surface.

The current results demonstrate that proteins and chiral organic molecules in general readily adsorb onto the ECM surface. This demonstrates that the ECMs may be used for detection of proteins and chiral organic molecules in a label-free way. Furthermore, the ease of cysteamine adsorption on the ECM surface suggests that other molecules such as ethanedithiol may be used to functionalize the ECM surface and provide the possibility to fabricate very sensitive sensor arrays.

Conclusion

In conclusion, a strong chiroptical response has been demonstrated from different achiral plasmonic hole arrays. The arrays were fabricated by a scaleable technique while retaining control and order of the resulting arrays. This signifies a substantial improvement to standard fabrication methods such as focused ion beam and electron beam lithography concerning cost and production time. Furthermore, the use of a small chiral organic molecule and a protein has been used as a proof of concept for the sensing of biological and chiral organic molecules in picogram quantities by CD spectroscopy. The response of the presented ECMs was tunable within the UVA and IR regions,

depending mainly on the interpore distance of the hole arrays. The deposition angle had an effect on the amount of resonance modes. Small glancing angle deposition resulted in complex ECM geometries and consequently more resonance modes were observed. The number of modes is larger than that which has been previously reported for PCMs [10,32,34]. This is a significant improvement, as more signals yield a more detailed protein fingerprint.

The enantiomeric form of the investigated ECMs were recorded by inverting the tilt of the same sample about the θ angle plane, effectively eliminating the disadvantages of PCMs having to fabricate two independent samples and conducting two separate experiments to probe the protein fingerprint. CD spectroscopy revealed that both cytochrome c and cysteamine readily adsorbed on the ECM gold surface, amounting to picogram quantities. Furthermore, the formation of a cysteamine layer on the ECM gold surface suggests that similar organic molecules may be used to fabricate functionalized surfaces applicable for sensors with increased sensitivity or arrays hereof in a cheap and scaleable way.

Experimental

Fabrication of extrinsic chiral metamaterials

The original molds were prepared by anodic aluminum oxidation using a custom-built anodization and wet-etching system. Al foils (99.98%, Advent Research Materials Ltd. AL103310) were used as substrates after cleaning in an ultrasonic bath with a sequence of acetone, deionized water and methanol for 1 min each. In total three types of molds were prepared with different interpore distances: 300, 430 and 600 nm. The substrate with 300 nm interpore distance was prepared by anodization in 0.3 M oxalic acid solution at 140 V and with a solution temperature of 283 ± 0.5 K for 40 min. The substrate with 430 nm interpore distance was prepared by anodization in 1 M phosphoric acid solution at 180 V and with a solution temperature of 273 ± 0.5 K for 100 min. The substrate with 600 nm interpore distance was prepared by anodization in 2 M citric acid solution at 285 V and with a solution temperature of 293 ± 0.5 K for 20 min. More details on the fabrication of the original mold has been reported previously [39]. The original molds were used to make negative imprints by thermal nanoimprint lithography using the EVG520HE semi-automated hot embossing system. This was done in TOPAS 5013L-10 substrates under vacuum with a stamping pressure of 1.25 bar and at 160 °C using the original molds. Next a 30 nm film was sputter-coated on the surface of the negative imprints. A monolayer of trichloro(1*H*,1*H*,2*H*,2*H*-perfluorooctyl)silane (25 vol % in toluene) was applied to the Al films by gas phase deposition for 1 h in a vacuum desiccator. These samples served as new molds for the second imprint in PMMA. The parameters of this imprint were similar to the once described above but were prepared at 120 °C. The negative molds were used several times without observable deterioration. The final ECMs were achieved by glancing angle deposition of 2 nm Cr followed by 50 nm Au at different deposition angles.

Scanning electron microscopy

SEM measurements of the ECM surfaces were done in high vacuum ($1{\cdot}10^{-6}$ mbar) and an accelerating voltage 10 kV using a Zeiss 1540XB system and standard procedure. The samples were coated by 2 nm gold as to prevent a buildup of static charge.

CD spectroscopy measurements

The ECMs were compatible with commercial available liquid CD cells with a path length of 0.1 mm and a total volume of 50 µL. The CD spectra were collected in normal incident mode where the samples were parallel to the detector and in tilted configuration, where the samples were tilted by 12°. CD spectra were collected using a commercial JASCO J-750 spectropolarimeter.

Adsorption of cytochrome c and cysteamine onto extrinsic chiral materials

Cytochrome c was adsorbed on the substrates by incubation of 50 µL protein solution (1 $mg{\cdot}mL^{-1}$) for 1 h. Cysteamine was adsorbed by incubating 50 µL of solution (10 mM) for 24 h. The cysteamine solution was prepared with degassed Milli-Q water and the cytochrome c solution was prepared using 5 mM PBS buffer at pH 7.4.

Surface regeneration of extrinsic chiral materials

ECMs were reused several times and before each experiment the substrates were submerged for 2 h in a sodium dodecyl sulfate solution, followed by a 30 min bath in a Hellmanex III solution at 37 °C. Finally, the substrates were cleaned in an oxygen-plasma cleaning unit for 1 h. After each step the ECMs were rinsed with Milli-Q water.

References

1. Valentine, J.; Zhang, S.; Zentgraf, T.; Ulin-Avila, E.; Genov, D. A.; Bartal, G.; Zhang, X. *Nature* **2008,** *455,* 376–379. doi:10.1038/nature07247
2. Atwater, H. A.; Polman, A. *Nat. Mater.* **2010,** *9,* 205–213. doi:10.1038/nmat2629
3. Zia, R.; Schuller, J. A.; Chandran, A.; Brongersma, M. L. *Mater. Today* **2006,** *9,* 20–27. doi:10.1016/S1369-7021(06)71572-3
4. Abb, M.; Wang, Y.; Papasimakis, N.; de Groot, C. H.; Muskens, O. L. *Nano Lett.* **2014,** *14,* 346–352. doi:10.1021/nl404115g
5. Kühler, P.; Weber, M.; Lohmüller, T. *ACS Appl. Mater. Interfaces* **2014,** *6,* 8947–8952. doi:10.1021/am5023418

6. Yanik, A. A.; Huang, M.; Kamohara, O.; Artar, A.; Geisbert, T. W.; Connor, J. H.; Altug, H. *Nano Lett.* **2010,** *10,* 4962–4969. doi:10.1021/nl103025u
7. Pendry, J. B. *Science* **2004,** *306,* 1353–1355. doi:10.1126/science.1104467
8. Zhang, S.; Park, Y.-S.; Li, J.; Lu, X.; Zhang, W.; Zhang, X. *Phys. Rev. Lett.* **2009,** *102,* 023901. doi:10.1103/PhysRevLett.102.023901
9. Hannam, K.; Powell, D. A.; Shadrivov, I. V.; Kivshar, Y. S. *Phys. Rev. B* **2014,** *89,* 125105. doi:10.1103/PhysRevB.89.125105
10. Hendry, E.; Carpy, T.; Johnston, J.; Popland, M.; Mikhaylovskiy, R. V.; Lapthorn, A. J.; Kelly, S. M.; Barron, L. D.; Gadegaard, N.; Kadodwala, M. *Nat. Nanotechnol.* **2010,** *5,* 783–787. doi:10.1038/nnano.2010.209
11. Bunn, C., Ed. *Chemical Crystallography;* Oxford University Press: Oxford, United Kingdom, 1945.
12. Plum, E.; Liu, X.-X.; Fedotov, V. A.; Chen, Y.; Tsai, D. P.; Zheludev, N. I. *Phys. Rev. Lett.* **2009,** *102,* 113902. doi:10.1103/PhysRevLett.102.113902
13. Maoz, B. M.; Ben Moshe, A.; Vestler, D.; Bar-Elli, O.; Markovich, G. *Nano Lett.* **2012,** *12,* 2357–2361. doi:10.1021/nl300316f
14. Zu, S.; Bao, Y.; Fang, Z. *Nanoscale* **2016,** *8,* 3900–3905. doi:10.1039/C5NR09302C
15. Zambrana-Puyalto, X.; Vidal, X.; Molina-Terriza, G. *Nat. Commun.* **2014,** *5,* 4922. doi:10.1038/ncomms5922
16. Arteaga, O.; Maoz, B. M.; Nichols, S.; Markovich, G.; Kahr, B. *Opt. Express* **2014,** *22,* 13719–13732. doi:10.1364/OE.22.013719
17. Feng, C.; Wang, Z. B.; Lee, S.; Jiao, J.; Li, L. *Opt. Commun.* **2012,** *285,* 2750–2754. doi:10.1016/j.optcom.2012.01.062
18. Shi, J. H.; Zhu, Z.; Ma, H. F.; Jiang, W. X.; Cui, T. J. *J. Appl. Phys.* **2012,** *112,* 073522. doi:10.1063/1.4757961
19. Wang, F.; Wang, Z.; Shi, J. *J. Appl. Phys.* **2014,** *116,* 153506. doi:10.1063/1.4898314
20. Sersic, I.; van de Haar, M. A.; Arango, F. B.; Koenderink, A. F. *Phys. Rev. Lett.* **2012,** *108,* 223903. doi:10.1103/PhysRevLett.108.223903
21. Yannopapas, V. *Opt. Lett.* **2009,** *34,* 632–634. doi:10.1364/OL.34.000632
22. Shaltout, A.; Liu, J.; Shalaev, V. M.; Kildishev, A. V. *Nano Lett.* **2014,** *14,* 4426–4431. doi:10.1021/nl501396d
23. Hashiyada, S.; Narushima, T.; Okamoto, H. *J. Phys. Chem. C* **2014,** *118,* 22229–22233. doi:10.1021/jp507168a
24. Kruk, S. S.; Helgert, C.; Decker, M.; Staude, I.; Menzel, C.; Etrich, C.; Rockstuhl, C.; Jagadish, C.; Pertsch, T.; Neshev, D. N.; Kivshar, Y. S. *Phys. Rev. B* **2013,** *88*, 201404–201409. doi:10.1103/PhysRevB.88.201404
25. Boutria, M.; Oussaid, R.; Van Labeke, D.; Baida, F. I. *Phys. Rev. B* **2012,** *86,* 155428–155435. doi:10.1103/PhysRevB.86.155428
26. Belardini, A.; Benedetti, A.; Centini, M.; Leahu, G.; Mura, F.; Sennato, S.; Sibilia, C.; Robbiano, V.; Giordano, M. C.; Martella, C.; Comoretto, D.; de Mongeot, F. B. *Adv. Opt. Mater.* **2014,** *2,* 208–213. doi:10.1002/adom.201300385
27. Yokoyama, A.; Yoshida, M.; Ishii, A.; Kato, Y. K. *Phys. Rev. X* **2014,** *4,* 11005–11011. doi:10.1103/PhysRevX.4.011005
28. Singh, J. H.; Nair, G.; Ghosh, A.; Ghosh, A. *Nanoscale* **2013,** *5,* 7224–7228. doi:10.1039/C3NR02666C
29. Yeom, B.; Zhang, H.; Zhang, H.; Park, J. I.; Kim, K.; Govorov, A. O.; Kotov, N. A. *Nano Lett.* **2013,** *13,* 5277–5283. doi:10.1021/nl402782d
30. Schreiber, R.; Do, J.; Roller, E.-M.; Zhang, T.; Schüller, V. J.; Nickels, P. C.; Feldmann, J.; Liedl, T. *Nat. Nanotechnol.* **2014,** *9,* 74–78. doi:10.1038/nnano.2013.253
31. Zhou, Y.; Yang, M.; Sun, K.; Tang, Z.; Kotov, N. A. *J. Am. Chem. Soc.* **2010,** *132,* 6006–6013. doi:10.1021/ja906894r
32. Chen, W.; Bian, A.; Agarwal, A.; Liu, L.; Shen, H.; Wang, L.; Xu, C.; Kotov, N. A. *Nano Lett.* **2009,** *9,* 2153–2159. doi:10.1021/nl900726s
33. Shen, X.; Asenjo-Garcia, A.; Liu, Q.; Jiang, Q.; García de Abajo, F. J.; Liu, N.; Ding, B. *Nano Lett.* **2013,** *13,* 2128–2133. doi:10.1021/nl400538y
34. Fan, Z.; Govorov, A. O. *Nano Lett.* **2010,** *10,* 2580–2587. doi:10.1021/nl101231b
35. Nemiroski, A.; Gonidec, M.; Fox, J. M.; Jean-Remy, P.; Turnage, E.; Whitesides, G. M. *ACS Nano* **2014,** *8,* 11061–11070. doi:10.1021/nn504214b
36. Chang, Y.-C.; Lu, S.-C.; Chung, H.-C.; Wang, S.-M.; Tsai, T.-D.; Guo, T.-F. *Sci. Rep.* **2013,** *3,* 3339. doi:10.1038/srep03339
37. Cataldo, S.; Zhao, J.; Neubrech, F.; Frank, B.; Zhang, C.; Braun, P. V.; Giessen, H. *ACS Nano* **2012,** *6,* 979–985. doi:10.1021/nn2047982
38. Oates, T. W. H.; Shaykhutdinov, T.; Wagner, T.; Furchner, A.; Hinrichs, K. *Adv. Mater.* **2014,** *26,* 7197–7201. doi:10.1002/adma.201402012
39. Tsao, Y.-C.; Søndergaard, T.; Skovsen, E.; Gurevich, L.; Pedersen, K.; Pedersen, T. G. *Opt. Express* **2013,** *21,* A84–A95. doi:10.1364/OE.21.000A84
40. Tsao, Y.-C.; Fisker, C.; Pedersen, T. G. *Opt. Express* **2014,** *22,* A651–A662. doi:10.1364/OE.22.00A651
41. Li, Y.; Su, L.; Shou, C.; Yu, C.; Deng, J.; Fang, Y. *Sci. Rep.* **2013,** *3,* 2865. doi:10.1038/srep02865
42. Luo, L.; Chatzakis, I.; Wang, J.; Niesler, F. B. P.; Wegener, M.; Koschny, T.; Soukoulis, C. M. *Nat. Commun.* **2014,** *5,* 3055. doi:10.1038/ncomms4055
43. Choi, J.-H.; Cho, M. *J. Phys. Chem. B* **2014,** *118,* 12837–12843. doi:10.1021/jp508547y
44. Liu, X.; Kim, C. N.; Yang, J.; Jemmerson, R.; Wang, X. *Cell* **1996,** *86,* 147–157. doi:10.1016/S0092-8674(00)80085-9
45. Liu, H.; Yamamoto, H.; Wei, J.; Waldeck, D. H. *Langmuir* **2003,** *19,* 2378–2387. doi:10.1021/la026378n
46. Shervedani, R. K.; Farahbakhsh, A.; Bagherzadeh, M. *Anal. Chim. Acta* **2007,** *587,* 254–262. doi:10.1016/j.aca.2007.01.053
47. Wirde, M.; Gelius, U.; Nyholm, L. *Langmuir* **1999,** *15,* 6370–6378. doi:10.1021/la9903245
48. Shervedani, R. K.; Bagherzadeh, M.; Mozaffari, S. A. *Sens. Actuators, B* **2006,** *115,* 614–621. doi:10.1016/j.snb.2005.10.027
49. Lin, S.; Jiang, X.; Wang, L.; Li, G.; Guo, L. *J. Phys. Chem. C* **2012,** *116,* 637–642. doi:10.1021/jp2063782
50. Zhou, Y.; Nagaoka, T.; Zhu, G. *Biophys. Chem.* **1999,** *79,* 55–62. doi:10.1016/S0301-4622(99)00038-1

Paper C

Langmuir, submitted May 2016

The Physical Properties and Self-Assembly Potential of the RFFFR Peptide

Morten Slyngborg, Dennis Achton Nielsen, and Peter Fojan*

Department of Physics and Nanotechnology, Aalborg University, Aalborg

E-mail: fp@nano.aau.dk

Abstract

The self-assembly of fibers from peptides have attracted a tremendous amount of attention due to the many applications such as drug-delivery systems, tissue engineering and electronic devices. Recently, the self-assembly potential of the designer peptide RFFFR has been reported. In the current study it is experimentally verified that the peptides form fibers that are entangled and form solid spheres without water inside. Upon dilution below the critical fiber concentration, the fibers untangle and become totally separated prior to dissolution. These structures readily bind Thioflavin T, resulting in a characteristic change in fluorescent properties coherent with β-sheet rich amyloid structures with aromatic-hydrophobic grooves. Circular dichroism spectroscopy data is dominated by a $\pi \rightarrow \pi^*$ transition indicating that the fibers are stabilized by π-stacking. Contrary to what was expected, the dissolution of the spheres/fibers results in increasing fluorescence anisotropy over time. This is explained by HomoFRET between phenylalanine residues with a T-shaped π-stacking mode, which was determined as the dominant mode by atomistic simulations and semi-empirical calculations in another study. Kelvin probe force microscopy measurements indicate that the spheres and fibers have a conductivity comparable to that of gold. Hence these self-assembled structures

*To whom correspondence should be addressed

may be applicable in organic solid-state electronic devices. The dissolution properties of the spheres further suggest that they may be used as drug-delivery systems.

Introduction

The ability of natural proteins to form supramolecular structures[1] has been known for a long time to be responsible for many biological functions such as S-layer proteins that cover the outer cell membrane of some organisms[2]. Peptides are also known to self-assemble in nature and apart from other structures[3,4] can form amyloid fibers related to natural biological functions[5,6] or several human disorders[7,8]. Recently, the self-assembly of designer peptides has also attracted a tremendous interest owing to their ability to form supramolecular structures with high bio-compatibility, chemical diversity and potential solubility in aqueous solutions.[9–11] The applications of the formed structures are numerous and include carrier-mediated drug delivery[12–15], tissue engineering[16], antimicrobial agents[17], fluorescent probes[18], energy storage[19], biomineralization[20], membrane protein stabilization[21] and bioinspired electronics such as field-effect transistors[22], microprobes[23], microarrays[23], biosensing devices[24], diodes[25] and nanotubes as conductive wires[23,26].

As self-assembling peptides are mainly known from amyloid fibers, these peptides are often used as scaffold to develop designer peptides. One scaffold that has been widely used is the core sequence of the Amyloid beta peptide (Aβ), β(16-20) KLVFF[27] or Aβ(17-21) LVFFA.[28] Due to the presence of the FF motif in both sequences and the identification of aromatic residues as having the highest propensity to cause amyloid formation[29], the peptides FF have been extensively studied by many groups.[30,31] Later the FFF peptide was also studied.[32] However, neither peptide forms amyloid fibers, but a variety of other structures. Instead, peptides that form amyloid fibers or fibers are often peptide amphiphiles or peptides with alternating hydrophobic and hydrophilic amino acids.

Fibers of peptides have attracted interest for many applications owing to the ease of synthesis, high biocompatibility and biodegradability.[33–35] This includes biomedical applications such as

drug-delivery systems[36], analyte detection[37], biomarker sensing[38], tissue engineering[39], immune response modulators[40] and cell fate controller[41]. Fibers of peptides also demonstrate potential for electronic devices as it allows for significant downscaling of the sizes of circuit components compared to what is possible with traditional inorganic semi-conductor technology.[42] Furthermore, peptide self-assembled fibers may also be applicable in material science due to their unique mechanical silk-like properties.[43,44]

Recently the self-assembly of the RFFFR peptide was investigated by coarse grained molecular dynamics (MD) simulations, atomistic MD simulations and semi-empirical calculations that indicated an amyloid fiber formation.[45] The motivation for the modification of the FF and FFF peptide is to direct the self-assembly process towards nano-fibers rather than the more random aggregated structures of FF or FFF. The arginine residues are intended to restrict the interaction of Phe residues in one direction only while the unprotected N- and C-termini ensures an anti parallel configuration by inducing a neutral C-terminus. In this way the charge of the neighboring peptides are not proximate, ensuring that the attractive effects are sufficiently strong for self-assembly. While the attractive effects may be dominated by "tugging in" of hydrophobic residues, computational data further suggests that the RFFFR amyloid fiber is stabilized by $\pi - \pi$ stacking interactions and a complex hydrogen bond network.

In this paper we report the synthesis and experimental data of the self-assembly of RFFFR. The self-assembly is investigated with different biophysical methods such as spectroscopy methods, atomic force microscopy (AFM) and scanning electron microscopy (SEM). These measurements indicate that the structure of the amyloid fibers fit very well with the *in silico* data of another study[45]. However, it is observed that the peptides not only form 1 dimensional fibers as predicted by simulations, but form more complex 3 dimensional fiber entangled structures in solution instead. The applications of these structures as molecular conductive wires or drug-delivery system is demonstrated, but applications may extend to material science, tissue engineering, advanced nanomaterial fabrication and encapsulation of biomolecules with purpose to stabilize/preserve their function.

Results and discussion

The self-assembly process

The self-assembly of the RFFFR peptides was investigated in milliQ water and PBS solutions with different concentrations, but the results were not significant different as the self-assembly is not solely governed by electrostatic interactions. To enable comparison with physiological conditions the following results in this paper are obtained by use of 1X PBS at pH 7.4. As the pH is far below the pKa values of the Arg side chains and termini, Arg and the N-terminus are positively charged while the C-terminus is negatively charged.

It was observed that the RFFFR peptides assemble into fibers that curl together and form spheres (Figure Figure 1 and Figure Figure 2a). Upon dilution below the critical fiber concen-

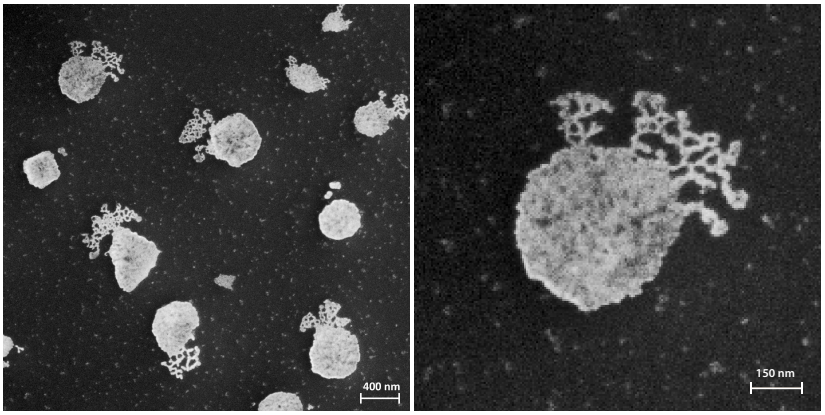

(a) (b)

Figure 1: SEM measurements of (a) RFFFR fibers untangling from spheres adsorbed on a silicon surface. (b) closeup of Figure Figure 1a.

tration (approximately 5mM) the fibers begin to untangle (Figure Figure 1 and Figure Figure 2b). When the fibers have totally untangled (Figure Figure 2c and Figure Figure 3), a dissolution process begins (Figure Figure 2d-f). These results are in agreement with the fluorescent anistropy measurements, discussed later, and it is therefor likely that the observed AFM measurements are

not a surface induced effect or that some other peptide structure existed which did not bind to the AFM surface. It is also unlikely that the rinsing of the AFM surface, after incubation of the peptide solution, removed any peptide structures as all peptide structures are tightly bound by electrostatic interactions to the surface. Furthermore, the short environmental change in buffer during rinsing of the sample is very short and induced configurational changes in the assembled structures are very slow, hence it is unlikely to effects what was observed with AFM.

The obtained sphere-like RFFFR structures are unique from almost any other self-assembled peptide structure, as the peptides form a structure (fibers) that again forms a structure (spheres). Typically, peptides form a structure comprised of the individual peptides which is also true for the closely related FFF peptide, that forms plate-like structures in aqueous solution[46] and sphere-like structures in chloroform[47]. These peptides aggregate in a more random way as to minimize solvent exposure and to maximize attractive forces, which is why the RFFFR peptide was designed with Arg residues in each terminus to intentionally force the self-assembly in one direction only. The observed entanglement of the fibers into sphere-like structures must then be an indication that the Arg residues are not completely sufficient to limit the self-assembly to only one direction.

The size of the spheres greatly depends on the peptide concentration above the critical fiber concentration. Hence the time it takes for the fibers to untangle also varies. The reason for the fiber entanglement may be to further decrease the water accessible surface of phenylalanine residues. This is indicated by the uniform shape of the spheres in the SEM measurements, as any water inside the spheres would have evaporated under the high vacuum conditions and deformed the spheres. Other studies of fibers that form complex structures report of microhydrogels that binds water in the interior.[48] The difference likely originates from the hydrophobicity level of the respective peptides. Hence it is possible that the compactness of RFFFR spheres may be controlled by reducing the polarity of the solvent or by reducing the stabilizing forces of hydrogen bonds and that RFFFR hydrogels or untangled fibers may be obtained under different conditions.

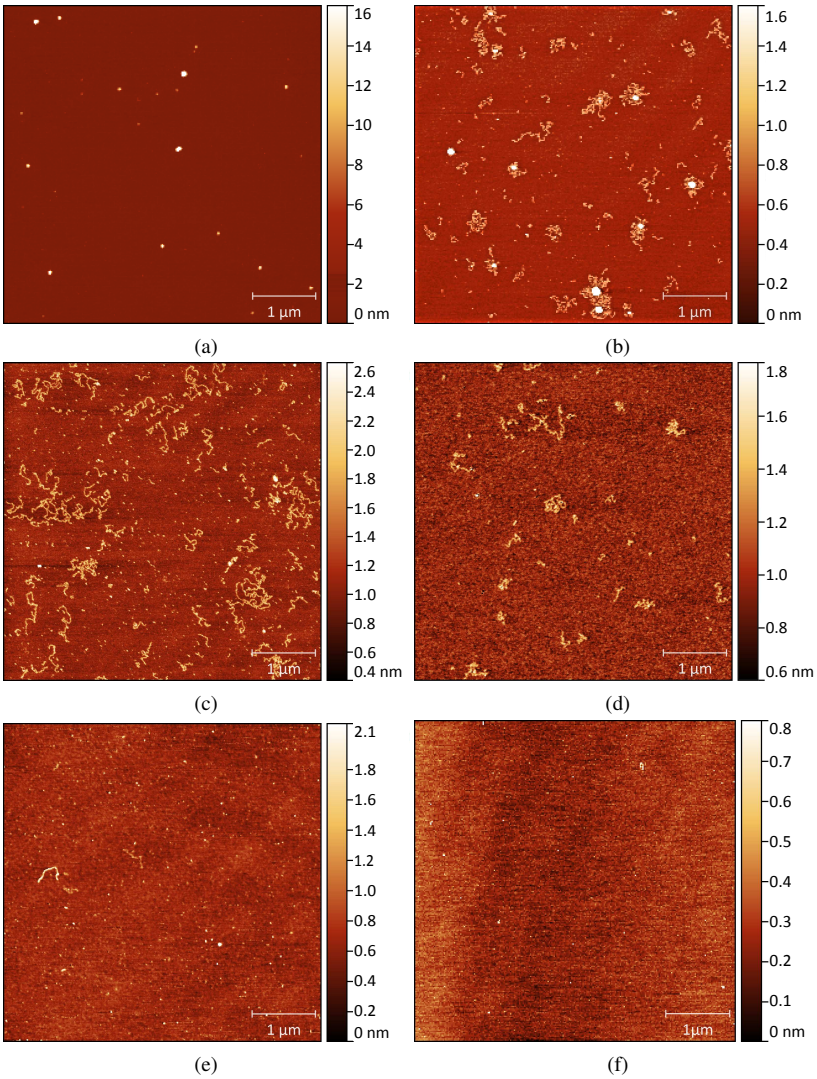

Figure 2: AFM measurements of 10mM RFFFR solution diluted to 1mM and measured at different time intervals. (a) 0 min. (b) 30 min. (c) 60 min. (d) 120 min. (e) 240 min. (f) 480 min.

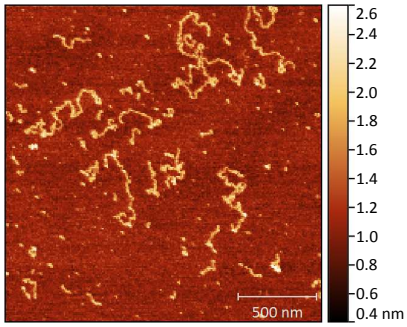

Figure 3: Closeup of Figure Figure 2c.

The height profile from the AFM measurements of the individual fibers (Figure Figure 4b) suggest a fiber height of 0.6-1.2 nm. This approximately coincides with the 0.8-2.4 nm reported earlier in a computational study of the self-assembly process (Figure Figure 4a).[45] The deviation is likely to originate from the environmental difference as the AFM measurements were performed on "dry" fibers with the arginine side chains attracted to the mica surface, while the simulations were performed in solution. Furthermore, the antiparallel assembly of the peptides, may cause the fibers to adsorb with the shorter width perpendicular to the mica surface, as only half of the positively charged arginine residues are in contact with the negatively charged mica surface otherwise. Hence the height difference between the height measured with AFM and predicted in the computational study[45] is sufficiently small, that it verifies a similar self-assembly. This demonstrates the potential of designing self-assembling peptides and predicting the resulting structure by the coarse grained MARTINI model[49] and the new PM7[50] semi-empirical approach.

The stabilizing forces of the RFFFR fibers

Most self-assemblies are driven by hydrophobic effects or electrostatic forces, however, the stabilizing intramolecular forces are equally important. Many structures are stabilized by hydrogen bonds between β-sheets and a recent trend is to use $\pi - \pi$ stacking in guided assembly.[42,51]

CD spectroscopy measurements did not show any signals that could be related to a beta sheet

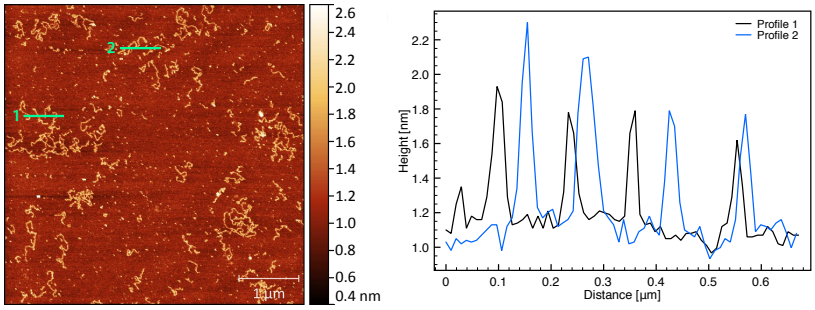

(a)

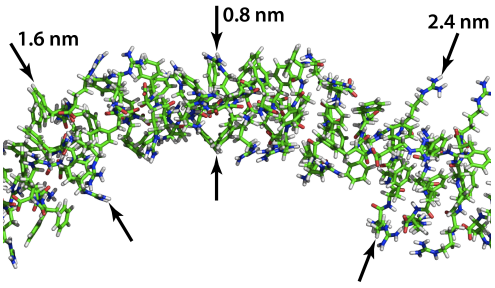

(b)

Figure 4: Comparison of measured and calculated fiber width. (a) Two height profiles of the RFFFR fibers and their position on the AFM measurement (Figure Figure 2c) indicated by the green lines. (b) Theoretical fiber width of the fiber self-assembled in a previously reported molecular dynamics study[45].

structure (Figure Figure 5). This is likely because of the small size of the peptides, the low solution concentration and the very compact form of spheres. Instead spectra are dominated by a single peak with a maximum located in the range of 219-224 nm depending on the peptide concentration. These peaks arise from either $n \rightarrow \pi^*$ or $\pi \rightarrow \pi^*$ transitions. However, the assignment is not unambiguous as $\pi \rightarrow \pi^*$ is often observed as a sharp strong peak at around 197-200 nm, while the $n \rightarrow \pi^*$ is the lowest energy amide band typically observed in the 210-230 nm range as a lower broader peak.[52] Spectra conforming to this have been reported for Aβ inspired peptides.[53,54]

The observed peaks of RFFFR are located in the range where $n \rightarrow \pi^*$ transitions typically occur and are relatively broad. However, very similar CD spectra of other short self-assembling peptides

and other aromatic systems have been observed before and assigned $\pi \rightarrow \pi^*$ transitions.[55–59] Furthermore, the peak position is red-shifted as a function of higher peptide concentrations. Though the peak position is sensitive towards secondary structure changes and β-sheet bending, it is more likely an effect of the increase in sphere size, similar to the one observed when substituting an organic solvent with water[60]. Due to the sphere formation by the "tugging in" effect of phenylalanine residues, it is likely that the $\pi \rightarrow \pi^*$ transition becomes more stable, resulting in a lower transition energy. A $n \rightarrow \pi^*$ transition is expected to blue-shift with increased sphere size, as the possibility for the lone pair electrons in the ground n state to form hydrogen bonds to other peptide groups increases. Hence the fibers are stabilized by $\pi - \pi$ stacking as previously suggested by computational data.[45]

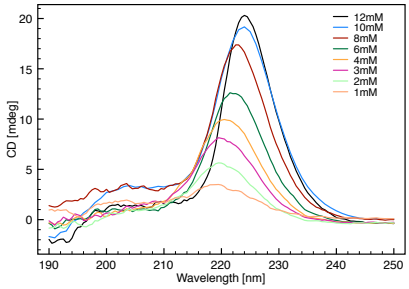

Figure 5: CD spectroscopy recorded from 190-250 nm with different RFFFR peptide concentrations.

To study the structure of the fibers and secondary structure of the composing peptides, Thioflavin T (ThT) was used as a fluorescent probe. ThT almost exclusively binds to β-sheet rich amyloid structures with aromatic-hydrophobic grooves that span more than four consecutive β-strands.[61–64] Upon binding the ThT fluorescent properties change significantly with a huge increase in quantum yield, emission and excitation shift which is why it is one of the most widely used probes for staining and identifying amyloid structures.[65]

Fluorescence spectroscopy measurements revealed an emission peak at 435 nm was observed when the ThT solution was excited at 353 nm (Figure Figure 6a). Upon addition of RFFFR

spheres/fibers, the 435 nm emission peak disappeared (Figure Figure 6a). Instead the emission peak had shifted to 485 nm when excited with 440 nm, which was not observed for the pure ThT solution. As previously reported, this is proof of a β-sheet rich amyloid structure in solution[61–65] even though the CD measurements did not yield any secondary structure information. Furthermore, it is likely that the observed structures seen in the AFM experiment are not the result of surface induced assembly.

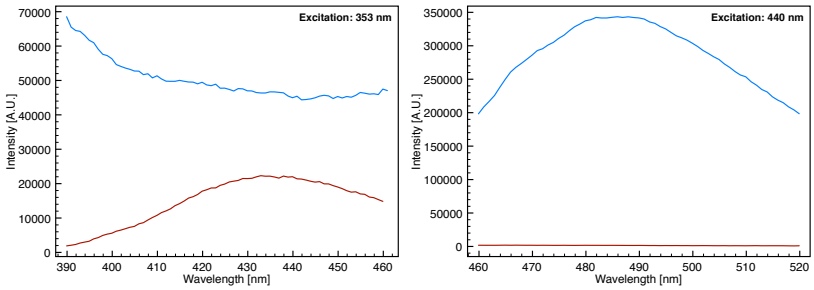

(a) (b)

Figure 6: Fluorescence spectroscopy spectra of ThT with RFFFR self-assembled structures (blue line) and without RFFFR self-assembled structures (red line). (a) Recorded spectra in the interval 390-460 nm with 353 nm excitation. (b) Recorded spectra in the interval 460-520 nm with 440 nm excitation.

Fluorescence anisotropy spectroscopy was measured with use of Phe residues over time with the same diluted RFFFR solution as was used for the AFM measurements, resulting in slow untangling of the fibers and subsequent dissolution (Figure Figure 7). In contrary to what is expected of a dissolution process, the anisotropy increases over time. Typically this would have been explained by Phe residues that moved more freely in fiber and sphere structures than in solution, however this is not likely in this case as the self-assembly is the result of Phe "tuggin in" effects, hydrogen bonds and $\pi - \pi$ stacking. Instead it can be explained by the previously computational study of the RFFFR fibers, where the phenylalanine residues assumed strict Phe-Phe configurations as a result of π-stacking.[45] This study further discovered by atomistic and semi-empirical quantum mechanical calculations that the Phe-Phe residues assume a T-shape π-stacking configuration.[45]

As HomoFRET[66,67] is known to occur between Trp residues[68] it is possible that energy is transferred from one phenylalanine residue to another perpendicular phenylalanine residue, explaining why the anisotropy behaves opposite of what is expected. Hence it is believed that the increase in anisotropy when spheres/fibers dissolve is indicative of a T-shaped π-stacking configuration which is in good agreement with high level computational calculations of the fibers[45].

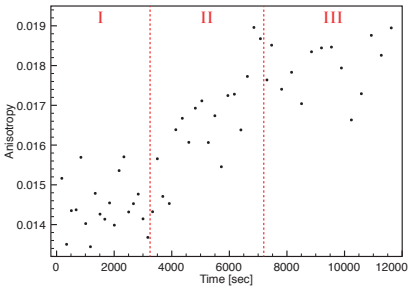

Figure 7: Fluorescence anisotropy over time of the same 10mM RFFFR peptide solution that was diluted to 1mM and used for the AFM measurements (Figure Figure 2). In time interval I the spheres are untangling. In time interval II the spheres are totally untangled and the fibers are dissolving. In time interval III the fibers have totally dissolved.

Molecular electronics

Molecular electronics is necessary for continued development of more powerful computers as it renders it possible for down-scaling electrical components, reduce fabrication cost, avoid poisons in the fabrication process and allow for diverse functions by tuning of the chemical properties. In this field DNA has attracted a tremendous amount of interest due to the self-assembly properties and size, however it is difficult to probe the conductive properties.[69] The conductive properties of some proteins, however, have been known for a long time, which has been explained by various theories such as ionic transport[70], proton transport[71] or tightly bound oriented ice-like water molecules around the protein[72]. However, in order to be applicable in solid-state electronic devices the proteins need to be conductive in a "dry" state (electron transport).[73] While most proteins are considered electrical insulators[26,74,75], some are known to be very efficient electron trans-

porters[76–78]. Today, two prevailing mechanisms responsible for the electron transfer, coherent tunneling[73,76,79] and charge hopping[73,80] exists, which may also occur concurrently.

Amide to amide groups are considered hopping sites and hydrogen bond networks aid in this coupling.[78,81] Furthermore, aromatic amino acids also facilitate hopping sites through the delocalized π orbitals.[82] Hence it is very likely that RFFFR will exhibit strong electron transport abilities through arginine-arginine, arginine-phenylalanine and phenylalanine-phenylalanine hopping sites enhanced by the previously reported complex hydrogen network[45]. Kelvin probe force microscopy (KPFM) measurements of the fibers entangled into large spheres (Figure Figure 8a) were used to measure the surface potential difference (Figure Figure 8b). Very small surface potential differences, below 2 mV, between the gold substrate and RFFFR spheres were measured (Figure Figure 9), which might indicate a strong conductivity. Furthermore, no charging effect was observed during the SEM measurements (Figure Figure 1) as is characteristic for insulating materials. Similar, conductivity in peptide structures induced by stabilized by intermolecular $\pi - \pi$ stacking have previously been reported.[23,26,51] KPFM have also previously been used to prove that peptide nanodots of FF peptides can store charges.[83]

It is expected that untangled fibers have relatively higher conductivity than the spheres, as the $\pi - \pi$ stacking interaction and hydrogen bond network is more elaborate when it is connected in only one direction. It is also unlikely that the conductivity observed in the KPFM measurements is related to ionic or water effects as any water bound by the spheres would have evaporated and deformed the spheres in the high vacuum environment of the SEM measurements. Hence it is likely that the untangled fibers are conductive in a "dry" state and have applications in solid-state electronic devices.

Drug delivery system

Self-assembled amyloid fibril networks or microgels from peptides have previously been suggested as potential drug-delivery systems.[48,84,85] The reported RFFFR spheres and fibers may also be used for such applications. As the spheres form due to a tugging in effect of the phenylalanine residues

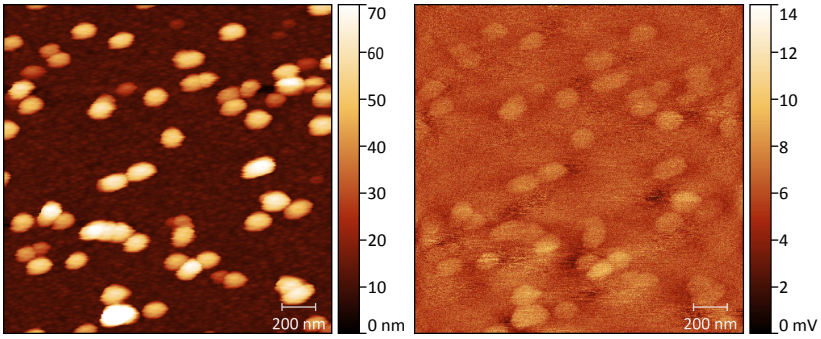

(a) (b)

Figure 8: AFM and subsequent KPFM measurement of RFFFR spheres on a 40 nm thick gold layer. (a) The topology measurements. (b) The surface potential.

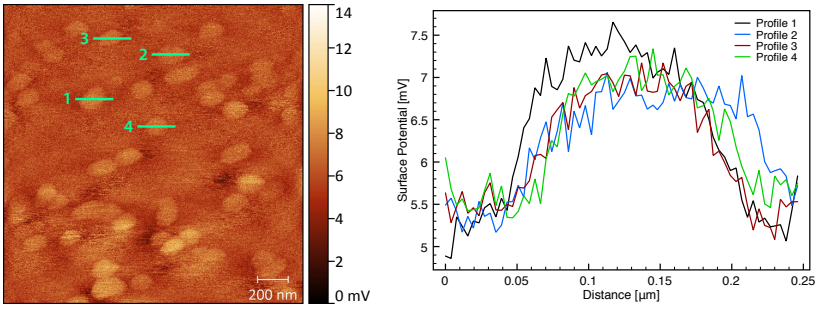

Figure 9: Four surface potential profiles and their position on the KPFM measurement (Figure Figure 8) indicated by the green lines.

to minimize water exposure, it is likely that hydrophobic drugs, resulting in low potency, could be incorporated into the fibers or spheres allowing for a much higher potency. This also enables a controlled longterm release of drugs with a short life time, that limits the use of many drugs, as the fibers untangle and dissolve and the drug is slowly released (Figure Figure 1). The release period may be optimized through the sphere size, simply by assembly at different peptide concentrations. No differences in sphere untanglement time at very low pH conditions (approximately pH 2), similar to those in the stomach, and normal physiological conditions were observed. This might indicate that the structures could be used for peroral medication. Furthermore, if the

sphere surfaces were to be functionalized with molecules having affinity towards specific targets, the encapsulated drugs would have an increased selectivity and potential side-effects would be diminished.

Conclusion

The self-assembly of the peptide RFFFR into fibers, as previously suggested, has been experimentally confirmed. The fibers have the same dimensions, within statistical error, as those determined by computational calculations, indicating the same configuration as predicted. It was observed that the fibers get entangled into spheres, possibly to further reduce the solvent accessible area of phenylalanine residues. When these spheres were diluted below a critical fiber concentration, the fibers untangled and dissolved after some time.

The spheres and fibers were observed to readily bind ThT, resulting in a significant increase in quantum yield, excitation and emission shift of ThT, proving the presence of amyloid structure. CD spectroscopy measurements were not indicative of any secondary structure but were dominated by electronic transitions originating from $\pi - \pi$ stacking interactions as predicted by previously reported computational calculations[45]. These computational calculations also indicated a very favorably T-shaped stacking mode, explaining why an increase in fluorescence anisotropy was observed during fiber dissolution in the present experimental study.

KPFM measurements were performed on self-assembled "dry" fibers/spheres, indicating a very high conductivity comparable to that of gold. It is expected that the untangled fibers are more conductive than the spheres as the fibers have a more dense $\pi - \pi$ stacking and hydrogen bond network in the fiber direction compared to the environment in the sphere where $\pi - \pi$ stacking and hydrogen bonds may be formed in all directions. These spheres contain no water as they remained intact during SEM measurements and did not show any charging effects. Hence the conductivity presumably originates from charge-hopping and overlapping delocalized aromatic π-orbitals as well. This allows the RFFFR fibers to be applicable in novel bioinspired solid-state electronic

devices.

The spheres untangle and dissolve into small fibers when diluted below the critical fiber concentration. Hence the spheres likely have potential as a drug-delivery system. The high pH stability of the spheres indicates that it may be a candidate for a peroral drug-delivery system.

Experimental

RFFFR peptide synthesis. RFFFR was synthesized by solid-phase peptide synthesis techniques. Standard 9-fluorenyl- methyloxycarbonyl (Fmoc)-protecting group and activation by 2-(1H-benzotriazol-1-yl)-1,1,3,3-tetramethyluronium hexa- fluorophosphate (HBTU) chemistry was used. The peptide was synthesized both manually and using a fully automated peptide synthesizer Activotec P-11 (ActivotecSPP, Cambridge, UK). After the final cleavage from the resin the product was precipitated with ice-cold diethylether. The precipitate was centrifuged down and resuspended in ice-cold diethylether, this step was repeated 5 times with no resuspension the last time after which the pellet was frozen in liquid nitrogen and freeze-dried. The lyophilized peptide was then dissolved in 5% acetic acid and frozen in liquid nitrogen and freeze-dried, this process was repeated once. The lyophilized peptide was then dissolved in 0.1% hydrochloric acid and frozen in liquid nitrogen and freeze-dried, this process was repeated three twice.

Some lyophilized peptide was analyzed by reverse-phase high-performance liquid chromatography (RP-HPLC) UltiMate 3000 Standard LC Systems (Dionex, California, USA) using a C18 semi-preparative column (Phenomenex, California, USA), for 60 min with a flow rate of 1 mL/min. A mobile phase of water with 0.1% TFA was used. Sample elution was monitored using a UV-VIS detector operating at 214, 240 and 260 nm. The peptide crude was found to be over 90% pure, hence no further purification steps were taken.

RFFFR peptide solution preparation. All protein solutions were prepared in 1x PBS buffer with pH 7.4. The exact concentrations were determined by lambert-beers law using a thermo scientific UV-VIS spectrophotometer (VWK International UV1 v4.60, West Chester, PA). As RFFFR

contains no amino acids suitable for absorption of 280 nm light, the recently developed protocol for concentration determination by absorption of 205 nm light[86], was used with a calculated $\varepsilon_{205} = 39620 M^{-1} cm - 1$.

Atomic force microscopy. AFM imaging of the untanglement of the RFFFR fibers were done at different time intervals (0min, 30min, 60min, 120min and 240min) after a 10 mM peptide solution in 1x PBS buffer (stored over night at room temperature) was diluted to 1mM peptide concentration. 30 μL solution of the diluted stock solution was placed on a freshly cleaved mica surface at the above specified time intervals and incubated for 10 min. After incubation, the mica surface was rinsed in 1 mL milliQ water three times before it was blow dried under a stream of dry nitrogen. The AFM measurements were performed with a Ntegra Aura (NT-MDT, Zelenograd, Russia) operating in tapping mode using OMCL-AC240TS cantilevers (Olympus, Japan). The data were analyzed using freeware image processing software Gwyddion.

Thioflavin T fluorescence and fluorescence anisotropy spectroscopy. Fluorescence characterization of the ThT binding to RFFFR fiber spheres was carried out using a RTC 2000 PTI spectrofluorimeter (PTI photon technology international, New Jersey, USA) at room temperature. Spectra in the range of 390-460 nm and 460-520 nm were acquired with an excitation of 353 and 440 nm, respectively, from 36 μM ThT in 1x PBS buffer and 36 μM ThT incubated with 10 mM RFFFR for 1h in 1x PBS buffer.

The same 10 mM peptide stock solution (stored over night at room temperature) that was diluted to 1 mM, used for the AFM measurements, was used to measure fluorescence anisotropy over time. Phenylalanine residues in RFFFR were used as fluorescent probe and an excitation and emission maxima of 260 and 284 nm were determined and used, respectively. A RTC 2000 PTI spectrofluorimeter in a L-shaped configuration with motorized polarizers was used to record the G-factor and subsequent anisotropy with 3 min intervals for 195 min at room temperature. The G-factor measurements lasted 10 sec each and the anisotropy measurements lasted 20 sec each. When measurements were not performed, the beam was blanked. The anisotropy calculations were performed in the PTI FeliX32 software using the formula:

$$r = \frac{I_{VV} - GI_{VH}}{I_{VV} + 2GI_{VH}}$$

where G is the correction factor:

$$G = \frac{I_{HV}}{I_{HH}}$$

Both experiments used slit widths of 5 nm and a quartz cuvette with path length of 0.2 cm.

Circular dichroism spectroscopy. CD spectra were obtained of a peptide stock solution diluted to specific peptide concentrations (1 mM, 2 mM, 3 mM, 4 mM, 6 mM, 8 mM, 10 mM and 12mM) in 1x PBS buffer and stored over night at room temperature before the measurements using a J-715 spectropolarimeter (Jasco Inc, Pennsylvania, USA). Spectra were recorded from 190 to 250 nm with 1 nm step, 1nm bandwidth and 2 sec collection time per step, taking 20 averages at room temperature. A 0.1 mm quartz cuvette was used.

Kelvin-Probe force microscopy. KPFM was used to generate a two-dimensional surface potential map of fibers entangled into spheres and adsorbed onto a 40 nm thick gold film. The substrates were prepared by sputter coating of 40 nm gold onto a Si wafer and the fiber/spheres were adsorbed on the substrate by incubating 50 μL of 25 mM peptide solution in 1x PBS buffer on the surface for 1 hour. The samples were investigated using an Ntegra Aura setup (NT-MDT, Zelenograd, Russia) in Kelvin Probe mode and Platinum-Iridium coated NSG01/Pt cantilevers (NT-MDT, Zelenograd, Russia). The sample was mounted on a sample holder with a metal spring in order to electrically connect the sample surface to the AFM ground, which is required for KPFM measurements. The measurements were carried out in a two-pass lift mode, where every line is scanned twice. In the first pass the topography of the sample is measured in AFM mode. In the second pass the recorded topography is used to keep the cantilever tip at a fixed predefined distance of 10 nm to the sample, while measuring the surface potential.

Scanning electron microscopy. SEM measurements were done at high vacuum ($1 \cdot 10^{-6}$ mbar) and an electron high tension of 15 kV using a Zeiss 1540XB system (Carl Zeiss, Jena, Germany) and standard procedure. The substrates were prepared by sputter coating of 40 nm gold onto a Si wafer and the fiber/spheres were adsorbed on the substrate by diluting a 25 mM peptide solution in 1x PBS buffer to 1 mM incubating 50 μL of the diluted solution on the surface for 15 min.

References

[1] Pieters, B. J. G. E.; van Eldijk, M. B.; Nolte, R. J. M.; Mecinovic, J. Natural supramolecular protein assemblies. *Chem. Soc. Rev.* **2016**, *45*, 24–39.

[2] Sleytr, U. B.; Beveridge, T. J. Bacterial S-layers. *Trends in Microbiology* **1999**, *7*, 253–260.

[3] Linder, M. B. Hydrophobins: Proteins that self assemble at interfaces. *Current Opinion in Colloid & Interface Science* **2009**, *14*, 1359–0294.

[4] Comas-Garcia, M.; Garmann, R. F.; Singaram, S. W.; Ben-Shaul, A.; Knobler, C. M.; Gelbart, W. M. Characterization of Viral Capsid Protein Self-Assembly around Short Single-Stranded RNA. *The Journal of Physical Chemistry B* **2014**, *118*, 7510–7519.

[5] Iconomidou, V. A.; Hamodrakas, S. J. Natural Protective Amyloids. *Current Protein and Peptide Science* **2008**, *9*, 291–309.

[6] Maji, S. K.; Perrin, M. H.; Sawaya, M. R.; Jessberger, S.; Vadodaria, K.; Rissman, R. A.; Singru, P. S.; Nilsson, K. P. R.; Simon, R.; Schubert, D.; Eisenberg, D.; Rivier, J.; Sawchenko, P.; Vale, W.; Riek, R. Functional Amyloids As Natural Storage of Peptide Hormones in Pituitary Secretory Granules. *Science* **2009**, *325*, 328–332.

[7] Bhak, G.; Choe, Y.; Paik, S. R. Mechanism of amyloidogenesis: nucleation-dependent fibrillation versus double-concerted fibrillation. *BMP reports* **2009**, *42*, 541–551.

[8] Stefani, M.; Dobson, C. M. Protein aggregation and aggregate toxicity: new insights into protein folding, misfolding diseases and biological evolution. *Journal of Molecular Medicine* **2003**, *81*, 678–699.

[9] Mandal, D.; Nasrolahi Shirazi, A.; Parang, K. Self-assembly of peptides to nanostructures. *Org. Biomol. Chem.* **2014**, *12*, 3544–3561.

[10] de la Rica, R.; Matsui, H. Applications of peptide and protein-based materials in bionanotechnology. *Chem. Soc. Rev.* **2010**, *39*, 3499–3509.

[11] Zelzer, M.; Ulijn, R. V. Next-generation peptide nanomaterials: molecular networks, interfaces and supramolecular functionality. *Chem. Soc. Rev.* **2010**, *39*, 3351–3357.

[12] Mart, R. J.; Osborne, R. D.; Stevens, M. M.; Ulijn, R. V. Peptide-based stimuli-responsive biomaterials. *Soft Matter* **2006**, *2*, 822–835.

[13] Prato, M.; Kostarelos, K.; Bianco, A. Functionalized Carbon Nanotubes in Drug Design and Discovery. *Accounts of Chemical Research* **2008**, *41*, 60–68.

[14] McDonald, T. O.; Qu, H.; Saunders, B. R.; Ulijn, R. V. Branched peptide actuators for enzyme responsive hydrogel particles. *Soft Matter* **2009**, *5*, 1728–1734.

[15] Thornton, P. D.; Mart, R. J.; Webb, S. J.; Ulijn, R. V. Enzyme-responsive hydrogel particles for the controlled release of proteins: designing peptide actuators to match payload. *Soft Matter* **2008**, *4*, 821–827.

[16] Cheng, T.-Y.; Chen, M.-H.; Chang, W.-H.; Huang, M.-Y.; Wang, T.-W. Neural stem cells encapsulated in a functionalized self-assembling peptide hydrogel for brain tissue engineering. *Biomaterials* **2013**, *34*, 2005–2016.

[17] Javadpour, M. M.; ; Barkley, M. D. Self-Assembly of Designed Antimicrobial Peptides in Solution and Micelles. *Biochemistry* **1997**, *36*, 9540–9549.

[18] Zhao, Y.; Ji, T.; Wang, H.; Li, S.; Zhao, Y.; Nie, G. Self-assembled peptide nanoparticles as tumor microenvironment activatable probes for tumor targeting and imaging. *Journal of Controlled Release* **2014**, *177*, 11–19.

[19] Adler-Abramovich, L.; Aronov, D.; Beker, P.; Yevnin, M.; Stempler, S.; Buzhansky, L.; Rosenman, G.; Gazit, E. Self-assembled arrays of peptide nanotubes by vapour deposition. *Nat Nano* **2009**, *4*, 849–854.

[20] Masica, D. L.; Schrier, S. B.; Specht, E. A.; Gray, J. J. De Novo Design of PeptideâĹŠCalcite

Biomineralization Systems. *Journal of the American Chemical Society* **2010**, *132*, 12252–12262.

[21] Midtgaard, S. R.; Pedersen, M. C.; Kirkensgaard, J. J. K.; Sorensen, K. K.; Mortensen, K.; Jensen, K. J.; Arleth, L. Self-assembling peptides form nanodiscs that stabilize membrane proteins. *Soft Matter* **2014**, *10*, 738–752.

[22] Kumar, R. J.; MacDonald, J. M.; Singh, T. B.; Waddington, L. J.; Holmes, A. B. Hierarchical Self-Assembly of Semiconductor Functionalized Peptide α-Helices and Optoelectronic Properties. *Journal of the American Chemical Society* **2011**, *133*, 8564–8573.

[23] Castillo, J.; Tanzi, S.; Dimaki, M.; Svendsen, W. Manipulation of self-assembly amyloid peptide nanotubes by dielectrophoresis. *ELECTROPHORESIS* **2008**, *29*, 5026–5032.

[24] de la Rica, R.; Pejoux, C.; Fernandez-Sanchez, C.; Baldi, A.; Matsui, H. Peptide-Nanotube Biochips for Label-Free Detection of Multiple Pathogens. *Small* **2010**, *6*, 1092–1095.

[25] Tovar, J. D. Supramolecular Construction of Optoelectronic Biomaterials. *Accounts of Chemical Research* **2013**, *46*, 1527–1537.

[26] Ashkenasy, N.; Horne, W. S.; Ghadiri, M. R. Design of Self-Assembling Peptide Nanotubes with Delocalized Electronic States. *Small* **2006**, *2*, 99–102.

[27] Sotoa, C.; Kindyc, M. S.; Baumannb, M.; Frangione, B. Inhibition of Alzheimer's Amyloidosis by Peptides That Prevent β-Sheet Conformation. *Biochemical and Biophysical Research Communications* **1996**, *226*, 672–680.

[28] Esler, W. P.; Stimson, E. R.; Ghilardi, J. R.; Lu, Y.-A.; Felix, A. M.; Vinters, H. V.; Mantyh, P. W.; Lee, J. P.; ; Maggio, J. E. Point Substitution in the Central Hydrophobic Cluster of a Human β-Amyloid Congener Disrupts Peptide Folding and Abolishes Plaque Competence. *Biochemistry* **1996**, *35*, 13914–13921.

[29] Pawar, A. P.; DuBay, K. F.; Zurdo, J.; Chiti, F.; Vendruscolo, M.; Dobson, C. M. Prediction of Aggregation-prone and Aggregation-susceptible Regions in Proteins Associated with Neurodegenerative Diseases. *Journal of Molecular Biology* **2005**, *350*, 379–392.

[30] Reches, M.; Gazit, E. Casting Metal Nanowires Within Discrete Self-Assembled Peptide Nanotubes. *Science* **2003**, *300*, 625–627.

[31] Hashemi, M.; Fojan, P.; Gurevich, L. The Many Faces of Diphenylalanine. *Journal of Self-Assembly and Molecular Electronics* **2013**, *1*, 195–208.

[32] Tamamis, P.; Adler-Abramovich, L.; Reches, M.; Marshall, K.; Sikorski, P.; Serpell, L.; Gazit, E. Self-Assembly of Phenylalanine Oligopeptides: Insights from Experiments and Simulations. *Biophysical Journal* **2009**, *96*, 5020–5029.

[33] Ulijn, R. V.; Smith, A. M. Designing peptide based nanomaterials. *Chem. Soc. Rev.* **2008**, *37*, 664–675.

[34] Tomasini, C.; Castellucci, N. Peptides and peptidomimetics that behave as low molecular weight gelators. *Chem. Soc. Rev.* **2013**, *42*, 156–172.

[35] Lim, Y.-b.; Moon, K.-S.; Lee, M. Recent advances in functional supramolecular nanostructures assembled from bioactive building blocks. *Chem. Soc. Rev.* **2009**, *38*, 925–934.

[36] Zhao, F.; Ma, M. L.; Xu, B. Molecular hydrogels of therapeutic agents. *Chem. Soc. Rev.* **2009**, *38*, 883–891.

[37] Ren, C.; Zhang, J.; Chen, M.; Yang, Z. Self-assembling small molecules for the detection of important analytes. *Chem. Soc. Rev.* **2014**, *43*, 7257–7266.

[38] Ikeda, M.; Tanida, T.; Yoshii, T.; Kurotani, K.; Onogi, S.; Urayama, K.; Hamachi, I. Installing logic-gate responses to a variety of biological substances in supramolecular hydrogelÐenzyme hybrids. *Nat Chem* **2014**, *6*, 511–518.

[39] Gelain, F.; Horii, A.; Zhang, S. Designer Self-Assembling Peptide Scaffolds for 3-D Tissue Cell Cultures and Regenerative Medicine. *Macromolecular Bioscience* **2007**, *7*, 544–551.

[40] Hudalla, G. A.; Sun, T.; Gasiorowski, J. Z.; Han, H.; Tian, Y. F.; Chong, A. S.; Collier, J. H. Gradated assembly of multiple proteins into supramolecular nanomaterials. *Nat Mater* **2014**, *13*, 829–836.

[41] Kuang, Y.; Xu, B. Disruption of the Dynamics of Microtubules and Selective Inhibition of Glioblastoma Cells by Nanofibers of Small Hydrophobic Molecules. *Angewandte Chemie International Edition* **2013**, *52*, 6944–6948.

[42] na, H. A. M. A.; Tovar, J. D. Peptide pi-Electron Conjugates: Organic Electronics for Biology? *Bioconjugate Chemistry* **2015**, *26*, 2290–2302.

[43] Rubin, D. J.; Nia, H. T.; Desire, T.; Nguyen, P. Q.; Gevelber, M.; Ortiz, C.; Joshi, N. S. Mechanical Reinforcement of Polymeric Fibers through Peptide Nanotube Incorporation. *Biomacromolecules* **2013**, *14*, 3370–3375.

[44] Knowles, T. P. J.; Buehler, M. J. Nanomechanics of functional and pathological amyloid materials. *Nat Nano* **2011**, *6*, 469–479.

[45] Slyngborg, M.; Fojan, P. A computational study of the self-assembly of the RFFFR peptide. *Phys. Chem. Chem. Phys.* **2015**, *17*, 30023–30036.

[46] Guo, C.; Luo, Y.; Zhou, R.; Wei, G. Triphenylalanine peptides self-assemble into nanospheres and nanorods that are different from the nanovesicles and nanotubes formed by diphenylalanine peptides. *Nanoscale* **2014**, *6*, 2800–2811.

[47] Handelman, A.; Kuritz, N.; Natan, A.; Rosenman, G. Reconstructive Phase Transition in Ultrashort Peptide Nanostructures and Induced Visible Photoluminescence. *Langmuir* **2016**, *32*, 2847–2862.

[48] Shimanovich, U.; Efimov, I.; Mason, T. O.; Flagmeier, P.; Buell, A. K.; Gedanken, A.; Linse, S.; kerfeldt, K. S. A.; Dobson, C. M.; Weitz, D. A.; Knowles, T. P. J. Protein Microgels from Amyloid Fibril Networks. *ACS Nano* **2015**, *9*, 43–51.

[49] Marrink, S. J.; de Vries, A. H.; Mark, A. E. Coarse Grained Model for Semiquantitative Lipid Simulations. *Journal of Physical Chemistry B* **2004**, *108*, 750–760.

[50] Stewart, J. J. P. Optimization of parameters for semiempirical methods VI: more modifications to the NDDO approximations and re-optimization of parameters. *Journal of Molecular Modeling* **2013**, *19*, 1–32.

[51] Xu, H.; Das, A. K.; Horie, M.; Shaik, M. S.; Smith, A. M.; Luo, Y.; Lu, X.; Collins, R.; Liem, S. Y.; Song, A.; Popelier, P. L. A.; Turner, M. L.; Xiao, P.; Kinloch, I. A.; Ulijn, R. V. An investigation of the conductivity of peptide nanotube networks prepared by enzyme-triggered self-assembly. *Nanoscale* **2010**, *2*, 960–966.

[52] Gupta, M.; Bagaria, A.; Mishra, A.; Mathur, P.; Basu, A.; Ramakumar, S.; Chauhan, V. Self-Assembly of a Dipeptide- Containing Conformationally Restricted Dehydrophenylalanine Residue to Form Ordered Nanotubes. *Advanced Materials* **2007**, *19*, 858–861.

[53] Krysmann, M. J.; Castelletto, V.; Kelarakis, A.; Hamley, I. W.; Hule, R. A.; Pochan, D. J. Self-Assembly and Hydrogelation of an Amyloid Peptide Fragment. *Biochemistry* **2008**, *47*, 4597–4605.

[54] Handelman, A.; Natan, A.; Rosenman, G. Structural and optical properties of short peptides: nanotubes-to-nanofibers phase transformation. *Journal of Peptide Science* **2014**, *20*, 487–493.

[55] Marchesan, S.; Easton, C. D.; Kushkaki, F.; Waddington, L.; Hartley, P. G. Tripeptide self-assembled hydrogels: unexpected twists of chirality. *Chem. Commun.* **2012**, *48*, 2195–2197.

[56] Marchesan, S.; Qu, Y.; Waddington, L. J.; Easton, C. D.; Glattauer, V.; Lithgow, T. J.;

McLean, K. M.; Forsythe, J. S.; Hartley, P. G. Self-assembly of ciprofloxacin and a tripeptide into an antimicrobial nanostructured hydrogel. *Biomaterials* **2013**, *34*, 3678–3687.

[57] Marchesan, S.; Styan, K. E.; Easton, C. D.; Waddington, L.; Vargiu, A. V. Higher and lower supramolecular orders for the design of self-assembled heterochiral tripeptide hydrogel biomaterials. *J. Mater. Chem. B* **2015**, *3*, 8123–8132.

[58] Frelek, J.; Szczepek, W. J.; Neubrech, S.; Schultheis, B.; Brechtel, J.; Kuball, H.-G. Chiroptical Properties of cisoid Enones from Circular Dichroism (CD) and Anisotropic Circular Dichroism (ACD) Spectroscopy. *Chemistry - A European Journal* **2002**, *8*, 1899–1907.

[59] Castelletto, V.; Cheng, G.; Furzeland, S.; Atkins, D.; Hamley, I. W. Control of strand registry by attachment of PEG chains to amyloid peptides influences nanostructure. *Soft Matter* **2012**, *8*, 5434–5438.

[60] Nielsen, E. B.; Schellman, J. A. The absorption spectra of simple amides and peptides. *The Journal of Physical Chemistry* **1967**, *71*, 2297–2304.

[61] Younan, N. D.; Viles, J. H. A Comparison of Three Fluorophores for the Detection of Amyloid Fibers and Prefibrillar Oligomeric Assemblies. ThT (Thioflavin T); ANS (1-Anilinonaphthalene-8-sulfonic Acid); and bisANS (4,4-Dianilino-1,1-binaphthyl-5,5-disulfonic Acid). *Biochemistry* **2015**, *54*, 4297–4306.

[62] Cloe, A. L.; Orgel, J. P. R. O.; Sachleben, J. R.; Tycko, R.; Meredith, S. C. The Japanese Mutant Aβ ($\triangle$E22-Aβ1-39) Forms Fibrils Instantaneously, with Low-Thioflavin T Fluorescence: Seeding of Wild-Type Aβ1-40 into Atypical Fibrils by $\triangle$E22-Aβ1-39. *Biochemistry* **2011**, *50*, 2026–2039.

[63] Biancalana, M.; Makabe, K.; Koide, A.; Koide, S. Molecular Mechanism of Thioflavin-T Binding to the Surface of Îš-Rich Peptide Self-Assemblies. *Journal of Molecular Biology* **2009**, *385*, 1052–1063.

[64] Wu, C.; Biancalana, M.; Koide, S.; Shea, J.-E. Binding Modes of Thioflavin-T to the Single-Layer β-Sheet of the Peptide Self-Assembly Mimics. *Journal of Molecular Biology* **2009**, *394*, 627–633.

[65] Biancalana, M.; Koide, S. Molecular Mechanism of Thioflavin-T Binding to Amyloid Fibrils. *Biochimica et biophysica acta* **2010**, *1804*, 1405–1412.

[66] Chan, F. T. S.; Kaminski, C. F.; Kaminski Schierle, G. S. HomoFRET Fluorescence Anisotropy Imaging as a Tool to Study Molecular Self-Assembly in Live Cells. *ChemPhysChem* **2011**, *12*, 500–509.

[67] Lindenburg, L. H.; Malisauskas, M.; Sips, T.; van Oppen, L.; Wijnands, S. P. W.; van de Graaf, S. F. J.; Merkx, M. Quantifying Stickiness: Thermodynamic Characterization of Intramolecular Domain Interactions To Guide the Design of Forster Resonance Energy Transfer Sensors. *Biochemistry* **2014**, *53*, 6370–6381.

[68] Moens, P. D. J.; Helms, M. K.; Jameson, D. M. Detection of Tryptophan to Tryptophan Energy Transfer in Proteins. *The Protein Journal* **2004**, *23*, 79–83.

[69] Livshits, G. I.; Stern, A.; Rotem, D.; Borovok, N.; Eidelshtein, G.; Migliore, A.; Penzo, E.; Wind, S. J.; Di Felice, R.; Skourtis, S. S.; Cuevas, J. C.; Gurevich, L.; Kotlyar, A. B.; Porath, D. Long-range charge transport in single G-quadruplex DNA molecules. *Nat Nano* **2014**, *9*, 1040–1046.

[70] Rosenberg, B. Electrical Conductivity of Proteins. *Nature* **1962**, *193*, 364–365.

[71] Cardew, M. H.; Eley, D. D. The semiconductivity of organic substances. Part 3.-Haemoglobin and some amino acids. *Discuss. Faraday Soc.* **1959**, *27*, 115–128.

[72] King, G.; Medley, J. D.C. conduction in swollen polar polymers. I. electrolysis of the keratin-water system. *Journal of Colloid Science* **1949**, *4*, 1–7.

[73] Ron, I.; Pecht, I.; Sheves, M.; Cahen, D. Proteins as Solid-State Electronic Conductors. *Accounts of Chemical Research* **2010**, *43*, 945–953.

[74] Hauser, C. A. E.; Zhang, S. Nanotechnology: Peptides as biological semiconductors. *Nature* **2010**, *468*, 516–517.

[75] noz Berbel, X. M.; noz, F. M.; Vigués, N.; Mas, J. On-chip impedance measurements to monitor biofilm formation in the drinking water distribution network. *Sensors and Actuators B: Chemical* **2006**, *118*, 129–134.

[76] Marcus, R.; Sutin, N. Electron transfers in chemistry and biology. *Biochimica et Biophysica Acta (BBA) - Reviews on Bioenergetics* **1985**, *811*, 265–322.

[77] R., W. J.; J., D. B. A.; A., F. N.; H., R. J.; B., G. H. Electron tunneling in biological molecules. *Pure and Applied Chemistry* **1999**, *71*, 1753–1764.

[78] Kraatz, H.-B.; Bediako-Amoa, I.; Gyepi-Garbrah, S. H.; ; Sutherland, T. C. Electron Transfer through H-bonded Peptide Assemblies. *The Journal of Physical Chemistry B* **2004**, *108*, 20164–20172.

[79] Paddon-Row, M. N. Superexchange-Mediated Charge Separation and Charge Recombination in Covalently Linked Donor-Bridge-Acceptor Systems. *Australian Journal of Chemistry* **2003**, *56*, 729–748.

[80] Jortner, J.; Bixon, M.; Langenbacher, T.; Michel-Beyerle, M. E. Charge transfer and transport in DNA. *Proc. Natl. Acad. Sci. U.S.A.* **1998**, *95*, 12759–12765.

[81] Morita, T.; ; Kimura, S. Long-Range Electron Transfer over 4 nm Governed by an Inelastic Hopping Mechanism in Self-Assembled Monolayers of Helical Peptides. *Journal of the American Chemical Society* **2003**, *125*, 8732–8733.

[82] Seyedsayamdost, M. R.; Xie, J.; Chan, C. T. Y.; Schultz, P. G.; ; Stubbe, J. Site-Specific Insertion of 3-Aminotyrosine into Subunit a2 of E. coli Ribonucleotide Reductase: Direct

Evidence for Involvement of Y730 and Y731 in Radical Propagation. *Journal of the American Chemical Society* **2007**, *129*, 15060–15071.

[83] Amdursky, N.; Shalev, G.; Handelman, A.; Litsyn, S.; Natan, A.; Roizin, Y.; Rosenwaks, Y.; Szwarcman, D.; Rosenman, G. Bioorganic nanodots for non-volatile memory devices. *APL Mater.* **2013**, *1*, 062104.

[84] Kumar, S. T. et al. Structure and Biomedical Applications of Amyloid Oligomer Nanoparticles. *ACS Nano* **2014**, *8*, 11042–11052.

[85] Castelletto, V.; McKendrick, J. E.; Hamley, I. W.; Olsson, U.; Cenker, C. PEGylated Amyloid Peptide Nanocontainer Delivery and Release System. *Langmuir* **2010**, *26*, 11624–11627.

[86] Anthis, N. J.; Clore, G. M. Sequence-specific determination of protein and peptide concentrations by absorbance at 205 nm. *Protein Science : A Publication of the Protein Society* **2013**, *22*, 851–858.

ISSN (online): 2246-1248
ISBN (online): 978-87-7112-736-2

AALBORG UNIVERSITY PRESS